LABORATORY STUDIES OF SUBMICRON PARTICLE FORMATION IN PULVERIZED COAL COMBUSTION

Thesis by

Dean Dalton Taylor

In Partial Fulfillment of the Requirements

for the degree of

Doctor of Philosophy

California Institute of Technology

Pasadena, California

1981

(Submitted May 21, 1981)

ACKNOWLEDGEMENTS

To refer to this work as "my thesis" would be a true misnomer, for it represents the combined efforts of many people. I should like to take this opportunity to mention a few of them and offer to them my thanks for their assistance.

First, I have appreciated the chance to work with my advisor, Prof. Richard (Rick) Flagan. His patience and faith in me, his willingness to offer counsel and ideas, and his insights and suggestions when problems were encountered have won my respect and appreciation.

Second, I would acknowledge the guidance and assistance offered by other professors at Caltech. Prof. Rolf H. Sabersky, my master's degree advisor, has always maintained an "open door policy" and I have sought his sound advice on several occasions. Prof. Robert (Bob) Koh is the author of the MAGIC data reduction routines which were used extensively in the preparation of this thesis, and he gave many helpful suggestions in using the computer. Prof. Glen R. Cass offered ideas and suggestions on several occasions for improving the experimental hardware and procedures.

There is also a list of Caltech staff members to whom I owe a debt of thanks for jobs well done. Special thanks go to Elton Daly for his patience, creative ideas, and good judgment, and to his top-notch staff, Joe Fontana, Rich Eastvedt, Dave Byrum, and Leonard Montenegro. I would also like to thank Concetto Geremia for making the thermocouples used in the experiments, the Keck Reference Room librarians, Rayma Harrison and Gunilla Hastrup whose cheerful competence is appreciated by all who know them, and Elaine Granger for her secretarial skill and ability to get things done. Well-deserved thanks also go to Theresa Fall for her outstanding drawings, and to Joanne Mathews and Melinda Hendrix-Werts for their assistance in completing the details of the thesis.

Next, I must say thanks to a long list of fellow students who have struggled to complete their own work and have yet found time to generously offer their time and talents when I have requested it. Among these people are Art Stelson, Connie Senior, Jim Ouimette, Mark Siddoway, Alan Stone, Greg McRae, Bill Brownlie, Wyman Clark, Daryl Roberts, Richard Beatty, Kathy van Ingen, and Jim Young.

I appreciate and acknowledge the support of the following people and agencies in providing funding for this work: (1)The National Science Foundation, which granted me a three-year graduate fellowship and also provided part of the funding for the costs of the research; (2)The Pasadena Lung Association which also supported the research costs; (3)Energy and Environmental Research, Inc. (EER, Santa Ana, Calif.) who provided the coal used in the experiments. Thanks to Mac McComis of EER who coordinated this service.

Finally, I offer heartfelt thanks to those who are closest to my heart, and whose love, understanding, help, and encouragement have sustained me through periods of frustration and discouragement and have enabled me to complete my work at Caltech. These people are my parents, Nile and Margaret Taylor, my brothers, Gary, Brent, and Doug, my sister, Kathleen, and a very true and dear friend, Margaret McDonnel. To them I owe a debt of gratitude.

ABSTRACT

A laboratory furnace was constructed to study the mechanism of submicron particle formation in pulverized coal boilers. Simulation was achieved by matching characteristic kinetic times in laboratory and field units. This was done by matching volumetric heat extraction rates. Reynolds number and geometric scaling were not deemed essential for the simulation.

Combustion-generated submicron aerosols from the laboratory furnace were characterized by size and composition distribution measurements using an electrical mobility analyzer and a low-pressure impactor. Elemental analysis of size-classified mass samples was done by alpha particle-induced X-ray emission spectrum analysis.

The influence of macroscopic combustion parameters on the characteristics of fine particle emissions was investigated. Total submicron particle volume concentration was found to depend on burner type and to increase with temperature for each burner type tested. The particle volume concentration was found to increase with exhaust NO concentration.

The fine particle composition was found to differ from that of larger residual ash particles which generally reflected the composition of the bulk ash. It was also found that combustion conditions (overall fuel-air equivalence ratio and wall temperature) influenced the composition of the smallest ash particles.

Species enrichment data are generally supportive of the vaporization-condensation mechanism of submicron particle formation. Measured dependence of particle volume-mean diameter is consistent with theoretical predictions based on free-molecular Brownian coagulation of particles formed by nucleation of vaporized ash. Strong dependence of submicron particle volume concentration on char particle temperatures in the hot zone further suggests vaporization of ash to be the principal source of material from which fine particles are formed.

A semi-quantitative combustion model was formulated to calculate char particle temperature-time histories in the laboratory furnace. An Arrhenius vaporization rate expression was fitted to the laboratory measurements of total submicron particle volume concentration using the particle temperature histories calculated from the combustion model. Estimates of kinetic parameters were compared with those of other investigators. The model calculations suggest that the mass-specific rate of ash vaporization is strongly dependent on parent coal particle size. This is due to higher burning temperatures of smaller particles together with a high apparent activation energy for ash vaporization.

Recommendations for further work are given.

TABLE OF CONTENTS

LIST OF FIGURES

LIST OF TABLES

NOMENCLATURE

NOTE: In order to keep equations as simple and readable as possible one-letter symbols were used wherever possible; consequently, some letters of the alphabet have multiple meanings. Wherever this is the case the chapter and section in the thesis at which the symbol appears with the indicated meaning is shown in parentheses (e.g., 3:1.2 indicates chapter 3, section 1.2).

a = Particle radius

A = Surface area (3:1.2, 4:2.1)

b = Radial position of edge of boundary layer (1:1.1)

$B(T)$ = Pre-exponential term in Arrhenius rate expression (4:3.0)

B = Constant correction to zero level for chemiluminescent NO analyzer (A:all sections)

B = Particle mobility (B:all sections)

c = Particle number concentration (B:all sections)

c = Molar concentration (4:3.0)

C = Ratio of CO oxidation rate to mass convection rate in the particle near field (1:1.1)

C_i = Conversion factor for EAA current in channel i (A:1.0)

C_k = Surface area/unit mass for particles in size class k (4:2.2)

d = Particle diameter

D = Diameter of duct, pipe, or zone (3:2.1, 4:2.2)

D = Turbulent macroscale or characteristic length (3:1.2)

D = Dilution ratio (A:all sections)

$\mathcal{D}_i$ = Binary diffusion coefficient for species i

E = Activation energy

f = Characteristic frequency for microscale turbulence (3:1.2)

f_j = Mass fraction of species j (B:all sections)

F = Normalization factor to correct aerosol concentrations to standard conditions (A:1.0)

F = Function (4:2.4)

G = Collision rate enhancement factor

$h_i(T)$ = Mass-specific enthalpy at temperature T

Δh_{vap} = Vaporization enthalpy

H_i = Enthalpy flow due to species i

I = Intensity of radiative flux (4:2.2)

I_i = Current output of EAA in channel i (A:1.0)

k = Rate constant (4:3.0)

$k(T)$ = Gas thermal conductivity at temperature T (4:2.1)

K = Degrees Kelvin

K_{EFF} = Effective vaporization rate constant in equation: $dm/dt = -K_{EFF}m$

ℓ = Turbulent microscale

L = Characteristic length

m = Particle mass (4:3.0, B:all sections)

$m(d_p)$ = Mass concentration of aerosol due to particles smaller in diameter than d_p (5:all sections)

$\dot{m}$ = Mass flow rate (4:2.3, 4:2.4, 4:2.1)

MW = Molecular weight

N_i = Molar flow of species i (4:2.1)

N_j = Mean of W_j (C:all sections)

$N(d_1,d_2)$ = Number concentration of particles in size range (d_1,d_2) (A:all sections)

Nt = Number of thermocouple measurements

P = Pressure

q = Energy flow rate (3:all sections, 4:all sections)

q = Volume flow rate of gas (A:all sections)

Q = Energy flow rate (3:all sections, 4:all sections)

Q = Volume flow rate of gas (A:all sections)

r = Radius or radial position

R = Universal gas constant (4:3.0)

R = Slit half width (E:all sections)

R_i = Reaction rate constant for reaction i

Re = Reynolds number

R^2 = Regression coefficient

s = Sticking coefficient

S = Swirl number (5:all sections)

S = Probe collection efficiency (B:all sections)

S = Normally distributed variable of zero mean (C:all sections)

SA_k = Mass-specific surface area of particle in k^{th} size class

St = Stokes number

T = Absolute temperature

U = Velocity

$v(d_p)$ = Volume concentration of particles smaller than d_p (5:3.1)

v_x = Velocity in x-direction (B:all sections)

v_y = " " y- " "

V = Fluid velocity into sampling probe (B:all sections)

V = Volume concentration of submicron aerosol:

$$V = (dv(d_p)/d\log(d_p))\cdot d\log(d_p) \quad (5:3.1)$$

Vol = Volume (3:1.2, 4:2.2)

w_j = Mass of species j in mass sample

W_j = Sum of masses of all species other than species j in mass sample (C:all sections)

W = Mass loss parameter (2:1.1)

x = x coordinate (B:all sections)

x = Mole fraction (4:2.1, 4:2.4)

y = y coordinate

Y = Mass fraction H_2O

Greek Symbols:

α = Constant

β = Pre-exponential term in Arrhenius rate expression

Δ = Incremental value

ε = Normally distributed variable of zero mean (A:all sections, B:all sections)

ε = Radiation emissivity (4:2.2, 4:2.4)

ξ = Dimensionless radial coordinate

ϕ = Fuel-air equivalence ratio (5:all sections)

ϕ = Angle between surface normal and direction of radiated energy (4:all sections)

γ = Concentration of NO in span gas used in calibration of NO instrument

κ = Absorption coefficient for radiation

μ = Viscosity (absolute)

Ω = Solid angle

ρ = Density (4:2.3)

ρ = Reflectivity (4:2.4, 4:2.1)

σ = Standard deviation

σ = Stefan-Boltzmann constant (4:all sections)

ν = Viscosity (kinematic)

ζ_i = Standard deviation of EAA current difference ΔI_i

Subscripts:

adv = Advective transport term

cond = Conductive " "

ei = Entrainment air for zone i

g = Gas

isec = Secondary air zone corresponding to zone i

p = Particle

pre = Preheat

prod = Products of reaction

w = Wall

CHAPTER 1

INTRODUCTION

1.0 SUBMICRON EMISSIONS FROM PULVERIZED COAL BOILERS

Current trends in development of energy resources calls for increased use of coal. One of the several current coal utilization technologies is the combustion of pulverized coal in utility boilers. Among the problems currently under study in applying this technology is its potential environmental impact.

A major environmental concern in pulverized coal combustion is the emission of particulate flyash. Using current particulate removal technologies a high percentage of the total suspended particulate matter can be removed from utility boiler exhaust gases. However, collection efficiency curves for fiber filters and electrostatic precipitators typically show a characteristic minimum for particle sizes around 0.1 to 1.0 microns (Friedlander, 1977), indicating the submicron particles penetrate such stack cleaning devices more readily than do larger particles. As a result, the particle size distribution is shifted toward smaller particle sizes than those which enter the control device. Consequently, while removing all but a small percentage of the flyash, on a mass basis, these devices permit large numbers of smaller (but much less massive) particles to escape into the atmosphere.

Fine particles represent a greater health risk than larger particles. Studies of aerosol deposition in flow passages which simulate those of the human lung have shown that the particles which are least efficiently removed by natural mechanisms before entering the alveolar sacs are, again, those in the 0.1 to 1.0 micron range (Bell, 1974). Thus, the particles which are most difficult to control in emissions from pulverized coal boilers are also those which are most effective in penetrating the body's natural filtering system.

Field studies of flyash composition as a function of particle size have shown dramatic enhancement of concentrations of volatile trace metals with decreasing particle size in flyash samples from pulverized coal boilers (Davison, et al., 1974). Since many such species are generally considered toxic, the need for controlling the emissions of submicron particles from pulverized coal combustion sources is further emphasized.

2.0 CONTROL OF SUBMICRON FLY ASH

There are generally two approaches to improving control of submicron particle emissions:

1. Through improvement of stack cleaning devices to improve collection efficiencies for submicron particles;
2. Through control of the formation of such particles during the combustion and cooling processes which precede the stack cleaning devices.

The latter approach may prove to be the most efficient and/or cost-effective, however, its application requires an understanding of the influence of various combustion parameters on the characteristics of the suspended particulate matter which leaves the combustor. This, in turn, requires an understanding of the basic mechanisms by which the fly-ash particles are formed. The work described herein has been directed toward this understanding.

3.0 OBJECTIVES OF PRESENT WORK

Specifically, this work has had the following major objectives: (1)To generate laboratory data on submicron flyash characteristics to aid in understanding the relation between fine particle emissions and macroscopic combustion conditions; (2)To discuss one of the currently-proposed mechanisms of submicron particle formation in pulverized coal combustion (vaporization-condensation mechanism) in light of the aforementioned data.

The presentation is organized as follows:

Chapter 2 is a discussion of some of the work reported to date relating to the problem of fine particle emissions from pulverized coal furnaces. Specific topics include the following: (1)An overview of ash behavior during pulverized coal combustion, (2)Coal mineral matter transformations, (3)Submicron particle formation mechanisms, (4)Ash vaporization.

Chapter 3 is a description of the laboratory experiments conducted in this investigation. The basic scaling considerations used in the design are first presented, followed by a detailed description of the components of the laboratory-scale combustion facility. The experimental procedure is described, together with some of the problems encountered, during the experiments.

Chapter 4 discusses the elements of the model used to describe the process of submicron particle formation. The discussion consists of two parts: (1)The combustion model used to describe the burning history of individual char particles. Part one also discusses the other models which were used to supply the necessary inputs to the particle combustion model; (2)A brief description of the Arrhenius rate law used to describe the vaporization process whereby condensable mineral vapors are formed during the combustion process. The model postulates that the bulk of the mass of submicron-size flyash particles, as well as a portion of the surface layer of larger, residual ash particles, originate through homogeneous nucleation and heterogeneous condensation of these mineral vapors.

Chapter 5 presents the results of the experiments. Statistical regression results are discussed together with their implications regarding the relative significance of some of the factors in fine particle formation. Laboratory measurements of total submicron particle mass concentrations are compared with field measurements and the relation between particle and NO concentration in exhaust emissions is discussed. Chapter 5 also discusses laboratory data on fine particle composition and its significance to the postulated vaporization-condensation model for particle formation.

Chapter 6 is a summary of the significant results of this investigation. The author's recommendations for further work in the area are also presented.

Appendix A is a description of the assumptions and rationale used in the error analysis of the particle concentration data. Appendix B discusses some specific aspects of the performance of the sampling system utilized in the laboratory experiments. Appendix C describes the assumptions and analysis used in obtaining confidence limits for species mass fraction calculations from aerosol composition data, discussed in Chapter 5. Appendix D is a discussion of the discrepancy between aerosol mass measurements indicated by the two techniques used to obtain these measurements, viz., use of an electrical mobility analyzer, and collection and elemental analysis of size-classified mass samples using a cascade impactor. Appendix E deals with the error involved in neglecting dissociation of gases in the computer modeling calculations discussed in Chapters 4 and 5. Finally, Appendix F is a tabulation of the experimental data discussed herein.

CHAPTER 2

LITERATURE REVIEW

1.0 OVERVIEW OF PULVERIZED COAL COMBUSTION AND ASH FORMATION

In this section is a brief summary of work reported in the literature relating to ash behavior during pulverized coal combustion processes. The author acknowledges having utilized the review prepared by Flagan and Friedlander (1976) in assembling this overview.

1.1 COMBUSTION PROCESSES

Coal burned in suspension in pulverized coal utility boilers is first crushed and ground to a fine powder form in large pulverizing mills (Breen, 1976; Field, et al.,1967). Depending on the particular installation, the mass mean diameter of the particles generally varies between 30 to 70 microns. Nearly all the mass of the coal is contained in the size range from 10 to 100 microns. The characteristic time for complete burnout of a 100-micron carbon particle is on the order of one second, and pulverized coal boilers are designed to achieve residence times at least this long.

The pulverized fuel is entrained in a primary air stream (usually comprising about 1/5 of the total combustion air) and is fed into several burners supplying the furnace. The remainder of the combustion air is pre-heated and fed into the burner registers coaxially with the primary fuel-air stream. The mixture is ignited by thermal radiation, and by mixing with the hot products of combustion inside the furnace. Mixing is generally slow inside the furnace and compostion non-uniformities within the furnace probably give rise to a broad spectrum of temperature and mixture composition.

Upon injection into the hot furnace environment, the coal particles experience heating rates of the order of 10000 C/sec, or more (Field, et al., 1967). At high combustion temperatures the coal begins to decompose, producing tars, carbon monoxide, carbon dioxide, hydrogen, water vapor, and various hydrocarbons. At the high heating rates experienced in pulverized coal furnaces, this early decomposition-devolatilization process takes place in a comparatively short time, generally being complete within 0.1 sec of the time of entry into the furnace. The coal particles also swell and become porous to varying degrees during the heating process, depending upon the coal type.

The residual carbon (char) burns comparatively slowly after devolatilization. Several theoretical models have been developed to investigate the influence of various parameters on the char burning process. Libby and Blake (1979) used the limiting cases of infinitely-fast and infinitely slow CO oxidation rates in formulating a numerical model for char particle combustion. They modelled particle combustion in an infinite quiescent medium, and assumed unity Schmidt and Lewis numbers, constant gas viscosity, and used kinetic coefficients of Field, et al. (1967) and Dobner (1976) to describe the heterogeneous oxidation of carbon at the char particle surface. Assuming wall temperatures of 1500 and 2000 K, O_2 mass fractions of 0.2 and 1.0, zero mass fractions of CO_2 and CO in the far field of the particles, and a gas temperature sufficient for carbon oxidation to occur (i.e., greater than 1000-1200 K), particle burning histories (temperature, burning rate, diameter) were calculated.

Their results indicated that under many conditions of interest particle burning rates are nearly diffusion-limited and that particle temperatures are from 1.3-2.0 times the ambient temperature, depending on whether slow or fast CO oxidation is assumed, and whether or not radiative heat transfer is assumed operative. In order to determine the extent of CO oxidation near the particle they defined a parameter, C, as the dimensionless ratio of the CO oxidation rate to the rate of mass convection in the near field:

$$C = (7\text{x}10\ )Y_{H_2O}(Pa\ \xi)^2 T^{-2} \exp(-15{,}000/T) W^{-1} \qquad (2.1)$$

where:

Y_{H_2O} = Mass fraction of water

P = Ambient pressure

T = Gas temperature near particle

ξ = (radius of region)/(particle radius)

W = Dimensionless mass loss parameter

= (mass flux from particle surface) x a/(gas viscosity)

a = Particle radius

Using this parameter, they determined those conditions for which the infinitely-slow and infinitely-fast kinetic assumptions are reasonable. However, calculations of the parameter C for conditions typical of the laboratory combustor used in these experiments (T=1800-2500 K, W=0.05-0.10, a=25 microns, Y_{H_2O}=.024-.048) gave values from about 2. to 500. Thus one could not conclude from this test whether one or the other of the two extreme kinetic assumptions is valid.

Mon and Amundson (1978) investigated combustion of carbon particles using a slightly-different model. They neglected Stefan flow and assumed a finite boundary layer thickness with uniform free-stream conditions outside the layer. Two values of the boundary layer thickness were used in the calculations; the first calculation assumed the thickness was equal to the particle diameter, and the second assumed a thickness given by Schlichting (1968):

$$(b-a) = 1.5a\sqrt{\nu/U_0 a} \qquad (2.2)$$

where:

a = Particle radius

b = Radius of edge of the B.L.

ν = Viscosity of fluid surrounding particle

U = Velocity of gas flowing past the particle (assumed to be 25 cm/sec, or approximately the sedimentation velocity of 100-micron particles of specific gravity 1.0 in air at 25 C).

In the model, particles were either assumed to radiate to a black wall at 1500 K, or to a black cloud of particles whose effective radiating temperature was 1400 K. Surface carbon oxidation kinetics were treated using kinetic expressions of Field, et al. (1967), Dutta, et al. (1975), and Howard, et al. (1973). Finite-rate CO oxidation in the boundary layer was treated using the kinetic expression of Howard, et al. (op cit.).

Calculations were performed for O_2 concentrations up to 21%, CO_2 concentrations to 5%, and bulk CO concentration was assumed to be zero. Results of these calculations indicated that oxidation of CO to CO_2 in the near field of particles less than 100 microns in diameter was negligible. The authors concluded that in the combustion of pulverized coal it may be assumed that CO oxidation takes place in the far field of the particle (i.e., in the free stream far from the particle surface).

Field, et al. (1967) performed a much simpler calculation assuming finite rate CO oxidation in the region near the particle. Using CO and O_2 profiles calculated assuming diffusion-controlled surface oxidation of carbon in the rate expression, a gas temperature of 2000 K, and free-stream O_2 and H_2O concentrations of 0.10 and 0.05 (by volume), respectively, Field's results indicate that for particle diameters less than 50 microns, the CO oxidation in the region near the particle is slight, while for 100-micron particles the CO oxidation becomes significant.

Based on the foregoing analytical descriptions it was assumed in the particle combustion calculations of the present study (See Chapter 4) that CO is not oxidized until it reaches the free stream region; i.e., the only effect of CO oxidation is on the temperature of the gas far from the particle surface.

1.2 MINERAL MATTER IN COAL

In addition to the combustible species in coal, pulverized coal particles contain non-combustible mineral matter. This mineral matter may be classified as follows (Reid, 1971):

1. Inherent mineral matter, which seldom exceeds 2% of the coal mass, is derived from the original plant substance;

2. Extraneous mineral matter, which was mixed with the coal during

the forming process;

3. Extraneous mineral matter, which was mixed with the coal during mining operations.

The mineral matter is present as fine inclusions in the coal matrix, or as large, distinct particles. Padia (1976) has reported measured mean volume diameters of 1.7 and 2.0 microns for mineral inclusions in a lignite and a bituminous coal, respectively. Mineral matter in coal consists primarily of kaolinite ($Al_2O_3 \cdot 2SiO_2 \cdot 2H_2O$), pyrites ($FeS_2$) and calcite ($CaCO_3$) (O'Gorman and Walker, 1971; Reid, 1971). The major elements in the coal minerals are those found in silicate rocks, Si, Al, Ca, Mg, Fe, S, Na, K, Cl, and Ti (Ruck, et al., 1974).

When coal is heated, the mineral matter undergoes a number of transformations (Mitchell and Gluskoter, 1976). At temperatures below about 500 K, dehydration and changes in mineral form occur. Pyrite is oxidized at temperatures below about 800 K. Carbonates and sulfates decompose at temperatures in the range 500 to 1100 K, evolving CO_2, SO_2, and SO_3. Alkali salts, such as chlorides, are volatilized at an appreciable rate when the temperature exceeds about 1350 K. Mercury and other extremely volatile ash components may be vaporized during the early phases of heat-up and combustion. Later, during the char burnout process, the more refractory species may fuse and vaporize, depending on the particle temperature-time history and the viscosity and vapor pressure curves of the respective components. Fusion temperatures of typical mineral components of coal ash range from 623 K (K_2O) to 2288 K (Al_2O_3) (Raask, 1969).

Ramsden (1969) has postulated that mineral inclusions melt within the carbon lattice as the combustion front approaches. Water vapor, carbon dioxide, and other gases are evolved due to the temperature rise. If the heating occurs rapidly, pressure increase within an inclusion may cause it to shatter into minute droplets. If the particle temperature is not high enough for complete fusion to occur sintering of several inclusions may occur as the carbon matrix disintegrates during burnout.

Hollow, spherical flyash particles known as cenospheres may form if gas evolution occurs within the particles and mineral temperatures are sufficiently high for fusion to occur but not high enough to permit bursting due to rapid expansion with low viscosity (Raask, 1968; Padia, 1976; Fisher, et al., 1976). Cenospheres generally comprise about 5% of the mass of flyash retained in power plant precipitators (Natusch and Taylor, 1980). Large cenospheres which contain other flyash and/or char particles have also been observed (ibid.; Fisher, et al., op cit.).

It is possible that the production of most of the particulate matter from pulverized coal combustion can be modeled by considering only a few of the processes described above. After initial chemical transformations of the mineral species, mineral inclusions begin to fuse and eventually coalesce as the carbon matrix is consumed and the inclusions come into contact with one another. At some point during the char burnout, the entire matrix (carbon and mineral matter) may break apart (due to internal burning and/or gas expansion within inclusions), giving rise to several fused ash particles.

Padia (1976) collected flyash particles from the combustion of pulverized coal particles, and demonstrated the relationship between the parent coal particle size distribution and the size distribution of the residual ash particles larger than a micron in diameter. Two size cuts, 38 to 45 microns, and 75 to 90 microns, of two coal types (A Pennsylvania bituminous coal and a Montana lignite) were used. Padia's measured size distribution of ash particles was well-correlated with the size distribution of the parent coal particles, by assuming 3 ash particles formed per lignite particle and 5 ash particles formed per bituminous coal particle. The number of ash particles produced did not vary significantly over this limited range in coal particle size.

Flagan (Flagan and Friedlander, 1976) has used the above breakup model to correlate the coal particle size distribution of Littlejohn (1966) with the measured residual ash particle size distribution reported by McCain, et al. (1975), normalized with respect to the total mass of aerosol expected from a coal containing 10% ash burned at a fuel/air equivalence ratio 0.85 (15% excess air). It was assumed that no ash was lost to the boiler walls. Reasonable agreement was obtained between the model prediction and the measured ash size distribution for particles larger than one micron.

2.0 SUBMICRON PARTICLE FORMATION

Observed particle size distributions of flyash particles larger than a micron may be correlated with the parent coal particle size distributions using a coalescence-break-up model. Flagan (op cit.) has indicated, however, that the high measured number concentrations of submicron-sized particles are difficult to explain with this model, indicating that another mechanism is responsible for the production of these smaller particles. A growing body of laboratory and field data (Davison, et al., 1974; Ragaini and Ondov, 1975; Coles and Prentice, 1979) indicates significant enhancement of mass concentrations for certain volatile ash components with decreasing particle size. Such trends are suggestive of vapor depositon and/or homogeneous nucleation of vaporized ash components. Mass-specific surface deposition rate by condensation varies inversely with particle diameter in the free-molecular regime and inversely with diameter squared in the continuum regime (Flagan and Friedlander, 1976). Thus, one would expect increasing mass concentrations of condensed species with decreasing particle size. Similarly, one might expect that homogeneous nucleation of vaporized species would result in higher mass-specific concentrations of volatile species in smaller particles than in larger ones, since, under these circumstances, the smallest particles would be composed exclusively of vaporized species. Flagan and Taylor (1980) assume that the principal source of submicron ash particles in coal combustion is homogeneous nucleation of vaporized species in regions of the furnace where vapor saturation ratios are sufficiently high.

Two models for condensation of ash vapor have been proposed. Davison, et al. (1974) have proposed an adsorption mechanism, which predicts a $1/d_p$-dependence on particle diameter (d_p) of mass concentration of condensed species. Flagan (op cit.) has shown that a $1/d_p^2$ -dependence would be predicted by a simple condensation model of vapor deposition in the continuum regime. He also indicated that available data show equally-good correlations using either model, indicating that neither model is clearly more accurate. Biermann and Ondov (1980) analyzed size-segregated ash samples using neutron activation techniques, and attempted to correlate the data using the two vapor deposition models discussed above. Their data were better correlated by the $1/d_p^2$ model.

Biermann and Ondov also deduced the thickness of the vapor-deposition layer by application of the models to their measured mass distributions with respect to particle size. They concluded that the maximum particle size for which the thickness of the deposition layer was at least equal to the particle radius was 0.045 microns, suggesting a possible upper bound on the size of particles formed entirely from vaporized species.

The above models for surface deposition of vaporized ash species assume the presence of a pre-existing aerosol upon which deposition takes place, including particles smaller than the expected residual ash particles. Two models have been proposed to explain the origin of these fine particles; they are discussed below and in the next section.

As discussed in an earlier section, a certain (usually small) percentage of the mass of the fly ash is present in the form of large, hollow spheres, known as cenospheres. If the particle temperature reaches a sufficiently-high level at some point, the viscosity of the ash forming the outer surface of a cenosphere may be low enough for the gas pressure within the sphere to cause it to burst. Such bursting may then produce ash fragments much smaller than the original particle. Smith, et al. (1979) have suggested that this cenospere bursting is the principal mechanism of formation of the submicron particles, which then act as condensation and/or adsortion sites for vapor deposition of volatilized ash components.

2.1 VAPORIZATION OF MINERAL MATTER IN COAL

Physical transformations of mineral matter in coal ash have been studied by several people. Raask (1969) investigated the viscosity-temperature relationship of various composites consisting of typical metal oxide components of mineral matter in coal. He measured temperatures at which definite morphological transformations occurred for these composite materials and for mineral matter in coal. Measured fusion temperatures for the composites were from 1275 to 1545 K, while those of the coal sample were from 1750 to 1975 K, with the bulk of the particles (approx 85%) fusing between 1575 and 1725 K. These data are interesting from two standpoints:

1. They indicate that fusion of mineral matter in coal does occur in pulverized coal furnaces.

2. The fact that fusion temperatures and viscosities of the composites were significantly different from those of the coal mineral matter indicate that mixture effects can be significant in predicting characteristics of flyash from the characteristics of the component species.

As particle temperatures rise above those required for fusion to take place thermodynamic considerations predict a monotonic rise of vapor pressure above the fused species with temperature. If thermodynamic data for the mineral composites in ash were available, vaporization rates could be calculated from diffusion equations, provided it may be assumed that thermodynamic liquid-vapor equilibrium is maintained at the particle surfaces.

Desrosiers, et al (1978) have formulated a transport-limited model to predict the masses of Si, Al, Ca, and Fe which are vaporized during combustion of coal in pulverized coal and cyclone-fired coal boilers. Their treatment incorporates a combustion model and assumes equilibrium concentrations of all species at the coal surfaces (For details of the combustion model and equilibrium calculations see Desrosiers, 1977). Diffusivities are calculated from molecular parameters and species are assumed to oxidize to stable forms after transport to the oxygen-rich bulk phase.

Agreement between measurements of fine particle elemental composition and model predictions is fair in the case of SiO_2 and FeO; in the case of Al_2O_3 and CaO, dicrepancies are between two and three orders of magnitude. The authors point out, however, that there are significant uncertainties in the calculation. Among these uncertainties are the following:

1. Errors in assumed ash temperatures, which can result in a two-fold (or more) change in the predicted amounts vaporized;

2. The assumption of vapor-liquid equilibrium between molten ash and metal-containing gases at the particle surfaces, which may not be fully justified;

3. Thermodynamic data used in the equilibrium calculations, which

may be in error;

4. The surface area of the exposed ash, which directly influences the net vapor transport rate and which is not well known.

Raask and Wilkins (1965) have demonstrated the influence of the presence of reducing species in the vaporization of silica (SiO_2). They compared measured losses of silica in slag from two types of experimental gasifiers (fixed bed and suspension) with predictions based on thermodynamic calculations of silicon vapor pressures for various assumed equilibria. Their results indicated that direct vaporization of SiO_2 cannot account for the measured losses of silica due to vaporization. Calculations for the possible reactions between SiO_2, CO, SiC, SiO, and Si metal showed that vaporization of silica in coal combustion probably takes place by reduction of SiO_2 to the more-volatile SiO. This reduction (which occurs in the reducing environment inside or on the surface of the coal particle) is followed by vaporization of the SiO at the particle surface, transport to the gas phase, and re-oxidation of the SiO when it reaches the lower gas temperatures and higher oxygen concentrations found far from the particle surface in the free stream.

Good agreement between predicted vapor pressures of SiO and pressures inferred from measurements of silica losses in a two fixed bed gasifiers studied was obtained by considering the reduction of SiO_2 in the presence of CO, CO_2, H_2, and H_2O, and the associated equilibria.

Neville, et al. (1980) have noted the influence of coal composition on the vaporization rates of mineral matter. In well-controlled laboratory experiments using an externally-heated laminar furnace, measurements of vaporization rates were performed by collecting the entire effluent stream from the furnace, size-segregating the aerosol, and then analyzing the samples for elemental composition. These investigators made the following observations:

1. Ash obtained using the A.S.T.M. procedure and fed into the furnace yielded smaller rates of vaporization than did coal, at the same temperature, suggesting that the char matrix and/or gas composition near the particle surface enhances vaporization. This is consistent with the reported results of Raask and Wilkins (op cit.).

2. Experiments performed using three different coals showed wide variation in the composition of the fine particles. This was attributed to the vaporized species. Although SiO_2 was the predominant mineral component in both the lignite and the bituminous coals tested, it was the predominant component in the fine particles only in the case of the bituminous coal. MgO was the predominant specie in the lignite. It was concluded that the presence of acidic and/or basic components

in the coal may significantly influence the activity coefficients of various mineral components.

2.2 TEMPERATURE EFFECTS ON VAPORIZATION PROCESSES

It is clear that the total mass vaporized of any given component is the sum of the vaporization rates of all species integrated over the time the coal is at high temperature in the furnace and/or cooling sections of the boiler. Since the vaporization rate of any substance in a given mineral mixture increases monotonically with temperature (both the equilibrium vapor pressure at the particle surface, and the transport rate away from the particle should increase with temperature), one would expect a strong dependence of the fraction vaporized of any given ash component on temperature.

Mims, et al. (1979) studied ash vaporization kinetics for a Montana lignite coal using an externally-heated laboratory furnace. The entire exhaust stream from the furnace was sampled, and size-classified aerosol samples were analyzed for elemental composition using neutron activation, atomic absorption, X-ray fluorescence, and energy dispersive X-ray analysis. Particle temperatures were calculated assuming oxidation of char to form CO at the particle surface, and oxidation of CO was assumed to occur far enough from the particle surface that it did not influence the particle temperature. Calculated particle temperatures were found to be in satisfactory agreement with temperatures measured using an optical pyrometer. Vaporization rates were measured by assuming all material in particle sizes smaller than 0.52 microns (aerodynamic diameter) was formed from vaporized matter.

Mims' results are summarized as follows:

1. The fraction of the total ash vaporized at particle temperatures between 1500 and 2600 K varied from approximately 0.03 to 0.2.

2. Changes in the fraction vaporized for individual species over the range of particle temperatures studied ranged from a factor of 75-100, in the case of Ca, to a factor less than 2, in the case of Na.

3. Consistent with a transport-limited vaporization model, vaporization rates were found to vary inversely with particle temperature. Using the transport-limited model effective heats of vaporization for various ash species were determined from the Arrhenius plots.

4. Model predictions of the dependence of vaporization rate on particle size were in good agreement with experimental data.

In the previously mentioned work of Neville, et al. (op cit.), studies similar to those of Mims were conducted. For comparable ranges of particle temperature (1800 to 2800 K), the fraction of the total ash vaporized ranged from 0.1%, at the lower temperature, to 20%, at the higher. As already indicated, measured composition of submicron aerosols from three coal types studied (Montana lignite, Montana sub-bituminous, and Illinois bituminous) varied widely, though mass concentrations of mineral species reported were comparable in the parent coals.

2.3 SUBMICRON PARTICLE FORMATION FROM VAPORIZED SPECIES

Since significant quantities of mineral species in coal ash may be vaporized during char combustion, the fate of this vaporized material during and after transport to the gas phase is next considered.

Various possible mechanisms of vapor condensation have been considered in the literature. Detailed analytical calculations have been done by Im and Chung (1980) which are illustrative of the possible mechanism of vaporization-nucleation in the formation of submicron particles from coal combustion. They modeled the evolution of ash particles originating in the combustion chamber preceding an MHD channel and diffuser, treating only the processes of vaporization, condensation, and nucleation of condensable vapor, and assuming vapor-liquid equilibrium at the surfaces of droplets of a hypothetical coal ash.

Nucleation rates were calculated as a function of position in the MHD channel. Two different assumed mass fractions of slag from the combustor and two different temperature profiles inside the channel were used in the calculations.

Conclusions are as follows:

1. Decreasing temperature in the channel and diffuser results in the vapor saturation ratio increasing to levels sufficiently high to initiate nucleation of vapor.

2. The location at which the nucleation occurs depends strongly on both the assumed temperature profile and the mass fraction of ash carried over from the combustion section.

3. Using an initial particle size distribution assumed to have a single mode with a mean particle diameter of 4 mm, the final size distribution is bi-modal, with the larger mode peak occurring between 1.0 and 5.0 microns. The shape of the distribution is strongly dependent on the mass fraction of ash carried over from the combustor, and relatively weakly dependent on both the temperature profile in the channel-diffuser, and the location (spatial or temporal) at which nucleation begins.

The work of Im and Chung is not directly applicable to the problem of generation of submicron aerosols in pulverized coal combustion because the assumed temperatures in the MHD channel are considerably higher than particle temperatures in pulverized coal combustion. Moreover, the model used in their study does not incorporate coagulation which is likely to be important in determining the final aerosol characteristics.

A general description of the nucleation, growth, and coagulation processes could be accomplished (in theory) through solution of the general dynamic equations for nucleation, condensation, and coagulation, treating all possible inter- and intra-particle interactions. Investigations to date utilize considerable simplifications of these equations in order to make the equations tractable.

Flagan (1978) has constructed a model for submicron particle evolution by assuming a known fraction of total ash is vaporized early in the combustion process and nucleates instantly forming large quantities (known) of molecular-size monomers. These monomers are assumed to be uniformly distributed across the cross-section of the combustor, and back-mixing in the combustor is neglected; i.e., plug flow is assumed. Particle interaction is assumed to take place through Brownian motion, augmented by inter-particle dispersion forces (Van der Waals forces), and all collisions result in instant coalescence. The general dynamic equation (GDE) for coagulation is simplified by using the self-preserving assumption (Lai, et al., 1978) to represent the particle size distribution in the equation. This assumption reduces the three-dimensional, time-dependent GDE to an ordinary integro-differential equation, and neglects condensational growth of particles. Numerical solutions to this equation have been published in the literature (ibid.).

Assuming that 1.0% of the total ash vaporizes and condenses homogeneously, the final particle size distribution of the flyash from a pulverized coal furnace was calculated and compared with measured size distributions (McCain, et al., 1975). The peak in the number distribution obtained was between one and two orders of magnitude higher than what was measured. This discrepancy is discussed in a paper by Flagan (1978). He considers the potential effects of interparticle dispersion forces and mixture inhomogeneities in reducing the number concentrations of fine particles, but concludes that neither of these mechanisms is probably responsible for all the above discrepancy. Flagan concludes that species (e.g., soot, sulfates) and mechanisms other than those considered may play a significant role in fine particle formation. This suggests the need to determine the chemical nature of the fine particles.

The model used by Flagan was also used in the present investigation to represent submicron particle growth in the laboratory furnace (Taylor and Flagan, 1980). Model predictions of submicron particle size distribution (based on a certain percentage of ash vaporized, inferred from mobility analyzer measurements) were again compared with measured distributions, obtained using an electrical aerosol analyzer. The assumption of homogeneity of the aerosol mixture across the furnace cross-section may be more reasonable for the laboratory furnace than for a full-scale boiler. The calculated number distribution in this case compared quite favorably (both the number concentration peak and the peak particle size) with inverted data (Twomey,1975) from a particle mobility analyzer (EAA).

Neville, et al. (1980) have also measured submicron particle size distributions. The sizes of particles collected on total filters were determined using an electron microscope with an automated image analyzer. The measured volume-mean particle diameter of the ash was measured at different axial positions in the externally-heated laminar furnace (corresponding to different residence times). Volume-mean particle sizes were calculated using the same assumptions as Flagan (1978). Calculated and measured profiles of mean particle size at various positions in the furnace show reasonable qualitative agreement. However, the measured profile suggests that the parameter s x G (sticking coefficient times rate enhancement factor, due to dispersion forces), which was assumed constant in the calculation, may vary from furnace entrance to exit.

Volume mean particle diameters at the furnace exit measured by Neville, et al., reflect a linear dependence on the fraction of ash vaporized raised to the 2/5 power. This is consistent with Friedlander′s predictions (Friedlander, 1977) using using the self-preserving model for long coagulation times.

Ulrich and co-workers (Ulrich, 1971; Ulrich, et al., 1976; Ulrich and Subramanian, 1977) studied the formation and growth of SiO_2 particles in oxide synthesis flames. They measured surface areas of laboratory-generated aerosols using gas adsorption techniques for various concentrations of silica, flame temperatures, residence times of particles in the flame, etc. Measurements were compared with values which were calculated by assuming (1)that nulceation of SiO_2 occurs when it is formed in the oxide synthesis process in the flame; (2)that particles grow by the mechanism of Brownian coagulation (no condensational growth); (3)that particles which collide either coalesce instantly, or separate, unchanged by collision. The sticking coefficient (or the fraction of collisions which result in coalescence) was treated as an adjustable parameter in the model.

Agreement between the measured values of surface area and the values predicted from the model was unsatisfactory unless a sticking coefficient of 0.004 was assumed, which value seemed unrealistic. However, observations of flocculated clusters of small particles in samples from a silica-yielding flame suggested that the assumption of instantaneous coalescence upon collision may be a poor assumption, and that a more detailed treatment of the process of coalescence in the growth model might yield better predictions.

In a later publication, Desrosiers, et al. (1978) suggested that coalescence is the limiting step in silica particle growth. This is attributable to an anomalously high viscosity of SiO_2. Using a transport-limited equilibrium model to compute vaporization rates, and assuming that nucleation of vapors occurs at some point in the combustor, they formulated a collision-coalescence model to predict particle morphology and composition in a cyclone-fired boiler. This model postulates that particles agglomerate by Brownian coagulation to form aggregates (or flocs). The primary particles constituting these flocs coalesce to form larger secondary particles and the rate of this coalescence is limited by the viscosity of the particles. In treating the particle coagulation equation in the model the particle size distribution is assumed to be monodisperse.

Results of the particle composition predictions were discussed earlier. The results of the comparison of measurements and predictions of particle morphology are:

1. Particles are predicted to be aggregates composed of primary particles approximately 0.04 microns in diameter. This value is somewhat lower than the measured size (approximately 0.06 microns) from electron micrographs.

2. The predicted number of primary particles in each aggregate is from four to eight. The number indicated by electron micrographs is about 10.

Ulrich, et al. (1977) have used the Brownian collision-coalescence model to describe the growth of aggregates in a laboratory silica-producing flame. It is pointed out that the collision cross-section of an aggregate, though slightly dependent upon surface area, is primarily a function of the mass. Thus, using the collision-coalescence model, predictions of mean particle mass as a function of growth time are made for various silica concentrations in the flame. Predictions show a very sharp decrease in growth rate as particles grow out of the free-molecular region into the continuum regime. Ulrich's laboratory measurements suggest a much narrower transition regime than that proposed by Fuchs (See Hidy and Brock, 1965). Ulrich plotted particle size predictions together with the prediction based on the Fuchs extrapolation, and with the experimental particle size vs. growth time profiles, as measured by laser light scattering. Measured values fall between the two predictions.

CHAPTER 3

EXPERIMENTS

1.0 OVERVIEW

1.1 INTRODUCTION

This chapter discusses the following aspects of the experimental program of the present investigation:

1. An overview of the philosophy and rationale used in the design of the laboratory system;

2. A discussion of the experimental system, including descriptions of the specific design objectives, the components of the laboratory combustion facility, and the sampling system;

3. A summary of the experimental procedures, including preliminary tests, problems encountered during the experiments, rationale of experiments, and details of the experimental procedures utilized in obtaining the data.

1.2 SCALING CONSIDERATIONS

Figure 3.1 is a conceptual diagram illustrating the processes that occur during combustion of pulverized coal. In designing a laboratory furnace to investigate the influences of macroscopic combustion parameters on such processes it was concluded that, because of the complexity of the chemical processes occurring during combustion it would not be feasible to scale the characteristic kinetic times associated with these processes. For this reason, it was necessary to duplicate these kinetic times by matching the particle temperatures achieved in full-scale systms. To accomplish this it was necessary to match (approximately) volumetric heat extraction rates between the two systems.

The major mode of heat transfer from the flame to the walls is radiation. For scaling purposes, the volumetric heat extraction rate by radiation from the combustor may be crudely written as:

$$Q = (T_g^4 - T_w^4)A/Vol \qquad (3.1)$$

where:

T_g = Gas temperature

T_w = Wall temperature

A/Vol = Surface area/Volume ratio inside combustor cavity.

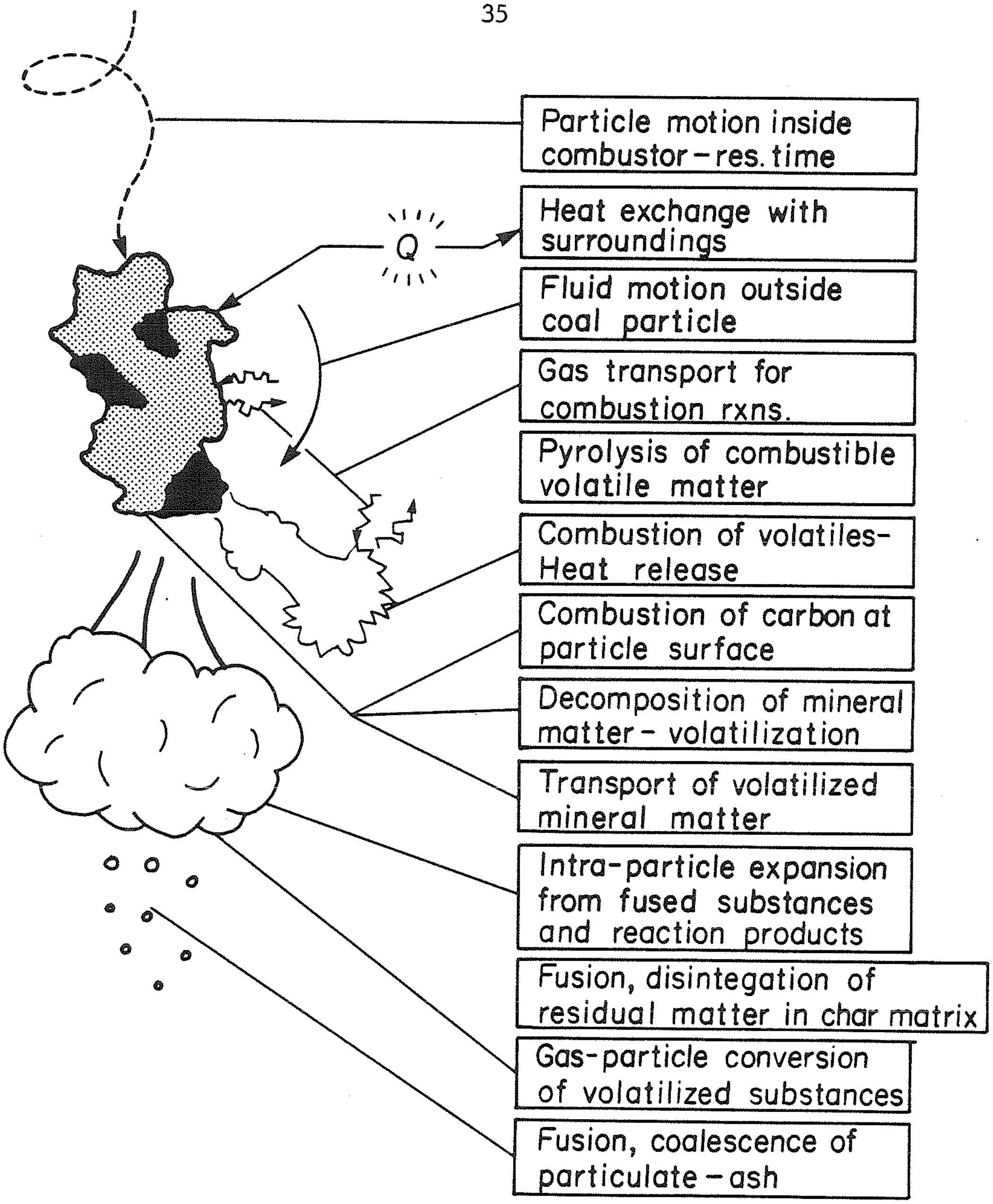

Figure 3.1: Schematic representation of micro- and macroscale processes occurring during combustion of pulverized coal.

Thus, if T_g is the same in both the laboratory and the full-size systems, and if:

$$(A/Vol)_{lab} >> (A/Vol)_{full\text{-}size} \tag{3.2}$$

then to achieve:

$$(Q)_{lab} = (Q)_{full\text{-}size} \tag{3.3}$$

it is required that:

$$(T_g^4 - T_w^4)_{lab} << (T_g^4 - T_w^4)_{full\text{-}size} \tag{3.4}$$

That is, since $T_g > T_w$, then:

$$(T_w)_{lab} > (T_w)_{full\text{-}size} \tag{3.5}$$

Taking $(T_w)_{full\text{-}size}$=900 K, T_g=2000 K, $(A/Vol)_{lab}=1m^{-1}$, $(A/Vol)_{full\text{-}size}=0.1m^{-1}$, in the above expressions for $(Q)_{lab}$ and $(Q)_{full\text{-}size}$, and equating the two values yields:

$$(T_w)_{lab} = 1950\ K. \tag{3.6}$$

Thus, for the laboratory system, it was required to achieve much higher wall temperatures than for the full-size system being simulated. This was the first design criterion.

In order to duplicate chemical kinetic times it was also necessary to match, as nearly as possible, gas composition in the near field of the particles. For comparable particle temperatures, this may be achieved by matching the mass transport rates.

Mass transport to the surface of burning char particles may be influenced by convective processes in the near field of the particle, as well as molecular diffusion. Mulcahy and Smith (1969) have studied the possibility of convective diffusion in char combustion and have reported that for 100-micron particles accelerations of the order of 1000 g (g=acceleration due to gravity) are required to double the rate of mass transfer by pure diffusion. Thus, they conclude that for conditions typical of pulverized coal combustion processes, pure molecular diffusion is the principal mode of mass transfer.

Field, et al (1967) have indicated that the length and time scales for the smallest turbulent eddies are scaled approximately as follows:

$$\ell = \text{(eddy length scale)} \propto D/Re^{3/4} \qquad (3.7)$$

$$f = \text{(turbulent eddy frequency)} \propto U(Re)^{3/4}/D \qquad (3.8)$$

where:

D = Largest turbulent eddy scale for flow

Re = Reynolds No. of flow

U = Mean velocity of flow.

Based on these scaling laws, and assuming Stokes flow to describe particle motions, particle Reynolds numbers for the conditions of the laboratory furnace used in the present experiments were estimated as follows:

Particle size (microns):	Particle Reynolds no:
100.	25.8
10.	2.58
1.	0.258

Consistent with the conclusions of Mulcahy and Smith (op cit.), the low particle Reynolds numbers suggest it is reasonable to assume that the principal mode of mass transfer is pure molecular diffusion, which is identical in laboratory and full-scale systems, provided particle diameters and gas temperatures are equivalent.

In order to complete the simulation of chemical reaction conditions in the near field of the particles in the laboratory and full-size systems, it would be desirable to match gas composition in the far field of the particles (i.e., in the bulk fluid of the flame). This might be achieved by matching flame jet Reynolds numbers in the two systems, thereby obtaining equivalent turbulent mixing rates between the primary fuel-air jet and the secondary conbustion air stream. This, however, would require:

$$(UD/\nu)_{lab} = (UD/\nu)_{full-size} \tag{3.9}$$

Assuming equivalent temperatures in the two systems, this would imply:

$$U_{lab}/U_{full-size} = D_{full-size}/D_{lab} \tag{3.10}$$

Typical industrial burner diameters are on the order of 1 m, while the laboratory burner was about .05 m in diameter. Thus, it would be required that:

$$U_{lab} = U_{full-size} \times 20. \tag{3.11}$$

Since full-scale burner jet velocities are typically around 36 m/sec (Breen, 1976) the difficulty of matching jet Reynolds numbers is evident.

Since it was not possible to match both residence times and jet Reynolds numbers the necessary bulk fluid gas compositions were controlled by a combination of (1)varying the shear rate between primary and secondary streams; (2)varying the swirl intensity of the burner jets; (3) varying the overall equivalence ratio. In this manner, while jet aerodynamics were not duplicated, the influence of the aerodynamic parameters could nonetheless be investigated.

The principal factors influencing the dynamics of particle-particle interactions and vapor condensation processes were assumed to be gas temperature and residence times in the hot and cool sections of the furnace. These parameters were matched within acceptable limits between the laboratory and full-size systems.

2.0 EXPERIMENTAL SYSTEM

2.1 DESIGN OBJECTIVES

The combustor design used in the experiments was similar to that of Pershing and Wendt (1976). Guided by the foregoing scaling considerations, several design objectives and constraints were formulated, a brief summary of which follows.

The first objective of any laboratory system is that the system be well characterized; i.e., it must be possible to measure and/or control as many of the significant parameters as is possible. To achieve this characterization for the present system a cylindrical combustor was constructed with axial downward firing from a top-mounted burner. The simple cylindrical shape simplified the flow field characterization and downward firing minimized buoyancy-induced recirculation flows, again simplifying the flow characterization.

This characterization is further simplified when the flow is laminar and not fully-developed; i.e., plug flow. Boussinesq found that the distance, L, required to establish fully-developed laminar pipe flow is approximately:

$$L = 0.03 \times Re \times D \qquad (3.12)$$

where:

D = Pipe diameter

Re = Reynolds No. based on D.

Thus, to achieve the simplicity of one-dimensional plug flow it was required that:

$$L/D \ll 0.03 \times \mathrm{Re}. \tag{3.13}$$

Though the flow pattern in the combustor was not a true plug flow, this criterion was used as a starting point in the design of the laboratory facility.

The second criterion in the design was to achieve a mean residence time of about 1 sec, which is typical of a large utility boiler (Flagan and Friedlander, 1976). This is also a representative time scale for complete burnout of the largest particles (100-150 microns) generally present in pulverized coal.

As previously discussed, the third criterion in the combustor design was to achieve particle temperatures comparable to those typical of large systems. For the relatively large surface area/volume ratio of the laboratory system, this required wall temperatures which were near the gas temperature inside the furnace. Thus, the third criterion was to minimize heat losses in order to maximize wall temperature.

Finally, there were constraints on the design imposed by limitations on available laboratory space and maximum air flow rates deliverable by the campus air supply. The ceiling height (about 3.6 m) restricted total furnace length (including convective cooling section) to about 2 meters. Maximum air supply rates (280-420 lpm) limited maximum possible coal burning rates to about 1.2-3.2 kg/hr (2.6-7.0 lbm/hr), corresponding to thermal inputs of about 9,700-26,000 watts (33,000-90,000 Btu/hr).

2.2 LABORATORY FURNACE COMPONENTS

2.2.1 Combustor -

A schematic of the combustor design is shown in Figure 3.2. The combustion chamber was formed by a cast cylinder of high-purity alumina (Harbison-Walker, Castolast-G). The cylinder had an inner diameter of 0.2 m, an outer diameter of approximately 0.3 m, and a length of approximately 1.0 m. This containment shell was surrounded by a multi-latered blanket of low-density refractory fibers. The inner layers of the blanket were of high-purity alumina fibers (Zircar Products, Inc.) with a maximum service temperature of approximately 1650 K. The outer layers of the blanket were of alumina and silica fibers (Cotronics Inc.) with a maximum service temperature around 1500 K. The blanket was ridigized by saturation with a dilute solution of alumina rigidizer/hardener (manufactured by Zircar Products, Inc.). Surrounding the low-density refractory blanket was a 5.1 cm layer of fiberglass insulation followed by a thin galvanized sheet metal shell. An additional layer of fiberglass was later added outside this shell.

Holes 3.2 mm in diameter were drilled in the cast cylinder at five equally-spaced axial locations. Within these drill holes were placed ceramic thermocouple wells, each with approximately 3.2 mm of refractory separating the Type S (platinum, 10% platinum-rhodium) thermocouple from the inner surface of the combustor shell. The

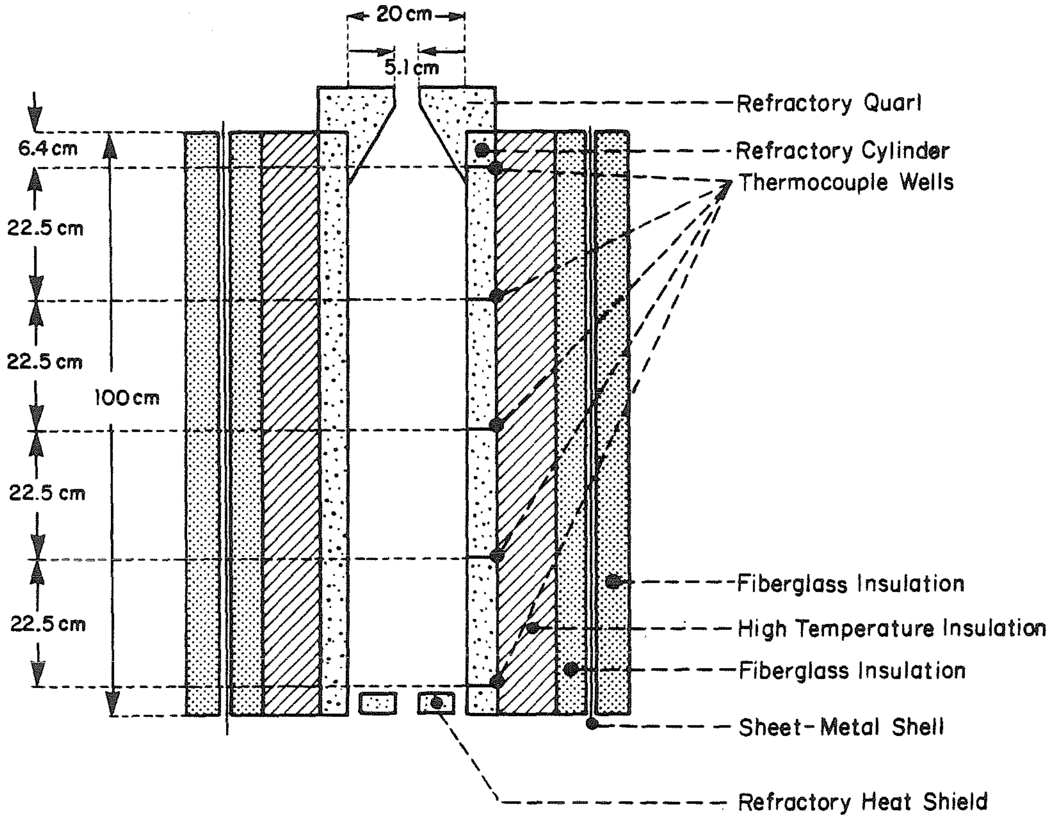

Figure 3.2: Laboratory combustor design. Figure illustrates cast refractory wall , quarl, and radiation heat shield. Multi-layer lightweight insulating blanket is also shown.

thermocouples were spaced as shown in Figure 3.2.

Additional combustor components included:

1. A cast refractory conical quarl having a minimum opening of 5.1 cm, and a half-angle of 30 degrees. The hot quarl served to simplify the flow (by minimizing recirculation) and together with the hot wall provided a stable ignition source for the coal-air combustion mixture entering the combustor from the burner above;
2. A cast refractory radiation shield at the base of the combustor which served to reflect thermal radiation from the flame and combustor walls back into the combustion zone and thus reduce heat losses from the combustor. Based on crude estimates, the shield reduced radiation losses from the combustor exit by about 20%. Pressure drop across the shield was estimated to be approximately five to twelve cm of water, which was tolerable, given that the burner-combustor was a forced draft system.

2.2.2 Burner -

The function of the burner-injector assembly located atop the combustor was was to mix the fuel-rich primary fuel-air stream with the preheated secondary combustion air and introduce the mixture into the combustion section where it was burned. The basic mixing pattern of the primary and secondary streams was similar to that used in full scale burners, viz., coaxial jets coupled by a mixing shear layer. The flame from such a burner is typically stabilized by imparting a degree of swirl to the flow which is characterized by a dimensionless number known as the ´swirl number´ , S (discussed below). In the present system the swirl number was determined by measuring the mass flow rates of the two secondary air streams which were introduced axially and tangentially into the burner head. From the measured air temperatures and the known burner geometry, the velocities of the air streams entering the burner could be computed and the magnitude of the swirl number determined. Also, by adjusting the air flows, any desired swirl number could be attained.

The basic design of the burner and fuel injector is illustrated in Figure 3.3.The primary fuel-air jet was introduced through the injector located on the combustor axis. Secondary combustion air was introduced tangentially and axially through separate ports in the burner. Tangential (´swirl´) air was introduced through eight machined vanes and the axial secondary air stream was introduced through a perforated plate with a nominal pressure drop of three to four times the dynamic pressure of the incoming air in order to guarantee a uniform distribution of the flow around the burner axis.

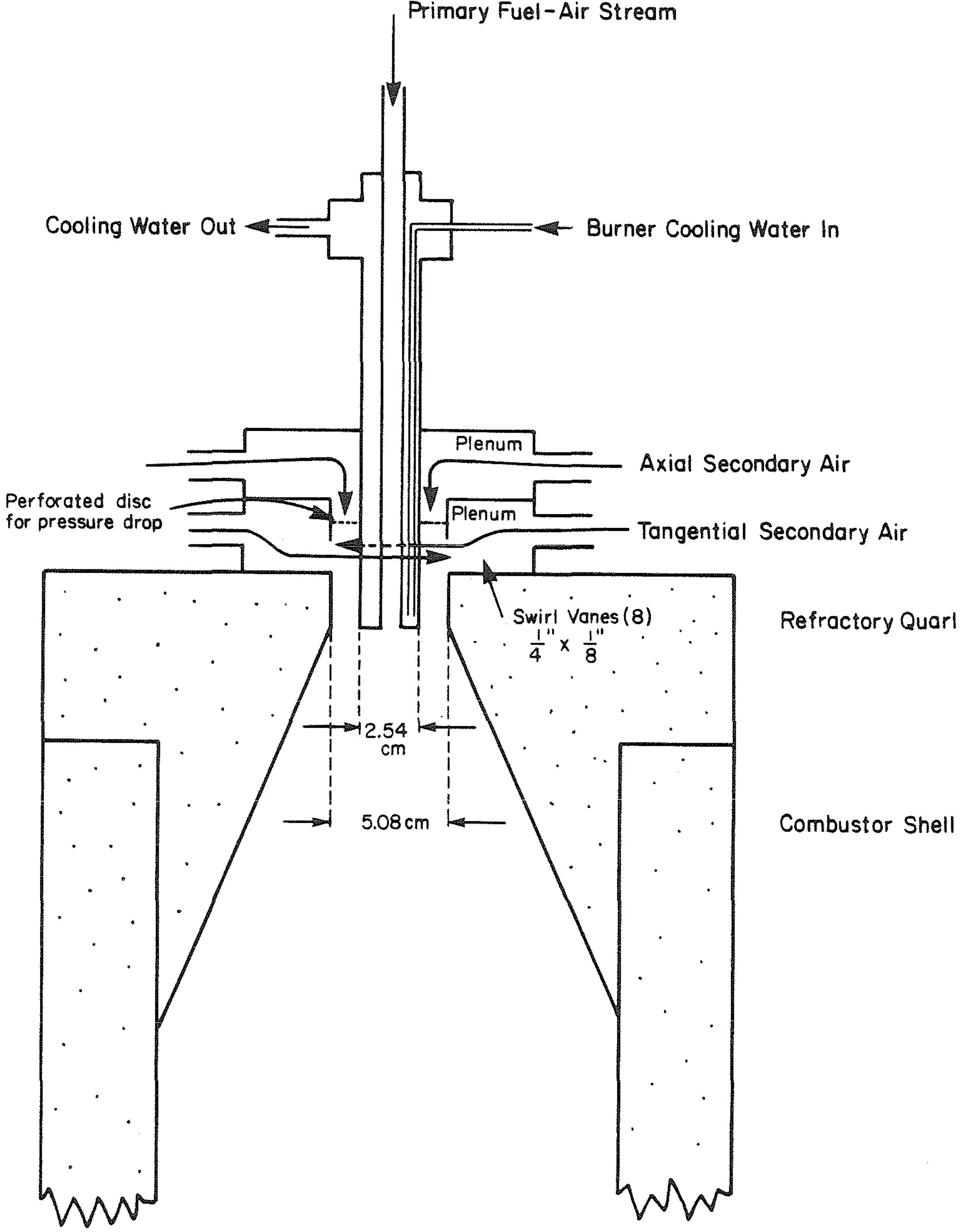

Figure 3.3: Burner and fuel injector design. Figure illustrates placement of swirl vanes and entry point for axial secondary combustion air and primary fuel-air stream. Burner outlet was located at entrance to refractory quarl.

Five types of burner were used in the experiments and are illustrated in Figure 3.4. The first (Burner 0, Fig. 3.4(a)) utilized a conical-tipped, water-cooled injector, chosen for its low mixing characteristics. The second (Burner 1, Fig. 3.4(b)) used an uncooled bluff cylinder injector with inner (jet) diameter of about .49 cm. The third burner (Burner 2, also shown in Fig. 3.4(b)) differed from the second only in the diameter of the primary fuel-air jet (.77 cm). The fourth burner (Burner 3, Fig. 3.4(c)) was a modification of the third, which utilized a bluff disc at the exit of the primary fuel jet. Burners 1, 2, and 3 were utilized because they enhanced the mixing rate of primary and secondary air streams over that of burner 0 (See 'Initial Tests'). The fifth burner type (Burner 4, Fig. 3.4(d)) was identical to burner 2 except that the injector was water-cooled.

2.2.3 Coal Feeder -

The most important design criterion for the pulverized coal feeder was that it provide a stable and steady mass flow rate of coal to the burner. This was also perhaps the most difficult of all the system design criteria to achieve, and a considerable amount of experimentation was necessary to achieve coal feed rates which were acceptably stable and steady.

The design chosen for the coal feeder utilized a 6.4 mm helical auger screw running through the base of a wedge-shaped coal hopper (see

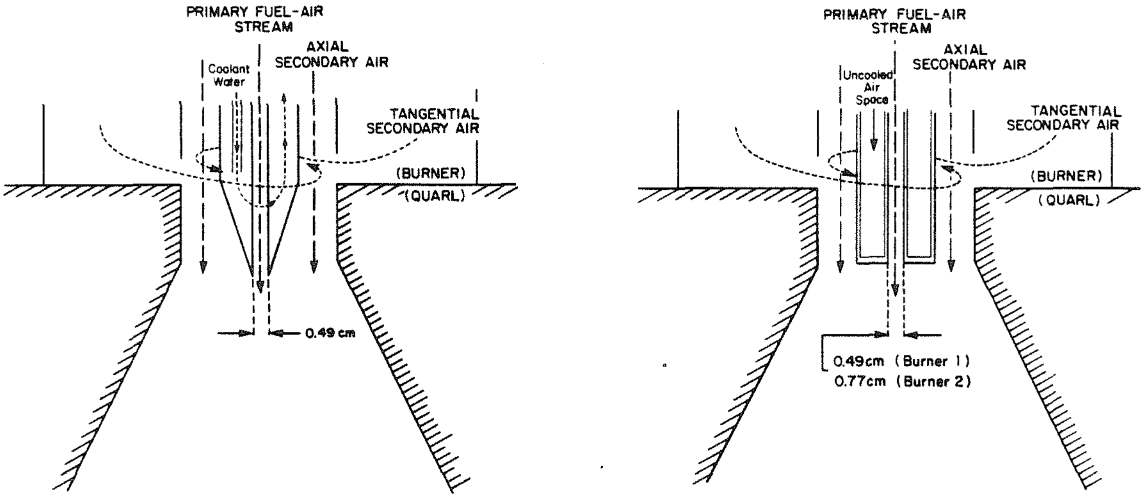

(a) BURNER 0

(b) BURNERS 1 & 2

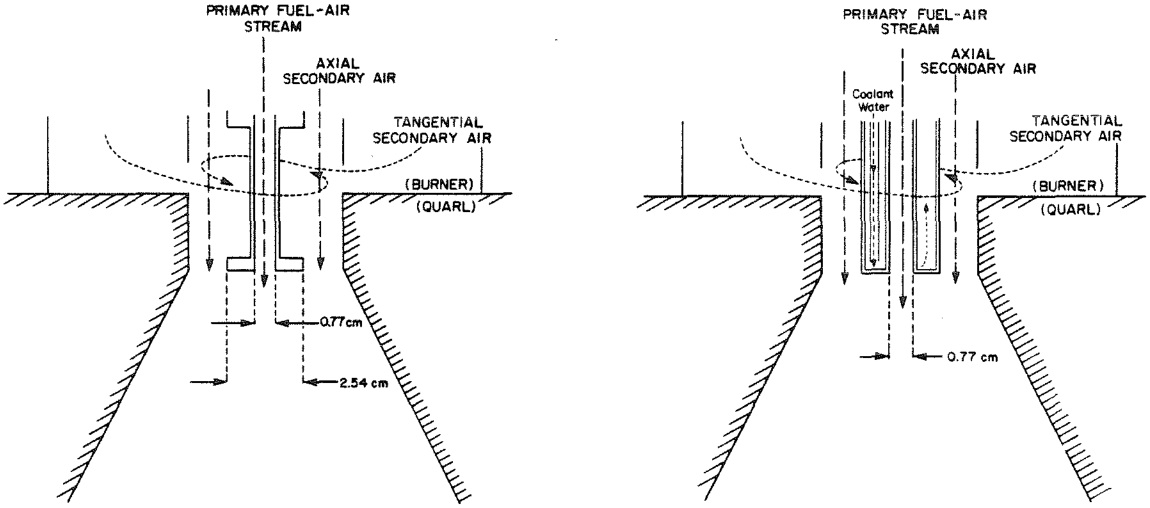

(c) BURNER 3

(d) BURNER 4

Figure 3.4: Four laboratory burners used in experiments. Burners 0 and 4 were water-cooled; burners 1, 2, and 3 were uncooled. Burner 0 was low-mixing due to conical tip.

Figure 3.5).The auger rotated inside a 2.5 cm helical spring whose rotation was opposite to that of the main auger. The purpose of this secondary screw was to assure a constant aggregate coal density and a steady mass flow rate delivered to the auger screw.

The auger carried coal from the hopper into a vertical venturi where it was mixed with the primary air stream which carried the coal into the burner. The venturi was used in order to reduce the amplitude of the pulsing flow rate which is inherent in any screw type feeder.

During several trial experimental runs several unanticipated effects were noted in the coal feeder:

1. It was found that the delivery rate of the screw was influenced by the depth of coal in the hopper.

2. Because of imperfect matching of the delivery rates of the inner and outer screws, a coal circulation pattern was established inside the hopper. It is believed that some of the feed rate instabilities which were observed were related to this circulation pattern. Possibly, the coal depth effect, mentioned above was due to the influence of the coal depth on the circulation pattern in the coal in the hopper.

3. The coal delivery rate also depended on the degree of incline

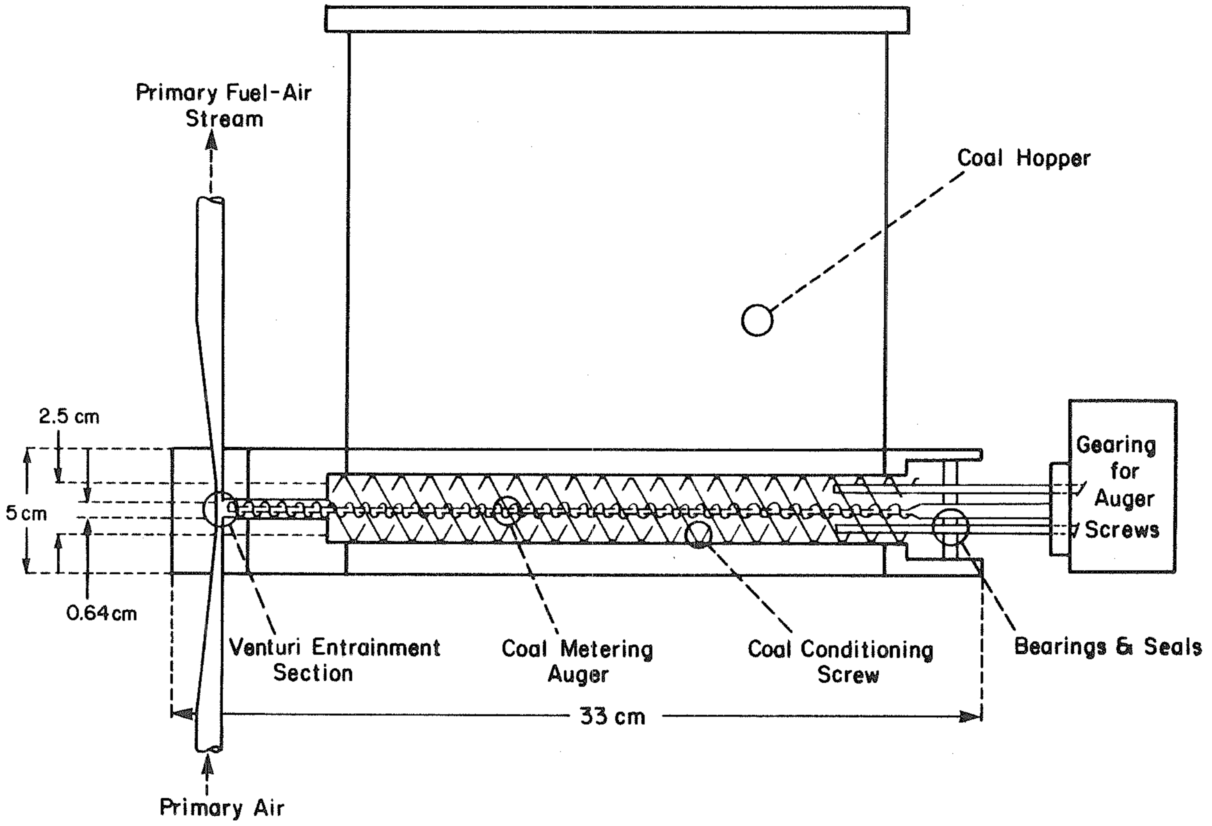

Figure 3.5: Double helical screw coal feeder. Large, outer conditioning screw was used to loosen coal, maintain constant density. Small, inner screw delivered coal to venturi entrainment section. Screws rotated in opposite directions.

of the auger from the horizontal, and on the fraction of the screw which was covered by the coal.

Because of the effects described above, it was necessary to infer the coal flow rate from the measured equivalence ratio, air flow rate, and known composition of the coal.

2.2.4 Air Flow Metering and Preheat System -

A schematic of the flow system is shown in Figure 3.6. The air flow rates were measured using sharp-edged orifices machined to the ASME specifications (Leary and Tsai, 1951). Differential pressure gauges (Magnehelic) were used to measure all but the total air flow, and for this a water manometer was used. All gas flows were controlled by use of standard globe valves. After metering, the axial and tangential air streams were preheated in two identical heaters designed for this purpose. Each heater directed the air stream into intimate contact with nichrome wire heating elements (Keith Co., Pico Rivera, Calif.) before being directed into two insulated plena atop the burner. Air temperatures in the two streams were measured by thermocouples just prior to entry into the burner plena. Utilizing the preheaters' maximum capacity, preheat temperatures up to 750 K (900 F) were achievable.

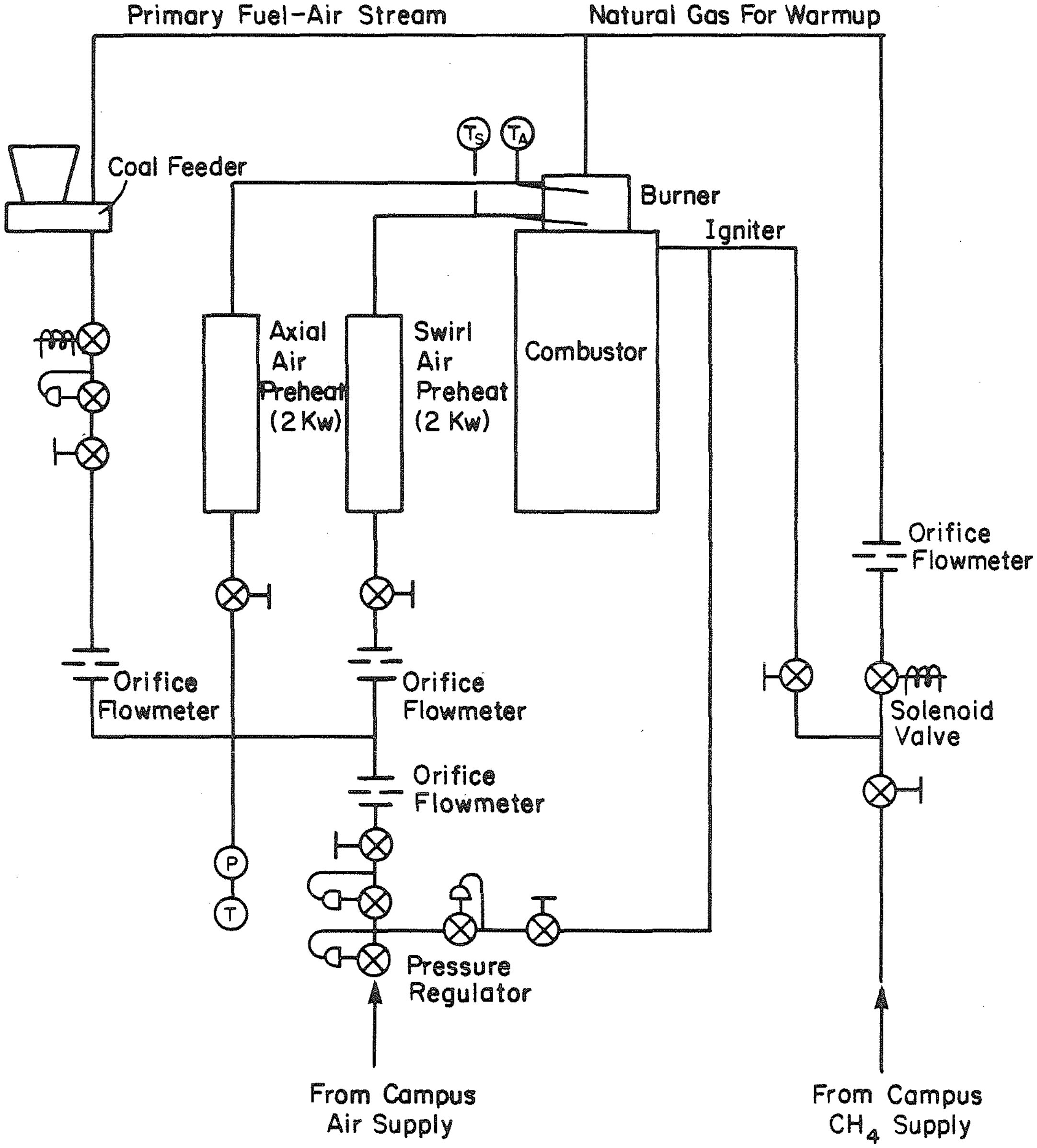

Figure 3.6: Schematic of air and fuel flow pattern for laboratory combustor (See also Figure 3.9).

2.2.5 Convective Cooling Section -

In order to simulate the aerosol formation processes which occur in a full-scale boiler, it was desirable to subject the exhaust gases from the combustor to a cooling process which would achieve a gas temperature-time history similar to that of a full-scale system. To achieve this end a tubular shell-and-tube heat exchanger, whose flow cross-section was equal to that of the combustor, was attached at the combustor outlet. Semi-empirical heat transfer correlations (e.g., see Eckert and Drake, 1972) were used to determine the required cooling coil geometry and surface area, and to estimate the required coolant flows. A sketch of the design is shown in Figure 3.7. Originally, three sets of .64 cm water-cooled tubes in series were included in the 76 cm length of the cooling section to ensure adequate cooling of the exhaust gases. Later it was found that the exhaust mixture was 'overcooled'; i.e., the final temperature was well below the dew point of the exhaust gases, and condensed water droplets were adversely affecting the aerosol measurements at the heat exchanger exit. Thus, the first and third banks of cooling coils were de-activated for the duration of the experiments.

2.2.6 Support Structure For Furnace -

The entire furnace (consisting of combustor plus insulating shell, refractory quarl, heat shield, burner, preheaters, heat exchanger

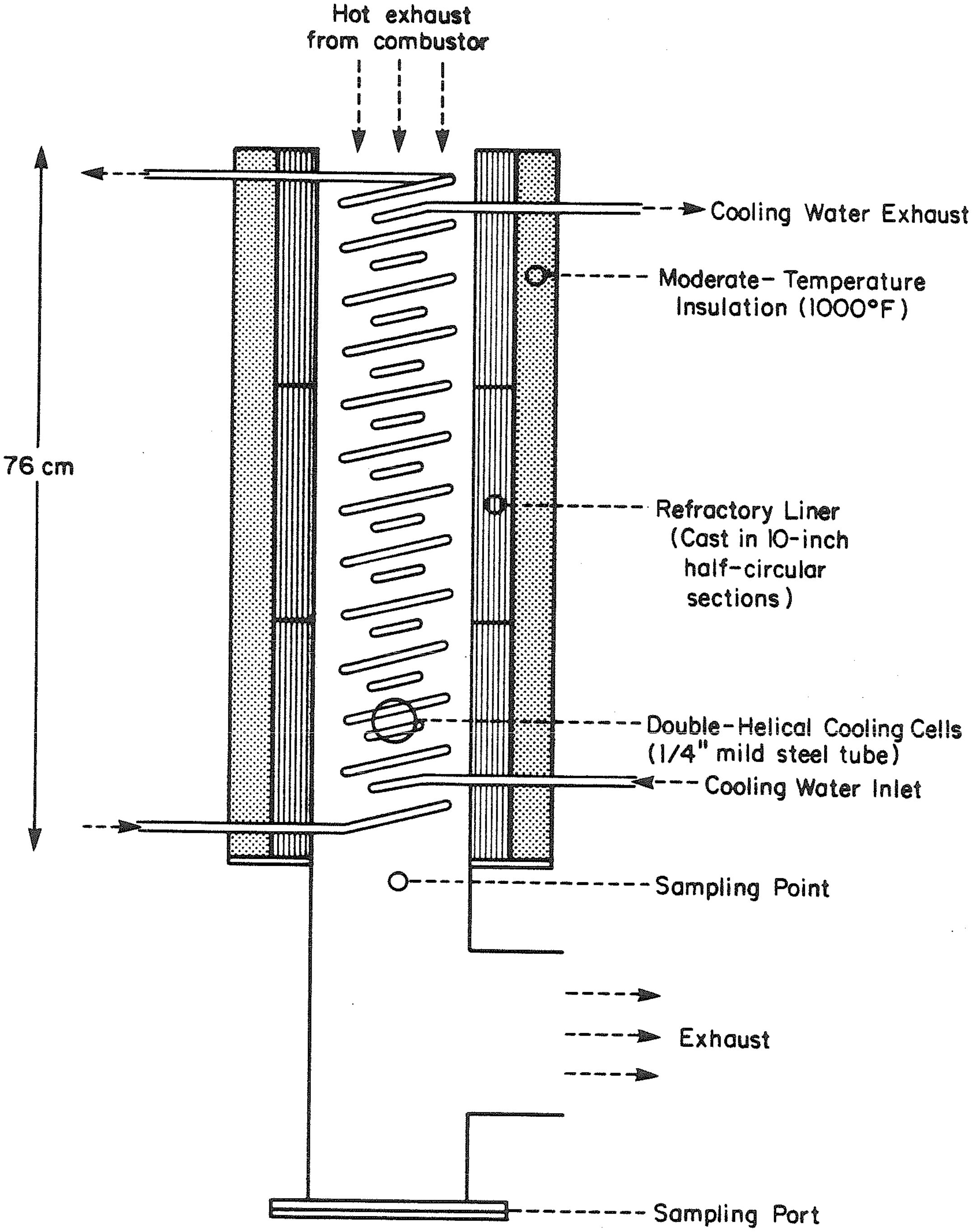

Figure 3.7: Convective cooling section for combustor exhaust gases. Two concentric coils (diameter 12.7 and 6.4 cm) were used. After preliminary tests coils in the first and third vertical sections of the heat exchanger were removed to prevent condensation.

shell plus insulation and cooling coils) had a weight of around 500-600 lbs., and was mounted on a vertical frame constructed of 4-inch cold-rolled steel (CRS) angle. The entire weight was supported on a cooled 1/4-inch steel plate which, in turn, rested on a shelf constructed of welded 3-inch CRS angle. The shelf was designed to be movable (vertically) on the support structure.

The finished configuration is illustrated in Figure 3.8. A scaffold was attached at one side of the superstructure to allow access to the burner. Liberal width dimensions were chosen to allow later system modifications as they became necessary.

2.2.7 System Control and Safety Measures -

System controls are illustrated schematically in Figures 3.6 and 3.9 The mass flow rates of combustion air, fuel (coal, methane), and coolant water were all adjusted manually. As indicated in the figures, the campus air supply was used to provide combustion air to the furnace. Pressure in the orifice flowmeters was maintained at about 10 psig via two diaphragm-type regulators. Primary, and secondary combustion air flow rates were adjusted with globe valves downstream of the flowmeters. Coolant water and natural gas flowrates were adjusted in like fashion though with the passage of time deposits inside cooling coils in the convective heat exchanger restricted the maximum coolant flow and ultimately caused the exchanger to fail.

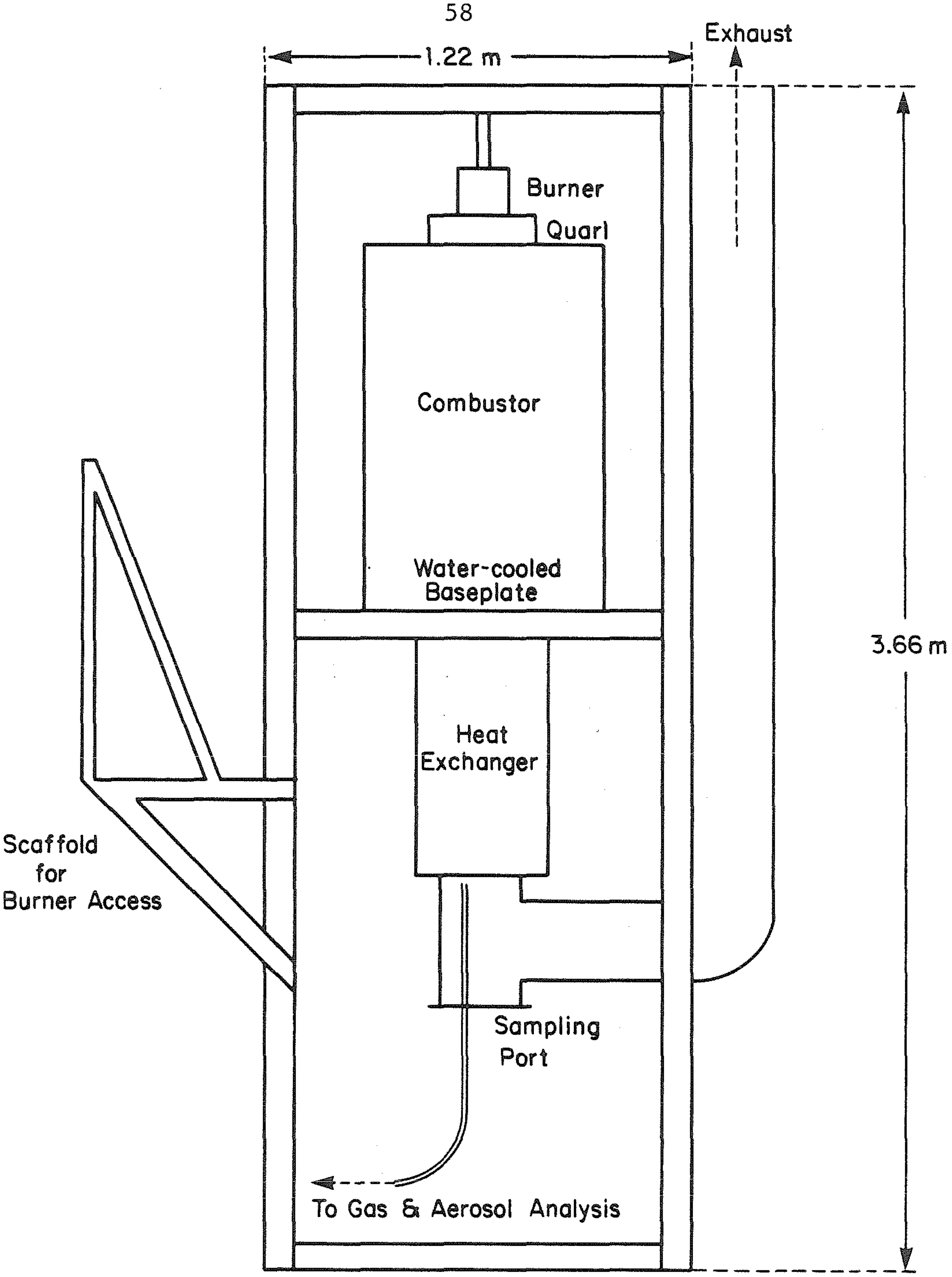

Figure 3.8: Assembled configuration of laboratory furnace and heat exchanger. Support structure and sampling point also shown. Sampling point was chosen 3.8 cm off center to smooth effect of slight radial variation in particle concentration.

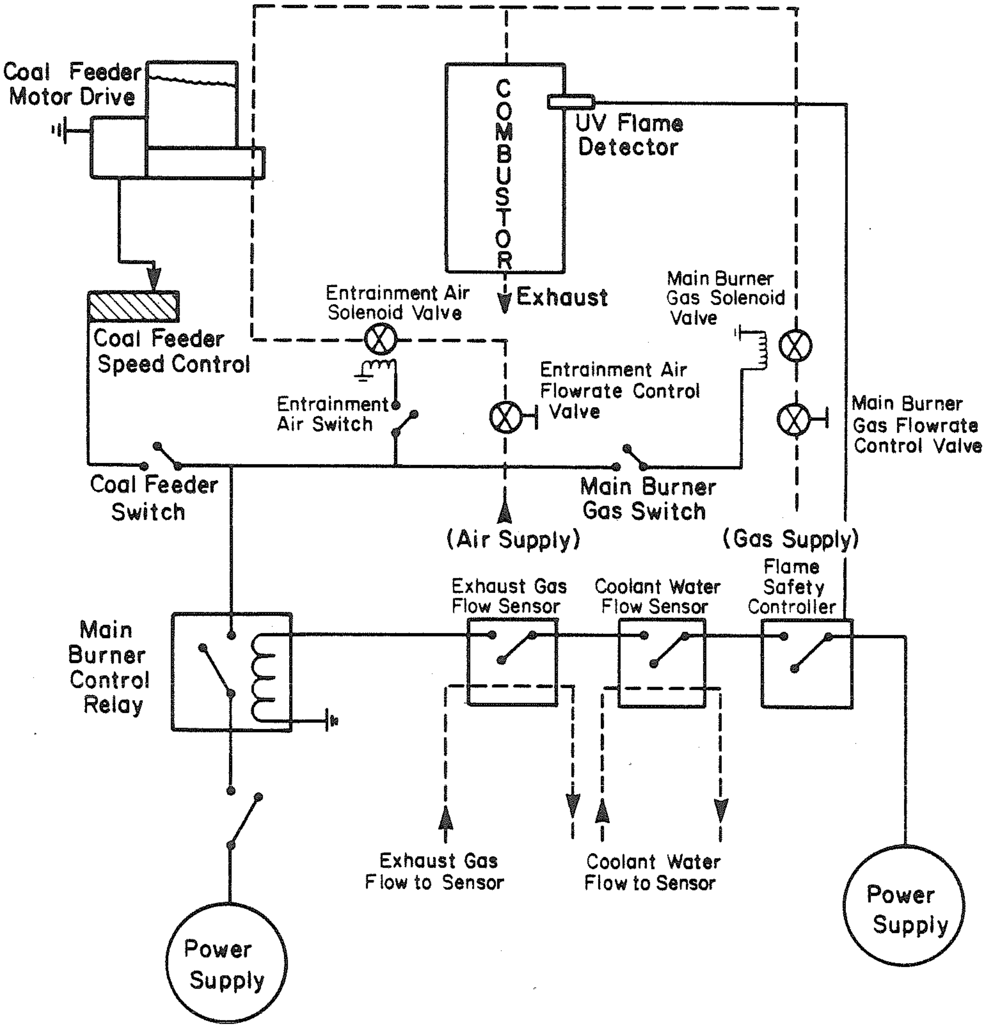

Figure 3.9: Laboratory furnace controls. Manual and electrically-actuated safety valves are indicated. Flame condition was monitored by an ultra-violet flame detector mounted in the refractory quarl. (See also Figure 3.6.)

Figure 3.9 illustrates the electrically-actuated system controls. The coal flow rate was manually adjusted via a rheostat in series with the coal feeder motor drive. Thus, the time-mean flow rate of coal could be controlled. The instantaneous flow rate was, however, subject to various sources of unsteadiness, as previously discussed.

As indicated in Figure 3.9 the main burner fuel flows were automatically shut down in the event of (1)an unstable flame or flame-out; (2)loss of coolant flow; (3)loss of suction for expelling exhaust gases. Flame status was monitored by an ultraviolet flame sensor mounted in the combustor quarl. Output from the sensor actuated a standard industrial flame-safety controller (Protection Controls model no 76057). Coolant and exhaust gas flows were monitored by flow sensors.

Flame controller and flow sensors were connected in series to the main relay which supplied power to the coal feeder, the coal entrainment air solenoid valve, and the natural gas solenoid valve. Thus, an interruption in any one of the three monitored parameters resulted in shutdown of the main burner fuel flows.

The system was also equipped with a switch to bypass the flame controller. The reason for incorporating such a bypass was to eliminate unwanted shutdown of the system because of temporary flame instabilities resulting from adjustments made during experiments.

The main burner components (coal feeder, entrainment air solenoid, and natural gas solenoid) all had manually-actuated switches in series with the main relay to allow rapid shutdown of individual components (during transition from methane to coal, for example). A single switch controlling the main relay was also included to permit rapid manual shutdown of all main burner flows.

2.3 SAMPLING SYSTEM

Combustion-generated aerosols from the laboratory furnace were sampled near the end of the cooling section as illustrated in Figure 3.8. The sampling train components are described below.

2.3.1 Sampling Probe -

The probe was placed directly in the exhaust stream from the furnace at the point where it was desired to sample and characterize the aerosol from the furnace. The probe used in this study is shown schematically in Figure 3.10. The components of the probe, together with their functions are as follows:

1. Probe Tip. The tip was the entry point for the sample aerosol stream. As indicated in Figure 3.10 the tip was streamlined and the flow entered at right angles to the streamlines of the main duct flow. The reason for this pattern was to eliminate from the sample stream particles which were outside the range of interest and which, because of their relatively large individual mass, would cause problems with probe fouling. By utilizing the design shown, particles larger than 20-50 microns could be eliminated from the sample stream (The probe tip is further discussed in Appendix B).

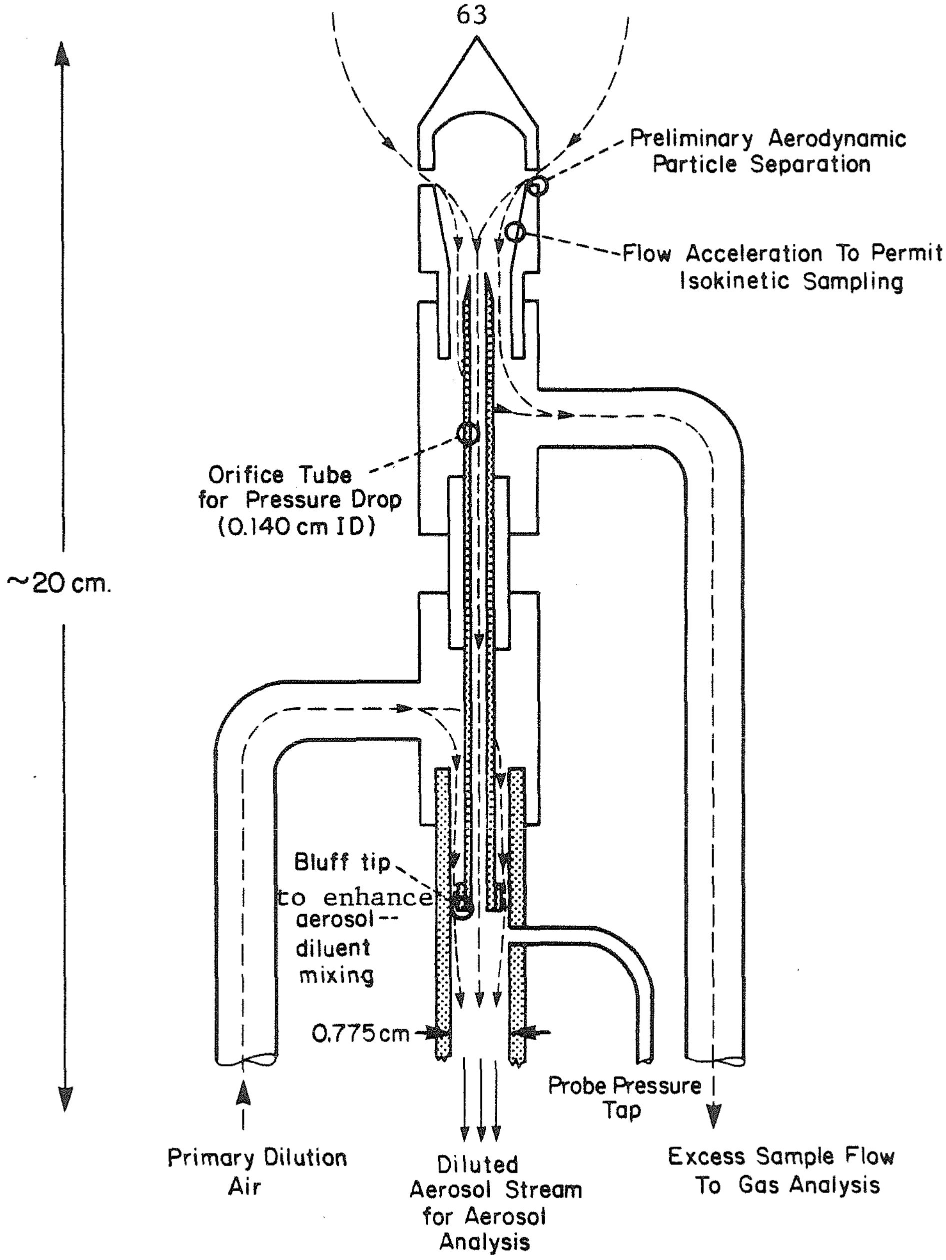

Figure 3.10: Schematic of probe used to sample exhaust gas from combustor. Figure illustrates basic flow pattern of aerosol and gas sample streams, mixing point of dilution air and sampled aerosol stream.

2. Secondary Sampling Probe. The primary sample stream was divided into two secondary streams (see Figure 3.10).The outer stream flowed past the secondary tip and was used for determining the exhaust gas composition. The secondary probe was where the sample stream was drawn which was used for aerosol characterization. By properly adjusting the gas and aerosol sample flow rates, the aerodynamic biasing of the secondary probe tip could, in theory, be eliminated or minimized. In practice, however, biasing of submicron particle concentration measurements due to non-isokinetic sampling was not a serious problem (See Appendix B).

3. Aerosol sampling tube. The aerosol sample stream passed through a small-diameter (1.4 mm) tube, through which there was a finite pressure drop. By controlling the downstream pressure, the sample flow rate could thus be controlled, and the effect of fluctuations in flow rates (to vacuum pumps and/or from dilution air supply) on the sample flow rate could be minimized. To achieve a sufficiently high pressure drop for maintaining a steady aerosol sample flow rate, a 15 cm tube was used (with about 5 cm water pressure drop for a flow of 1 LPM air at 25 C, 760 mm Hg). The susceptibility of this flow tube to fouling by large particles was the primary motivation for using the aerodynamic particle size separation at the probe tip previously discussed.

4. Primary aerosol diluter. In order to relate the sample aerosol characteristics to those of the stack aerosol at the sampling point in the exhaust gas stream, it was desirable to slow the rate of particle-particle interactions after entry into the probe. The major dynamic process occurring in the aerosol is Brownian coagulation. Since this process is second order in the aerosol concentration, and since the coagulation rate is a monotonically increasing function of gas temperature, the rate of coagulation could be reduced by dilution cooling of the aerosol stream.

For this reason the sample was diluted with dry, filtered air immediately downstream of the aerosol sampling tube. The annular dilution air jet was concentric with the sample aerosol stream, and mixing between the two streams was enhanced by using a bluff tip on the end of the aerosol sampling tube (as shown in Figure 3.10). The minimum dilution ratio used in these experiments was about 20:1. Neglecting the temperature change in the gas, the dilution effect alone would decrease the coagulation rate by a factor of 400 (=20X20). Since residence times in the cooling section were of the order of 1-2 sec, and residence times in the sampling line were estimated to be of the same magnitude, it was concluded that the coagulation of the diluted aerosol in the sampling line was small in comparision with that which occurred prior to sampling in the exhaust duct.

2.3.2 Cyclone Separators -

After dilution in the probe the sample stream passed through two cyclone separators which were constructed to the specifications of the California Air Industrial Hygiene Laboratory Respirable Particle Samplers (John and Reischl, 1980). For the flow rates of the diluted sample stream (around 20 lpm) the cyclones have a 50% cutoff diameter (aerodynamic around 3.5 microns. Since the primary focus of these experiments was investigation of the submicron particles, it was necessary to eliminate as many of the larger-size particles as possible in order to minimize instrument and sample line fouling, and to reduce the possibility of contamination of the fine particles on the lower cascade impactor stages by overloading the upper stages (See below for discussion of the use of the cascade impactor in aerosol characterization).

2.3.3 Secondary Diluter -

In those experiments where the low pressure impactor was used to collect mass samples, the primary dilution ratio was minimized (subject to the coagulation freezing constraints, already mentioned) in order to minimize the time necessary to collect suitable mass samples for elemental analysis. Because of the high number concentrations in the combustion aerosol, a second dilution was necessary prior to entry of the aerosol sample stream into the EAA. This was accomplished by using a jet pump (Air Vac, model TDH-260) inserted into the flow stream, into which air from the campus air supply, or bottled air was metered.

2.3.4 Gas Analysis Instrumentation -

Combustor exhaust gas composition was measured using the following instruments:

1. O_2 concentration was determined using a Beckman Model 755 Paramagnetic Oxygen Analyzer. The instrument has four concentration ranges: 0-5%, 0-10%, 0-25%, and 0-50%, by volume. Typical concentrations measured in these studies were from 3% to 12%;

2. CO_2 and CO concentrations were determined using an Anarad Model AR-600 Non-dispersive Infrared Analyzer. The CO_2 concentration range of the instrument is 0-20%, and the two CO ranges are 0-2.5% and 0-20%. Measured CO_2 concentrations were typically from 7% to 18%; CO concentrations were generally less than 0.5%;

3. NO concentration was determined using a Thermo-Electron model 10B Chemiluminescent NO-NOX Gas Analyzer, which has several concentration ranges. The lowest scale of the instrument

measures 0-2.5 ppm NO and the highest scale, 0-10,000 ppm. Undiluted exhaust gas concentrations measured in the experiments were from 200 to 1000 ppm, and diluted concentrations were generally from 1 to 25 ppm.

2.3.5 Aerosol Analysis Instrumentation -

The aerosol size distributions were measured using an electrical aerosol analyzer (EAA) (Thermo Systems Inc. Model 3030 Electrical Aerosol Size Analyzer). This instrument has been used to measure particle concentrations in ambient aerosols for particles sizes from around .01 to 1.0 microns (Liu, et al., 1976).

Elemental composition of combustion-generated aerosols was measured by the following procedure:

1. Diluted aerosol samples were size-segregated using three Caltech low pressure impactors (LPI′s) (Hering, et al., 1977). One set of samples was collected using a substrate preparation technique described by Ouimette (1981). These samples were used to obtain composition measurements of fine particles. A second set of samples was collected to permit an independent measure of sulfur species concentrations in addition to that provided by analysis of the first set of samples (See

Appendix D). Contamination of submicron particle mass samples was minimized by using cyclone separators as discussed previously.

In addition to using the cyclones, the first three stages of the impactor were duplicated using the first three stages of the third LPI which was available. This was done so that large particles not collected on the first three stages (due to bounce-off) were ultimately collected on one of the duplicate stages. Thus, in assembling the impactor cascade, a total of eleven stages (jets) were utilized in the following order:

1-2-3-1-2-3-4-5-6-7-8,

where the numbers refer to the position of the stage in the normal configuration of the LPI. This arrangement was fairly effective in achieving the desired objective.

In the case of the second LPI (for independent sulfur analysis) duplicates of the first, second, and third impactor stages were not available. However, the 7th and 8th stages of the Caltech LPI are identical to the 2nd stage, and the 6th stage is identical to the 3rd. Hence, these stages were utilized to collect the bulk of the larger particles for the second impactor. This may have skewed the measured mass distributions of sulfur in the particle sizes corresponding to the first three LPI stages but shouldn't have affected the distribution in the lower particle sizes.

2. The first set of samples was mounted, sealed, and sent to the Crocker Nuclear Laboratory at the University of California at Davis for elemental analysis by alpha particle-induced X-ray emission (PIXE) (Cahill, 1975).

3. The masses of sulfur in the second set of samples were determined by flash vaporization/flame photometric detection of sulfur (Roberts and Friedlander, 1976).

Details of the sampling procedure are found in the following section.

3.0 EXPERIMENTAL PROCEDURE

3.1 INITIAL TESTS

3.1.1 Initial Heating of Refractory -

Initial firing of the completed furnace was done as per instructions given by Harbison-Walker for initial heatup of cast refractories. Free water and water of hydration are driven off during this period and recommended maximum heating rates are around 50 F per hour, with temperature holds at 400-500 F, 1000-1200 F and at the maximum pre-heat temperature.

3.1.2 Measurements and Modifications of Combustion Efficiency -

After the initial heat-up procedure, tests were performed to determine coal combustion efficiency for the furnace using the type 1 fuel injector (burner 0) previously discussed. These tests were done by collecting isokinetic total filter samples of combustor exhaust gases (filters used were Gelman glass fiber filters, type A). Filter samples were examined visually and using an optical microscope to determine the extent of carbon carryover. Filter samples were weighed and then oxidized at 600 C for approximately 8-10 hours, and then reweighed to estimate the percent carbon carryover.

The results of these tests showed significant quantities of unburned carbon and necessitated modifications in operating conditions to increase combustion efficiency. Initially, these modifications included:

1. Installation of a refractory shield at the combustor outlet to reduce radiation heat losses and hence increase the mean gas temperature;

2. Increasing the degree of swirl (see next section for discussion of swirl) in the burner to enhance mixing in the combustor and promote higher burning rates (and thus higher combustion efficiency).

These two modifications substantially improved the combustion efficiencies. Before modifications, total filter samples were completely black; after modifications these samples were whitish-grey to yellowish grey and microscopic examination showed relatively few large unburned char particles.

Total isokinetic filter samples were also used to check for mass balance of mineral matter entering and leaving the combustor. Results of such checks performed with the high-swirl condition indicated that roughly 80-90% of the mineral matter in the coal was unaccounted for in the filter samples. It was believed that this was due to centripetal forces carrying particles out onto the combustor wall where they burned and deposited their ash content. Because of heat transfer to the relatively cold walls considerably lower particle temperatures would be expected than if particles burned in suspension. This combustion condition would be quite atypical of pulverized coal fired boilers. Thus, in hope of improving the mineral matter mass balance and eliminating this suspected wall burning of particles, the high swirl conical injector (see Figure 3.4(a))was replaced with the type 2 bluff-tip cylindrical fuel injector (Figure 3.4(b)). This injector facilitated operation at low swirl numbers due to the recirculation and mixing induced in its wake. Various modifications of the basic bluff-tip injector were also used (See Figures 3.4(c), and (d)).The mixing characteristics of the wake zone of a bluff cylinder and of a bluff disc in a non-reacting flow has been discussed by Winterfield (1965)).

Using the high mixing injectors and decreasing the equivalence ratio of the fuel-air stream, it was possible to achieve good combustion efficiencies at very low swirl. Combustion efficiencies were estimated by measuring the weight loss of isokinetic total filter samples after oxidation in air at 600 C for 8-12 hours. Results of these estimates indicated carbon combustion efficiencies between 98% and 99.9%, depending on combustion stability and overall equivalence ratio.

Contrary to expectations, the lower swirl did not substantially improve the ash mass balance between ash input (indicated by coal feed rate) and ash measured in the exhaust gas (from total filter measurements). In fourteen such checks of mass balance the range of the fractions of mineral matter unaccounted for in filter samples was 0.66 to 0.87, with a mean of 0.77. The problem of ash mass balance is further discussed in Chapter 5.

3.1.3 Coal Feed Stability Problems -

In numerous experiments it was found that the most troublesome component of the laboratory furnace was the coal feeder. As previously mentioned, it was essential to achieve and maintain during experiments a constant and steady flow rate of coal into the burner. In practice, this condition was often difficult to achieve for several reasons, including the following:

1. Movement of coal dust opposite to the direction of the auger screw motion resulted in coal penetration of bearings. This frequently resulted in a gradual slowing of the feed rate, and occasionally caused the screw to freeze. This problem was eventually partially overcome by installing double oil seals in front of the bearings for the auger drive, and sloping the feeder downward away from the directions of the seals.

2. The rate of feed was dependent on the level of coal in the

hopper and the degree of compaction of the coal. This dependence became especially pronounced when any portion of the down-sloping auger screw became exposed. The problem was alleviated, to some extent, by adding coal in small but frequent increments to maintain a constant level inside the hopper.

3. Before being entrained in the primary air stream, the coal was carried, by the auger, through a stainless-steel metering journal. Close tolerance between the screw and the journal (initally, about .010 inches) resulted in fairly-rapid wear of the journal. This, presumably together with alternate compacting and loosening of coal in different sections of the hopper and the primary fuel-air line, caused a gradual drift in coal feed rate which was difficult to control for extended periods of time. During tests at fuel-air equivalence ratios above around 0.65, pulses of unburned carbon were observed leaving the combustor with a frequency on the order of 0.1 hz. Presumably this was due to such long-term instabilities in the coal movement inside the coal feeder.

4. For reasons noted above the mass flow rate of coal into the primary fuel-air stream could not be inferred from the rotational speed of the auger. Consequently, the coal mass flow rate was not measured directly but was inferred from the

stoichiometric relationship between measured oxygen (air) flow rate, and the measured composition of exhaust gases (the only major components of the exhaust gases were assumed to be CO_2, H_2O, O_2, and N_2; based on measurements of CO, which seldom exceeded 0.1-0.2%, this assumption was not unreasonable).

3.1.4 Room Air Penetration Into The Sampling Region -

As indicated in Figure 3.8, the sampling access was via a steel 'tee' at the end of the cooling section of the furnace. Initially, this access port was left open to allow easy access to the exhaust stream for probe, filter, and temperature sampling, as well as for easy visual observation of the flame. It was discovered, however, that eddies of room air, entering the port under the influence of the slight negative pressure in the exhaust duct (the exhaust gases were drawn from the duct by a squirrel-cage fan, in line with the duct) would actually penetrate up into the heat exchanger section to the point where the sampling probe was located (a distance of approximately 36 cm from the port). Thus, to avoid unwanted dilution of the sampled exhaust gas, a sampling port cover was fabricated and installed, with openings just large enough for the total filter probe inlet (which was simply a 6.4 mm steel tube) and for the gas-aerosol sampling probe.

3.2 RATIONALE OF EXPERIMENTS

The objective of these experiments was to generate size and composition distribution data for submicron flyash particles from pulverized coal generated under various combustion conditions. By measuring various primary parameters, a set of secondary parameters was calculated to characterize the combustion condition. The data were then examined to determine the influence of the macroscopic secondary parameters on the mass concentration of the submicron aerosol.

A Utah sub-bituminous coal was used in all experiments described herein. Proximate and ultimate analyses of the bulk coal, and the elemental analysis (by X-ray fluorescence) of the mineral matter in the coal are given in Table 3.1.

The primary experimentally-measured parameters were the following:

1. Wall temperature profile;
2. Secondary combustion air preheat temperatures (both tangentially- and axially-injected streams);
3. Primary and secondary air mass flow rates;

Table 3.1

Ultimate and Proximate Analyses of Utah II
Sub-bituminous Coal Used in Experiments

Proximate Analysis (% by weight	Dry Basis
Ash	9.54
Volatile Matter	41.94
Fixed Carbon	44.52
	100.00
Calorific Value (j/kg)	6.15×10^6
Sulfur (%)	0.76
Mineral Matter Free (j/kg)	6.87×10^6
Ultimate Analysis (% by weight)	
Carbon	72.24
Hydrogen	5.75
Nitrogen	1.55
Sulfur	0.76
Ash	9.54
Oxygen (by difference)	10.16
	100.00
X-Ray Fluorescence Analysis of Ash	
Na_2O	0.61
K_2O	0.94
CaO	4.92
MgO	0.87
Al_2O_3	13.14
SiO_2	59.00
Fe_2O_3	3.58
TiO_2	0.67
SO_3	16.46
	100.19 (error due to rounding)

4. Coal composition (See Table 3.1);

5. Combustor exhaust gas composition;

6. Aerosol particle size distribution in diluted exhaust sample stream from combustor;

7. Sample stream nitric oxide concentration (for determining dilution ratio).

From these primary data the following secondary parameters were calculated:

1. T_w='effective wall temperature'; this temperature was defined as follows:

$$LT_w^4 = \int_{wall} T_w^4(x)dx \tag{3.14}$$

where:

L = Total wall (combustor) length

$T_w(x)$ = Local wall wall temperature at x.

It was assumed that this parameter would be the significant wall temperature parameter, since the radiated thermal energy reaching a particle inside the combustor from a small section of the wall at temperature $T_w(x)$ is proportional to $T_w(x)$ x (area of wall section);

2. T_{pre}=mass-mean temperature of the preheated incoming secondary air streams;

3. t=total residence time inside the combustor;

4. ϕ=fuel-air ratio normalized by the stoichiometric fuel-air ratio;

5. S=dimensionless swirl parameter, used to characterize the angular momentum of the fuel-air stream leaving the burner; this parameter is defined as:

$$S = \text{angular momentum flux}/(\text{axial momentum flux} \times \text{jet radius}) \quad (3.15)$$

The swirl parameter is often used to characterize the recirculative tendency of the flame jet and thus was assumed to influence the rate and temperature of the combustion reactions occurring in the flame;

6. U=velocity difference between the primary fuel-air stream and the coaxial secondary air stream; the burning rate of the char particles is profoundly influenced by the local gas composition, which in turn is dependent on the rate of entrainment of secondary combustion air and the rate of mixing

in the flame jet. It is known that for cold, non-reacting jets and coaxial jets, the entrainment and mixing rates are dependent on the velocity difference between the two jets;

7. V=total submicron volume concentration. This parameter was calculated directly from the histogram approximation to the size distribution which resulted from aerosol sizing measurements.

Besides measuring the influence of combustion parameters on the size distribution of fine particles, it was also desired to obtain composition data for these particles. Thus, size-segregated mass samples were collected and analyzed.

Detailed experimental procedures used to accomplish the above objectives are described in the following section.

3.3 COLLECTION OF DATA

3.3.1 System Startup -

Instruments were always given at least six to twelve hours of warmup time before experiments. They were usually turned on the night before a sampling run. Calibration of the instruments was performed just prior to the start of sampling. Calibration gases were mixed from bottles of pure gases.

It was found that the drift of the oxygen analyzer was negligible. The drift of the the CO-CO_2 instrument was less than 1%, though the drift of the zero of the CO indicator on the low concentration range was generally substantial. Actual CO levels were usually less than 0.2%, though zero drift of the instrument over the course of an experiment was sometimes as high as 0.5%.

The upper scales of the NO instrument were fairly stable. Calibration was performed with a 206-PPM span gas and the calibration drift was usually less than 2%. Zero drift on the lowest scale was, however, substantial, particularly when there was frequent shifting between high (500 PPM) and low (5 PPM) levels of NO.

Typically, the heat-up of the combustor was begun early in the morning on the day of a sampling run. After activation of exhaust duct fans and cooling water in the support structure and the various cooled furnace components (i.e., fuel injector, flame safety sensor, cooling section coils), the natural gas pilot flame was ignited. Upon establishing a stable pilot flame (as indicated by the UV flame detector situated near the burner) an electrically-actuated solenoid valve controlling the main flow of natural gas to the burner was automatically activated by the flame safety controller. Natural gas firing rates in excess of 30 LPM (heating value in excess of 17,000 watts) were typically applied for a period of 6 to 10 hours to achieve refractory wall temperatures on the order of 1500 K.

After igniting the main burner flame, the electrical air preheaters were activated. Because of large thermal inertia in the heaters, a period of 30 to 60 minutes was required to attain the desired preheat temperatures (500-700 K) and thermal equilibrium.

The rate of heating of the refractory in the furnace was significantly enhanced when there were radiating particles in the region of the flame. This was accomplished during the initial phases of heatup by using a fuel-rich mixture of methane and air, thereby producing a soot-laden luminous flame. After the combustor walls were hot enough to ignite coal particles, the methane-air flame was seeded with a small quantity of pulverized coal dust (the methane and coal-air streams were merged in the fuel injector). The increased wall heating rate was indicated by the thermocouples in the furnace wall.

It was also observed that flame geometry was influenced by flow rates, degree of swirl, primary air mass flow rate, equivalence ratio, preheat temperature, and presence or absence of the radiation shield at the base of the combustor. The influence of these parameters was manifest by the character of the furnace wall temperature profile (e.g., location of the peak, flatness of the profile, etc.).

After reaching the desired wall temperature, the coal feeder and primary air flow were activated, thus commencing the flow of the primary coal-air mixture to the burner. Shortly thereafter, the natural gas solenoid valve was deactivated. Flow rates of air and coal were then adjusted to desired levels, and fine adjustments were performed as needed to achieve the desired operating conditions. For initial firing of coal, the sampling port cover was not installed, in order to permit good visual access to the flame, during the adjustment and equilibration period prior to exhaust sampling. Coolant temperatures were monitored by visual inspection of exit coolant streams, and flow rates were adjusted as required.

3.3.2 Sampling Procedures -

After the visual appearance of the flame indicated reasonable stability and complete burnout of the char particles, the sampling port cover was installed and gas sampling was commenced. Final adjustments of coal flow rate were then performed as dictated by the measured concentrations of CO_2 and O_2 compared with the required concentrations to achieve the desired equivalence ratio.

Independent variation of macroscopic combustion parameters (swirl, burner shear rate, etc.) was difficult to achieve and in most experiments several parameters varied simultaneously from run to run. However, in one of the last series of experiments (the 92380 and 92680 runs; see Chapter 5 for explanation of run designations), the separate effects of wall temperature and fuel-air equivalence ratio were investigated. The variation of these parameters was achieved in the following manner:

1. For equilibrium conditions, furnace wall temperature was established by the degree of preheat total throughput, and equivalence ratio. Because of the large thermal inertia of the combustor refractory, the relaxation time for equilibration of wall temperature was of order 10-20 minutes. Consequently, by heating the combustor with the natural gas flame to the desired temperature condition, and then switching to coal for 5 to 10 minutes at a time, and then reheating to the desired condition, a combustion condition was achieved which was approximately constant (temporarily), within limits considered reasonable compared with the total wall temperature variation of the various runs.

2. The fuel-air equivalence ratio was easily varied, independent of all other parameters, by varying the delivery rate of coal from the coal feeder. The only limitation of this technique was that the constancy of the speed of rotation of the motor drive for the feeder became poor at low rotation speeds, and consequently, various gearings had to be utilized to be able to run the motor at or near its maximum speed.

In all experiments, after the desired operating condition had been reached, combustion parameters were constantly monitored and periodically recorded (manually). Recorded data included wall temperature profile, preheated air temperatures, air mass flow rates (total, swirl, primary, axial (by difference)), and exhaust gas concentrations of CO_2, CO, O_2, and NO.

When obtaining particle size distributions with the EAA, the NO instrument was switched to its lower concentration scales, and a portion of the sample flow to the EAA was diverted to measure diluted concentrations of NO (Since only one NO instrument was used, this necessitated intermittent, rather than continuous monitoring of stack NO concentrations).

After commencing the diluted NO measurement, the dilution air flows and probe suction were adjusted until the particle concentration in the diluted stream was within a range which was measurable by the EAA. In order to keep diluted NO concentrations as high as possible (to guarantee acceptable signal to noise ratios in the NO instrument) the particle concentrations were near the saturation limit of the EAA.

After the desired dilution ratio was achieved, final adjustment of EAA flow rate was performed and EAA outputs were manually recorded. Typically, four or five measurements were recorded for each channel of the instrument for statistical purposes, resulting in a total sampling time of 2 to 4 minutes for each particle size distribution determination.

The procedure followed for collecting the LPI samples was essentially the same as that for the EAA size distributions. Again, since only one NO instrument was used, and since dilution ratios for EAA and LPI were necessarily different (as previously discussed), it was not possible to sample with EAA and LPI concurrently (except in the case of run 110179.01; for this run smaller mass samples were collected and a longer sampling time was used than for the other LPI samples). Thus, EAA sampling was performed just before and after collection of LPI samples. Pairs of EAA measurements so obtained were generally in good agreement.

Since LPI mass samples were cumulative, it was desirable to establish flow rates and dilution ratios prior to the commencement of LPI sampling, to assure good dilution measurements. This was accomplished by setting up a ′dummy′ flow in parallel with the LPI. During flow adjustments, the LPI was not activated, and the dummy flow was set at approximately the same value as the combined flows of the two LPI′s used for sampling. When the desired flow rates had been established, the dummy flow was deactivated simultaneously with the commencement of sampling with the LPI′s.

Reduction of raw data for flow rates, temperatures, equivalence ratio, sampling flow rates, and particle size distributions from EAA measurements was performed on the PDP-11 computer located in the Keck Laboratory of Environmental Engineering at Caltech. This facility was also used to obtain the statistical regressions discussed in Chapter 5.

CHAPTER 4

THEORY

Data indicate (see Chapter 5) that the mass distribution function for submicron flyash particles is well-characterized by two parameters: (a)the particle size at which the peak in the distribution occurs, (b)the total submicron particle mass concentration. In this investigation, primary interest is in the second of these parameters. The majority of the mass of submicron ash particles is thought to arise from condensation of vaporized mineral components of the parent coal particles. The processes which determine the extent of this vaporization will be examined. An overview of this mechanism of fine particle formation is first presented below, followed by the development of a first order model to describe the vaporization of coal mineral matter.

1.0 OVERVIEW

After entering the furnace, coal particles undergo rapid heating, due primarily to radiative and convective thermal exchange with the furnace walls, the flame, and the combustion gases inside the furnace. During the initial heating, the volatile matter present in the coal is driven off. This devolatilization process is probably completed in a time period on the order of tens of milliseconds or less (Lilley and Wendt, 1977; Field, et al., 1967). Combustible components of the volatile matter burn in the free stream far from the surface of parent coal particles. Again, the time scale for combustion of the major fraction of these species is probably less than a hundred milliseconds.

Following the devolatilization and volatiles combustion processes, the residual particulate carbon (char) is oxidized by heterogeneous reaction with furnace gases such as carbon dioxide and oxygen. The principal product of this surface oxidation of the char is carbon monoxide, which diffuses away from the particle and is later oxidized in the gas phase away from the particle surface.

The net exothermicity of the oxidation of carbon to carbon monoxide and/or carbon dioxide results in high particle temperatures. Because of these high temperatures, the mineral matter present in the char softens, melts, and vaporizes at a finite rate, depending on the particle temperatures, local gas composition, and mineral composition. As the mineral vapors diffuse away from the burning char particle, they encounter temperature and/or oxidizing conditions which favor (thermodynamically) the condensed form of these substances, resulting in nucleation or condensation of vapors on the surfaces of existing ash particles. Minute particles which may arise from nucleation ultimately either coagulate as a result of their Brownian motion, or diffuse to the surfaces of larger particles. It is the coagulation of nucleated vapors which is thought to give rise to the particles which constitute the observed submicron peak in the particle size distribution of the flyash which leaves the furnace.

Many interacting phenomena must be described in modeling the processes in a combustor. Since the data available in the present study were limited to the combustor wall temperature, input mass flow rates, and characteristics of the combustion products downstream of the convective cooling section, the quality of the simulation of the flame region is difficult to evaluate. The model described below is, therefore, a first order approximation of the major processes which was used for a qualitative and semi-quantitative examination of the ash vaporization process.

2.0 PARTICLE TEMPERATURE-TIME HISTORY IN COMBUSTOR

For a given coal type (composition) the vaporization of mineral matter in the coal is likely to be governed largely by the temperature history of the coal in the hot zone of the combustor. For example, if one assumes that vaporization of ash mineral species may be represented by Arrhenius rate expressions, then particle temperature history determines the extent to which these species vaporize during the combustion process. Thus, one must know this temperature history in order to understand and predict species vaporization for a fixed coal type. Since the combustor configuration in the present experiments made it impossible to measure particle temperatures in the hot zone directly, a computer model was used to calculate particle temperature histories from measured combustion parameters.

A particle burning model was used to calculate the particle temperature and burning rate as a function of position inside the combustor. This calculation required knowledge of the net radiative heat flux to the particle, and the gas composition and temperature in the free-stream far from the particle surface.

The following macroscopic processes were modelled to provide the data for the particle combustion calculations: (a)Radiative exchange between particles and surroundings (combustor walls, combustion gases, and other particles); (b)Entrainment and mixing of secondary combustion air in the flame jet; (c)Thermal exchange between the flame jet (wherein the particles are burned) and the surroundings (combustor walls, secondary air stream, and the flame itself).

All processes in the furnace were assumed to be steady; no transient phenomena were considered. The flame jet was assumed to spread linearly with axial distance from the jet origin, and the jet was represented in the calculation as a series of N uniform zones (See Figure 4.1) of equal lengths. Particle temperatures and burning rates were computed at the center of each zone, and zone residence times were computed using the jet mass entrainment model (See ´Entrainment and Mixing Model´) together with the assumed temperature and geometry of the zone being considered. Finally, an energy balance for each zone constituted the basis of a Newton-Raphson iterative calculation of the temperatures in the respective zones. The particle temperature-time profiles were re-computed at each step of the iteration until convergence was achieved. Convergence was obtained when the maximum fractional change of the absolute zone temperatures in the iteration was less than 0.0005.

The details of each component of the combustor model are described below.

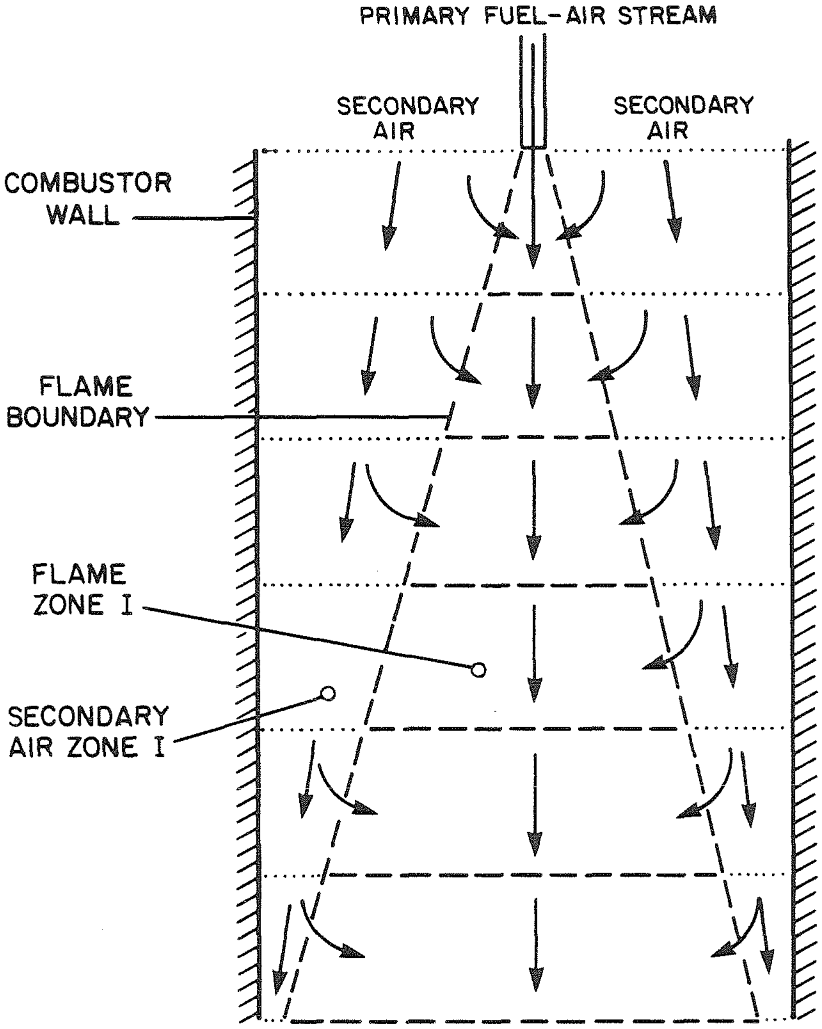

Figure 4.1: Model representation of flame region inside combustor. Each truncated cone is a zone throughout which conditions were assumed uniform.

2.1 PARTICLE COMBUSTION MODEL

The temperature-time history of a particle was determined by consideration of the four phases of the particle's lifetime in the combustor: (1)The initial heatup and devolatilization, (2)Volatile hydrocarbon combustion, (3)Burning, (4)Post char combustion phase. Each of these phases was described separately as follows:

(1)Initial heatup and devolatilization. As previously stated, the heatup and devolatilization processes occur with time scales much shorter than that of the burnout process of the char. Since the primary objective was to model the vaporization of ash mineral species which presumably occurs on the same time scale as the char burnout, the heatup and devolatilization processes were assumed to be instantaneous, and thus to have no effect on particle temperature-time profiles.

The composition of the volatile matter was calculated from the proximate and ultimate analyses of the coal by assuming that all hydrogen and oxygen in the coal are driven off during devolatilization (Sulfur, which comprised about 0.76%, by weight, of the parent coal, was also assumed to be driven off with the volatile hydrocarbons). The balance of the volatile fraction from the proximate analysis was assumed to be carbon.

(2)Volatile hydrocarbon combustion. The rate at which the volatile matter burns was assumed to be limited by the rate of entrainment of secondary combustion air. The rate of char burning during combustion of volatile matter was assumed to be insignificant because of the low concentration of oxygen in the flame. Thus, the particle temperature during volatile matter burnout was determined solely by thermal exchange with the walls and surrounding gas.

Since all processes were assumed to be steady (quasi-steady, in the case of the char burnout), the temperature of non-reacting char particles was determined by an energy balance for each particle size, considering radiation and conduction of heat to and from the particle surface as follows:

$$Q_{rad} + k(T_p)A_p(dT/dr)_{r_p} - A_p\sigma T_p^4 = 0 \qquad (4.1)$$

where:

Q_{rad} = Total radiation absorbed by particle surface from walls and surrounding gas.

It was assumed that particles are spherical black-body radiators, and the thermal conductivity of the gas was approximated by the linear least-squares correlation of conductivity with temperature for air. The calculation of the incident radiation on the particle surface is described below (See 'Radiative Transfer between Particles and Surroundings').

(3)Char combustion. Due to the exothermicity of the carbon oxidation reactions peak particle temperatures occur during the period when the char particles burn. Char burning was assumed to begin after volatile matter is burned, and to continue until all the carbon in the residual char particle is consumed. The particle temperature during this period is affected by both thermal exchange with surroundings and by the heat release due to the carbon oxidation.

The complete combustion of the carbon in the char particles is generally considered to involve two types of oxidation reactions, viz., (a)Heterogeneous oxidation of carbon at the surface of the char by oxygen and/or carbon dioxide from the free-stream (or particle far field). The principal product of the char oxidation is presumably carbon monoxide, as suggested by Caram, et al. (1977), Mon, et al. (1978), and Libby and Blake (1979); (b)Homogeneous gas phase oxidation of carbon monoxide during transport (by diffusion and convection) from the particle surface into the free stream.

As previously indicated, various models have been proposed to describe the quantitative aspects of the char oxidation process. Following Libby and Blake (op cit.), the rate of oxidation of CO may be approximated by using the more appropriate (depending on conditions) of the following limiting cases: (a)The reaction rate is considered to be infinitely fast, in which case a flame sheet is formed either at, or displaced from, the particle surface, depending on conditions. For this case, CO and O_2 do not coexist at any point; (b)The reaction rate is considered to be zero in the boundary layer, or near field, of the particle. The assumption in this case is that the oxidation of CO occurs in the free stream, far from the particle surface.

For the purposes of this investigation, the principal difference between these two possibilities lies in the manner in which the energy released in the CO oxidation is felt by the char; i.e., whether the effect of this thermal release is simply to increase the temperature of the free stream, or whether the reaction occurs sufficiently close to the particle surface to result in a higher particle temperature than would otherwise be expected from direct heating of the free stream only.

Clearly the true CO oxidation rate lies somewhere between these two extreme cases; i.e., CO oxidation proceeds at a finite rate throughout the near field of the particle and beyond in the free stream, subject to conditions of gas temperature and composition, and equilibrium considerations. However, it has been shown (See Chapter 2) that under the conditions of particle size, temperature, and gas composition typical of pulverized coal combustion it is reasonable to assume that all CO oxidation takes place in the free stream far from the particle. Thus, in constructing the combustion model to describe the present system, this assumption was made.

The particle combustion process was described using a quasi-steady-state model in which the particle diameter was assumed to be constant in the solution of the transport equations at any given point. The particle was assumed to be in an infinite quiescent medium. For particles less than 100 microns in diameter, and aerodynamic conditions typical of pulverized coal combustion, this assumption is reasonable (Mulcahy and Smith, 1969). Considering both convective and molecular diffusion terms, the conservation equations for O_2, CO_2, and CO may be written (assuming steady conditions, and no gas phase reactions) together with Fick's diffusion law (e.g., see Bird, et al., 1960), as follows:

$$N_i r^2 = (\text{constant}) \tag{4.2}$$

$$N_i = c\mathcal{D}_i (dx_i/dr) + x_i \sum N_j \tag{4.3}$$

where:

N_i = Molar flux of species i

c = Total molar concentration of gas (P/RT)

$\mathcal{D}_i$ = Binary diffusion coefficient of species i in N_2, assumed to vary linearly with temperature

x_i = Mole fraction of species i.

The global carbon oxidation reactions kinetics of Field (1967) and Dobner (1976) were used as follows:

$$C + \frac{1}{2}O_2 = CO \tag{4.4}$$

$$C + CO_2 = 2CO \tag{4.5}$$

where:

R_1 = Molar consumption rate of carbon by reaction 4.4

= (8710 gm/cm sec-atm)x_{O_2} exp(-18,000 K/T)

R_2 = Molar consumption rate of carbon by reaction 4.5

= (247 gm/cm sec-atm)x_{CO_2} exp(-21,060 K/T).

The energy balance for a particle may be written:

$$Q_{\text{rad in}} + H_c = Q_{\text{rad out}} + H_{\text{prod}} + Q_{\text{cond}} \tag{4.6}$$

where:

$Q_{\text{rad in}}$ = Total radiation incident on (and absorbed by) carbon surface (See ´Radiative Transfer Between Particles and Surroundings´)

H_c = Enthalpy flow to particle surface due to diffusion of carbon to particle surface (as prescribed by the quasi-steady assumption)

$= \dot{m}_c h_c(T_p)$

$Q_{\text{rad out}}$ = Total radiation from particle surface

$= \sigma A_p T_p^4$

H_{prod} = Total enthalpy flow away from particle surface due to diffusion of reactants and products

$$= \sum \dot{m}_j h_j (T_p)$$

Q_{cond} = Energy flow from particle surface due to conduction

$$= -A_p k(T_p)(dT/dr)$$

In the above equations there are five unknowns:

$$T_p,\ x_{O_2}(r_p),\ x_{CO_2}(r_p),\ \dot{m}_{O_2},\ \dot{m}_{CO_2}$$

the gas temperature and composition at $r = \infty$ were supplied by the entrainment and thermal exchange models previously mentioned. Solution for the five unknown variables was accomplished by assuming a starting estimate for T_p. Using this estimate the transport equations were solved subject to the boundary conditions supplied by the kinetic expressions. This yielded the other four unknown variables. A test for particle energy balance was then performed and the particle temperature estimate was adjusted. The calculation was repeated iteratively until the energy balance was satisfied. After convergence was achieved the final values of particle temperature and concentrations of oxygen and carbon dioxide at the particle surface were used in the kinetic expressions to calculate the overall carbon consumption rate.

(4)Post combustion phase. The time and location of char burnout varies with particle size. After char burnout residual ash was assumed to break into a fixed number of fragments, as prescribed by the break-up model described in Chapter 2. The temperatures of these fragments were determined in the same manner as during the volatiles burning period; i.e., by an energy balance on the particle considering thermal exchange (radiative and conductive) with the surroundings.

2.2 RADIATIVE TRANSFER BETWEEN PARTICLES AND SURROUNDINGS

A number of simplifying assumptions were made in order to facilitate heat transfer modelling. Scattering of radiant energy by gas molecules and by particles was neglected, as were wall reflections. Moreover, particles were assumed to be black-body radiators. With these assumptions the net radiative exchange between a particle and the surroundings is given by:

$$Q_{net\ rad} = Q_{rad\ in} - A_p \sigma T_p^4 \qquad (4.7)$$

where:

$Q_{net\ rad}$ = Net thermal radiation to particle

$Q_{rad\ in}$ = Total radiation incident on particle.

The incident radiation was assumed to originate from the wall and from the gas-particle cloud in the flame surrounding the cloud.

Since the only gaseous components of the furnace which contribute significantly to gas radiative exchange are CO_2 and H_2O (Field, et al., 1967), only these components were considered. The secondary air stream as well as other gases in the flame were considered to be transparent to radiation, and thus, non-emitting. Each flame zone was treated as a uniform, isothermal, spherical volume grey emitter (See Figure 4.2). The radius used for the sphere was the volume-equivalent radius of the zone. An ′effective′ zone temperature, T_i, and emissivity, ε_i, were calculated

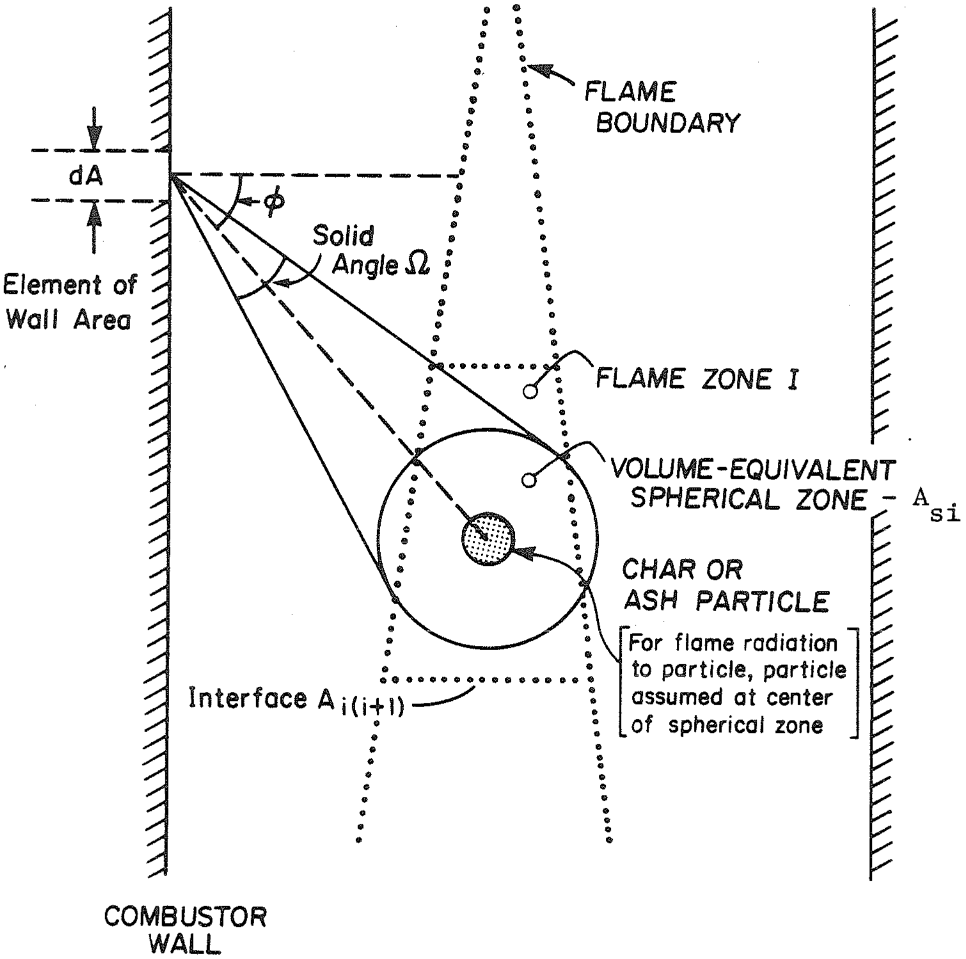

Figure 4.2: Schematic of typical flame zone (truncated cone) in model calculation. For radiative exchange calculations the truncated cone was replaced with a volume-equivalent sphere.

such that:

$$Q_{i,\text{rad out}} = \varepsilon_i A_{si} \sigma T_i^4 \qquad (4.8)$$

where:

$Q_{i,\text{rad out}}$ = Total radiant emission from zone i.

T_i and ε_i were calculated as suggested by Field, et al. (1967) in the following manner.

For a mixture of several non-interacting, grey components, the overall absorption coefficient is the arithmetic sum of the individual absorption coefficients:

$$\kappa = \kappa_1 + \kappa_2 + \ldots \qquad (4.9)$$

The overall emissivity of a cloud of thickness L is then given by:

$$\varepsilon = 1 - \exp(-\kappa L). \qquad (4.10)$$

The effective radiation temperature for a mixture is computed by considering the basic relation for emission by a volume radiator. At temperature T an elementary volume dVol having absorption coefficient κ emits at a rate:

$$4\kappa\sigma T^4 d\text{Vol} \qquad (4.11)$$

Thus, for an elementary volume containing several components at different temperatures the rate of emission is:

$$4\sigma dVol \sum \kappa_j T_j^4 \qquad (4.12)$$

Using the above expression for overall absorption coefficient, the effective radiating temperature T of the mixture is thus defined in terms of the mixture absorption coefficient and the component temperatures and absorption coefficients according to:

$$4\kappa\sigma T^4 dVol = 4(\sum \kappa_j \sigma T_j^4)dVol \qquad (4.13)$$

which implies:

$$T^4 = \sum(\kappa_j T_j^4)/(\sum \kappa_j) \qquad (4.14)$$

To use the above expressions in radiative transfer calculations treating a radiating cloud as a single radiator, it is necessary to compute a mean ´whole- body´ emissivity ε for the cloud. This parameter is defined by the equation:

$$Q_{rad} = \varepsilon A_i \sigma T^4 \qquad (4.15)$$

where:

Q_{rad} = Total radiant emission by the zone

A_i = Total exterior surface area of the cloud.

To evaluate ε, the cloud radiation Q_{rad} must be calculated by considering the interaction of infinitesimal volume elements within the zone. This calculation has been done analytically by Booth (1949) for a spherical zone. His analytical result is approximated within 10% (See Field, op cit.) by the expression:

$$\varepsilon_{sphere} = 1 - \exp(-0.6\kappa D) \qquad (4.16)$$

for values of κD ranging from 0 to 10 (D= diameter of spherical zone). This expression was used to approximate the overall emissivity of the volume-equivalent sphere used to represent each zone in the radiative exchange calculations involving zone-to-zone and zone-to-wall heat transfer. For calculations involving zone radiation to particles inside the zone itself, the expression for the whole-body emissivity of a uniform, grey sphere, evaluated at the center of the sphere, was used (See below).

The extinction coefficients of the gaseous components CO_2 and H_2O were approximated using graphical representations (McAdams, 1954) for whole-body emissivity of these gases as a function of PL and T, where P=gas pressure, L=characteristic dimension of gas volume, and T=gas temperature.

The extinction coefficient of the particles in the zone was calculated from the relation (Field, 1967)

$$\kappa = 1/4 \sum C_k SA_k \tag{4.17}$$

where:

C_k = Mass concentration of particles of initial size d_k

SA_k = Mass-specific surface area of particles of initial size d_k .

The above relation follows directly from the previous expression for emission from a differential volume radiator plus the assumption that all particles radiate as black bodies.

The radiation to any particle in the i-th flame zone was estimated by treating the particle as though it was located at the center of the equivalent spherical volume radiator discussed above (The mean path length between points within a sphere and the spherical surface was estimated by a simple two-dimensional calculation using a circle instead of a sphere. In this case the mean path length was about 13% greater than the radius. Thus, the use of the spherical radius as a mean path length for the equivalent spherical zone was reasonable). The radiation to a black particle, so located, is given by:

$$Q_{\text{gas-part}} = (1-\exp(-\kappa_i D_i/2))A_p \sigma T_i^4 \tag{4.18}$$

where:

D_i= Diameter of equivalent spherical volume radiator for zone.

The radiation reaching a particle from the refractory furnace wall is next considered. Again, treating the particle as though it were at the center of a spherical radiating cloud (of diameter D), the attenuation factor for wall radiation passing through the cloud to the particle surface is given by:

$$\exp(-\kappa D/2).$$

For the combustion mixtures in these experiments, values of κD (optical thickness) were generally below 0.16. implying an attenuation factor of about 0.92. That is, nearly all the wall radiation directed toward a particle at the center of the cloud would reach the particle, unattenuated. Thus, to simplify calculations the optical thickness of the flame was neglected in calculating the amount of wall radiation absorbed by a particle.

Total wall radiation incident on a particle surface was calculated by integration over the entire combustor wall of the radiant energy reaching the particle from a differential element of wall surface area. The separate contributions and geometry of the combustor quarl and radiation shield were accounted for in the calculation, and the radiation intensity I of the refractory wall was assumed to be given by:

$$I = \frac{1}{\pi} \sigma T_w^4 \qquad \text{(Wall assumed black).} \qquad (4.19)$$

Thus, the integral expression for the wall radiation to a particle is :

$$Q_{rad,wall} = \int_{wall} \frac{1}{\pi} \sigma T_w^4 (\cos\phi) \Omega dA \qquad (4.20)$$

where:

$Q_{rad,wall}$ = Total wall radiation absorbed by particle

ϕ = Angle between surface normal at dA and ray from dA to zone center

Ω = Solid angle subtended by particle, measured from dA.

The integral above was evaluated numerically using a Simpson's rule algorithm.

2.3 ENTRAINMENT, MIXING, GAS COMPOSITION MODELS

Due to the geometry of the laboratory burner and combustor and the exothermic combustion reactions occurring in the flame jet, it was necessary to use simplifying assumptions in modeling the entrainment and mixing processes. A first-order jet entrainment and mixing model was used which utilized empirical entrainment and spreading rate data for non-reacting jets. Following is a brief quantitative description of this model.

2.3.1 Entrainment Rate -

For a non-reacting jet of density ρ entering a quiescent fluid of density ρ_1, the mass entrainment rate in the far field of the jet has been found to be (Ricou and Spalding, 1961):

$$d\dot{m}/dx = 0.32(\rho_1/\rho)^{1/2}(\dot{m}_o/D_j) \qquad (4.21)$$

where:

$\dot{m}$ = Mass flow rate of jet fluid

x = Distance measured parallel to combustor axis

$\dot{m}_o$ = Initial mass flow rate of jet fluid

D_j = Initial diameter of jet.

This entrainment relation was used as a basis for the entrainment rate expression in the present model.

The actual geometry of the fuel injector was such that the primary fuel-air stream was injected directly into the wake of a bluff cylinder or disc (depending on which burner was used). Studies of turbulent exchange in pure wakes have been performed (e.g., see Winterfield, 1965). However, empirical data for the jet-wake configuration used in the present experiments was not available. Thus, as a first-order approximation the entrainment of secondary combustion air into the flame region was described using the above two-fluid entrainment model with the density ratio calculated locally. Wake geometry was not considered nor was the influence of the non-zero velocity of the annular secondary air jet.

2.3.2 Mixing Rate -

To describe accurately the finite mixing rate distribution throughout the flame jet is a complex task. Again, given that the current analysis was intended to be a first-order approximation, the simplest possible assumption was made to describe quantitatively the mixing rate of the entrained secondary combustion air in the fuel-air (flame) jet; viz., that the rate is infinitely fast and that the gas concentration throughout the jet (in the far field of individual particles) is uniform.

2.3.3 Gas Composition -

Using the foregoing aerodynamic model, the free stream gas composition of the jet was calculated by separate consideration of the combustion of volatile matter and residual char after devolatilization. In the early flame zone, before sufficient secondary air had been entrained to completely consume the volatile combustible matter, the char oxidation rate was assumed to be zero. The gas composition in this early zone was calculated as follows. For very fuel rich conditions (explained below) all oxygen (from the fuel itself and the entrained air) was assumed to be consumed by the following reaction:

$$C + xH + \frac{z}{2}O_2 + mO_2 + 3.76mN_2 \rightarrow 2nCO + nxH_2 + (1-2n)CH_x + 3.76mN_2$$

where;

$$n = (2m + z)/2.$$

The carbon/hydrogen ratio in the unburned hydrocarbon 'CH_x' was assumed to be the same as in the parent coal and the $\frac{z}{2}O_2$ term is due to oxygen in the coal itself. For moderately fuel rich conditions equilibrium concentrations were assumed for CO_2, H_2, and H_2O at the temperature of the zone ('Very fuel rich' meant the ratio of total atomic oxygen (including oxygen in both the fuel itself and the entrained air) to total volatile carbon was between 0 and 1; 'moderately fuel rich' meant the above ratio was between 1 and the stoichiometric value for complete oxidation of all volatile carbon to CO_2 and all hydrogen to H_2O).

After sufficient air was entrained to completely oxidize all the combustible volatiles, the gas composition was determined using a 2nd-order predictor-corrector numerical technique in the following way. The mass flow rate of burned fuel at the zone entrance was calculated from the mass flow rate of burned volatile matter plus the total char consumed to that point. The oxygen and carbon dioxide concentrations at the point in question were then calculated using stoichiometric relations represented in the overall oxidation reaction:

$$CH_x + yS + zO + mO + 3.76mN_2 = CO_2 + x/2H_2O + nO_2 + 3.76mN_2 + ySO_4 \qquad (4.22)$$

where:

$n = (m + z/2 - 1 - x/4 - y).$

x, y, and z represent hydrogen, sulfur, and oxygen present in the coal, and were computed locally based on the ratios of H, S, and O to total burned C at that point.

After determining the gas composition at the zone entrance, the gas composition at the zone exit was estimated by using the particle burning rates at the zone entrance to estimate the change in the amount of burned carbon at the end of the zone. The particle burning rates (and temperatures) were then recalculated using the mean values of the gas concentrations between the zone entrance and exit.

2.4 MODEL FOR THERMAL EXCHANGE BETWEEN FLAME AND SURROUNDINGS

A principal input to the char combustion model was the axial gas temperature profile in the free stream of the flame jet. Since this profile was not known, a priori, it was necessary to use a thermal exchange model for the flame. This was done by writing energy balances for the flame zones previously discussed.

The following components of the energy balance were considered in these equations:

1. Advective exchange between flame zones;

2. Advective exchange between each zone and the secondary combustion air stream (i.e., secondary air entrainment);

3. Radiative exchange between zones and the refractory wall.

Heat release by combustion reactions was computed by considering total enthalpy (chemical and thermal) in the advective exchange terms. The components of the heat balance equation for a representative zone are illustrated schematically in Figure 4.3 and the manner in which these components were represented is considered below.

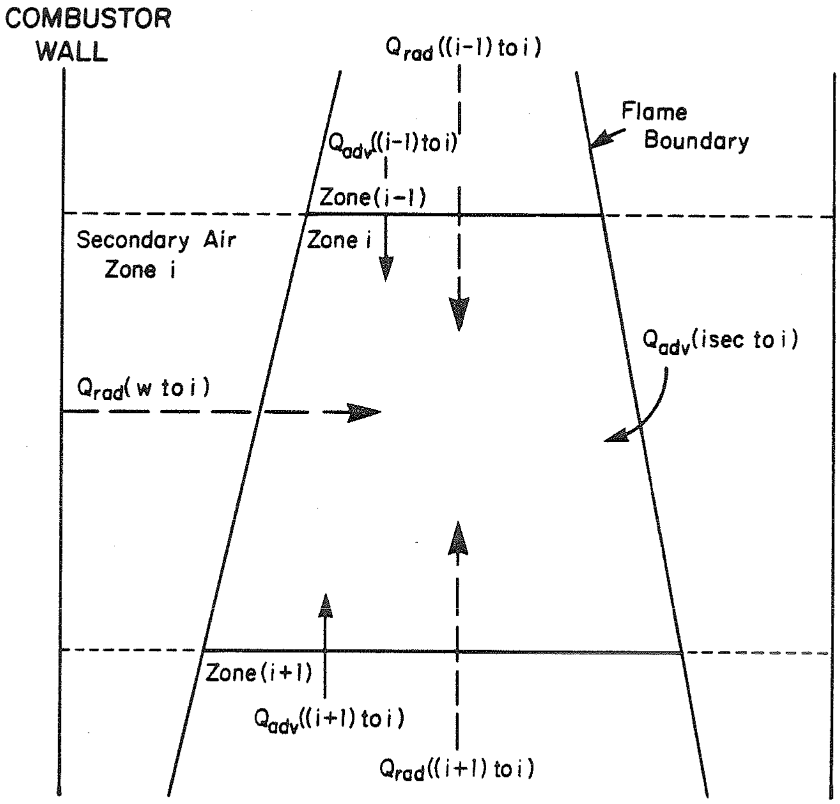

Figure 4.3: Schematic of typical flame zone in model calculation illustrating components of the heat balance for the zone.

2.4.1 Advective Exchange Model -

Advective exchange was treated by considering its three components. The first component is enthalpy inflow due to the influx of entrained secondary combustion air. For each flame zone there is a corresponding annular zone of equal length outside the jet which was assumed to consist only of unentrained secondary combustion air (See Figure 4.1). The temperature of the air stream in this zone varies because of the stream's contact with the hot combustor wall and the flame jet. The change in the temperature of the secondary air in this zone from that of the previous secondary zone was estimated by writing an energy balance equation for the secondary air zone, considering advective flows into and out of the zone, and convective heat transfer from the wall and from the adjacent flame zone. The resulting equation is linear in the respective temperatures and was used to calculate the secondary air temperature in terms of the wall and flame zone temperatures, and the previous secondary air zone temperature.

Using the secondary air temperature, the enthalpy influx of the entrained secondary air was calculated as follows:

$$H_{adv}(\text{isec to i}) = \dot{m}_{ei} h (T_{isec}) \qquad (4.23)$$

where:

H_{adv} (isec to i) = Advective enthalpy inflow to zone i from secondary air zone i

$\dot{m}_{ei}$ = Entrainment air mass flow rate into zone i.

The second component of the advective exchange is enthalpy inflow due to the influx of combustion gases and particles from the preceding zone. Enthalpies of all mixture components (including all combustion products, unburned gaseous hydrocarbons, nitrogen, oxygen, solid carbon, and ash) were calculated from published thermochemical data (Stull and Prophet, 1971) for each species at the gas temperature of the previous zone (distinct from the effective zone radiation temperature used in radiative exchange calculations). The form of this enthalpy inflow term in the model is as follows:

$$H_{adv}\Big((i-1) \text{ to } i\Big) = (\dot{m}_i)_{in} \sum_j (x_j h_j)_{i-1} \tag{4.24}$$

where:

$H_{adv}\Big((i-1) \text{ to } i\Big)$ = Advective enthalpy inflow to zone i from zone (i-1)

$(\dot{m}_i)_{in}$ = Mass flow rate of combustion gas mixture entering zone i from zone (i-1)

x_j = Mixture mass fraction of species j.

Mixture composition used to calculate the mass fractions of species in each zone was calculated on the basis of the arithmetic mean of the entry and exit mixture compositions. Mass-specific enthalpies were calculated at the temperature of the gas in the the zone.

The third component of advective exchange is due to the efflux of combustion gases and particles at the temperature of the current zone. The form of this term is analogous to that of the inflow term:

$$H_{adv}\Big(i \text{ to } (i+1)\Big) = (\dot{m}_i)_{out}\sum_j (x_j h_j)_i \qquad (4.25)$$

where:

$H_{adv}\Big(i \text{ to } (i+1)\Big)$ = Advective enthalpy outflow from zone i to zone (i+1)

$(\dot{m}_i)_{out}$ = Mass flow rate of combustion gases from zone i to zone (i+1).

2.4.2 Gas Radiation Model -

In writing the transport expressions for radiative heat transfer between two flame zones, or between a single zone and the wall, similar assumptions to those discussed previously in the particle calculation were made. Each zone was treated as a uniform, isothermal, grey, spherical volume radiator (See ´Radiative Transfer Between Particles and Surroundings´), and effective zone temperatures and emissivities were calculated for each zone by considering radiative properties of H_2O, CO_2, and particles within the zone.

The calculation was simplified by neglecting reflection of radiation from the combustor walls. This was justified by the following reasoning. If a spherical gray surface is centered inside a gray spherical radiating cavity the net radiant exchange between the enclosed surface and the wall is:

$$q_{w-s} = \sigma(T_w^4 - T_s^4) \times A_w \times \frac{1}{\frac{\rho_w}{A_w\varepsilon_w} + \frac{1}{A_w} + \frac{\rho_s}{A_s\varepsilon_s}} \qquad (4.26)$$

where:

σ = Stefan-Boltzman constant

T_w = Wall temperature (absolute)

T_s = Surface temperature

ε = Surface (or cloud) emissivity

ρ = Surface reflectivity

A_w = Radiating area of cavity.

If the spherical surface inside the cavity is now replaced by a uniform gray radiating cloud the same expression should be valid with ε_s replaced by ε_C, and ρ_s replaced by $(1-\varepsilon_C)$, since in either case, the non-absorbed radiation ultimately returns to the cavity wall, by reflection in the case of the enclosed surface, and by transmission in the case of the enclosed cloud.

Using the above expression it was found that the maximum difference between the radiant exchange for $\varepsilon_w = 1.0$ (no wall reflection) and $\varepsilon_w = 0.85$ (Kreith (1965) gives a value of 0.84 for surface emissivity of silica refractory brick at 1640 K) is about 8% (ε_C was taken to be 0.1, which is representative of overall cloud emissivity calculated by the model). This difference is sufficiently small that it may be neglected in the present simplified model and it was assumed in the model calculations that the furnace walls were black and non-reflecting.

In considering the radiative exchange between any given zone and the others only adjacent zones were considered, again, in order to simplify the calculation. The exchange between two adjacent zones was crudely estimated in the following manner. In Figure 4.4 is shown the assumed geometry of the isothermal zones. Based on this geometry it is reasonable to assume that all of the exchange between two such zones would occur across the interface A. The total radiation (q_{12}) from zone 1 across the interface was estimated by using the whole-body emissivity (ε_1) for the zone, together with the equivalent zone temperature (T_1) (See 'Radiative Transfer Between Particles and Surroundings') as follows:

$$q_{12} = A_{12}\varepsilon_1\sigma T_1^4 \tag{4.27}$$

where:

A_{12} = Interfacial area between zones 1 and 2.

The radiation from zone 1 which is absorbed by zone 2 (q_{12}') was thus estimated as follows:

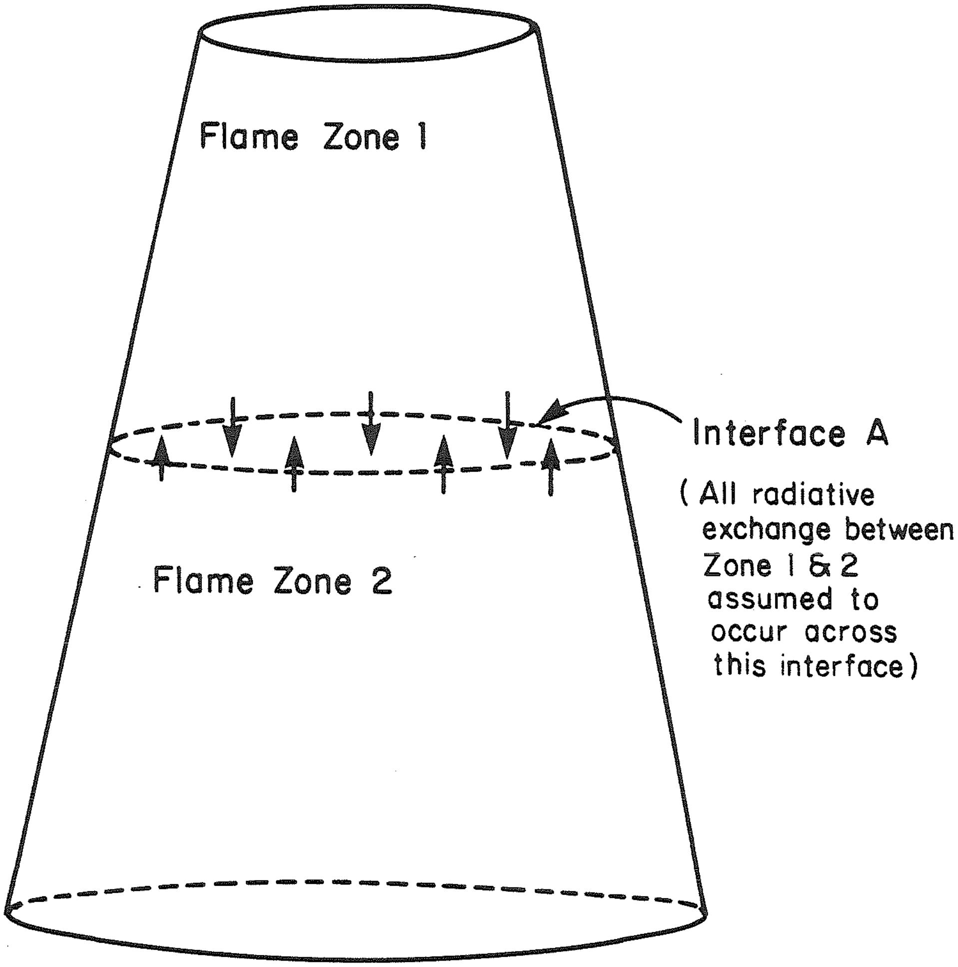

Figure 4.4: Schematic of adjacent isothermal zones in model calculation. Effective area across which radiative exchange was assumed to occur is shown.

$$q'_{12} = A_{12}\varepsilon_1\varepsilon_2\sigma T_1^4 \qquad (4.28)$$

An analogous expression was used for the radiation from zone 2 absorbed by zone 1, and the net heat lost by zone 1 through radiative exchange with zone 2 is:

$$Q_{rad}(1 \text{ to } 2) = A_{12}\varepsilon_1\varepsilon_2\sigma(T_1^4 - T_2^4) \qquad (4.29)$$

where:

$Q_{rad}(1 \text{ to } 2)$ = Net radiant heat transfer from zone 1 zone 2.

The net radiative heat loss by a flame zone to the walls was calculated by replacing the zone with a volume-equivalent sphere at the location of the zone. A constant fraction (equal to the calculated whole-body zone emissivity) of all radiation which reaches the spherical zone boundary was assumed to be absorbed by the zone, independent of the angle of incidence to the surface. Using these assumptions the wall radiation absorbed by the zone was estimated to be:

$$Q_{rad}(w \text{ to } i) = \int_{\text{wall}} \frac{1}{\pi}\, \varepsilon_1 \sigma T_w^4 (\cos\phi)\Omega dA \qquad (4.30)$$

where:

$Q_{rad}(w \text{ to } i)$ = Total wall radiation absorbed by zone i

dA = Element of wall surface

ϕ = Angle between surface normal at dA and ray from dA to zone center

Ω = Solid angle subtended by spherical zone at dA.

The net heat loss by the zone to the wall is the difference between the emitted radiation from the zone and the wall radiation absorbed:

$$Q_{rad}(1 \text{ to } w) = \varepsilon_1 A_{si} \sigma T_1^4 - \int_{wall} \frac{1}{\pi} \varepsilon_1 \sigma T_w^4 (\cos\phi) \Omega dA \qquad (4.31).$$

As in the particle radiative calculation, the above integration included quarl and radiation shield surfaces as well as combustor wall surfaces. Entry and exit ports were treated as perfect radiation sinks.

2.4.3 Iterative Calculation to Determine Gas Temperatures in Zones -

The overall energy balance for zone i was formulated expressing all heat exchange terms as heat flows into the zone (illustrated in Figure 4.3). The resulting equation is of the form:

$$\begin{aligned} &Q_{rad}(w \text{ to } i) + Q_{rad}((i+1) \text{ to } i) + Q_{rad}((i-1) \text{ to } i) + \\ &Q_{adv}((i+1) \text{ to } i) + Q_{adv}((i-1) \text{ to } i) + Q_{adv}(isec \text{ to } i) \\ &= (\text{Total heat flow into zone } i) = 0 \qquad (4.32) \end{aligned}$$

where:

$Q_{rad}(w \text{ to } i)$ = Net radiative transfer, wall to zone i

$Q_{rad}((i+1) \text{ to } i)$ = " , zone (i+1) "

$Q_{rad}((i-1)\text{ to }i)$ = " , zone (i-1) "

$Q_{adv}(\text{isec to }i)$ = Net advected energy, entr. air to zone i

$Q_{adv}((i+1)\text{ to }i)$ = " , zone (i+1) "

$Q_{adv}((i-1)\text{ to }i)$ = " , zone (i-1) "

The entire set of N heat balance equations for the N zones may be written conceptually as follows:

$$\overline{F}(\overline{T}) = 0 \tag{4.33}$$

where:

$\overline{F}$ = Vector valued function whose ith component is the left-hand side of the heat balance equation for zone i

$\overline{T}$ = Vector of zone gas temperatures.

The zone gas temperatures were computed by finding the value of the zone temperature vector $\overline{T}$ which satisfies this equation. This was done by first using an initial estimate for $\overline{T}$, and then calculating the terms in the heat balance equation for each zone in succession. An under-relaxed Newton-Raphson iterative method was then used to refine the estimate of the temperature $\overline{T}$ until the above vector equation was satisfied. At each stage of the iteration the particle temperature-time profile was recalculated and the profile corresponding to the final set of zone gas temperatures was assumed correct.

3.0 KINETICS OF MINERAL VAPORIZATION AND SUBMICRON PARTICLE FORMATION

The rate of vaporization of any species from a particle is limited by transport or by kinetic factors. For kinetic control of the vaporization rate, classical kinetic theory (e.g., see Carberry, 1976) suggests that the rate of vaporization is proportional to the surface area or volume of ash present, depending on whether one assumes surface kinetic control (corresponding to zero intra-particle diffusivity) or volume kinetic control (corresponding to infinite intra-particle diffusivity). The appropriate vaporization rate expressions for these cases are as follows:

$$dm/dt = -k \times d_p^2 \text{ (surface kinetic control)} \qquad (4.34)$$

$$dm/dt = -k \times d_p^3 \text{ (volume kinetic control)} \qquad (4.35)$$

where:

m = Mass of particle undergoing vaporization

k = Proportionality (or rate) constant

$= \beta(T) \times \exp(-E/T)$

$\beta(T)$ = Pre-exponential or Arrhenius factor

E = Activation energy for vaporization

d_p = Particle diameter.

For external transport limited vaporization from a spherical particle one assumes equilibrium vapor pressure at the particle surface and calculates the rate of diffusion of vapor away from the particle. Solution of the diffusion equation for a single species with spherically-symmetric geometry gives:

$$dm/dt = -2\pi(MW)d_p c \mathcal{D} \ln(\frac{1}{1 - x_{r_p}}) \tag{4.36}$$

where:

dm/dt = Mass rate of vaporization

MW = Molecular weight of vaporizing species

d_p = Particle diameter

c = Total molar concentration in surrounding gas (P/RT)

$\mathcal{D}$ = Binary diffusion coefficient for species in ambient gas ($=\mathcal{D}(T)$)

x_{r_p} = Mass fraction of vapor at particle surface.

For refractory minerals, the equilibrium partial pressure of vapor is small compared with the total pressure; thus, $x_{r_p} \ll 1$. Hence, the log term can be approximated by the first term in the Taylor series expansion. The above equation then becomes:

$$dm/dt = -2\pi(MW)d_p c \mathcal{D} x_{r_p} . \tag{4.37}$$

The Clapeyron equation may be integrated to approximate the dependence of the equilibrium vapor pressure on temperature as follows:

$$(dP/P)_{sat} = \Delta h_{vap}/R \cdot (dT/T^2) \quad (4.38)$$

implying:

$$P_{sat} = P_{sat_0} \cdot \exp(-\Delta h_{vap}/RT + \Delta h_{vap}/RT_0) \quad (4.39)$$

where:

P_{sat} = Equilibrium vapor pressure

Subscript 0 indicates a reference temperature.

Since x (mass fraction) is proportional to P_{sat} it follows that:

$$dm/dt = -\alpha d_p \mathcal{D} \exp(-\Delta h_{sat}/RT) \quad (4.40)$$

where:

α = Constant (independent of temperature and particle size)

Hence, the limiting cases for either kinetic or transport-limited vaporization give the following form of the vaporization rate expression:

$$dm/dt = -B(T) \cdot m \cdot F(d_p) \cdot \exp(-E/RT) \quad (4.41)$$

where:

$F(d_p)$ is of order between 0 and -2.

Using an expression of this form one can calculate the fraction of a given mineral species which is vaporized during the combustion process, if the temperature-time history of the species is known. Thus, the mass concentration, as well as the aggregate composition of the submicron particle mode of the flyash can be predicted if the kinetic constants in the vaporization rate expression are known for the parent mineral species (given the coal type, composition, and particle size distribution) together with the temperature-time history of the char particles in the combustor.

The above vaporization model was used in the present investigation, together with the combustion model described previously, to estimate the effective values of the Arrhenius parameters for the composite ash of the coal used in these experiments. Estimates were done assuming both zero order and inverse square dependences of F on d_p. The values obtained for the Arrhenius factor (i.e., $B(T) \times F(d_p)$ in Eq. 4.41) and the activation energy (E) were compared with similar data obtained by other investigators. The procedure was as follows.

First, the foregoing combustion model was used to calculate the temperature-time histories of individual char particles in the combustor using the measured combustion conditions from selected experiments. A lower bound of activation energy was then chosen (below the lowest values reported in the literature for vaporization of ash species. See Chapter 5 for a tabulation of some of these reported values). A computer searching program was used to locate the value of the parameter

B (assumed to be a constant for all particle sizes, and independent of temperature) which would minimize (approximately) the sum of squares of differences between the measured total mass concentration of vaporized ash and that predicted from the Arrhenius vaporization model with the calculated temperature-time history of the particles. The value of the activation energy was then incremented by some fraction, and the process was repeated until the approximate values of B and E were located which would yield the absolute minimum of the sum of squares of differences. The precise minimizing values could then be quickly located using a Newton-Raphson iterative calculation.

The results of these calculations are discussed in Chapter 5.

CHAPTER 5

RESULTS

1.0 OVERVIEW OF RESULTS PRESENTED

In this chapter the results of the experimental program and the computer modeling discussed in Chapter 4 are presented and discussed. The order of presentation is as follows.

(A)Laboratory System Performance--This section first discusses reproducibility of experimental conditions as reflected in the measurements. Probable sources of error in the measured and calculated characteristic parameters, and stability of experimental conditions are next discussed. Finally, a short discussion of modifications and rationale of changes to the laboratory system is given.

(B)Presentation of Results--This section first discusses size distribution data for submicron ash particles from EAA measurements. Shape invariance of the volume distribution functions from several laboratory measurements is noted. The measured dependence of the volume-mean particle diameter on the total submicron aerosol volume concentration is compared with the predicted dependence from self-preserving Brownian coagulation theory. Correlations of total submicron particle volume concentration with NO concentration and with effective wall temperature are discussed (Effective wall temperature is defined in Chapter 3). Results of composition measurements of size-segregated mass samples of fine fly ash particles are presented. Multiple linear regression analysis results for the laboratory data are presented and inferences about the relative importance of the combustion parameters are suggested.

(C)Computer Modeling--In the last section the results of the computer modeling of the combustion and vaporization processes are presented. Calculations of particle temperature histories are first discussed. Results of fitting an Arrhenius rate expression to estimate ash vaporization rates from laboratory measurements of total submicron particle volume (mass) are then presented. Estimates are given for vaporization kinetic parameters for the Utah sub-bituminous coal burned in these experiments. Inferences from the modeling of the influence of macroscopic combustion parameters on the ash vaporization process are discussed.

2.0 LABORATORY SYSTEM PERFORMANCE

2.1 REPRODUCIBILITY OF DATA

The measured and calculated parameters used to characterize combustion conditions and submicron fly ash particles are described in Chapter 3. These parameters are tabulated in Appendix F. Numbers in the first column represent the dates and run numbers of the data points (e.g., 92380.51 indicates run 51 on Sept 23, 1980). The second parameter is the principal dependent parameter of interest (See Chapter 4), viz., the total volume concentration (V) of submicron particles, corrected to standard conditions, defined to be:

1. Fuel-air equivalence ratio 85% of stoichiometric (3.2% O_2 in flue gases);

2. Exhaust gas dried;

3. Exhaust gas at 760 mm Hg, 25 C.

The next seven numbers to the right are the six combustion parameters used to characterize the combustion condition, and the NO concentration in the exhaust gas.

In Figure 5.1, the submicron aerosol volume, V, is plotted with

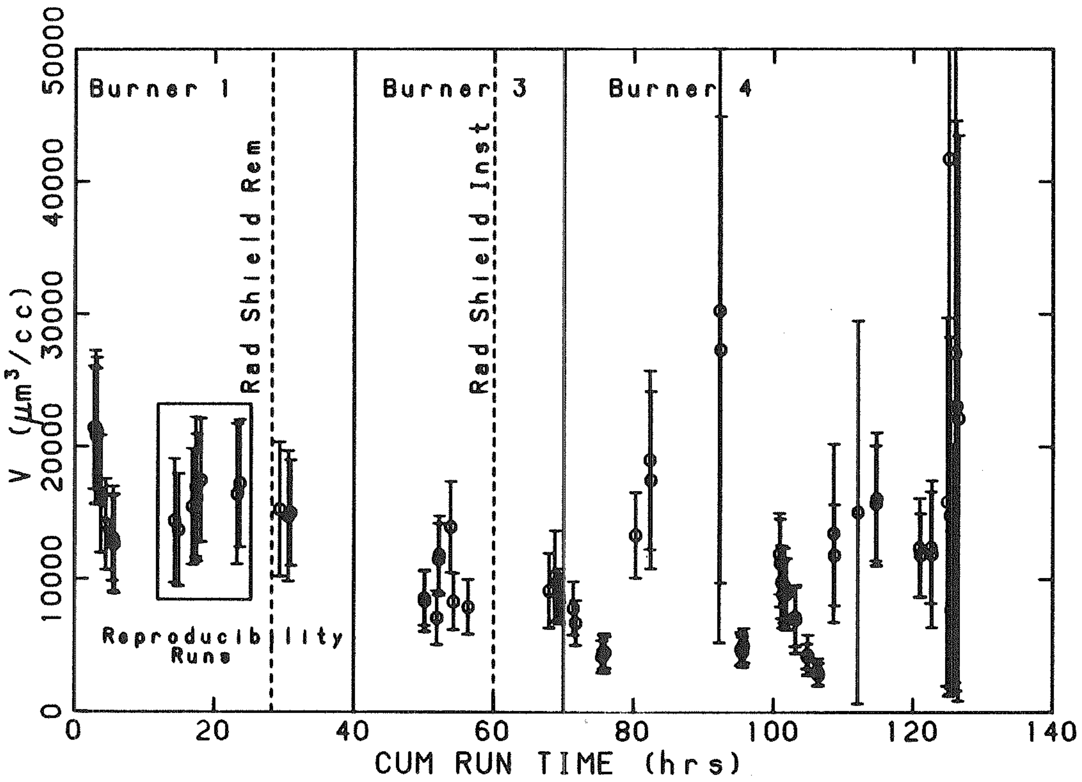

Figure 5.1: Total submicron particle volume concentrations vs cumulative experimental run time. 90% confidence limits are shown together with system modifications. Concentrations are normalized to standard conditions defined in Chapter 5.

error bars (See Appendix A for an explanation of error bar determination--all error bars for the parameter V represent 90% confidence limits). The abscissa is cumulative time burning coal in the laboratory combustor, measured from the first day for which experimental data are presented (A considerable number of shakedown runs and preliminary tests were done prior to the first run for which data are presented. Thus, the ′ cumulative run time′ parameter in the figure is actually cumulative run time beyond these preliminary runs). The figure illustrates the range of measured submicron particle volume concentrations, as well as an idea of the expected error in the measurements.

Reproducibility of the experimental results was checked by establishing a baseline combustion condition, and then attempting to recreate the condition on successive days. The baseline condition for this test was established during the 31080 runs. The 31180 and 32380 runs were attempts to replicate this condition. The maximum variations and standard deviations from the mean values of the eight parameters tabulated in Appendix F were as follows:

Parameter	Maximum Variation	Standard Deviation
V:	14.%	8.5%
T_w:	0.3%	0.2%
T_{pre} :	0.3%	0.2%
ϕ :	2.1%	1.2%
t:	0.5%	0.3%
NO:	1.8%	1.1%
S:	4.9%	3.0%
U:	0.3%	0.2%

The reproducibility of the data is illustrated in Figure 5.1 where the boxed points represent the eight duplicate runs.

The 14% variation in the value of the V parameter should be compared with the total variation of this parameter over all runs. The maximum and minimum values of V recorded in all valid runs prior to run 92680.53 were 21,455 and 2,847, respectively. Thus, the variation of V over all runs was about 750%. On this basis, the 12% variation during duplicate runs was considered to constitute acceptable reproducibility, given the overlap of the confidence limits (See Figure 5.1). The submicron particle size distributions reported in the three days of duplicate runs are plotted for comparison in Figures 5.2, 5.3, and 5.4. The shapes of the histogram distributions are seen to be similar, with the peaks in the distributions occurring between particle diameters of 0.03 and 0.10 microns.

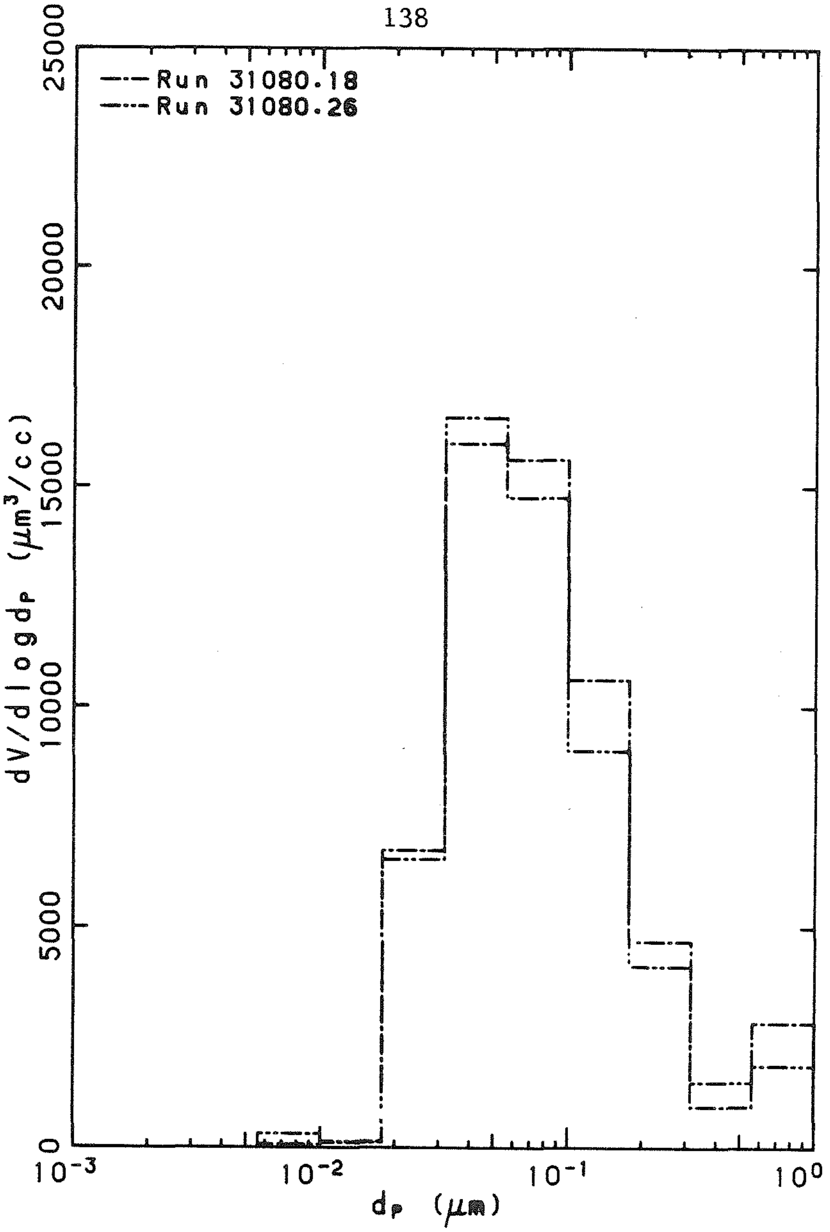

Figure 5.2: Submicron particle volume distribution for representative runs of 31080. measured by EAA. Error limits are suppressed for clarity.

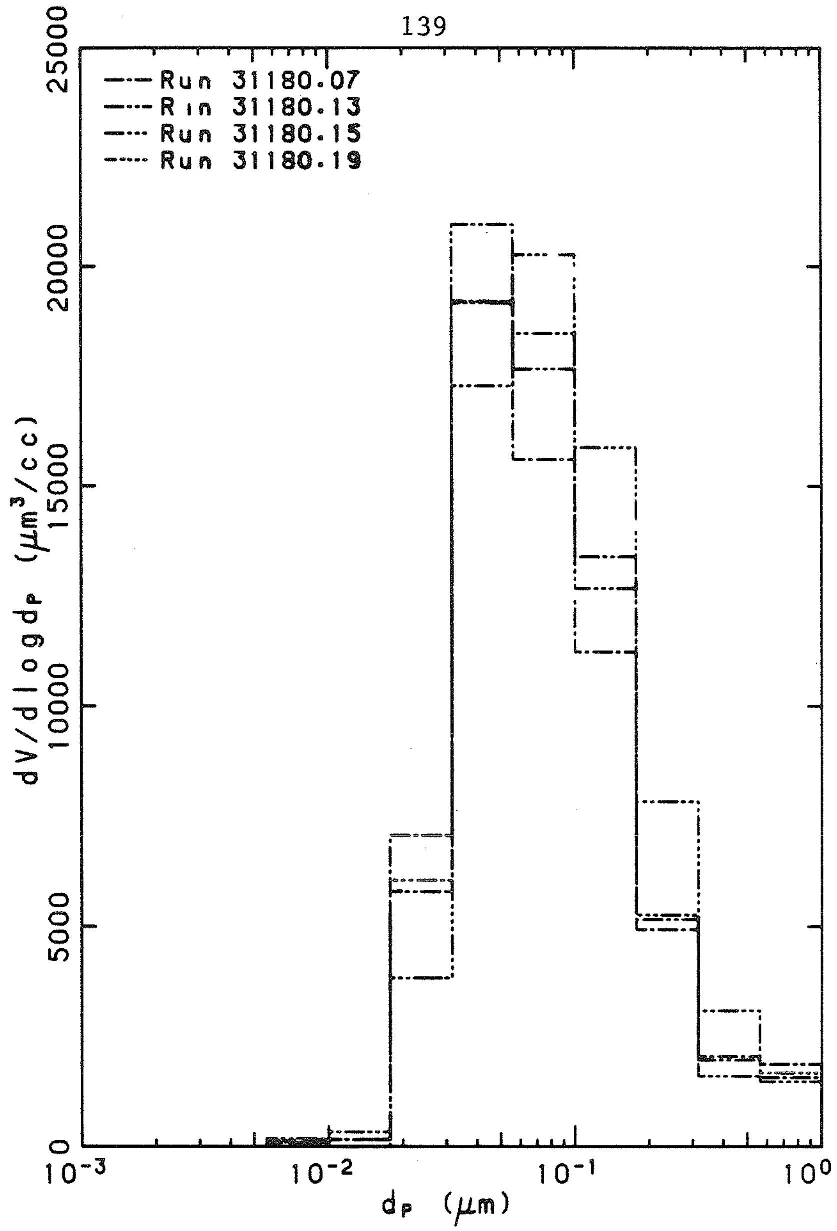

Figure 5.3: Submicron particle volume distribution for representative runs of 31180. measured by EAA. Error limits are suppressed for clarity.

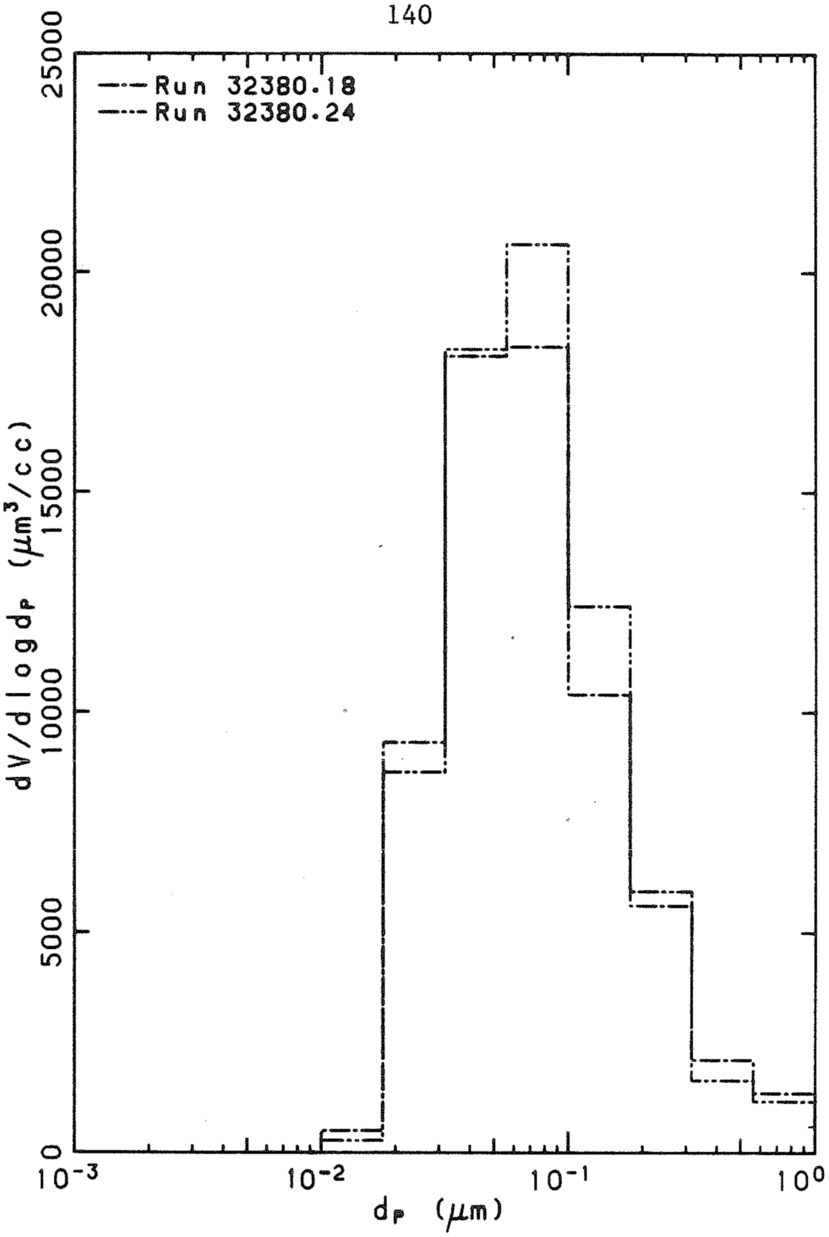

Figure 5.4: Submicron particle volume distribution for representative runs of 32380. measured by EAA. Error limits are suppressed for clarity.

2.2 DATA ERROR AND STABILITY OF EXPERIMENTAL CONDITIONS

With each measured and calculated parameter there is a degree of uncertainty due to possible errors in the measurements. Among the possible sources of these errors are the following:

1. T_w was calculated by fitting a polynomial to the wall temperatures measured by thermocouples at three, four, or five axial positions along the length of the combustor. The order of the polynomial was equal to (Nt-1), where Nt is the number of thermocouple measurements. Thus, the fitted polynomial representing the axial wall temperature profile gave the measured temperatures exactly at the axial locations of the thermocouples. The polynomial was used together with a Simpson's rule algorithm to compute the effective wall temperature parameter defined in Chapter 3.

   The thermocouples used to measure the wall temperature profile were originally located within 3 mm of the inner surface of the combustor refractory shell. Thus, during early runs, the measured wall temperatures were reasonably accurate. However, after several tens of hours of burning coal inside the combustor, a layer of slag accumulated on the inner refractory wall, creating an insulating layer which may have biased the measurements of the wall temperature profile.

In Figure 5.5 are shown three of the fitted temperature profiles, determined for the following combustion conditions (runs 21880.10, 51280.02, 92380.57): Figure 5.5(a) is for burner 1, with t=2.01 sec, U=715 cm/sec, ϕ=0.51, T_w=1323 K, T_{pre}=807 K, S=0.21. Figure 5.5(b) is for burner 3, with t=1.74 sec, U=160 cm/sec, ϕ=0.56, T_w=1263 K, T_{pre}=701 K, S=0.16. Figure 5.5(c) is for burner 4 with t=1.63 sec, U=175 cm/sec, ϕ =0.58, T_w=1349 K, T_{pre}=742 K.

The figure shows that the fitted polynomials are smooth with 2nd-, 3rd-, or 4th-order polynomials used to fit the measured temperatures. The 2nd- and 3rd-order polynomials, however, give profiles which are less flat near the midpoint (probably less accurate, since fewer measured temperatures were used to obtain the profiles) than in the case of the 4th-order polynomial.

To illustrate the error in the calculated effective wall temperature used to characterize the wall temperature profile which accrued by using three measured temperatures as opposed to five, both calculations were performed for run 92380.51. The two values of T_w which resulted were 1413 and 1434 K, respectively. The two values differ by about 1.5%.

2. T_{pre} represents the true mass mean temperature of the secondary

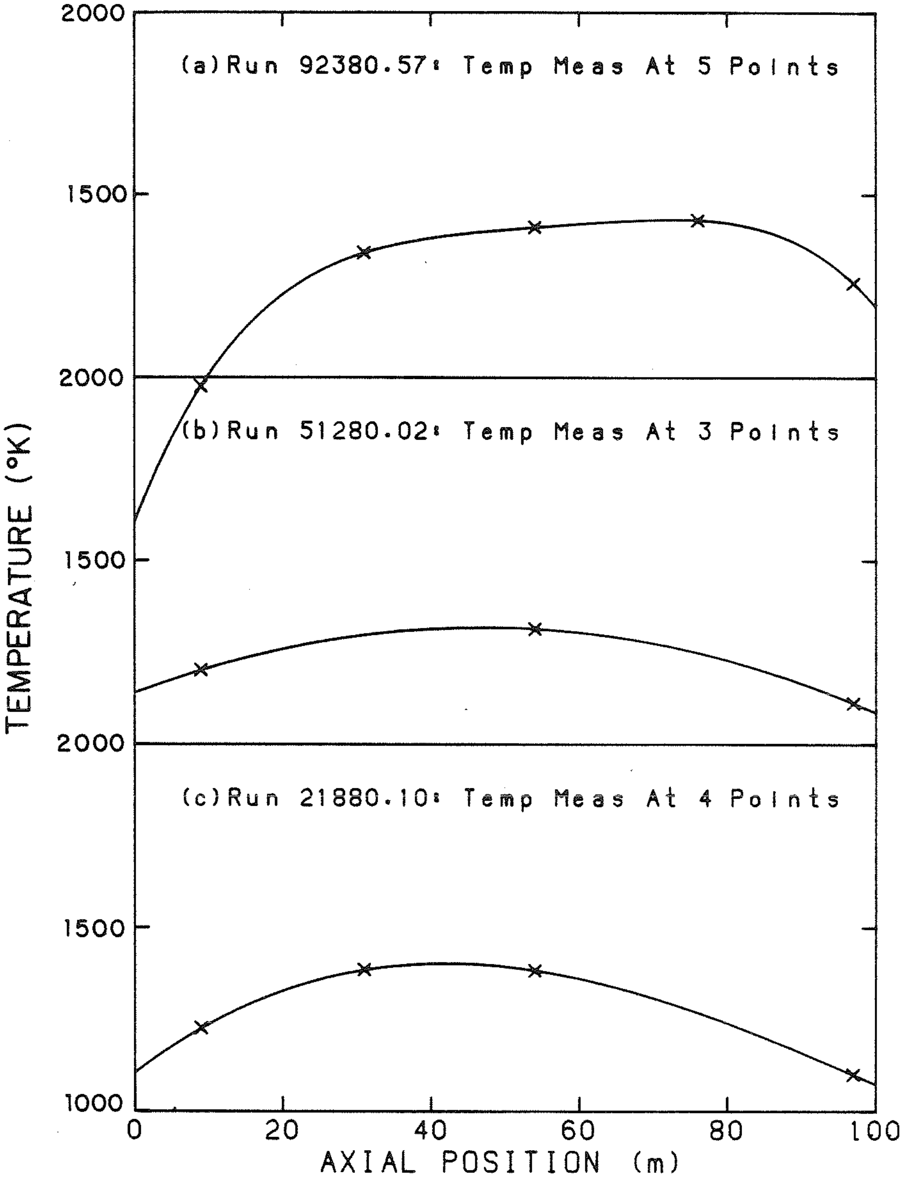

Figure 5.5: Typical fitted wall temperature profiles for temperature measurements at 5, 3, and 4 points. Crosses indicate locations of thermocouple temperature measurements.

combustion air when it entered the combustor and began to mix with the primary fuel-air jet. This secondary air stream was made up of two independently-heated and controlled air streams, one of which entered the burner axially, and the other tangentially. The purpose of this configuration was to provide control of the degree of ′swirl′ imparted to the flame.

Thermocouples to measure the temperatures of the two streams were located in stainless-steel thermocouple wells in the entrance ducts of these streams into the burner. Thus, after the temperature measurement and before the streams entered the combustor they passed through the burner assembly. This assembly was located directly above the refractory quarl of the combustor, and was thus heated above the mean temperature of the incoming secondary air streams. Consequently, the actual temperature of the secondary combustion air entering the combustor was probably higher than the temperature indicated by the thermocouples. Crude heat transfer calculations suggested a possible error of about 40 K for the measured temperature of the axial secondary combustion air stream, 180 K for that of the swirl air stream, and 50 K for the mass mean preheat temperature.

3. The fuel-air equivalence ratio, ϕ, was determined by measuring the concentration of CO_2 and O_2 in the exhaust gas stream, and

by assuming that the concentration of CO was negligible. Measured concentrations of CO were generally less than 0.2%. For a typical oxygen concentration of 8%, the calculated equivalence ratio is 0.627; if 0.2% CO were present with the same O_2 concentration, the true equivalence ratio would be 0.633. Thus, the assumption of zero CO may have resulted in an error of at most 1.0% in the calculated value of ϕ. In calculating the equivalence ratio, it was assumed that all H_2O was removed from the sampled exhaust gas in the drying apparatus, and that the composition of the coal was uniform and given precisely by the measured composition given by the coal supplier. Since the sampled gas was drawn by vacuum through the probe, drier, sampling lines, and instruments, it was subject to possible contamination by leaks. However, except when the sampling probe became fouled, or instrument filters became overloaded, there was no evidence of leakage.

4. The swirl number, S, and shear velocity of the burner jets, U, were determined from the mass flow rates and temperatures of the incoming air streams, and from the known geometry of the burner. The flow rates were calculated from the measured pressure drops across thin-edged orifices and absolute pressure of the flows. Thus, the accuracy of the calculated values of the swirl number and shear velocity, S and U, is limited by the accuracy of the measurements of the air temperatures leaving

the burner (discussed above) and the orifice measurements used to determine the mass flow rates. Again, using crude heat transfer calculations to estimate errors in the measured air temperatures, a possible error of about 25% of the nominal value was calculated for the swirl number. The error estimate for the shear velocity varies according to burner type, due to differences in the primary jet diameter and the estimated error in the assumed temperature of the primary fuel-air stream. For burner 1 this estimate is about 70%, for burners 2 and 3, about 30%, and for burner 4, about 10% of the nominal value.

Ideally, the experiments in this investigation were to be done under steady combustion conditions with no fluctuation of any of the parameters used to characterize the combustion. In practice, such conditions were often difficult to achieve. The degree of unsteadiness varied in different experimental runs.

As indicated in Chapter 3, the rate of delivery of coal to the burner was the most difficult of all combustion parameters to stabilize. The fluctuations in the coal feed rate were most apparent with higher fuel-air equivalence ratios (above approximately 0.65). Under such conditions the flame character changed periodically from brightly emitting yellow-orange, to non-emitting (i.e., unburned char and/or soot apparently absorbed all visible flame radiation), and then back to the brightly emitting character.

Although most of the data reported were collected under sufficiently fuel-lean conditions (fuel-air equivalence ratio about 0.55) that visible puffs of unburned char were seldom observed in the combustor exhaust, the above observation under fuel-rich conditions suggests that the fuel-air equivalence ratio was fluctuating under all experimental conditions.

The magnitude of fluctuations in the fuel-air equivalence ratio is indicated by the chart record of the oxygen concentrations during representative runs. Figures 5.6, 5.7, and 5.8 are reproductions of three such records. In each figure both the O_2 and NO concentrations in the combustion exhaust gas are indicated as functions of time. Figures 5.6 and 5.7 are representative of the most unstable and the most stable conditions, respectively, observed during the experiments for which aerosol data are reported, while Figure 5.8 is typical.

Under the most unstable conditions the maximum variation in exhaust gas oxygen concentration was from approximately 5.2% to 6.6%. This corresponds to equivalence ratios between 0.76 and 0.70; i.e., 4.1% variation from the mean value. This is a lower bound on the true variation since the amplitude of the concentration fluctuation would be damped by mixing in the sampling lines. Under the most stable conditions the maximum variation in oxygen was from approximately 10.6% to 11.1%, corresponding to equivalence ratios between 0.50 and 0.48, or about 2.0% variation from the mean value.

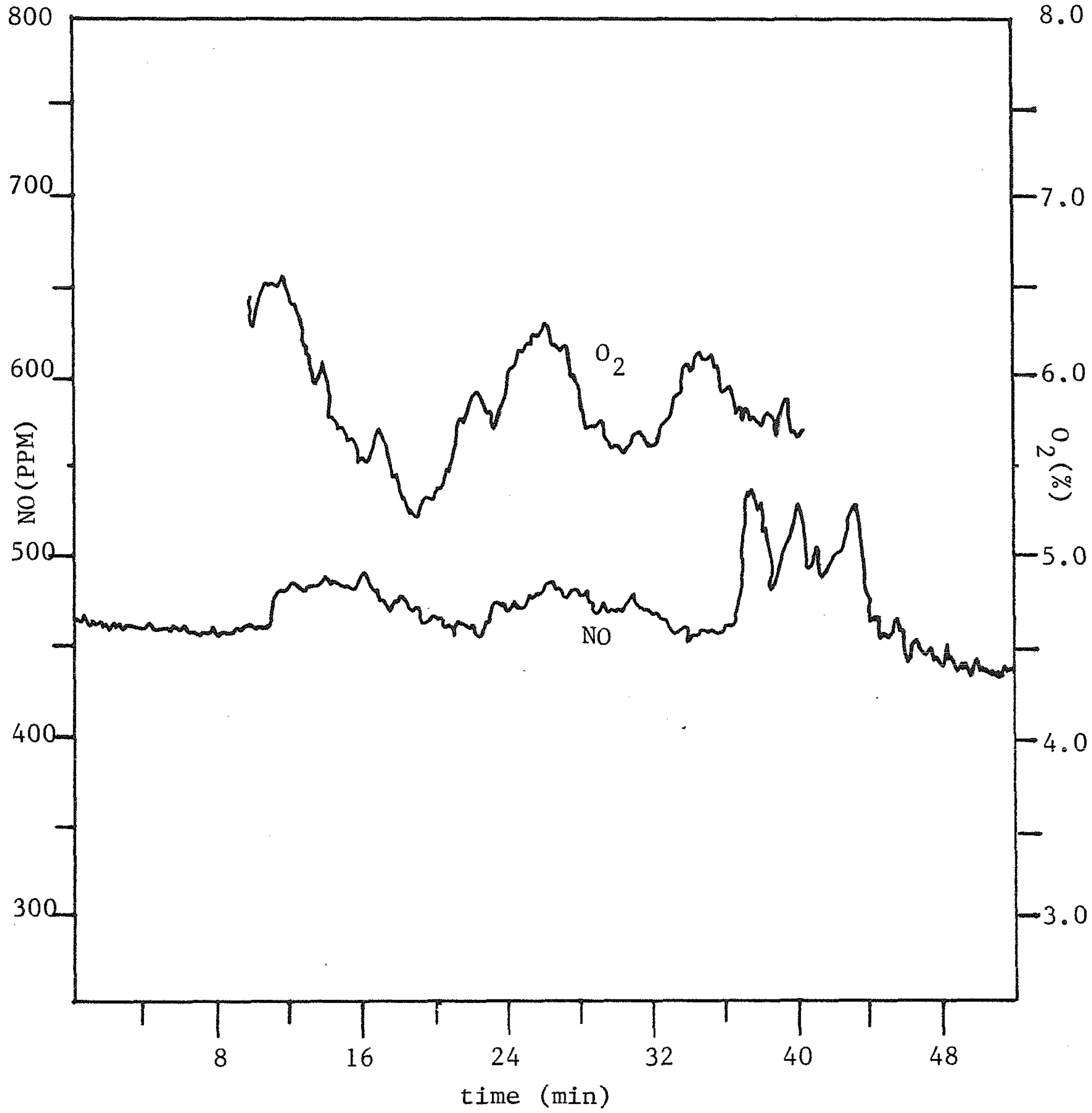

Figure 5.6: Reproduction of chart record of NO and O_2 concentrations measured in combustor exhaust for run 82980. Record shown is representative of runs with large-amplitude combustion instabilities.

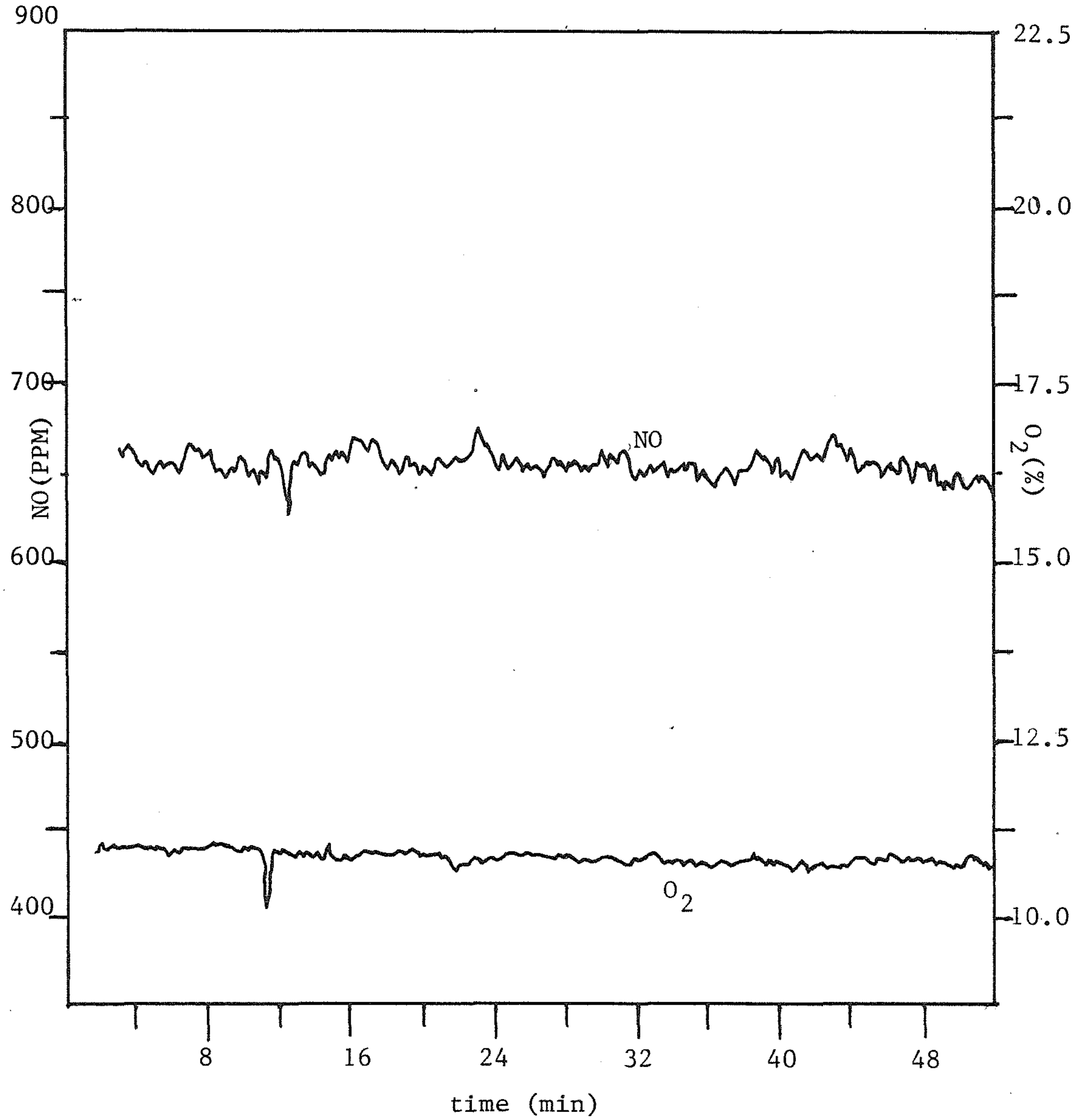

Figure 5.7: Reproduction of chart record of NO and O_2 concentrations measured in combustor exhaust for run 21880. Record shown is representative of runs with small-amplitude combustion instabilities.

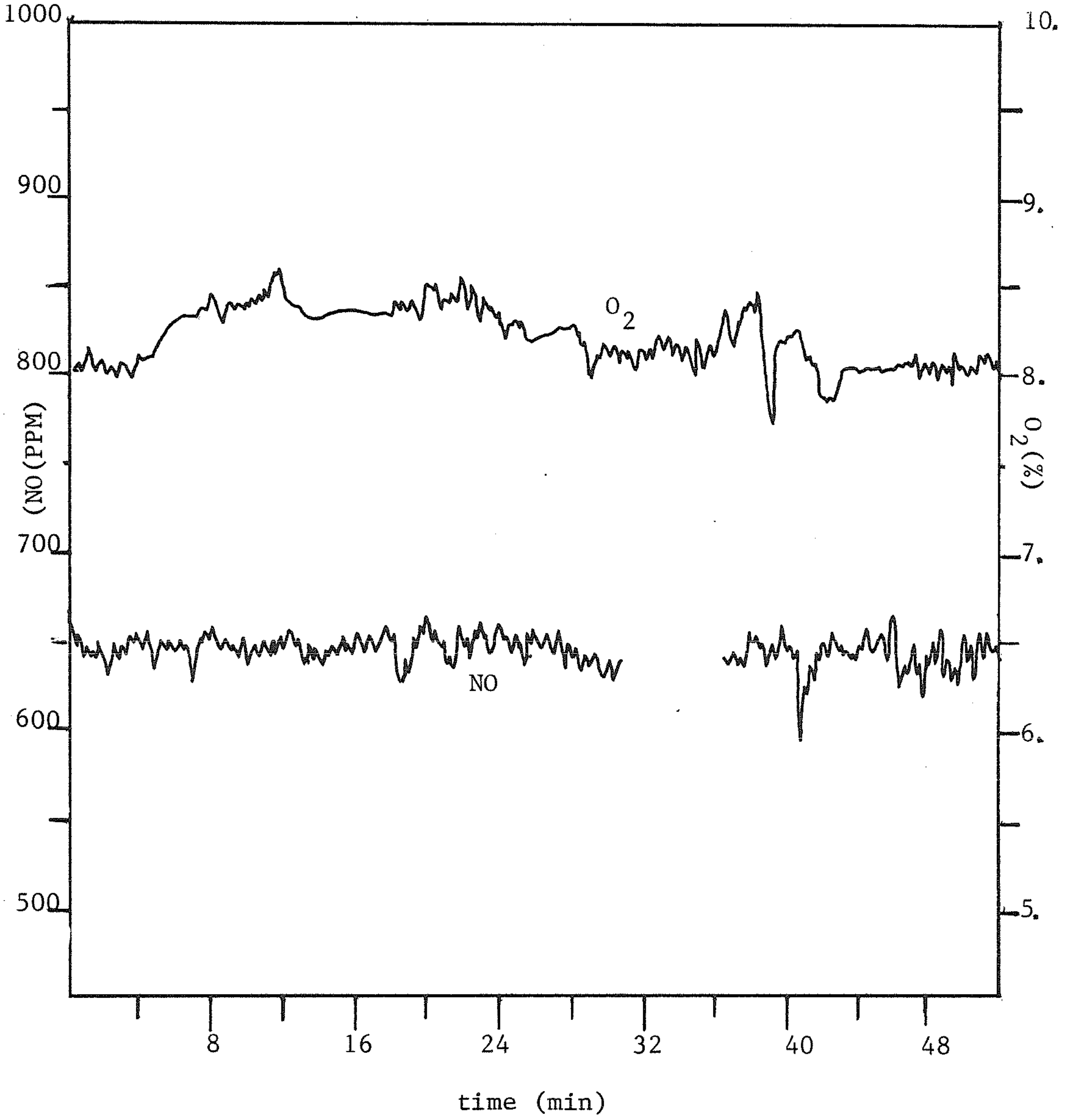

Figure 5.8: Reproduction of chart record of NO and O_2 concentrations measured in combustor exhaust for run 31080. Record shown is representative of runs with typical combustion instabilities.

The chart records indicate the period of the variation in ϕ. Both small- and large-amplitude variations occurred with periods of the order of a minute or more. Since rotational speed of the screw in the coal feeder was typically around 300 RPM, corresponding to a period of about 0.2 sec, it seems likely that the instability in the coal feed rate was not due to screw rotation (Probable causes of coal feed rate instability are discussed in Chapter 3).

The chart records also show substantial variation of NO concentration. Approximately 3% and 13% variation from the mean value are indicated for the most stable and least stable cases, respectively. It has been shown (Pershing and Wendt, 1976) that most NO from pulverized coal is due to fuel-bound nitrogen, and that an important factor influencing NO concentration in exhaust gas is local oxygen concentration during char combustion. Thus, the NO instability might be attributed to variations in either the coal feed rate (and hence the overall fuel-air equivalence ratio) or in the burner aerodynamic processes (mixing rate of oxygen at the length scale of char particles).

Another difficulty encountered during laboratory experiments was the control of combustor wall temperatures. The steady-state temperature profile of the wall was influenced by flame geometry (burner aerodynamics), fuel-air equivalence ratio, and by total throughput of fuel. Thus, the wall temperature profile could not be controlled independently of other combustion parameters.

As previously noted, all air flow rates were controlled manually, using globe-type valves, and were measured either directly with sharp-edged orifices or by difference of such measured flows. ASME (Leary and Tsai, 1951) specifications for the orifice design used indicate mass flow rate measurement precision of about +/-0.5%. Calculated air mass flow rates from orifice meter pressure drops were compared to flow rates indicated by volume displacement through a dry test meter (Singer model DTM-325). The two measurements were found to agree within 3.0% for mass flow rates varying over a factor of four up to the maximum air mass flow rate measured in the experiments. Indicated pressure drop across orifices was maintained by periodic monitoring and adjustment of globe valves, as required. Maximum drift in the pressure drop across the main (total air) flow orifice meter was of order 3.0%. It was concluded that previously-discussed combustion instabilities were probably not caused by unstable air mass flow rates. The basis of this conclusion was the fact that the periods of these instabilities were sufficiently long to be indicated by variations in orifice meter measurements, and such variations were not noted on the time scale of the instabilities.

In Chapter 2 the problem of obtaining an ash mass balance was discussed. In Figure 5.9 the ratio of the ash concentration deterimined by total filter samples to that calculated from the measured equivalence

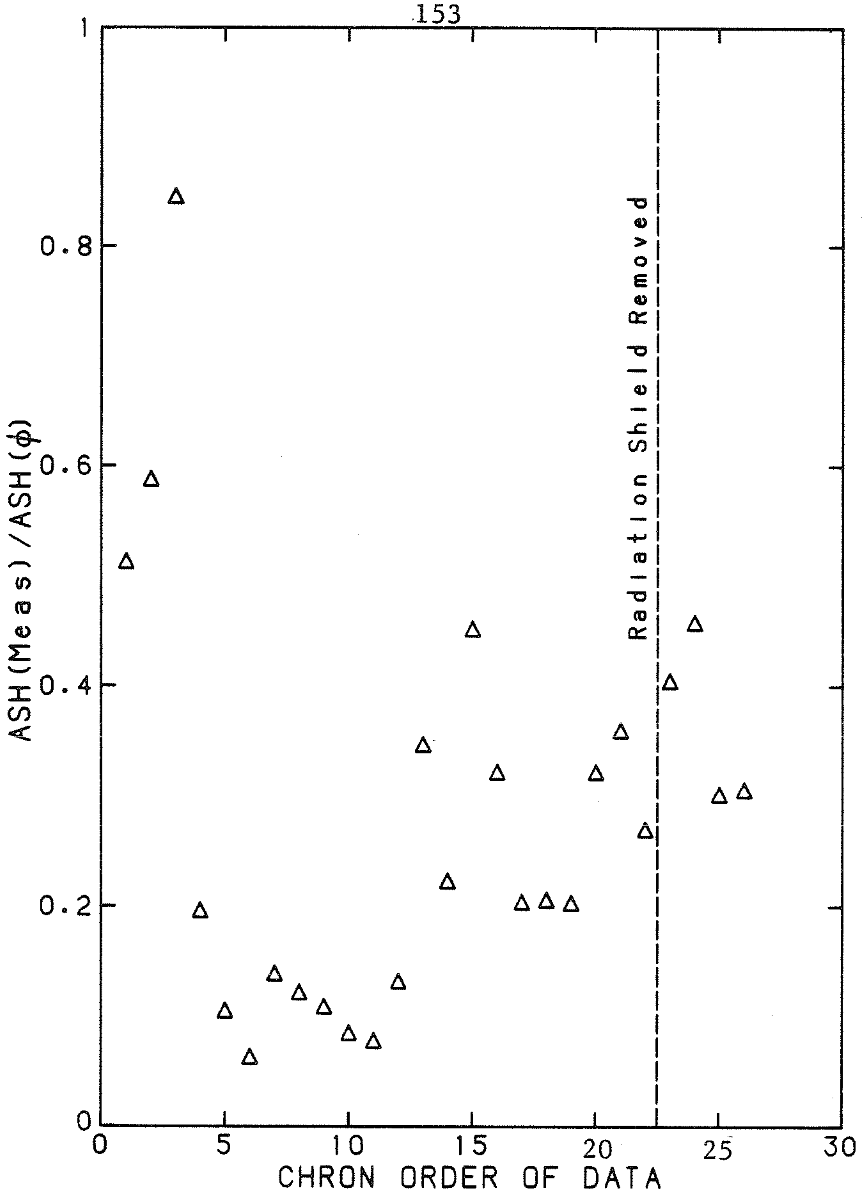

Figure 5.9: Overall ash mass balance for several days of experiments. Ordinate value is ratio of ash mass concentration from exhaust gas filter measurements to ash mass concentration computed from measured equivalence ratio.

ratio and coal ash content is plotted for several different runs. The data were taken over a period of about 3-1/2 months and the abscissa in the figure indicates their chronological order.

Most of the mass of the ash is not accounted for in the ash collected on the total filter. Inspection of the inside surfaces of the combustor walls indicated large deposits of (once-molten) slag. There were also substantial amounts of ash deposited (loosely) on the surfaces of the heat exchanger walls and cooling coils. Particle losses to the walls were attributed to inertial deposition of particles much larger than one micron in diameter. The basis for this assumption is as follows.

(a)Calculations of plug flow diffusional losses to walls indicated at least 95% penetration through the furnace and heat exchanger of all particles above 0.01 micron in diameter. Thermophoretic losses to cooling coils were difficult to estimate theoretically; however, during runs 91980.43 and 91980.45 40% of the cooling coils were deactivated to investigate this effect. No change in the volume concentration of submicron particles was noted from the previous run (91980.41) and thus it was assumed that thermophoretic deposition of submicron particles on cooling coil surfaces did not significantly bias the measured size distributions.

(b)Approximate Stokes number calculations indicated that inertial deposition losses of all particles below 10.0 microns were negligible. Based on these observations, it was assumed that measured concentrations of submicron particles were representative of the combustion conditions investigated.

Figure 5.1 illustrates the effects of system changes on the total volume of submicron aerosol produced. Points at which burner changes were made are marked, as well as the runs for which the radiation shield in the combustor was removed. The ordinate values for the points from 0 to 108 hours of cumulative run time show a decreasing trend as burner type was changed. The removal of the radiation shield at 27 hours of cumulative run time apparently had no statistically significant effect on the total volume concentration of submicron aerosol, nor did reinstallation of the shield at 60 hours.

The unusual trend and high error represented in the runs above 110 hours cummulative run time are indicative of the fact that some type of change (degradation) of the system occurred. Ash composition data for the runs above 108 hours of cummulative run time shows a dramatic increase in the mass concentration of iron and zinc in the aerosol (primarily in the particles above 1.0 micron in diameter), suggesting that a source for these species was introduced, in addition to the coal input to the combustor.

The mass throughputs of iron and zinc during questionable runs were calculated based on the measured concentrations of these metals in the aerosol, and were compared with the mass throughput of iron based on the bulk ash composition and the mass throughput of coal. The results of these calculations are as follows:

RUN	Mass Throughput of Fe		Mass throughput of Zn
	from aerosol meas	from ash throughput	from aerosol meas
92380.53	3.4gm/hr	2.3gm/hr	0.20gm/hr
92680.51	1.8 "	3.0 "	0.48 "
92680.53	2.9 "	3.1 "	1.8 "

The two calculations of iron throughput are comparable for each run. However, unless all iron in the bulk ash vaporized and condensed on the sub-3μm particles, it is unlikely that all the iron measured in the LPI samples originated in the bulk ash since: (a)Only a fraction of the ash in the coal was measured in the fly ash at the sampling location, and (b)The majority of the mass of the bulk ash from the coal was probably concentrated in particles larger than 5 microns. These particles should have been eliminated in the cyclone separators prior to the aerosol stream's entering the LPI.

Zinc and copper mass concentrations in the coal were not reported in the ash composition data and were presumed to be trace species. However, both these metals appeared in the exhaust aerosol in significant quantities after 110 hours of cumulative run time, further supporting the idea that additional sources of vaporizable species were introduced at this time. The additional material may have come from the coal feeder where the abrasive action of the rotation of the metering journal and the motion of the coal resulted in the erosion of some of the metal (brass, stainless steel, and mild steel) components of the feeder. However, the erosion rates suggested by the metal throughput figures above would indicate about 10% mass loss/hr for the suspected feeder components. While such erosion rates are possible for short periods of time, they probably were not sustained over the duration of the three runs (total mass loss of the metering journal of the feeder over several hours of operation was less that 10%). Thus, it was concluded that other sources of these species were present. For example, oxidation of multi-metal-plated surfaces in the burner may have introduced some copper and iron into the secondary combustion air stream entering the combustor.

Whatever the source of the additional aerosol mass, the data from runs above 110 hours cumulative run time are suspicious, and thus were not considered in the presentation and analysis which follow.

3.0 EXPERIMENTAL RESULTS

3.1 SIZE DISTRIBUTION OF FINE PARTICLES

Data from current experiments indicate that the volume distribution according to size in the submicron mode is relatively invariant when normalized by the total volume concentration in this fine-particle mode. In Figures 5.10-5.15 are plotted the histogram approximations to the actual particle size distributions, obtained by direct reduction of the raw data from the electrical mobility analyzer (EAA), using the data reduction procedure supplied by the manufacturer and calibration data of Whitby and Cantrell (1979), together with the dilution parameters determined from the reduction in the NO concentration after dilution (See Chapter 3). The distributions are presented as histograms, and the Y-axis represents the parameter:

$$\{dv(d_p)/d\log(d_p)\}/V$$

where:

$v(d_p)$ = Volume concentration of particles smaller than d_p

V = Total volume concentration of submicron particles

$= \int \{dv(d_p)/d\log(d_p)\}d\log(d_p)$

d_p = Particle diameter.

Plotted in this form, the area under the curve represents the fraction of the total aerosol mass within the size interval shown. The ordinate

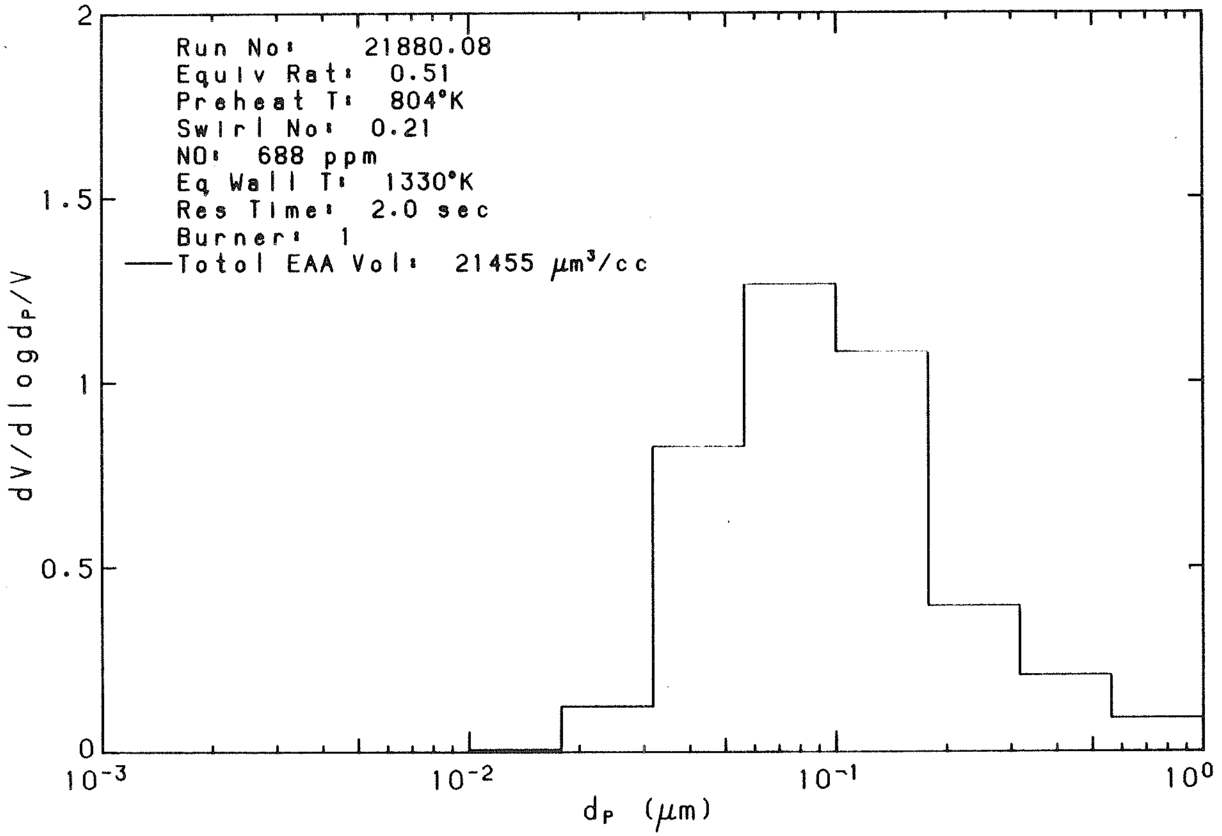

Figure 5.10: Submicron particle volume distribution (EAA) normalized by total submicron particle volume. Total EAA volume indicated is maximum measured for burner 1.

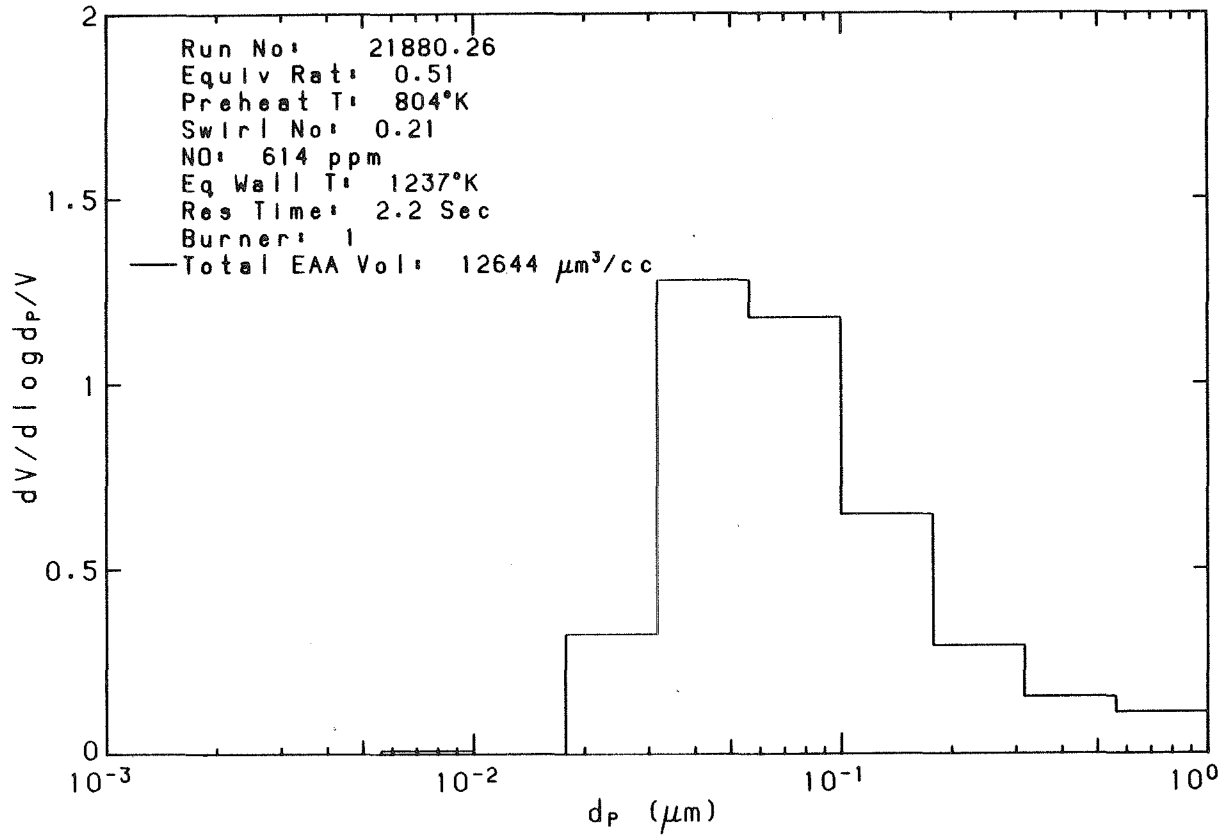

Figure 5.11: Submicron particle volume distribution (EAA) normalized by total submicron particle volume. Total EAA volume indicated is minimum measured for burner 1.

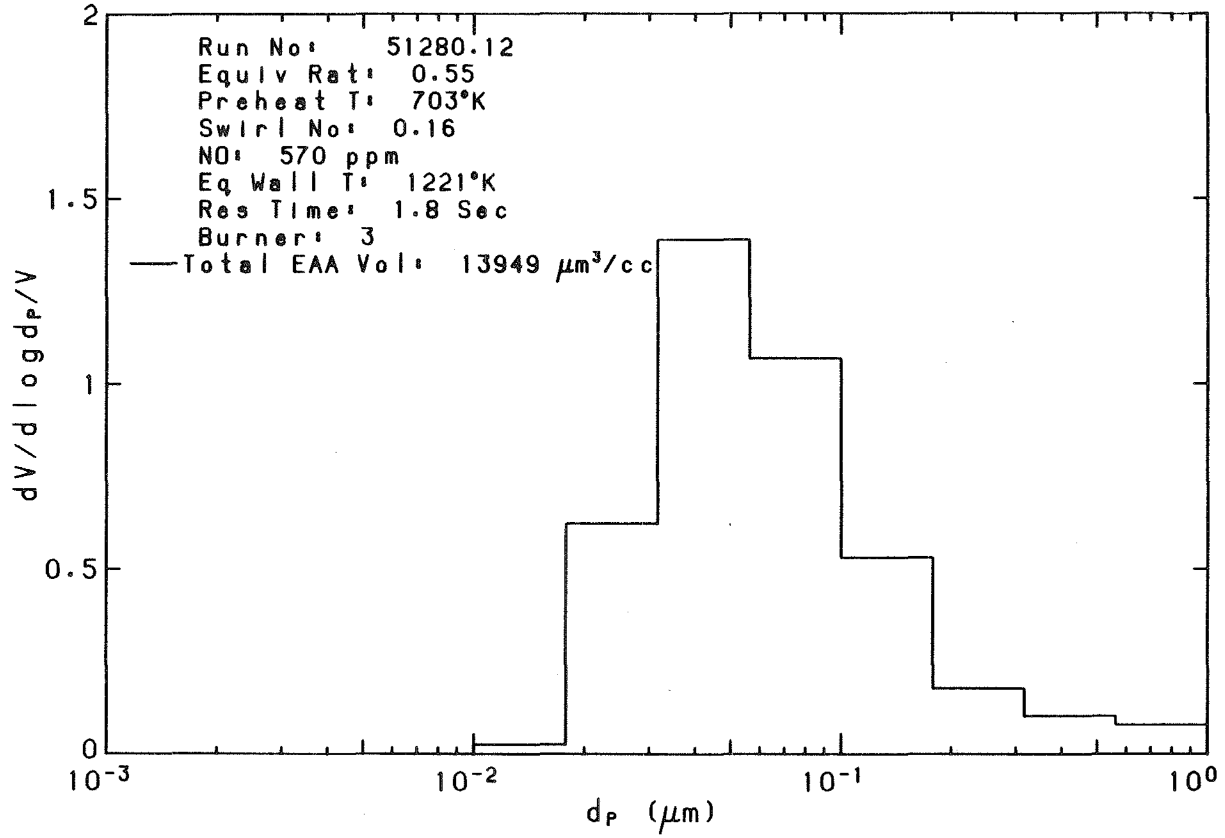

Figure 5.12: Submicron particle volume distribution (EAA) normalized by total submicron particle volume. Total EAA volume indicated was maximum measured for burner 3.

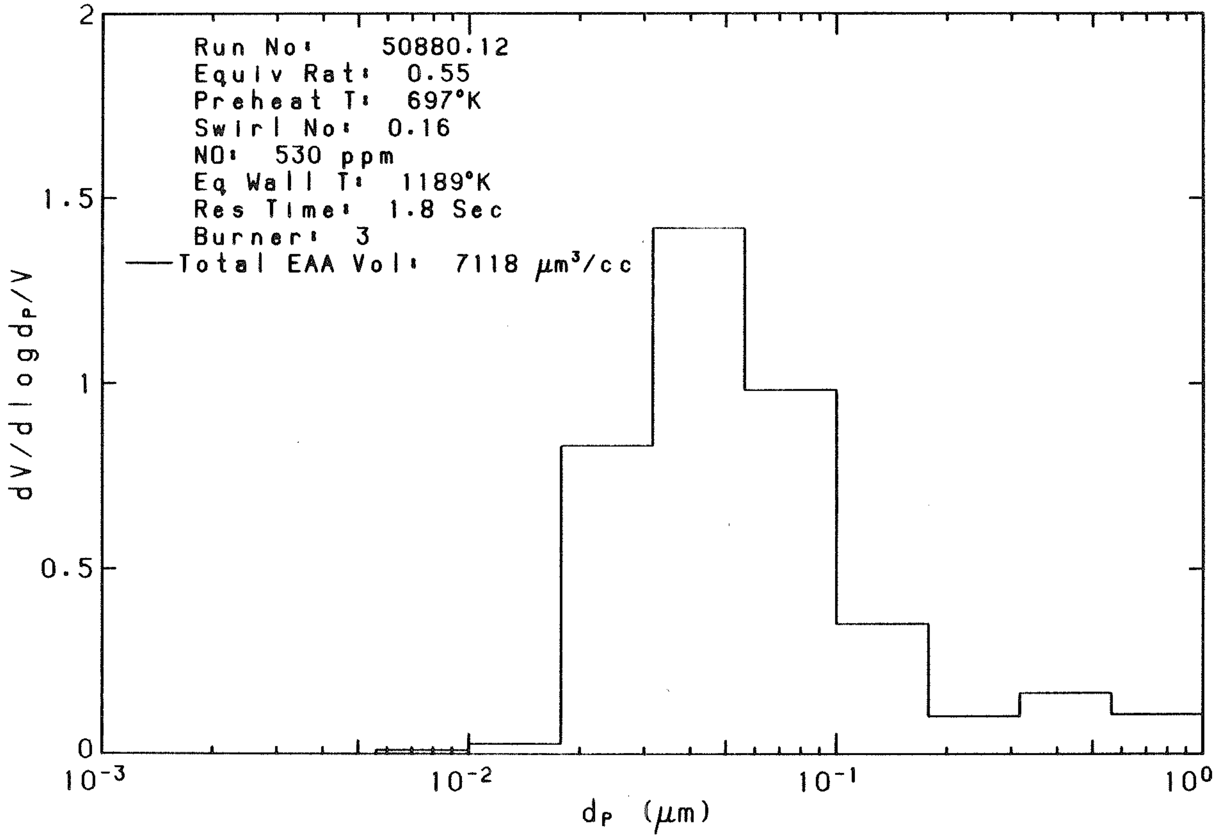

Figure 5.13: Submicron particle volume distribution (EAA) normalized by total submicron particle volume. Total EAA volume indicated was minimum measured for burner 3.

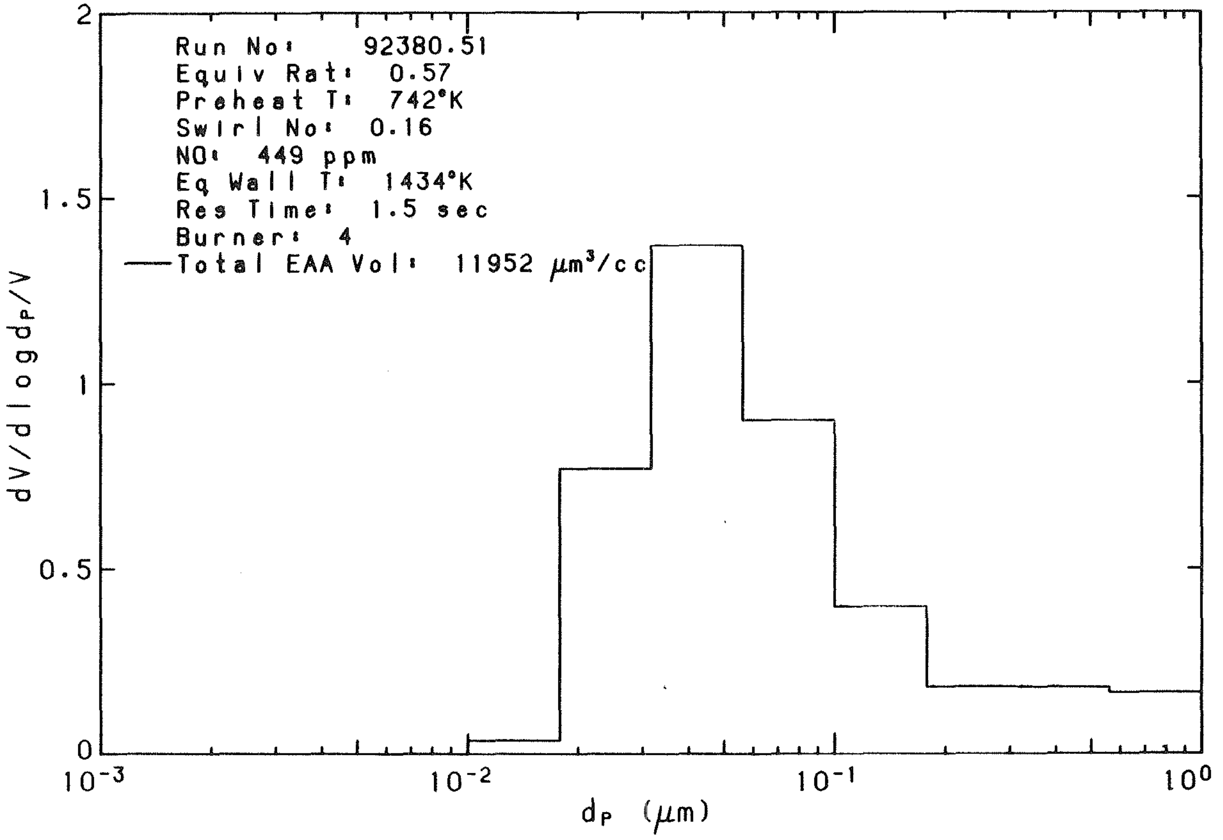

Figure 5.14: Submicron particle volume distribution (EAA) normalized by total submicron particle volume. Total EAA volume indicated was maximum measured for burner 4.

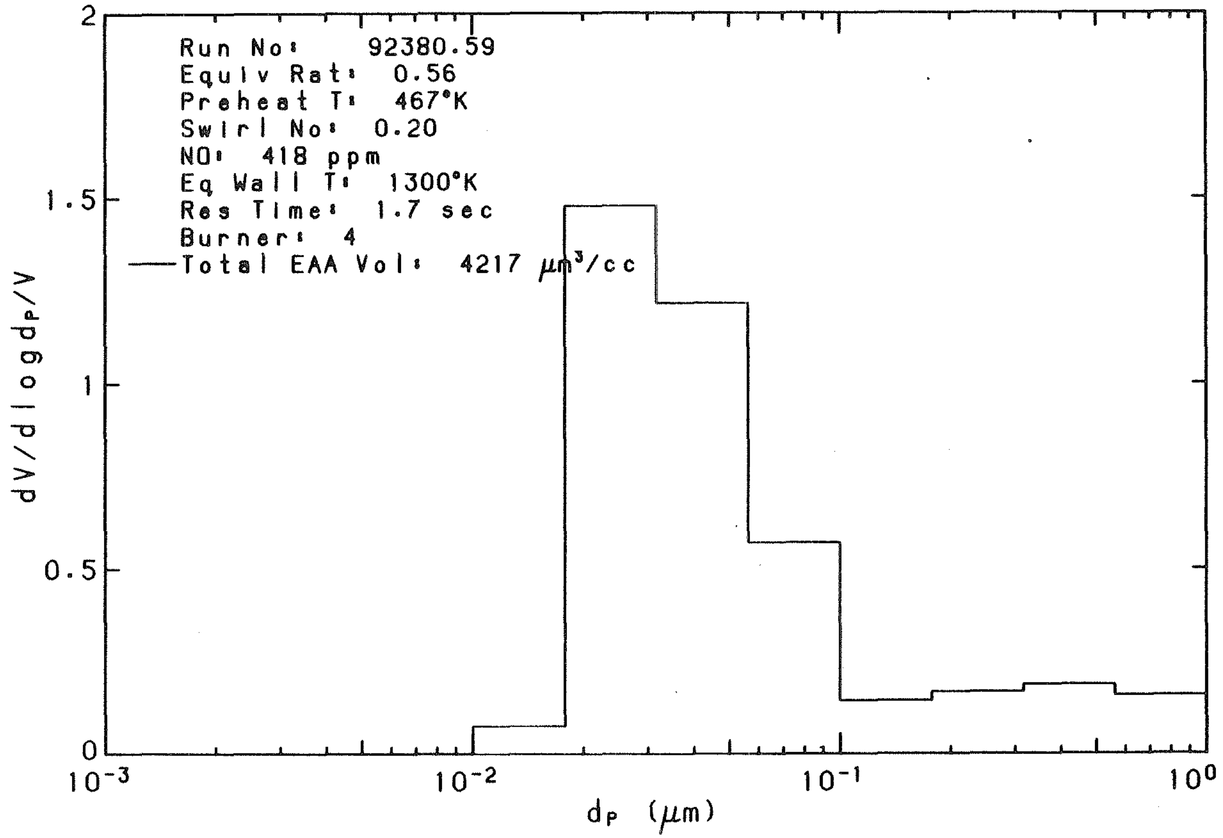

Figure 5.15: Submicron particle volume distribution (EAA) normalized by total submicron particle volume. Total EAA volume indicated was minimum measured for burner 4.

values have been normalized by the total volume concentration of all particles in the submicron size range.

The various curves shown represent the entire spectrum of measured volume concentrations of submicron particles. Two size distributions are plotted for each burner type, one for the highest total volume concentration measured and one for the lowest volume concentration. In all cases, the particle concentrations are corrected to standard conditions ($\phi = 0.85$, dry, 760 mm Hg, 25 C). Mean values of $(dV/d\log(d_p))/V$ are shown without error bars for clarity. For all experiments represented in the figures, the measured fuel-air equivalence ratio was in the range of 50-62% of stoichiometric.

Each figure is labeled with the total submicron volume concentration measured with the EAA for the particular run. The shapes of the distributions vary little, except for the upward shift of the peak particle size with increasing total particle volume concentration.

As discussed previously in Chapter 2, Neville, et al. (1980) have noted that for free-molecular coagulation kinetic theory predicts that after long coagulation times (typically, >> 1 msec) the volume-mean particle diameter (for fixed coagulation time) is proportional to $V^{2/5}$. They have also presented laboratory data supporting this prediction. In Figure 5.16, the volume-average particle diameter is plotted versus this parameter for several data points from the present experiments. Error

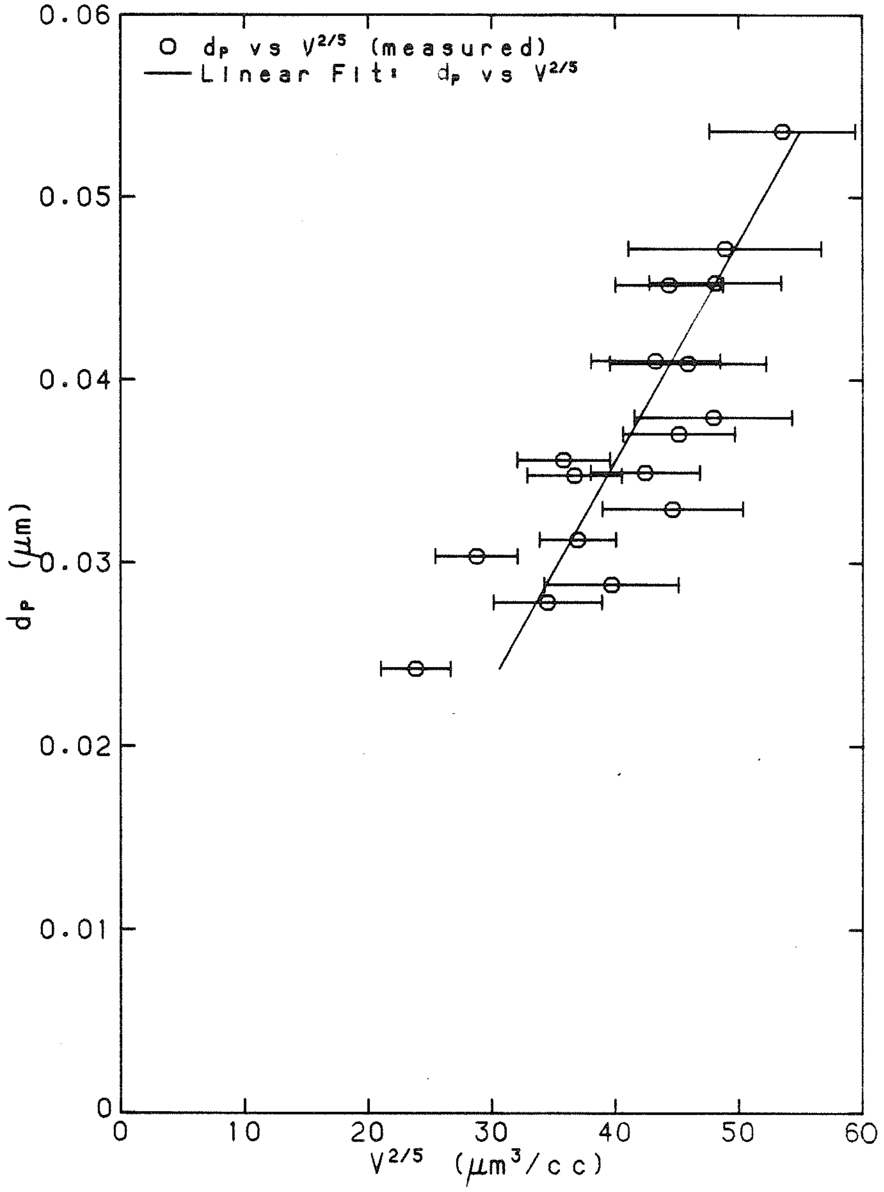

Figure 5.16: Volume mean diameter of submicron particle size distribution vs total submicron particle volume concentration raised to the 2/5 power. Data shown are for burner types 1, 3, and 4.

bars indicate 90% confidence limits on the measured values of $V^{2/5}$ (See Appendix A). The solid line indicates the least-squares linear correlation between the two parameters. The figure indicates that the linear theoretical relation between d_p(vol mean) and $V^{2/5}$ is reasonably well supported by the data, given the confidence limits.

3.2 CORRELATION OF SUBMICRON PARTICLE VOLUME WITH WALL TEMPERATURE

As discussed in Chapter 4, one of the determinants of particle temperatures is the wall temperature. Thus, on the basis of the vaporization-condensation model for fine particle formation one would expect to observe a correlation between total submicron particle volume concentration (V) and equivalent wall temperature (T_w). To investigate this correlation, the two parameters are plotted in Figure 5.17. Only points within a limited band of equivalence ratio (0.5-0.62) are plotted, and data for different burner types are indicated by different symbols. The figure indicates that burner type is a significant factor in determining the volume (mass) of submicron particles formed. Data for burners 1 and 3 apparently fall into one identifiable band (or correlation with T_w) while data for burner 4 fall into a second band. This is consistent with physical intuition, since burners 1 and 3 were uncooled, resulting in a lower heat loss from the flame than in the case of burner 4, which was water-cooled.

The data for burner 4 indicate a strong dependence of V on T_w, as expected. For an equivalent wall temperature variation of about 200 K (16% variation of absolute temperature) the variation in total volume concentration is over 300%. This non-linear variation of V with T_w is consistent with a large activation energy for the vaporization of ash species. The statistical significance of the apparent correlation of V with T_w will be discussed later.

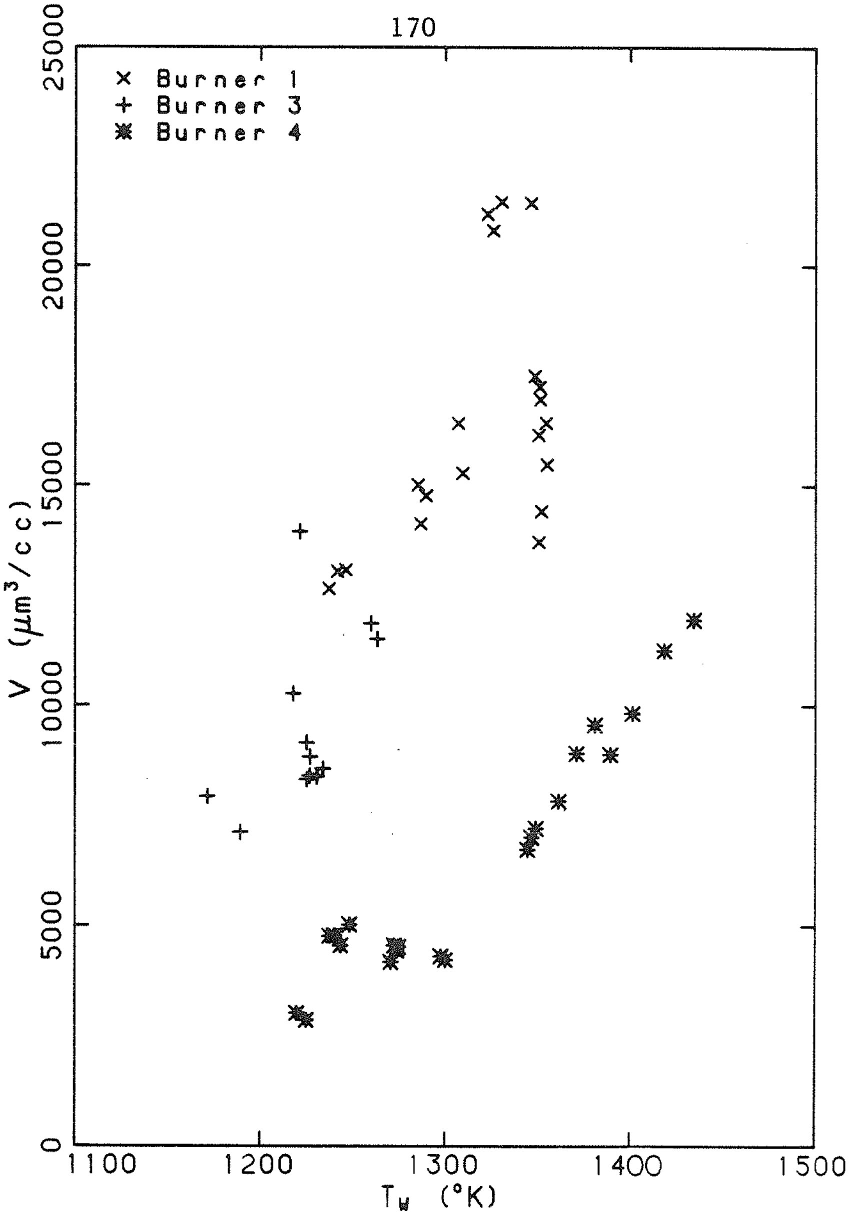

Figure 5.17: Total submicron particle volume concentration (V) from EAA vs effective furnace wall temperature (T_w). T_w is defined in Chapter 3.

3.3 CORRELATION OF SUBMICRON PARTICLE VOLUME WITH NO CONCENTRATION

It has been suggested in the literature (Ensor, 1980) that fine particulate mass concentration and exhaust nitric oxide (NO) concentration are correlated in field data for a full-size pulverized coal boiler. In order to investigate this correlation and also to compare present measurements with those obtained in the field, the submicron aerosol volume data from the present experiments were plotted against the NO concentration. The results are shown in Figures 5.18 and 5.19. Figure 5.18 indicates the mean measured values of V, together with the error estimates, on the Y-axis, and the measured values of NO concentration on the X-axis. Data for different burners are identified with different symbols. The lower NO concentrations for burner 4 suggest that the dynamics of the combustion chemistry for the cooled burner are significantly different from those of the uncooled burners.

Comparison of Figures 5.18 and 5.17 indicates a better correlation of V with NO than with T_w. Pershing and Wendt (1976) have reported that the majority of NO produced in pulverized coal combustion arises from organic nitrogen contained in the coal rather than from nitrogen in the combustion air. They also found (Wendt and Pershing, 1977) that burner aerodynamics are among the most significant physical factors influencing the rate of formation of NO, suggesting that the local oxygen concentration in the flame is the dominant factor in the oxidation of nitrogen. The equilibrium particle temperature also increases with

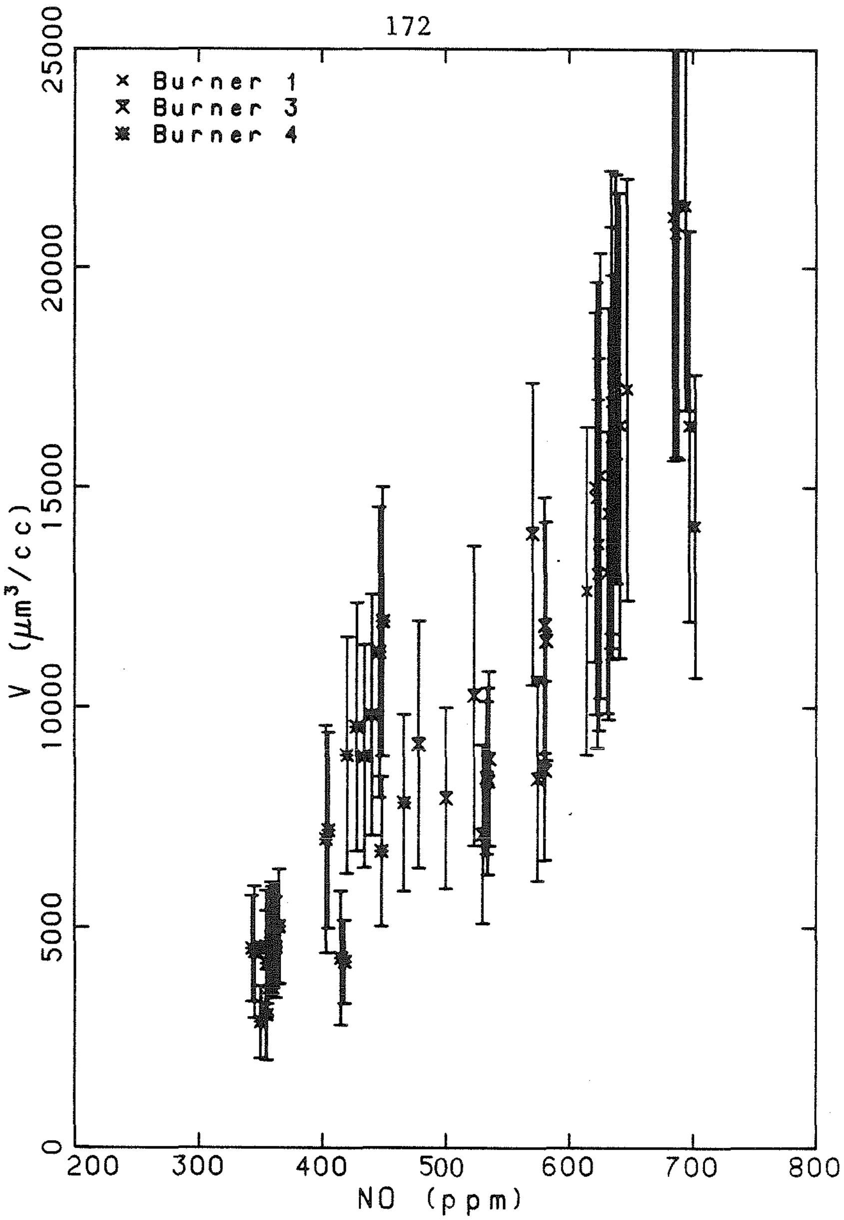

Figure 5.18: Total submicron particle volume concentration (V) with 90% confidence limits vs NO concentration in combustor exhaust. NO concentration is not normalized.

local oxygen concentration in the flame (Libby and Blake, 1979). Since ash vaporization is endothermic this suggests that the total amount of ash vaporized should similarly increase with local oxygen concentration.

If both the oxidation rate of fuel nitrogen and the equilibrium particle burning temperature increase with local oxygen concentration, then the correlation between NO and V may be explained on the basis of burner aerodynamics, both processes being enhanced by higher mixing rates between the primary fuel jet and the secondary combustion air stream. The statistical correlation of NO with burner aerodynamics will be discussed later.

In Figure 5.19 these laboratory data and measurements of the submicron particle mass concentrations from a single coal-fired utility boiler are plotted as a function of NO concentrations (Boiler data are from Ensor, 1980). Mass concentrations of fine particles were calculated from EAA volume concentration measurements by assuming fine particle specific gravity of 2.6 (consistent with Ensor's assumption; elsewhere in this presentation the particle specific gravity was assumed to be 2.3). NO concentration is reported as NO corrected to 3% oxygen in the stack gas, which indicates an equivalence ratio of about 0.85. Thus, the corrected NO concentrations for the laboratory combustor data are somewhat higher than in the previous figure.

From Figure 5.19 it is evident that the observed trend of V as a

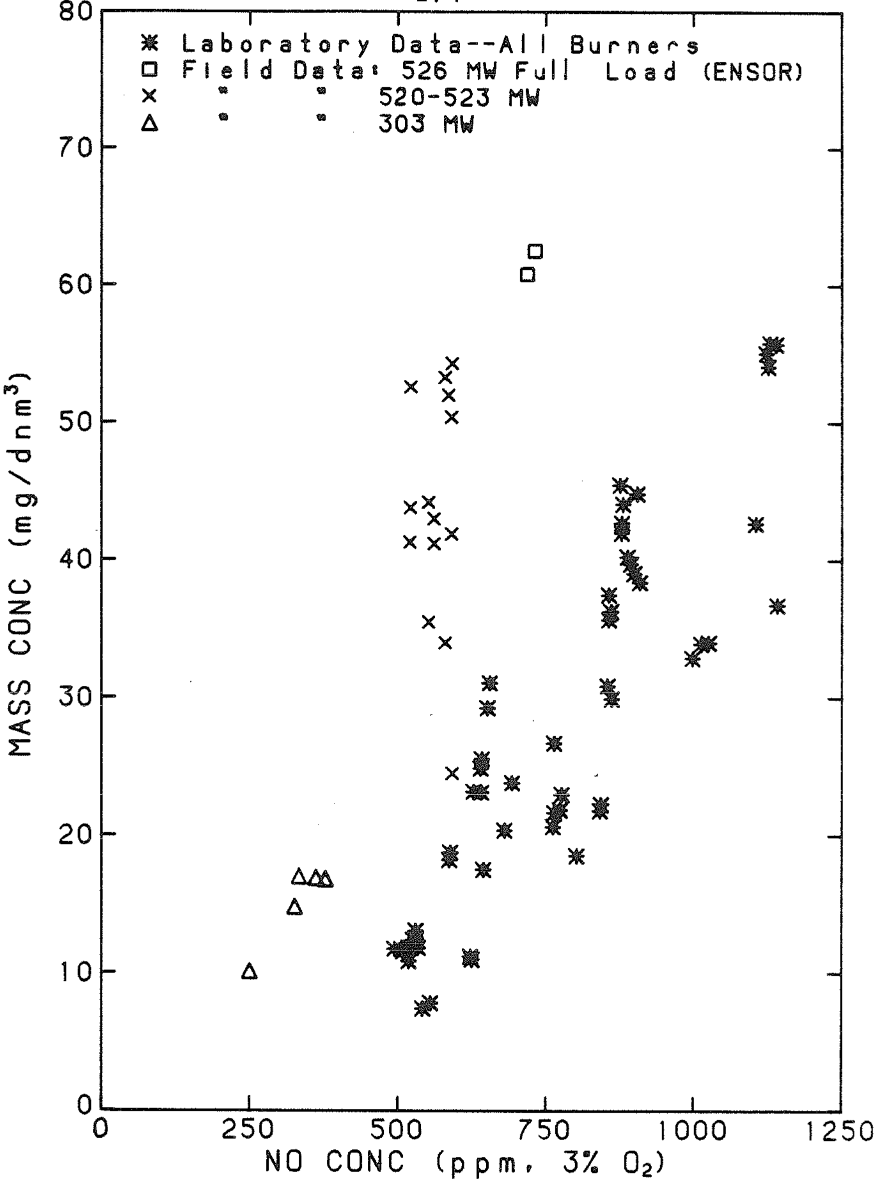

Figure 5.19: Total submicron particle mass concentration vs normalized NO concentration for laboratory and field data. Laboratory measurements assume particle specific gravity of 2.6. Field data is from Ensor (1980). Vertical axis units are milligrams per cubic meter (dry, normalized).

function of NO in the data from the current experiments is consistent with that observed in field data. However, it should also be noted that the measured particle mass concentrations in the laboratory data are lower than those in the field data for comparable levels of NO. This could be due to lower particle temperatures in the laboratory system due to wall temperatures which are lower than required for complete simulation (See Chapter 3). It may also be due to the difference in the coal types used in the laboratory experiments and in the field unit for which data were given.

The fact that the NO levels achieved in the laboratory furnace were comparable with those measured in the field, together with the fact that the observed trend of increasing particle mass concentrations with increasing NO levels is consistent in the laboratory and field measurements, suggests that the quality of the laboratory simulation is reasonably good.

3.4 FINE PARTICLE COMPOSITION-SIZE DISTRIBUTION DATA

Results from PIXE (Particle-Induced X-ray Emission) analyses of four sets of mass samples, representing as many different days of experiments and combustion conditions, are presented in Figures 5.20-5.27. In each histogram, the area of each distinctly-shaded region represents:

$$\left[(\Delta m)/(\Delta \log(d_p))\right]_j$$

where:

m = Total mass concentration of flyash aerosol
d_p = Particle diameter
Subscript j indicates contribution due to species j

which is an approximation to the function:

$$\left[dm/d\log(d_p)\right]_j$$

i.e., the area in each shaded region approximates the contribution of the j^{th} mineral species to the total mass concentration due to particles in the particular size interval.

The total submicron aerosol mass distribution inferred from EAA

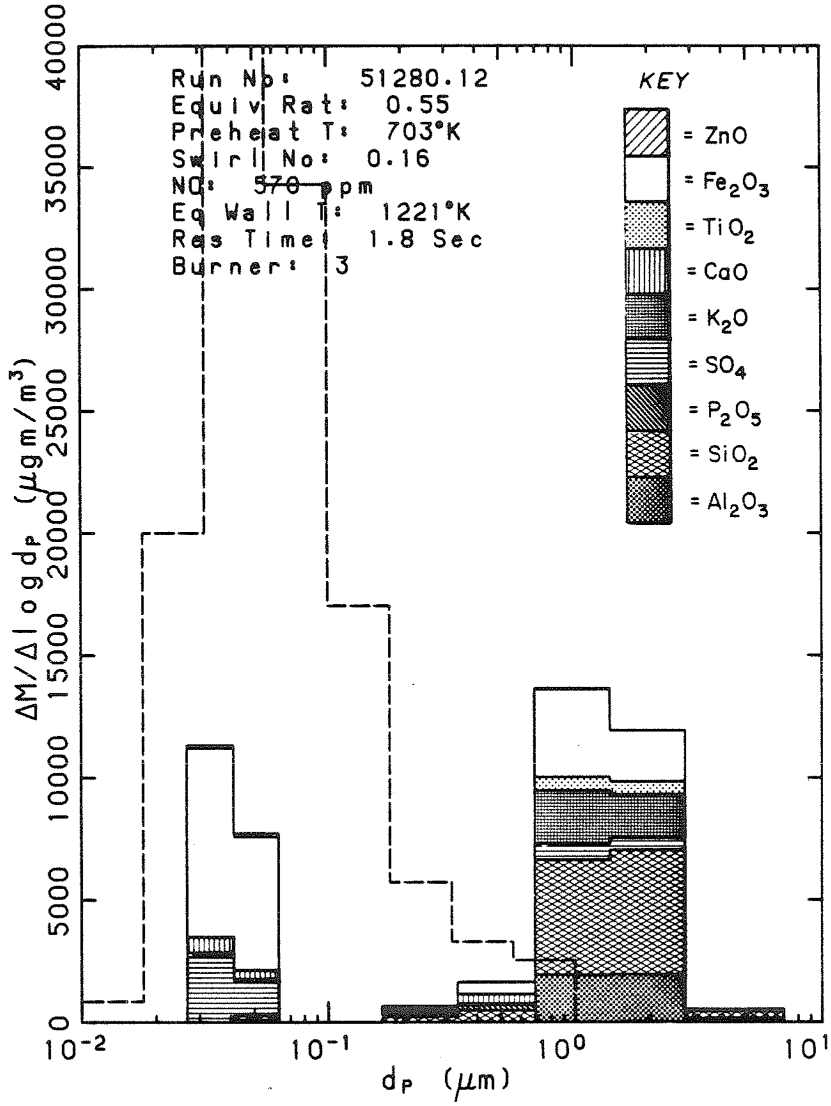

Figure 5.20: Composition distribution of fine particles as measured by PIXE for run 51280.12. Dashed line is EAA measurement of mass distribution based on particle specific gravity of 2.3. Total submicron particle mass concentration indicated by PIXE and EAA are 7,570 and 32,100 μg/m^3, respectively.

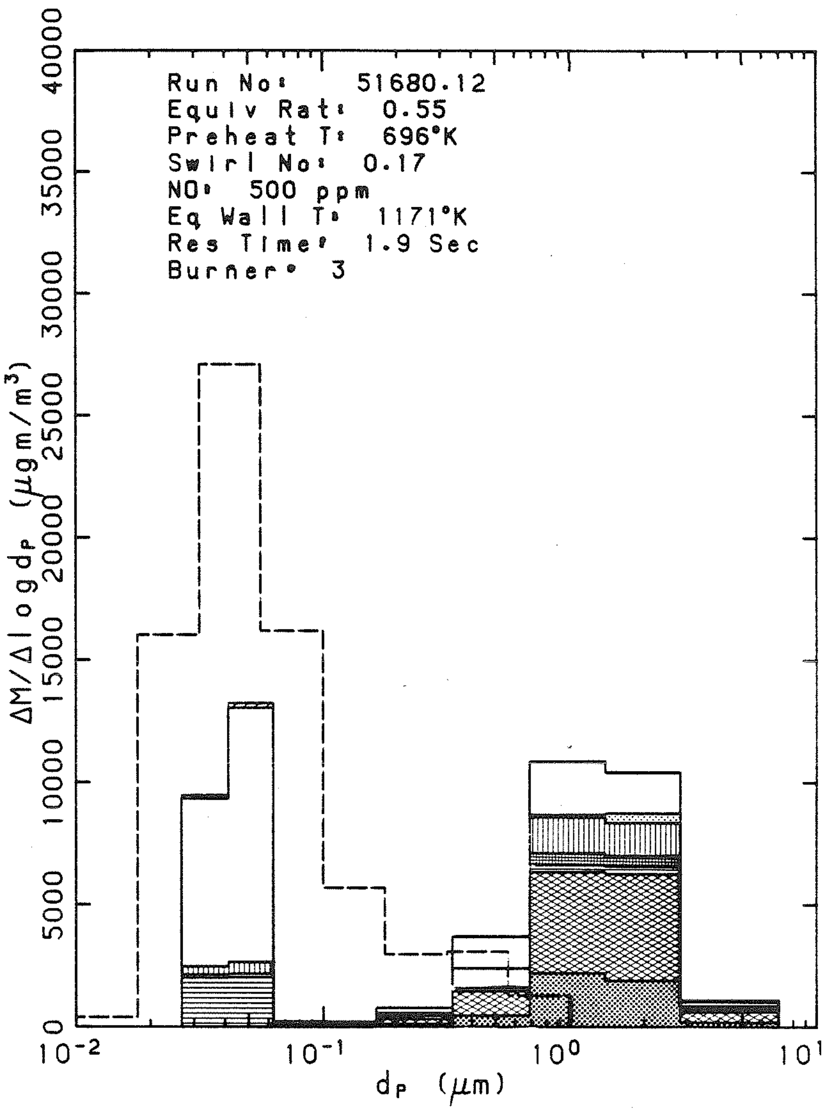

Figure 5.21: Composition distribution of fine particles as measured by PIXE for run 51680.12. Dashed line is EAA measurement of mass distribution based on particle specific gravity of 2.3. Total submicron particle mass concentration indicated by PIXE and EAA are 9,236 and 18,200 μg/m^3, respectively. See Figure 5.20 for key.

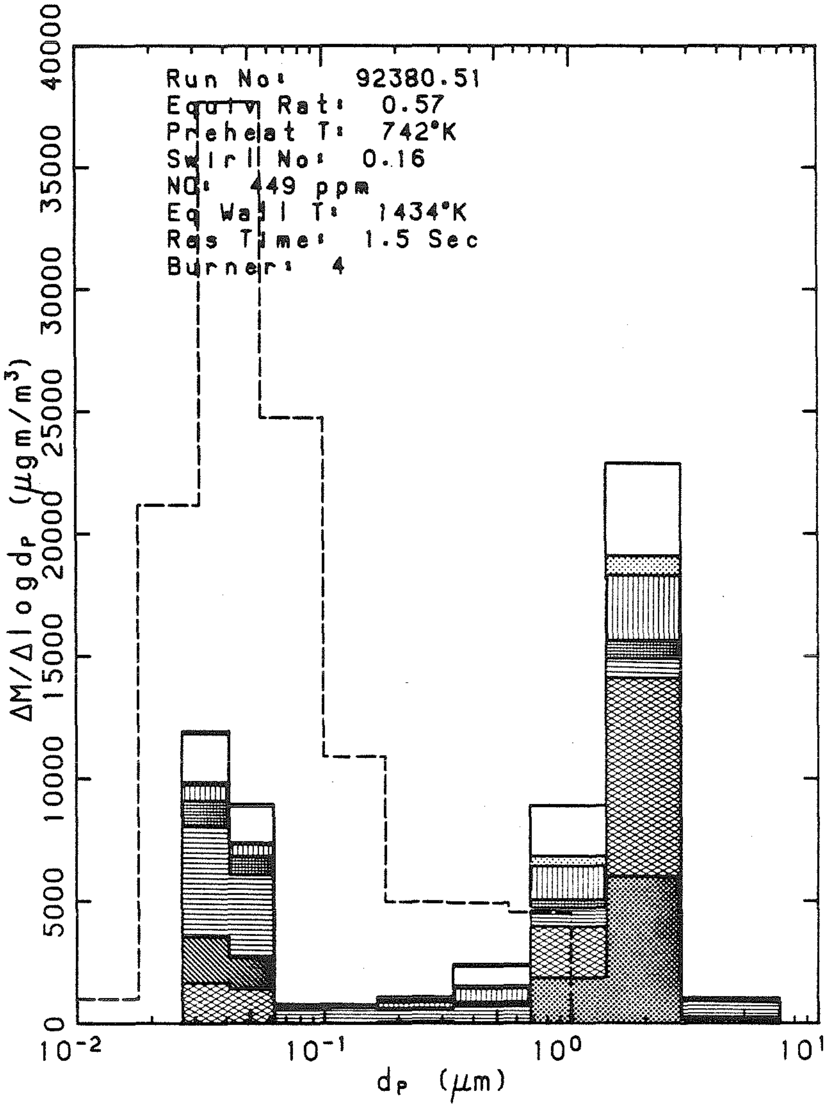

Figure 5.22: Composition distribution of fine particles as measured by PIXE for run 92380.51. Dashed line is EAA measurement of mass distribution based on particle specific gravity of 2.3. Total submicron particle mass concentration indicated by PIXE and EAA are 8,810 and 27,500 μg/m^3, respectively. See Fig. 5.20 for key.

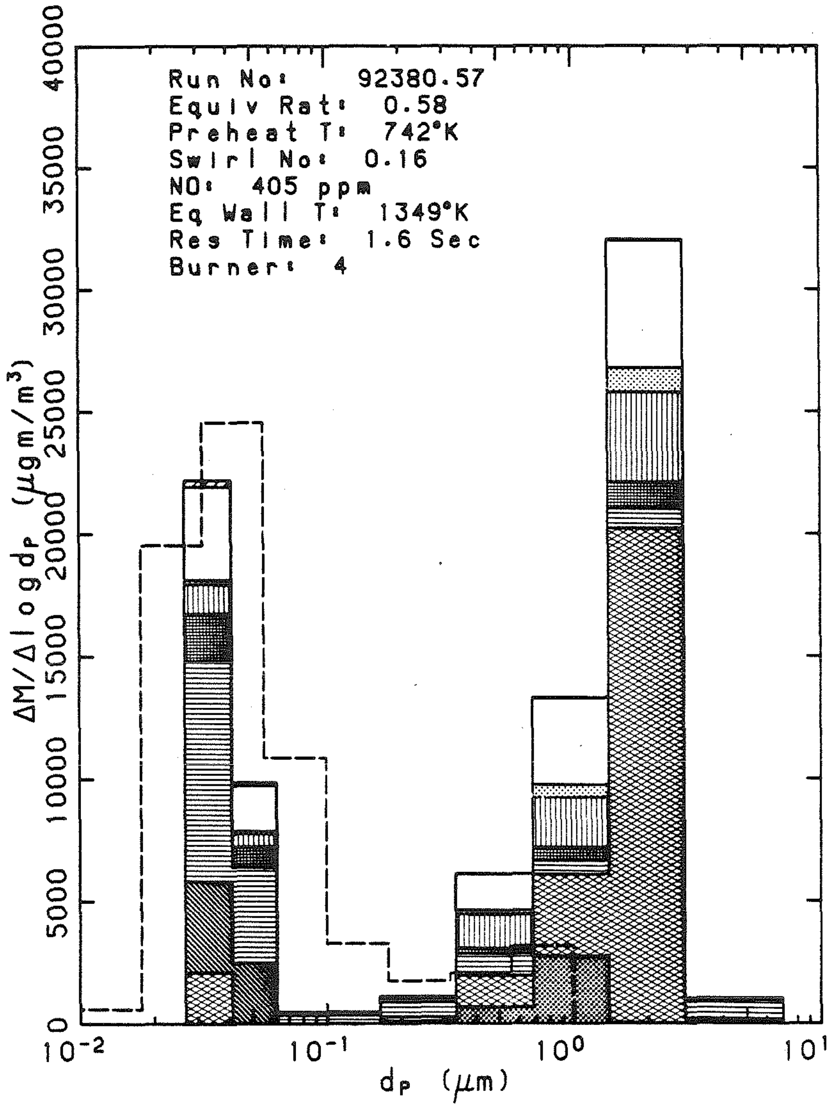

Figure 5.23: Composition distribution of fine particles as measured by PIXE for run 92380.57. Dashed line is EAA measurement of mass distribution based on particle specific gravity of 2.3. Total submicron particle mass concentration indicated by PIXE and EAA are 14,200 and 16,600 μg/m^3, respectively. See Fig. 5.20 for key.

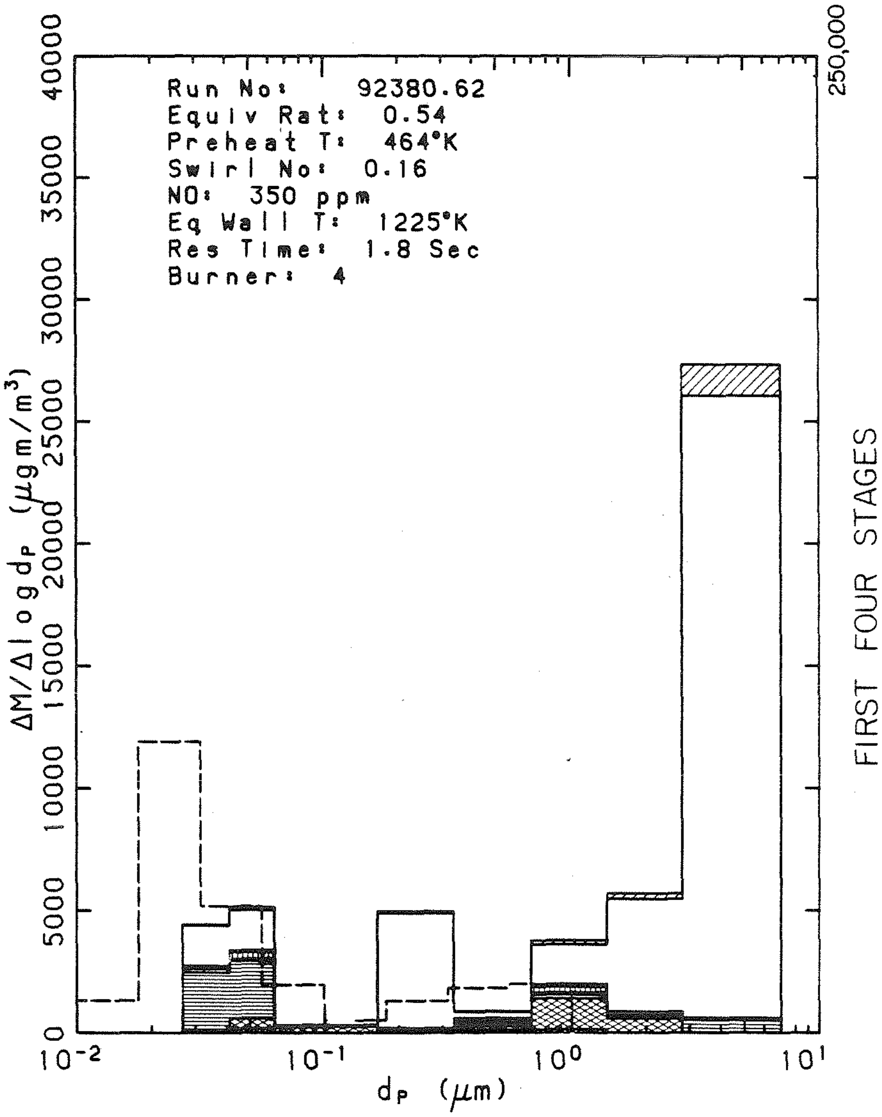

Figure 5.24: Composition distribution of fine particles as measured by PIXE for run 92380.62. Dashed line is EAA measurement of mass distribution based on particle specific gravity of 2.3. Total submicron particle mass concentration indicated by PIXE and EAA are 6,640 and 6,916 μg/m^3, respectively. Scale for upper four particle sizes has been compressed. See Fig. 5.20 for key.

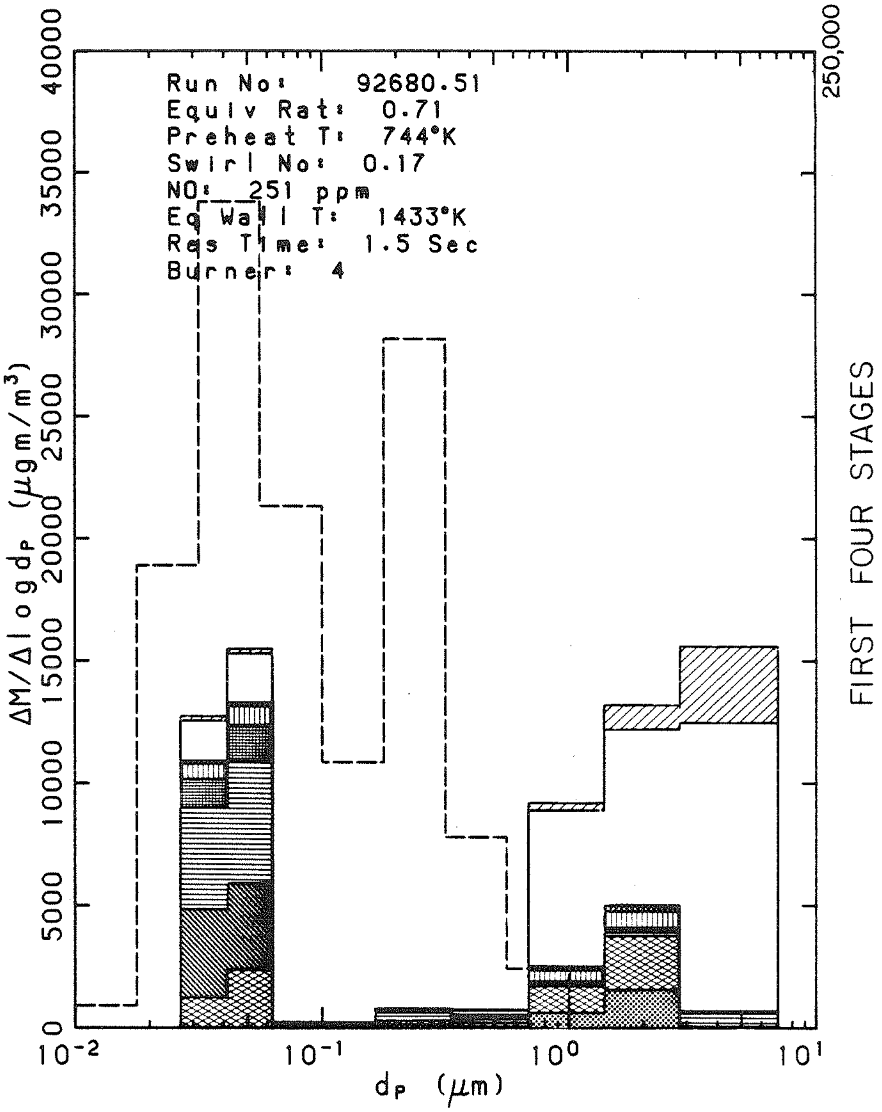

Figure 5.25: Composition distribution of fine particles as measured by PIXE for run 92680.51. Dashed line is EAA measurement of mass distribution based on particle specific gravity of 2.3. Total submicron particle mass concentration indicated by PIXE and EAA are 11,500 and 31,050 μg/m^3, respectively. Scale for upper four particle sizes has been compressed. See Fig. 5.20 for key.

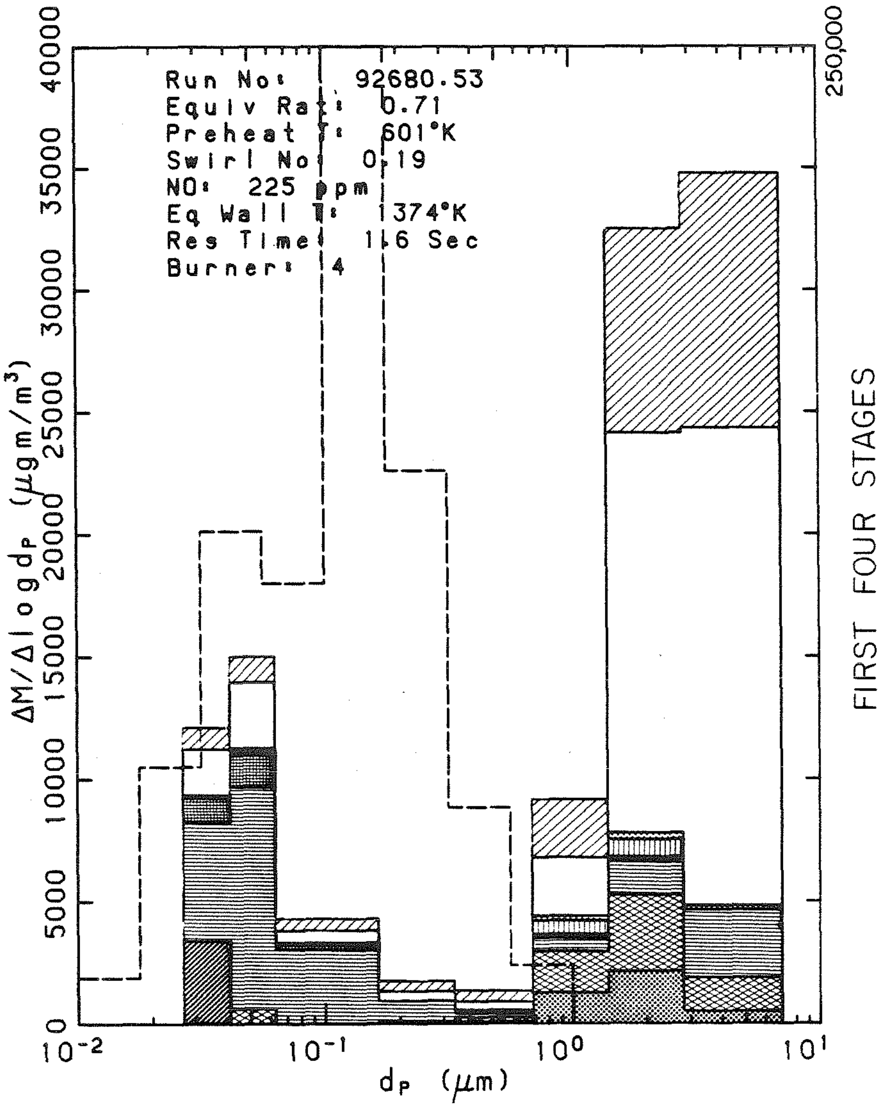

Figure 5.26: Composition distribution of fine particles as measured by PIXE for run 92680.53. Dashed line is EAA measurement of mass distribution based on particle specific gravity of 2.3. Total submicron particle mass concentration indicated by PIXE and EAA are 13,800 and 34,700 μg/m^3, respectively. Scale for upper four particle sizes has been compressed. See Fig. 5.20 for key.

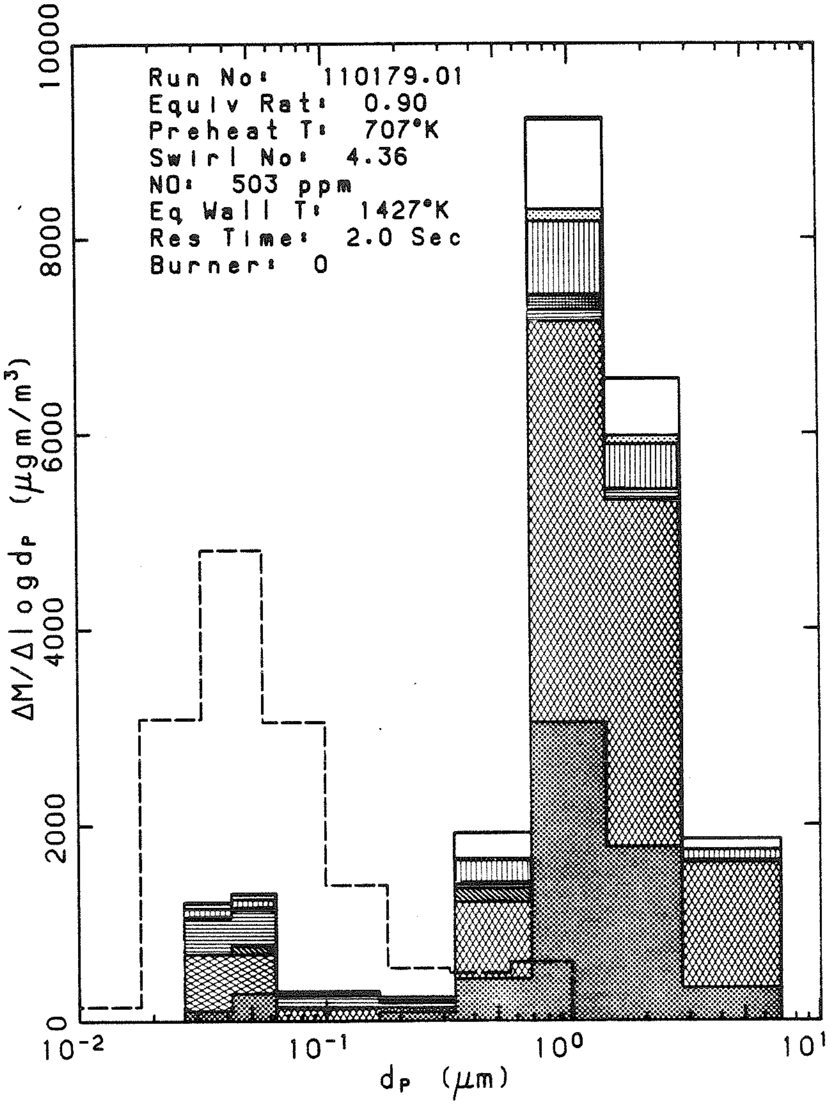

Figure 5.27: Composition distribution of fine particles as measured by PIXE for run 110179.01. Dashed line is EAA measurement of mass distribution based on particle specific gravity of 2.3. Uncertainty in absolute concentrations greater than 30%. See Fig. 5.20 for key.

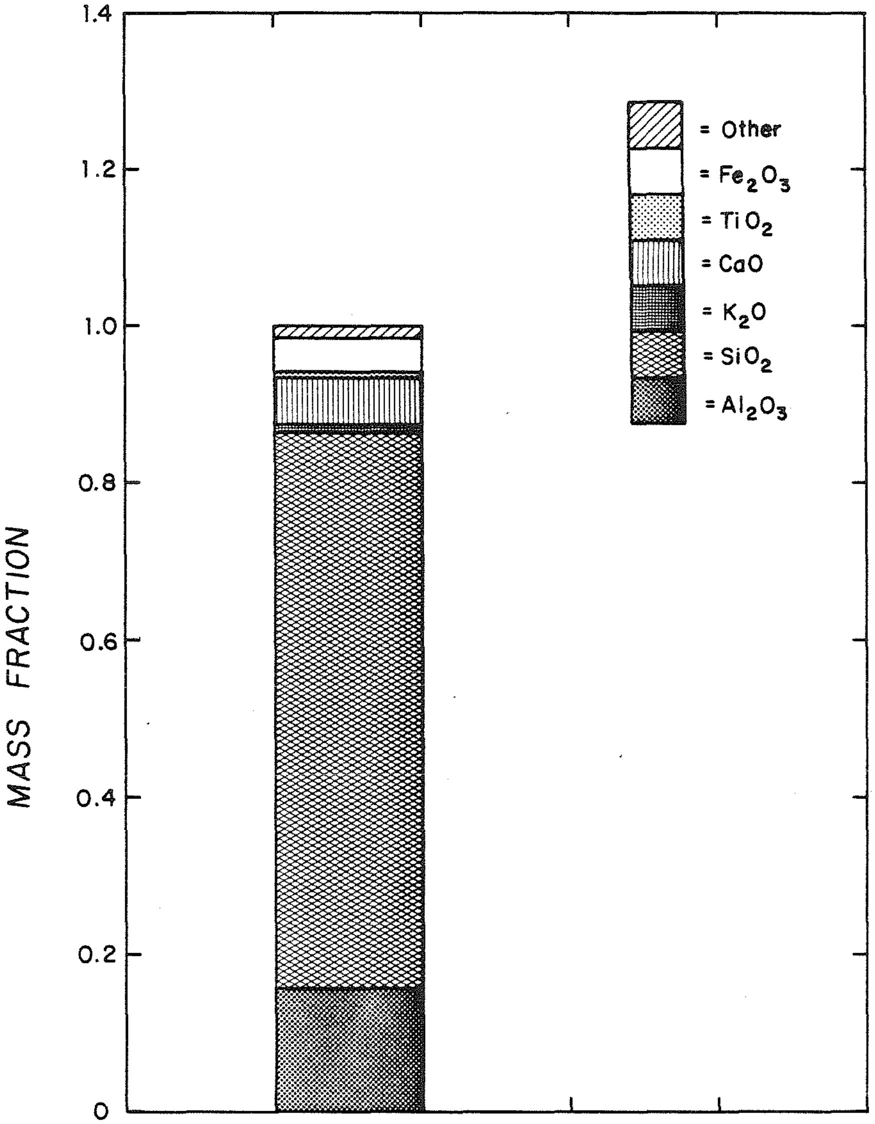

Figure 5.28: Mass fractions of major species in bulk ash of Utah II sub-bituminous coal used on experiments.

measurements is also plotted for comparison with the total mass concentration of particles as indicated by the elemental analysis of the mass samples. It should be noted that in order to achieve good resolution of individual species' contributions, two different scales were utilized for the upper and lower four size intervals indicated in figures for runs 92380.62, 92680.51, and 92680.53. In these figures the scale on the left axis applies to the four smaller size fractions, and that on the right axis to the four larger size fractions. The combustion conditions for each plot are indicated in the legends. The particle composition in each size class may be compared with that of the bulk ash by reference to Figure 5.28, which is a histogram representation of bulk ash composition.

Figure 5.27 illustrates composition distribution data for particles collected under conditions significantly different from those represented in Figures 5.20-5.26. Due to uncertainty in the total dilution ratio used in in this early run, the probable error in the absolute aerosol concentrations indicated is at least 30% of the indicated values. The concentrations indicated by EAA and PIXE measurements are, however, in correct relative proportion, since the EAA and LPI sampled the same diluted aerosol streams.

Several features of the figures are noteworthy:

1. There is a distinct peak in the size distribution function

indicated by both the EAA measurements and the PIXE measurements. The PIXE measurements indicate the start of a rise in the size distribution function toward the second (much-larger) peak which generally occurs at around 10-20 microns diameter.

2. The composition of the particles collected on the last two stages of the LPI varies with combustion conditions. Data in Figure 5.22 indicate significant quantities of silica (SiO_2) and phosphorous (P_2O_5 was the assumed form) while data in Figure 5.24 (collected at lower wall temperature) indicate neither of these minerals to be present in fine particles. Data of Figures 5.20 and 5.21 indicate that iron oxide (Fe_2O_3) is clearly the dominant species in the fine particles, while sulfate (SO_4) is dominant in Figures 5.22-5.26.

Data in Figure 5.27 were collected using burner 0, which was low-mixing and water-cooled (See Chapter 3 for a description of burners 0-4). A higher equivalence ratio and swirl number were achieved than in the runs indicated in the previous figures. Significant composition differences are apparent from the data. Alumina (Al_2O_3), which was not indicated in the fine particles of the other runs is indicated to be present in significant amounts in Figure 5.27. Although the equivalent wall temperature is comparable with that indicated in Figure 5.22, the contribution of silica to fine particle mass is significantly higher. Finally, iron appears to constitute a smaller fraction of the fine particle mass in Figure 5.27 than in previous figures.

The fact that the particle composition data in Figures 5.20 and 5.21 are similar supports the assertion that the differences noted above are attributable to differences in combustion conditions and not simply due to experimental error, since the combustion conditions during the runs represented in these two figures were nominally the same.

3. Particle composition changes significantly from the largest to the smallest particle sizes. The contributions of alumina and silica to the masses of the smallest particles is slight, whereas these species are major components of the larger particles (and of the bulk ash). Sulfates, which probably condense somewhere in the cooling section of the furnace, are major species in the smaller particles, presumably because of higher mass-specific condensation rates for the smaller particles compared with those for the larger particles. The relative contribution of more-volatile metals, such as potassium, iron, and zinc, to the mass of the smaller particles are generally significantly higher than their contributions to the masses of the larger particles; i.e., the smaller

particles appear to be enriched with the more-volatile metal oxides present in the parent coal mineral matter.

Two features regarding the acuracy of either the PIXE or the EAA data should be noted. First, there is a considerable discrepancy between the total mass distribution indicated by PIXE and that indicated by EAA data (See Appendix D for a discussion of possible sources of this discrepancy). Second, as previously noted, Figures 5.24, 5.25, and 5.26 indicate that a major change occurred in both the composition and the total mass concentration of the larger particles. The contribution of iron in these runs is much higher than in prior runs, and the contribution of zinc, previously small, is substantial. This composition change from the previous runs (and from bulk ash composition) indicates that a qualititative change in the laboratory combustor occurred at this point. If, as previously suggested, there were an input of any mineral species other than that due to the coal itself, then the interpretation of those species′ contributions to the mass of the submicron fly ash for the questionable runs is suspect.

To illustrate graphically how individual species′ contributions to particle composition changes with particle size, the species mass fractions are plotted against particle size in Figures 5.29–5.36 for each of the runs represented in Figures 5.20–5.27. The error bars in each figure indicate the 95% confidence limits for the value of the mass fraction, as described in Appendix C.

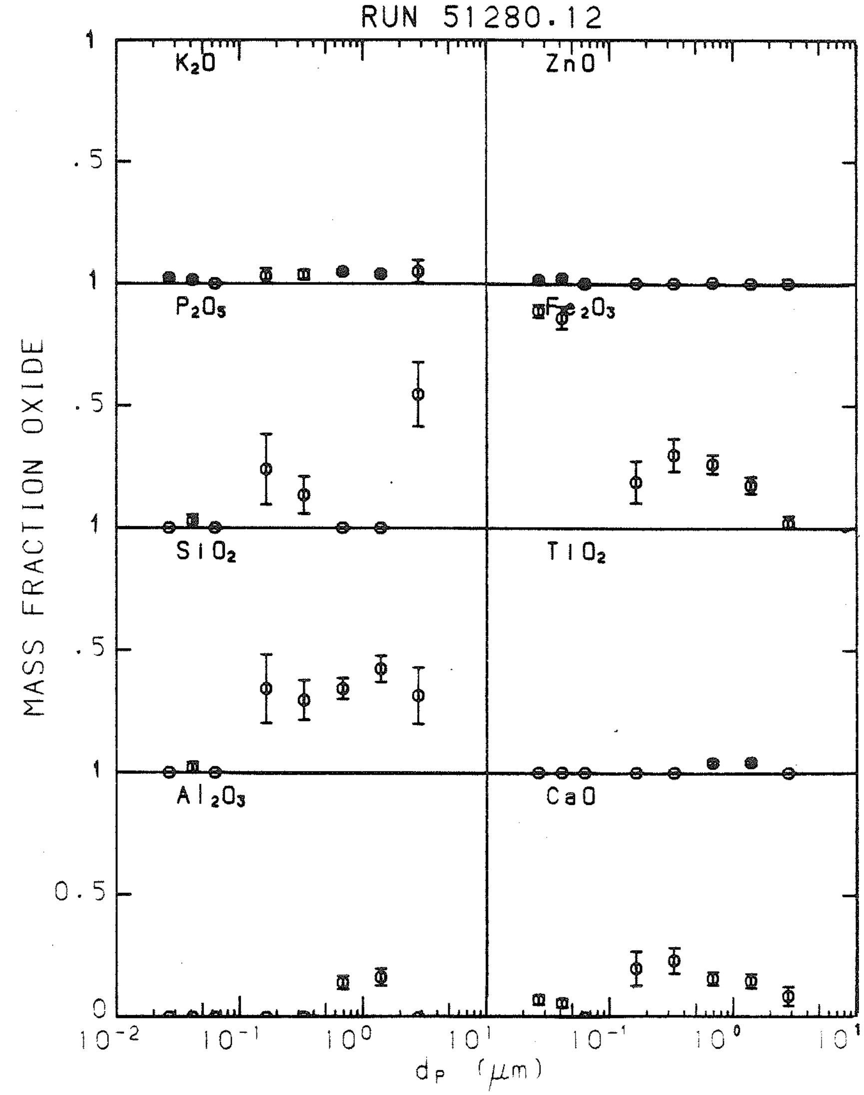

Figure 5.29: Mass fractions of major metallic oxides in fine ash particles. Mass of sulfate (SO_4) is not included in the calculation. Error bars are 95% confidence limits.

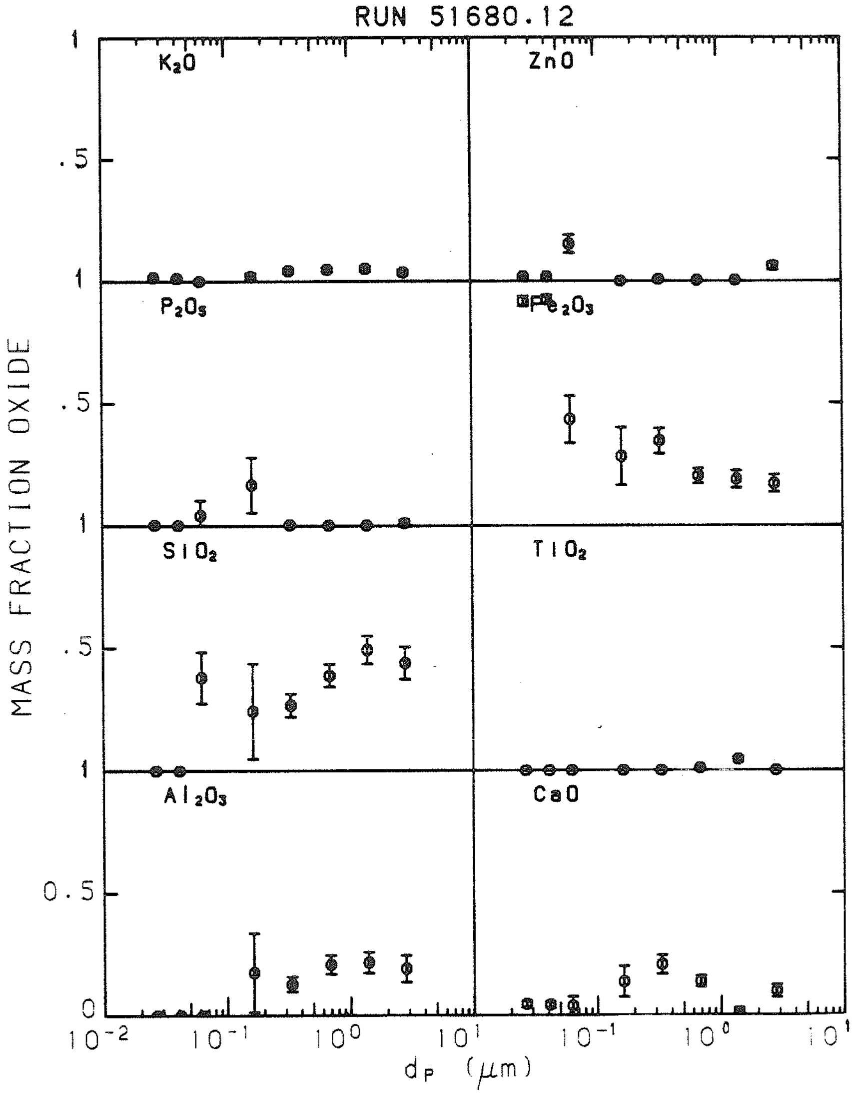

Figure 5.30: Mass fractions of major metallic oxides in fine ash particles. Mass of sulfate (SO_4) is not included in the calculation. Error bars are 95% confidence limits.

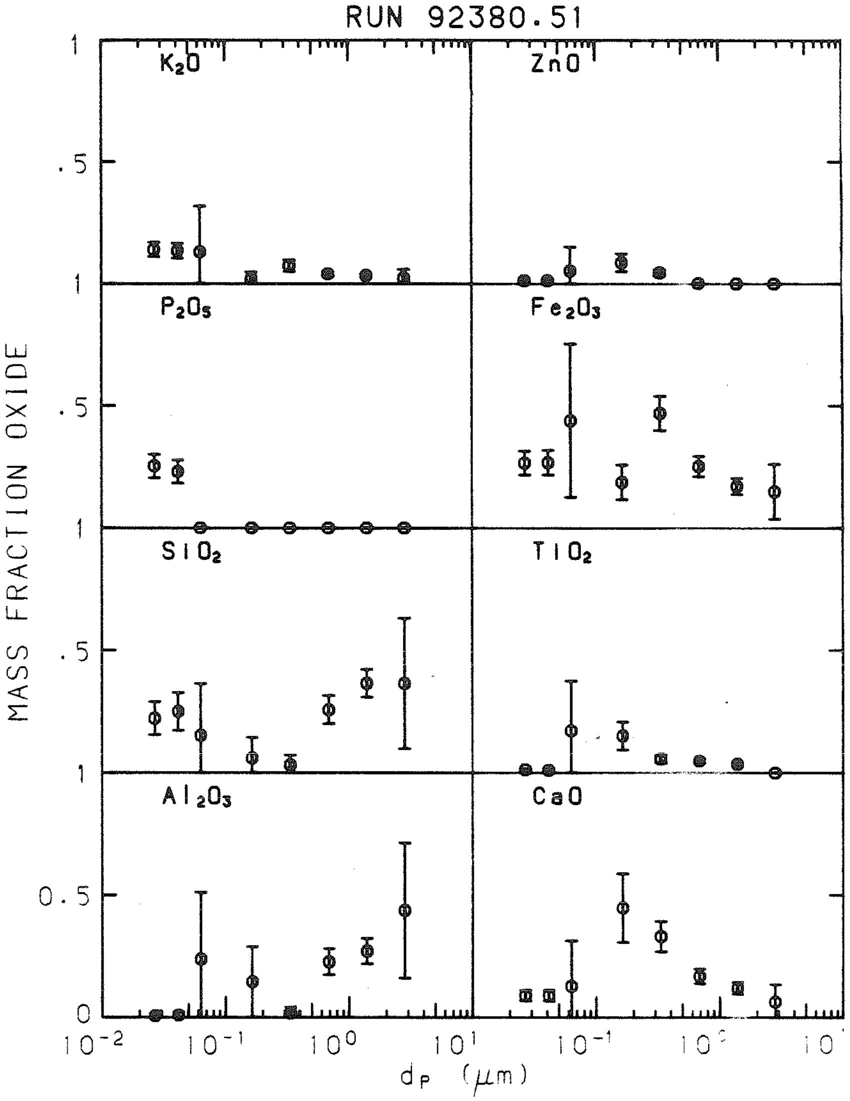

Figure 5.31: Mass fractions of major metallic oxides in fine ash particles. Mass of sulfate (SO_4) is not included in the calculation. Error bars are 95% confidence limits.

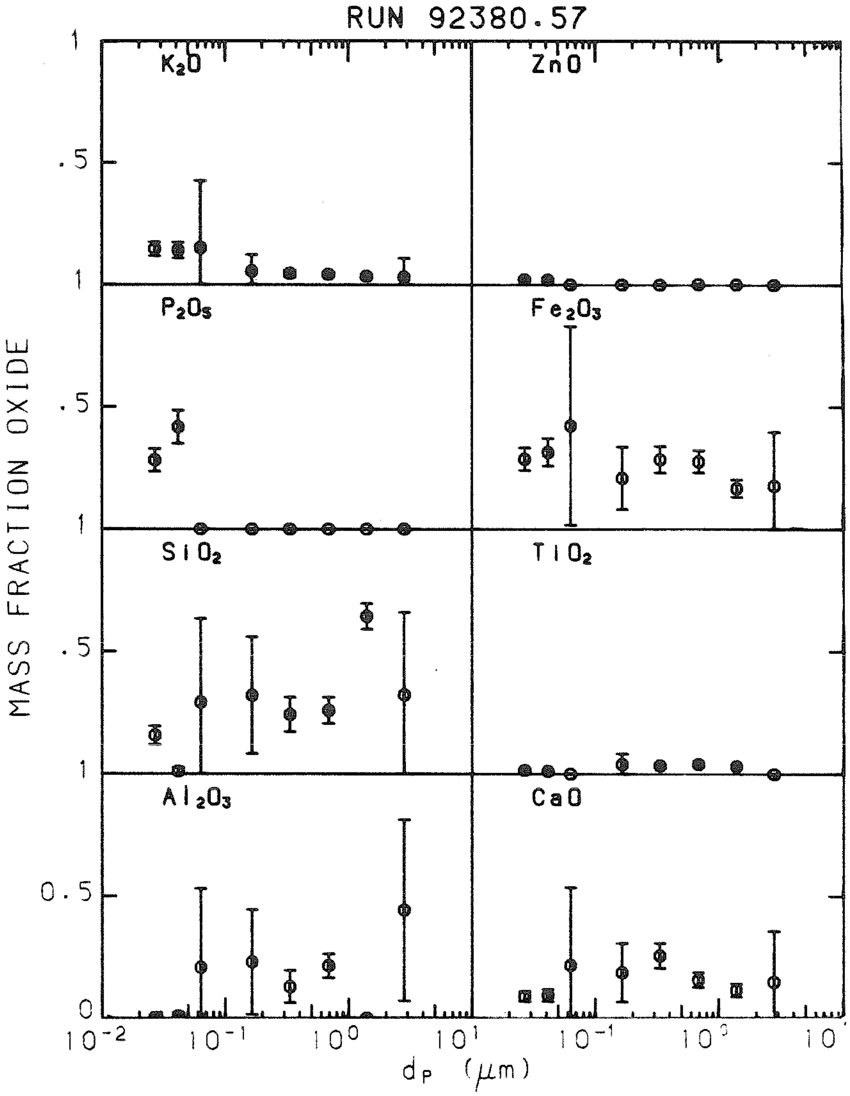

Figure 5.32: Mass fractions of major metallic oxides in fine ash particles. Mass of sulfate (SO_4) is not included in the calculation. Error bars are 95% confidence limits.

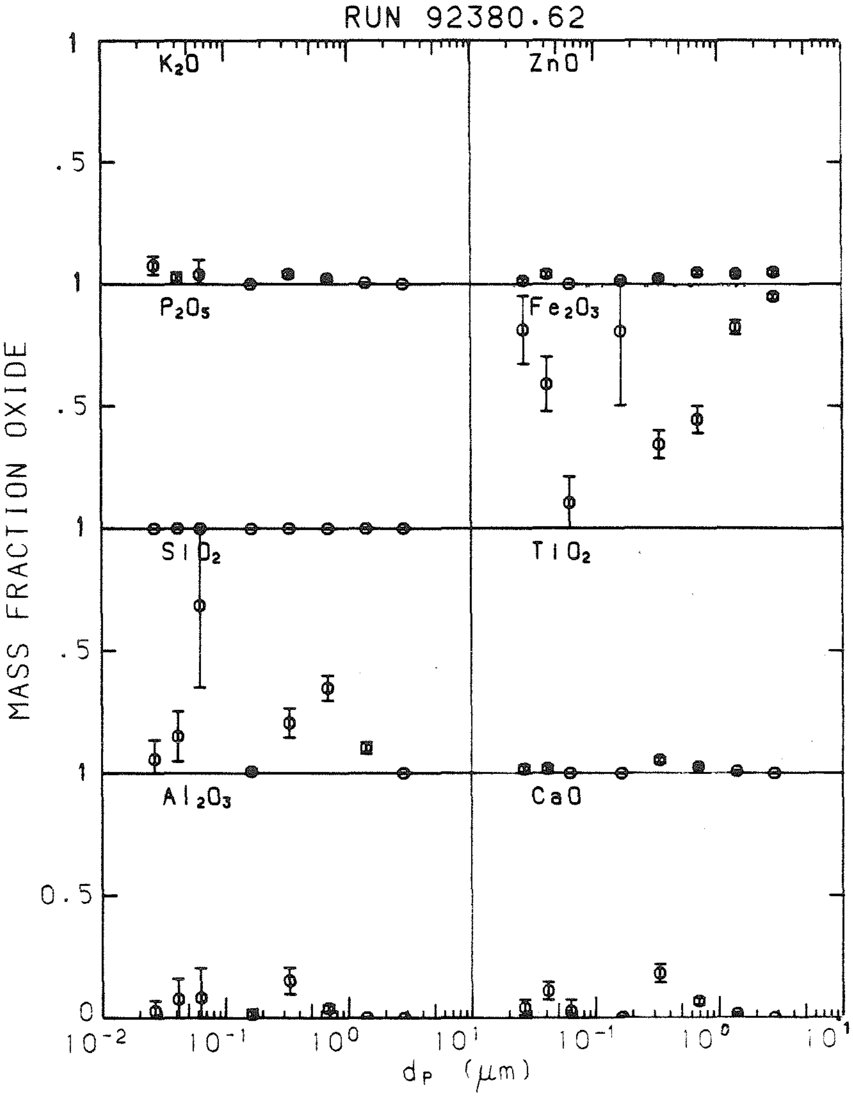

Figure 5.33: Mass fractions of major metallic oxides in fine ash particles. Mass of sulfate (SO_4) is not included in the calculation. Error bars are 95% confidence limits.

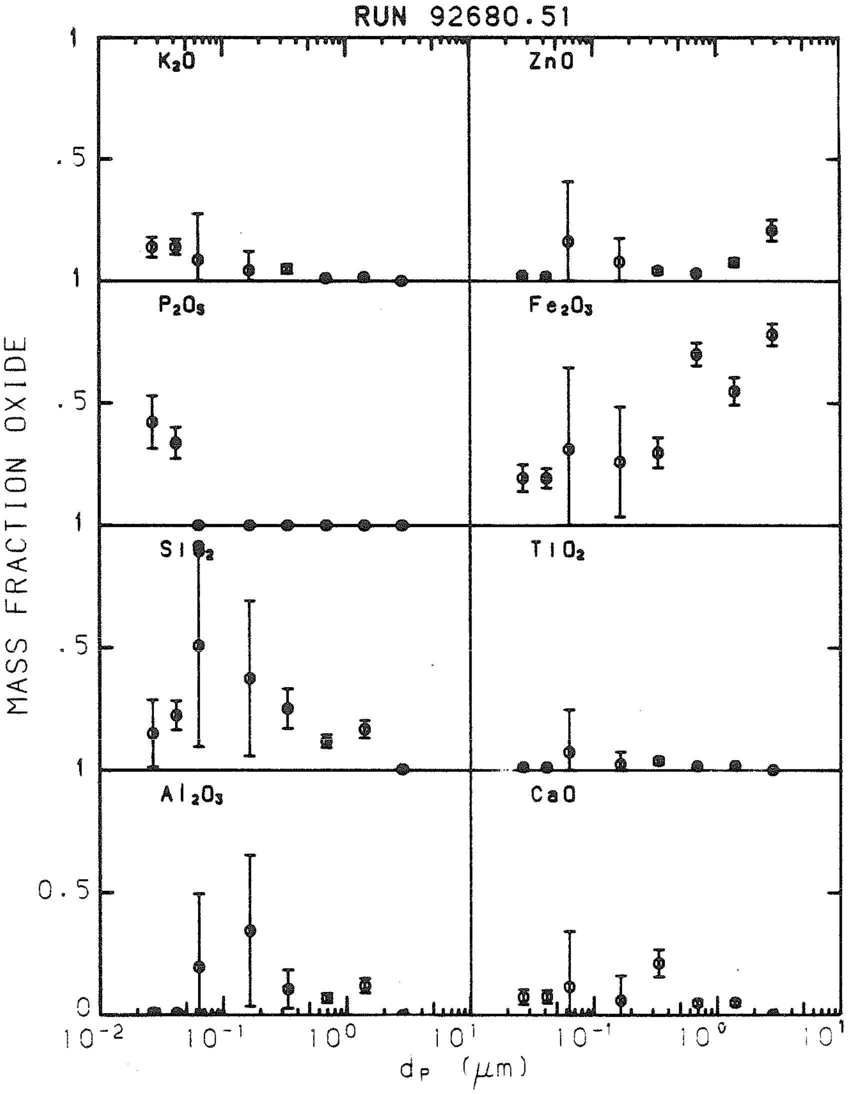

Figure 5.34: Mass fractions of major metallic oxides in fine ash particles. Mass of sulfate (SO_4) is not included in the calculation. Error bars are 95% confidence limits.

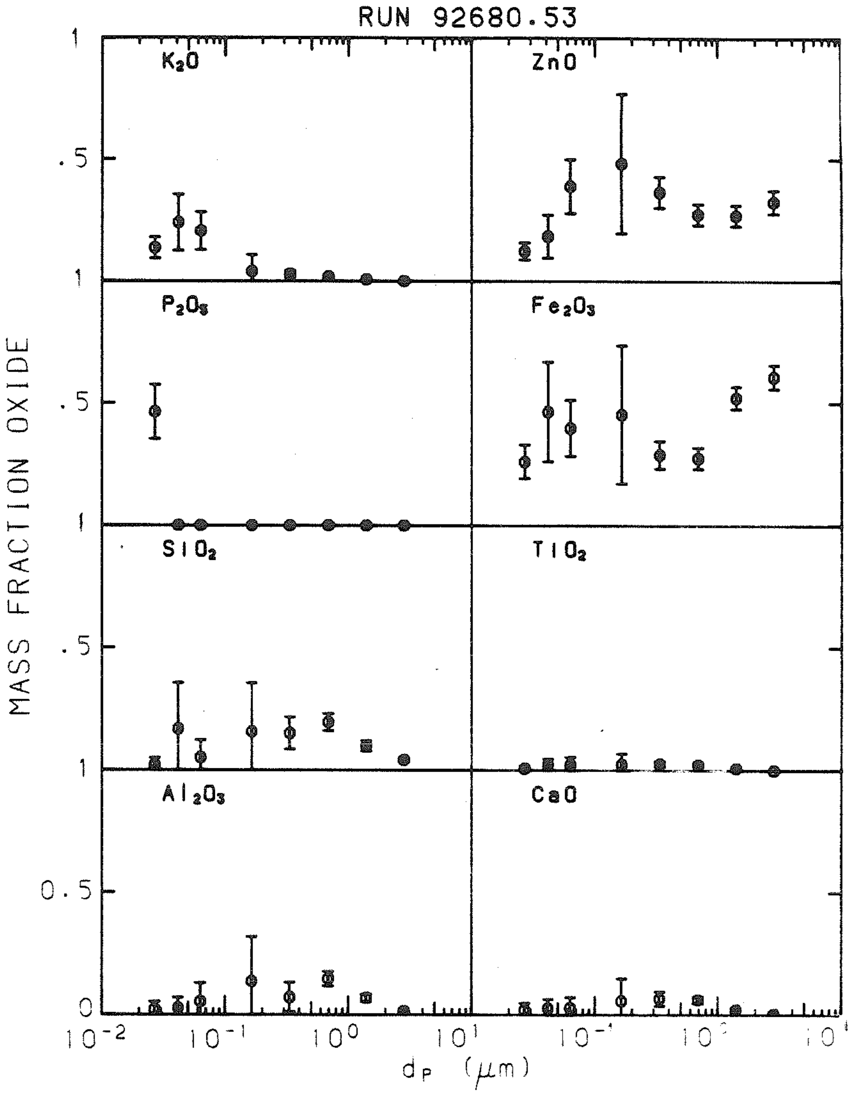

Figure 5.35: Mass fractions of major metallic oxides in fine ash particles. Mass of sulfate (SO_4) is not included in the calculation. Error bars are 95% confidence limits.

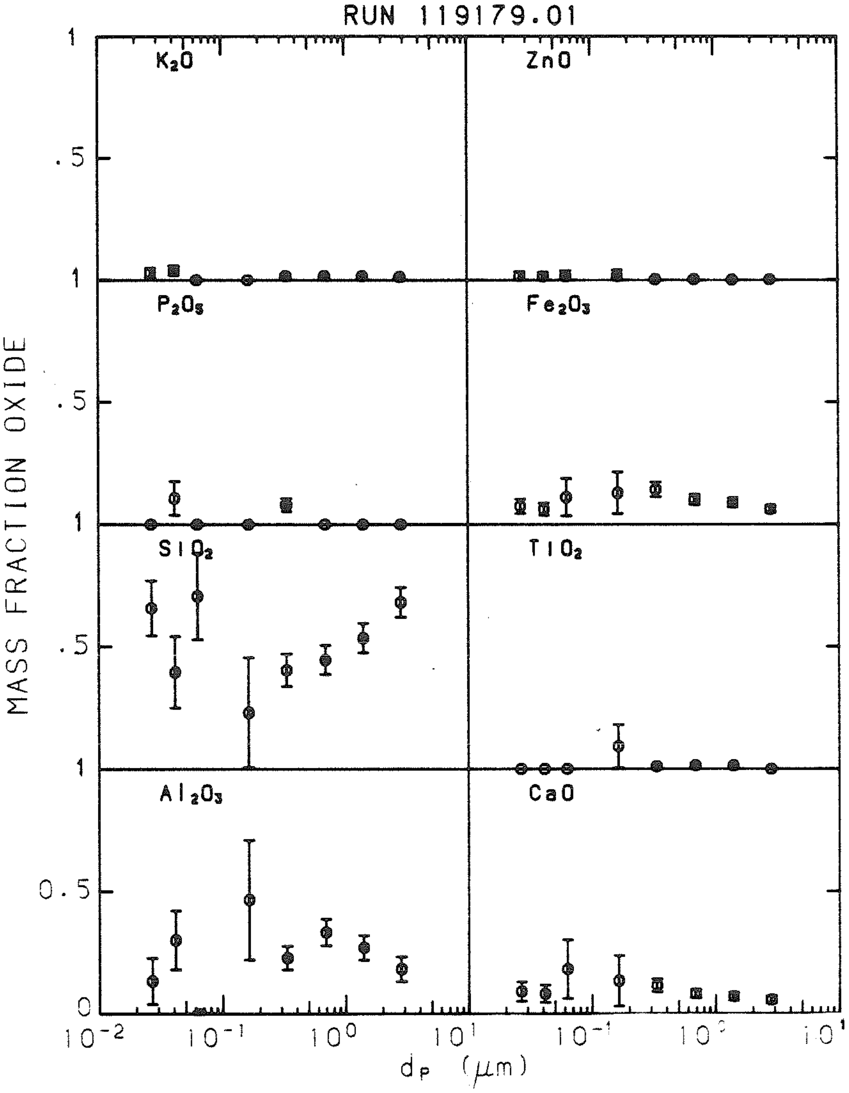

Figure 5.36: Mass fractions of major metallic oxides in fine ash particles. Mass of sulfate (SO_4) is not included in the calculation. Error bars are 95% confidence limits.

In calculating the mass fractions shown in the figures, only the refractory metal oxides were considered. Thus, the mass of SO_4 was excluded in the calculation on the assumption that the mechanism and time of sulfate deposition on fine particles is different from that of the refractory species. In light of previous comments regarding the validity of composition data for runs after 110 hours cumulative furnace run time, only the mass fraction data for runs prior to that time are here considered; i.e., the discussion which follows will be limited to Figures 5.29-5.32, and 5.36.

The data in the figures appear to reflect the result of two processes occuring in the furnace: (a)Vaporization of mineral matter from the larger, residual ash particles, (b)Nucleation of vaporized species to form small particles. The calcium (Ca) data in the above-mentioned figures show a fairly consistent trend. The value of the mass fraction first rises with decreasing particle size and then falls. The initial rise may be due to condensation of vaporized calcium. To examine this possibility the mass fraction of Ca was calculated as a function of particle size, assuming both free-molecular and continuum regime condensation. The surface layer of particles was assumed to consist entirely of calcium and the calcium concentration in the remainder of the particle was assumed equal to the bulk concentration (about 5.7%, excluding sulfates). Results of the calculations are compared with the measured enrichment data in Figure 5.37. The measured enrichment shows a trend which is similar to the

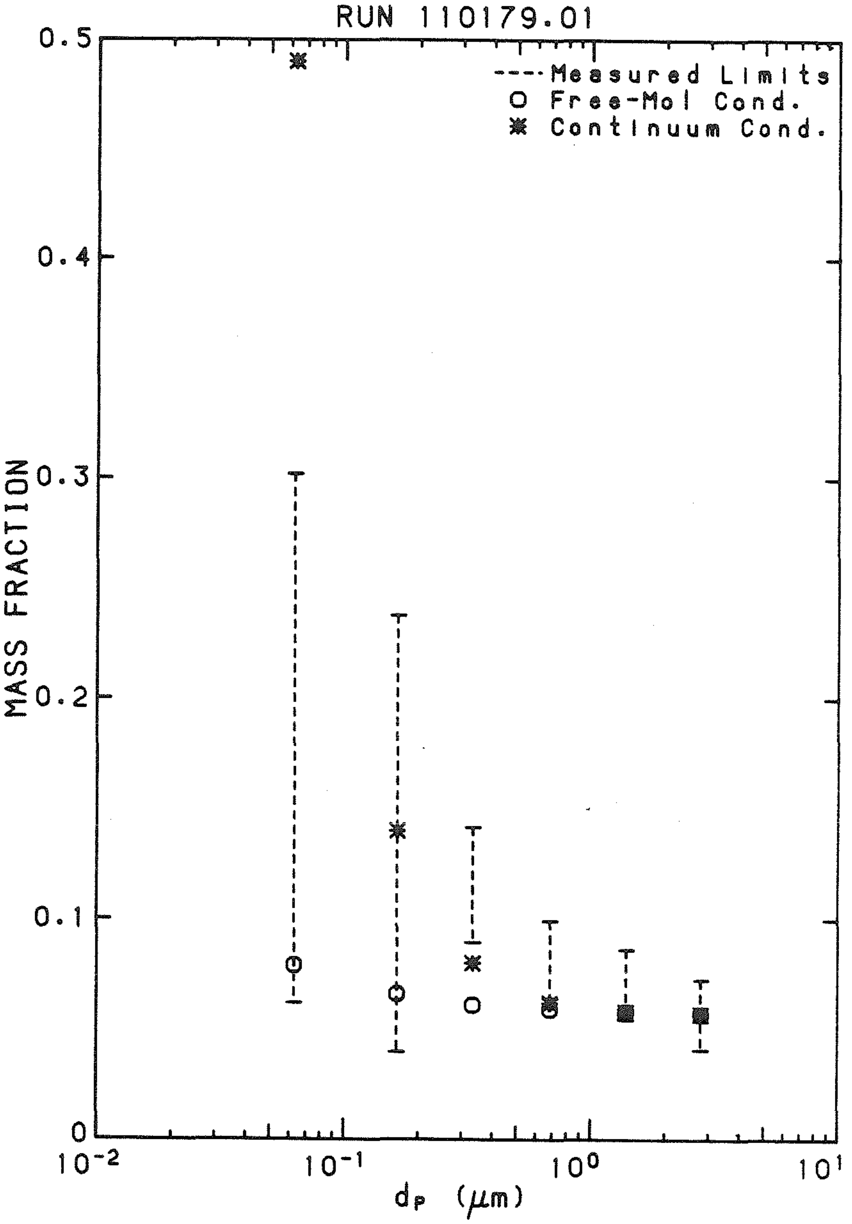

Figure 5.37: 95% confidence limits of measured mass fraction of CaO in fine fly ash particles vs particle diameter (d_p). Symbols show predicted mass fraction assuming continuum and free-molecular regime condensation of pure CaO on residual ash particles assumed to have the same composition as bulk ash.

calculation. However, precise comparison is not warranted due to gross assumptions made in the calculation.

The drop in Ca mass fraction for the smallest particle sizes may reflect the different formation mechanism of those particles. If they are composed entirely of condensed vapors the amount of Ca may be small compared with that of other vaporized species, resulting in dilution of calcium and a decrease in the Ca mass fraction.

The iron mass fraction data are also supportive of the vaporization-condensation hypothesis for fine particle formation. In figures 5.29-5.32, and 5.36 the iron mass fraction first rises, then either rises still more or drops in the very fine particles. The initial rise may, again, be due to condensation on the surface of residual ash particles. In Figures 5.29 and 5.30, iron is the major species in the very fine particles since the combustion conditions corresponding to those figures (low wall temperature) did not cause silica to vaporize in significant amounts. In Figures 5.31, 5.32, and 5.36 (corresponding to higher wall temperatures) silica is vaporized in significant quantities. The iron contribution to the fines is thus reduced and its mass fraction drops in these particle sizes.

The figures also indicate a fairly consistent trend of decreasing silica mass fraction with decreasing particle size down to about 0.1 micron. The model calculations (discussed later) indicate that char particle burning temperature increases with decreasing particle size. This would suggest increasing rates of silica vaporization and decreasing final mass fractions in the residual ash from the burning char. If the vaporized silica nucleated early in the near field surrounding the char particle then there would be little surface condensation of silica on residual ash particles. The very fine particles, however, would show high silica mass fraction, as is observed.

3.5 STATISTICAL INFERENCES FROM LABORATORY DATA

To explain the large variation in the measurements of submicron aerosol volume, V, on the basis of variations in the combustor operating parameters (See Chapter 3) the data were analyzed using multiple linear regression techniques on the PDP-11 digital computer in the Keck Laboratory of Environmental Engineering at Caltech.

In performing the regression analysis the measured values of V for a given data set were fitted to a linear function of the six combustion parameters mentioned above using a least-squares technique. The results of the analysis are indicated in Table 5.1. The first data set includes all runs for which valid aerosol data were recorded. The values of V predicted by the linear model are plotted against the measured values in Figure 5.38. The second, third, and fourth data sets in Table 5.1 include only the data for a particular burner type. The tabulated data suggest the following observations:

1. The parameter with the highest contribution to the explained variance in the first data set is U. In the second, third, and fourth sets, the variation of U is considerably less, and contributes correspondingly less to the explained variance of V, than in the case of the first data set. This suggests that the most significant difference between burner types (in explaining the observed difference in fine particle

Table 5.1

Results of Multiple Linear Regression Analysis of V

Data Set	Combustion Conditions	Parameter Coefficient[†], % Contribution to Explained Variance of V[§]												Regr Coef[‡]	Data Pts.
		T_w		ϕ		t		T_{pre}		S		U			
		Coef.	Ctrb.	Coef.	Ctrb.	Coef.	Ctrb.	Coef.	Ctrb.	Coef.	Ctrb.	Coef.	Ctrb	R^2	Pts.
1	$0.50 \leq \phi \leq 0.62$ All burners	32.	24.	2.7×10^4	1.8	6.0×10^3	3.0	11.	5.4	5.1×10	1.7	7.6	63.	.82	54
2	$0.50 \leq \phi \leq 0.62$ Burner 1 only	56.	28.	-1.2×10^5	47.	-1.9×10^4	9.8	48.	2.6	9.3×10^4	4.6	-45.	8.0	.82	20
3	$0.50 \leq \phi \leq 0.62$ Burner 3 only	.48	0.0	-1.3×10^4	1.9	-3.8×10^4	.44	1.5×10^2	26.	3.3×10^3	58.	590.	14.	.90	12
4	$0.50 \leq \phi \leq 0.62$ Burner 4 only	226.	46.	1.5×10^4	1.2	1.5×10^5	31.	-1.8×10^2	10.	-1.3×10^4	.33	-210.	11.	.98	22

Notes: [†] Parameter coefficients are the coefficients a_i for the six combustion parameters in the fitted linear correlation of V:

$$V = a_1 T_w + a_2 \phi + a_3 t + a_4 T_{pre} + a_5 S + a_6 U$$

The paramters T_w, ϕ, t, T_{pre}, S, U are defined in Chapter 3.

[§] The % contribution of each parameter represents the percentage of the total variation in V which is attributable (from the linear correlation) to variation of that parameter.

[‡] The regression coefficient R^2 is an unbiased measure of the quality of the fit of the linear correlation of the data (for a discussion of linear regression analysis, see Draper and Smith (1966)).

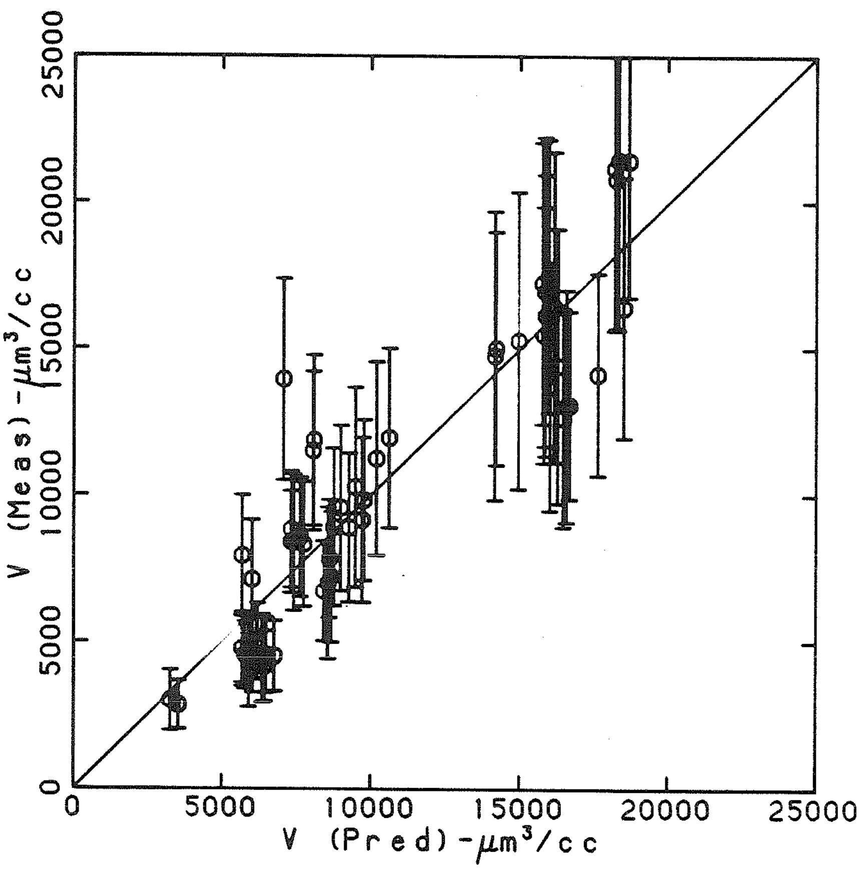

Figure 5.38: Predicted submicron particle concentration from multiple linear regression analysis vs measured concentrations. Error bars are 90% confidence limits. See Chapter 3 for description of regression parameters.

concentrations) may be burner aerodynamics.

2. Comparison of the regression results for individual burner types indicates that the relative significance of the combustion parameters in the explained variance is different for each burner; e.g., for burner 1 data, ϕ contributes most to the explained variance, while for burner 3 and burner 4 data, S and T_w, respectively, contribute most. From this observation any or all the following conclusions might be drawn: (a)The above list of characteristic parameters does not fully characterize the combustion condition; (b)The error in the measured parameters used to calculate the six characteristic parameters is sufficient to overshadow the linear correlation; (c)The true correlation between V and the six characteristic parameters above is extremely non-linear and not well approximated by a linear correlation.

The above conclusions suggest the need for further work.

In light of the strong correlation observed between NO and total submicron volume it is worthwhile to examine the correlations of NO with the six characteristic combustion parameters. Thus, the regression analysis described above was applied to the measured values of NO. In this case a considerably larger set of data was available for burner 1 since a number of preliminary experiments were performed during which valid gas composition data (but not particle data) were obtained.

The results of the analysis are tabulated in Table 5.2. The first entry represents data from all runs (including the preliminary runs mentioned but excluding those after 110 hours of furnace run time). The predicted and measured values of NO for this data set are plotted in Figure 5.39. The second, third, and fourth entries are respectively the data for burners 1, 3, and 4. Comparison of the regression results for the four data sets suggests the following:

1. The regression results for data set 5 indicate that the variation in U contributes most to the explained variance of the data. As in the case of the analysis for V, the strongly-dominant contribution of U to the explained variance of NO is not seen in individual burner data, again suggesting that the principal difference in the three burner types is in the aerodynamics (reflected in the U parameter).

2. The relatively low multiple correlation coefficients in the cases of burner 1 and combined burner data suggest, as in the regression analysis of V, that the linear correlation of NO with the six characteristic combustion parameters is inadequate to account for the measured variation of NO.

Table 5.2

Results of Multiple Linear Regression Analysis of NO

Data Set	Combustion Conditions	Parameter Coefficient[†], % Contribution to Explained Variance of NO[§]												Regr. Coef[‡]	Data Pts.
		T_w		ϕ		t		T_{pre}		S		U			
		Coef.	Ctrb.	Coef.	Ctrb.	Coef.	Ctrb.	Coef.	Ctrb.	Coef.	Ctrb.	Coef.	Ctrb	R^2	Pts.
5	All burners	-.23	1.7	-150.	1.4	-105.	2.5	.25	2.4	22.	.76	.14	91.	.46	125
6	Burner 1 only	-.72	33.	74.	1.0	-95.	8.0	-.05	.14	-450.	35.	.43	23.	.29	83
7	Burner 3 only	-13.	16.	110.	.09	-9.3×10^3	18.	5.1	21.	-83.	26.	25.	18.	.78	12
8	Burner 4 only	-5.9	15.	-139.	1.1	-5.6×10^3	20.	7.4	20.	-6.1×10^3	20.	9.1	23.	.61	30

Notes: [†] Parameter coefficients are the coefficients a_i for the six combustion parameters in the fitted linear correlation of NO:

$$NO = a_1T_w + a_2\phi + a_3t + a_4T_{pre} + a_5S + a_6U$$

The paramters T_w, ϕ, t, T_{pre}, S, U are defined in Chapter 3.

[§] The % contribution of each parameter represents the percentage of the total variation in V which is attributable (from the linear correlation) to variation of that parameter.

[‡] The regression coefficient R^2 is an unbiased measure of the quality of the fit of the linear correlation of the data (for a discussion of linear regression analysis, see Draper and Smith (1966)).

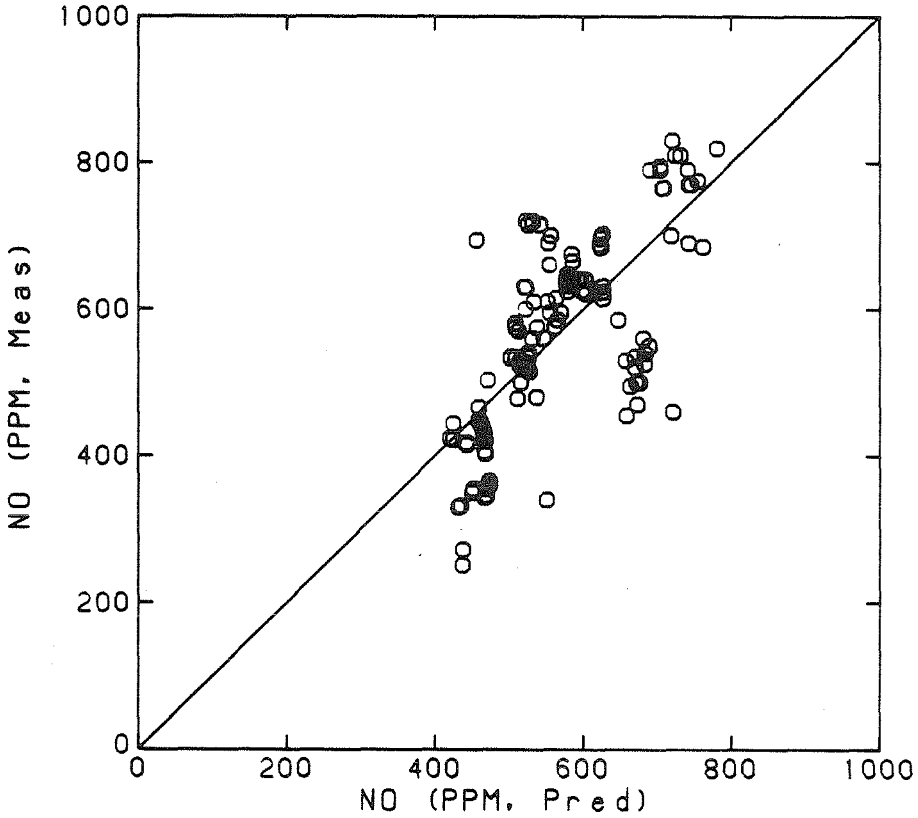

Figure 5.39: Predicted NO concentration from multiple linear regression analysis vs measured concentrations. See Chapter 3 for description of regression parameters.

4.0 RESULTS OF COMPUTER MODELING OF THE LABORATORY COMBUSTOR

4.1 MODEL PREDICTIONS OF PARTICLE TEMPERATURE-TIME PROFILES

The combustion model was first applied using the combustion conditions obtained during runs 92380.51 through 92380.62 (burner 4). This set of conditions was chosen for the following reasons: (a)The fuel-air equivalence ratio of these runs was sufficiently lean (approximately 0.55) that satisfactory combustion efficiency was achieved; (b)The wall temperature profiles for these runs is better-characterized than in other runs at the same equivalence ratio; (c)A larger range of wall temperatures was achieved during these runs than in any other set of runs, and thus correspondingly larger ranges of particle temperatures, vaporization rates, and total volume concentrations were obtained on which to base the least-squares estimate of vaporization kinetic parameters.

The entire set of inputs to the computer model is as follows:

1. Fitted axial wall temperature profile;

2. Measured inlet and estimated outlet gas temperatures;

3. Measured mass flow rates of primary and secondary combustion air;

4. Mass flow rate of coal (inferred from known coal composition, measured air flow rates, and exhaust gas composition);

5. Combustor and burner geometry;

6. Coal composition and initial coal particle size distribution (approximated by a finite discrete spectrum of particle sizes inferred from sieving data);

7. Thermodynamic and kinetic parameters for the combustion reactions considered.

The combustor model computed the temperature-time histories of the particles in each size range of the input coal particle size distribution. Figure 5.40 shows the calculated particle temperature-time profiles for the combustion conditions obtained during run 92380.51. Initial particle size on entry into the combustor is indicated as a parameter, and the gas and wall temperature profiles are also plotted.

The figure illustrates how particle burning temperature increases with decreasing particle size. The time at which the char burnout for larger particle sizes is clearly indicated by the drop in particle temperature after a gradual rise to the peak temperature. The burnout point of the smallest particles is obscured by the fact that particle

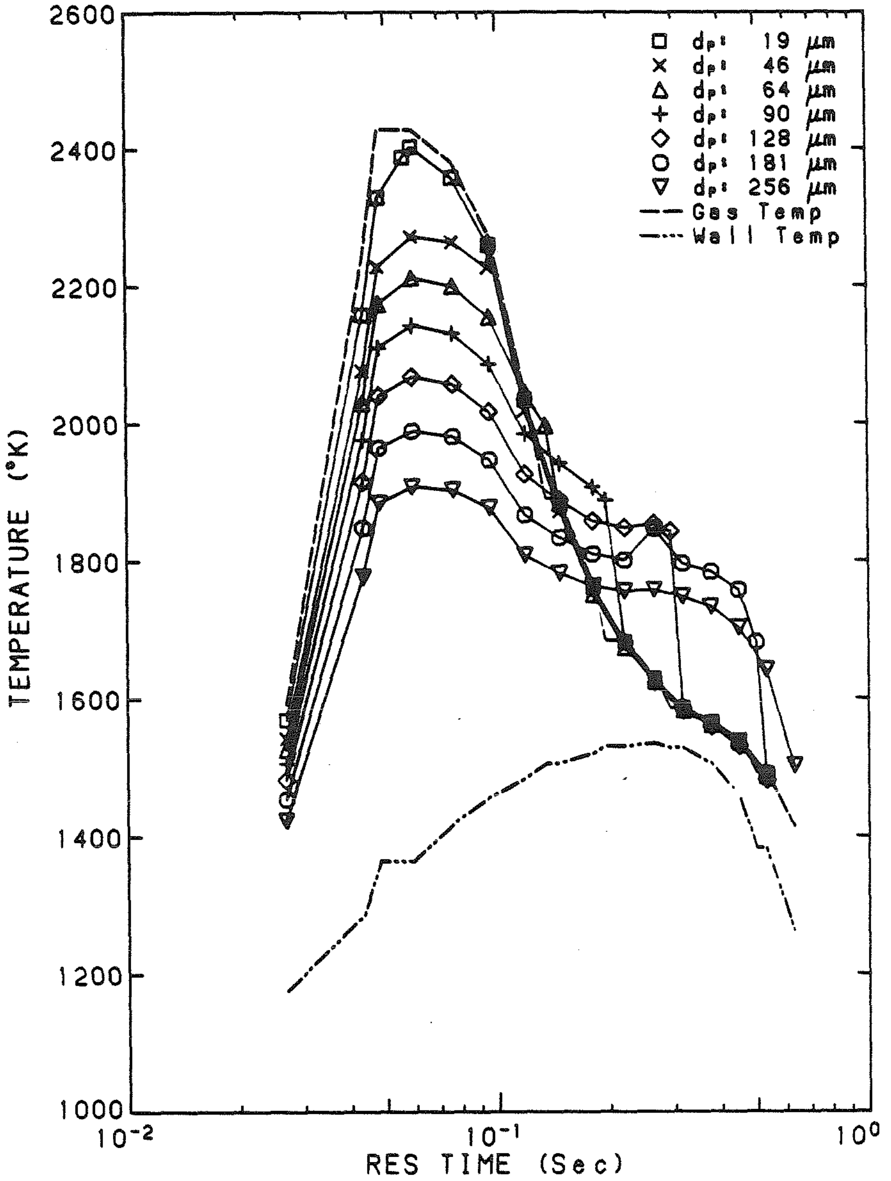

Figure 5.40: Particle temperatures vs combustor residence time from model calculation for run 92380.51. Gas and wall temperatures for corresponding residence times are also indicated. CO oxidation assumed slow.

burning temperature decreases with gas temperature after the initial rise due to volatiles combustion. The smaller particles burn out in a fraction of the total residence time in the combustor (the model prediction of total residence time is about 0.6 sec, about half the design residence time of 1.0 sec based on assumed plug flow in the combustor), while the larger particles burn at lower temperatures for a longer period of time. On this basis, one might suspect that the mass-specific contribution of larger particles to the total mass of vaporized material (submicron particles) would be lower than for smaller particle sizes. This will be discussed later.

Figure 5.41 shows the calculated mole fraction of oxygen as a function of particle residence time in the combustor. Comparison with Figure 5.40 indicates that high initial burning temperatures of the smallest particles is primarily due to the high gas temperature. The initial steep rise in the gas temperature is a consequence of the early heat release due to volatile hydrocarbon combustion.

In Figure 5.42 the ratio of oxygen concentration at the particle surface to that in the far field of the particle is plotted for all particle sizes. This ratio is suggestive of the relative importance of diffusion and kinetic limitations to the combustion rate of the char (Low values of this ratio indicate strong diffusion limitation; zero values indicate periods when no combustion occurs, during volatile hydrocarbon combustion and after char burnout). The importance of the

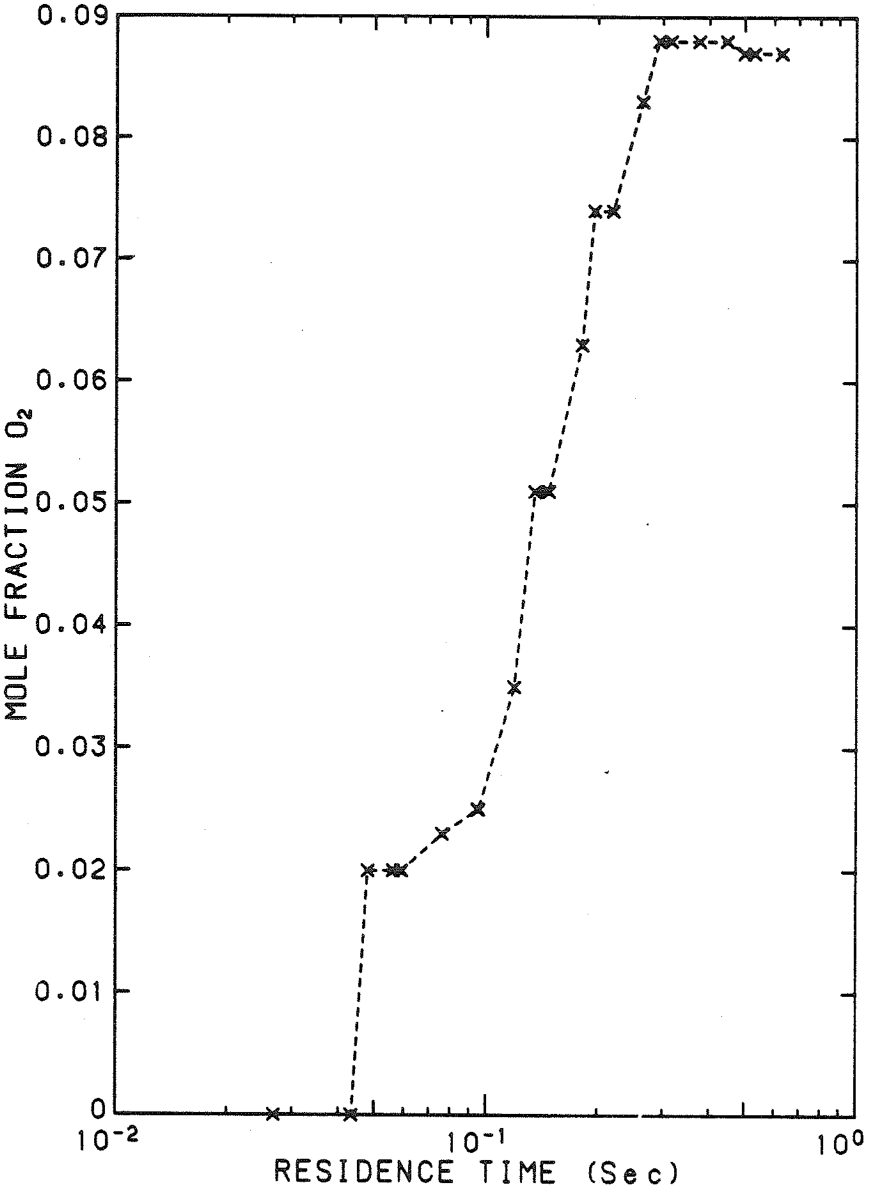

Figure 5.41: Mole fraction of oxygen in the flame free stream (particle far field) vs combustor residence time for run 92380.51.

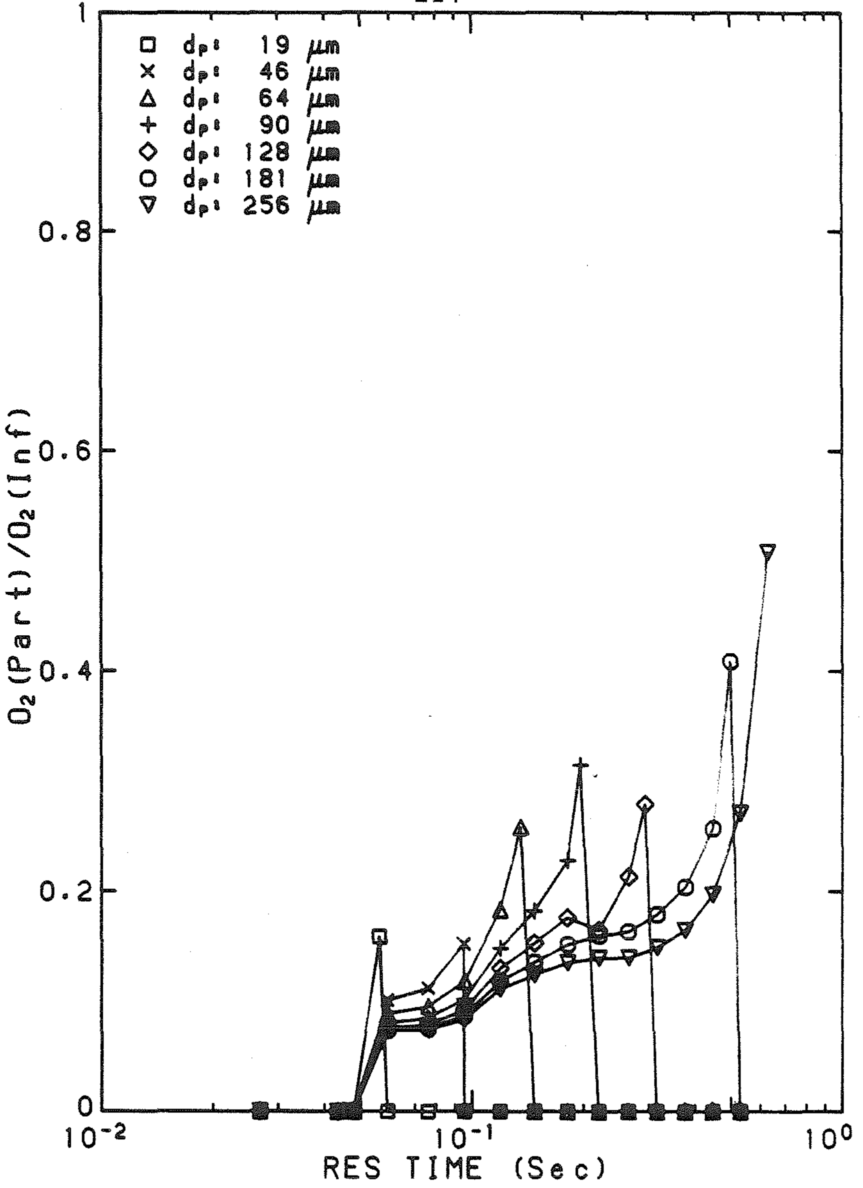

Figure 5.42: Ratio of oxygen concentration at particle surface to that in the flame free stream (particle far field) for run 92380.51 (slow CO oxidation).

diffusion limitation increases with particle size early in the combustion, as theoretical considerations would predict. For a given initial particle size, the diffusion limitation becomes less severe as the particle diameter decreases, again consistent with theory.

The diffusion limitation for the largest particles, just prior to burnout is less severe than for the initial combustion of the smallest particles even though the final burning diameters of the particles are 180 and 19 microns, respectively. This is probably a consequence of the higher gas temperature prevailing during the period of combustion of the smaller particles.

In Figure 5.43 the ratio of radiation heat loss to conduction heat loss is plotted for various particle sizes. The figure illustrates that radiation is significant at all times during the combustion process. The steep rise in the curves just after 0.1 sec is due to the equilibration of particle and gas temperatures at this time, which causes conduction to decrease to zero. The influence of radiation is strongest during the burnout of the larger particles when the particle temperature is significantly higher than the gas temperature.

In Figure 5.44 the particle temperature-time profiles are plotted for the conditions of run 92380.57. The principal difference between this operating condition and that of Figure 5.40 is that the effective wall temperature is 1345 K, about 90 K lower than in Figure 5.40. The

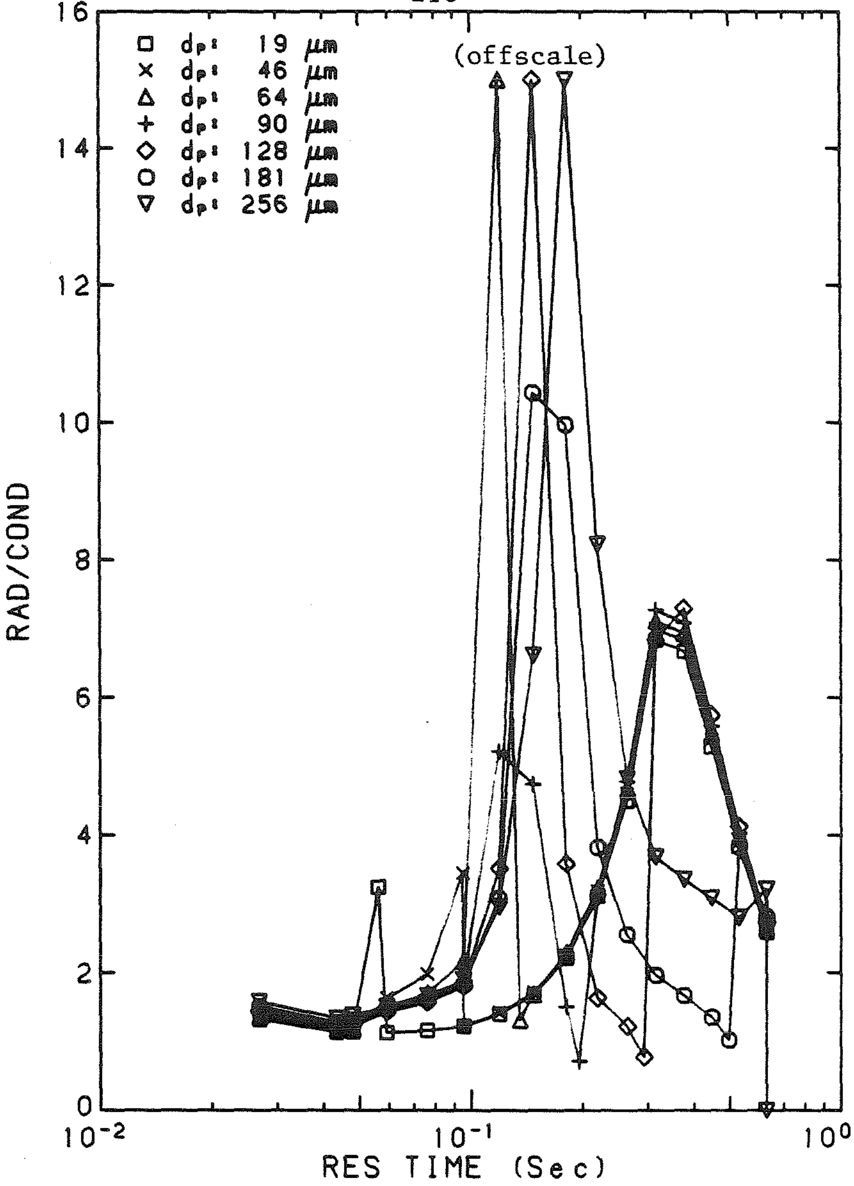

Figure 5.43: Ratio of particle heat loss by radiation to particle heat loss by conduction to the gas vs combustor residence time for run 92380.51.

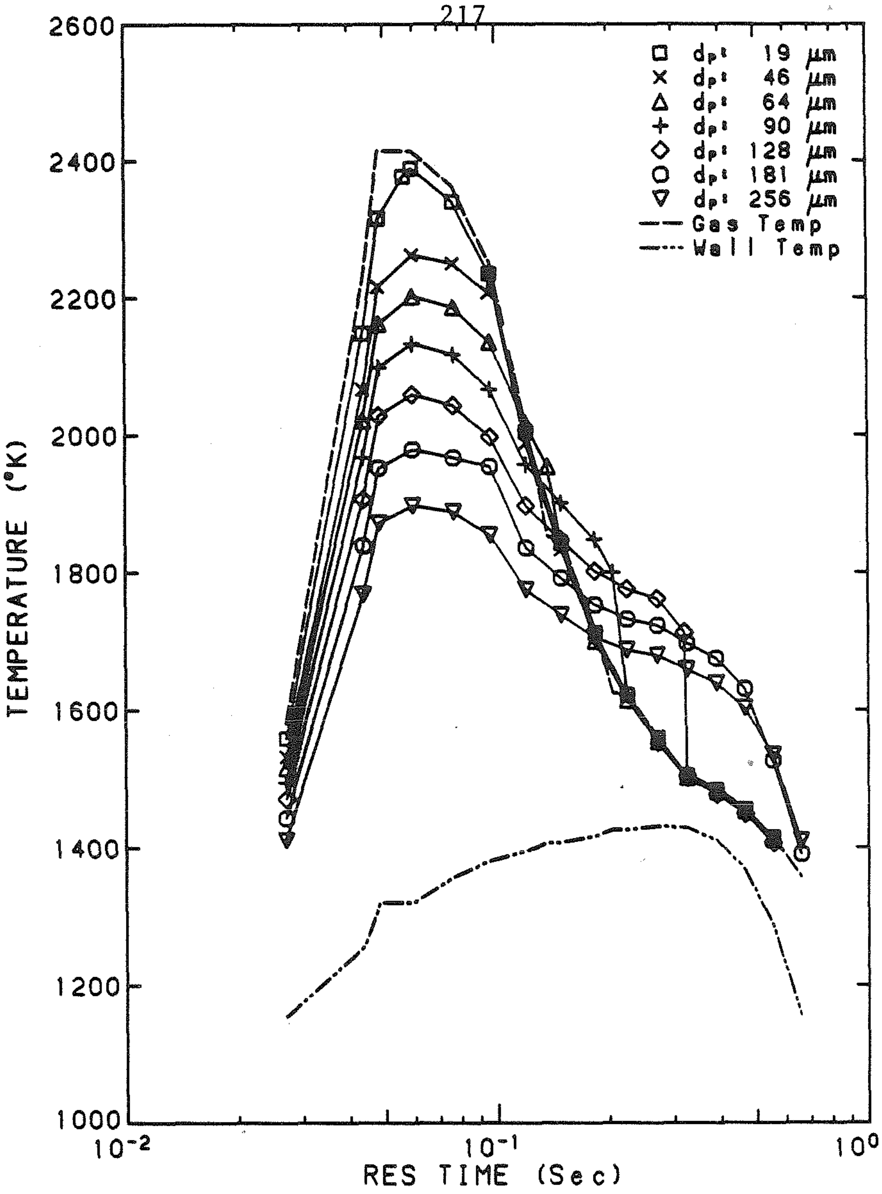

Figure 5.44: Particle temperatures vs combustor residence time from model calculation for run 92380.57. Gas and wall temperatures for corresponding residence times are also indicated. CO oxidation assumed slow.

effect of this lower wall temperature is to decrease the peak particle temperatures by about 15 K, and the exhaust gas and particle temperatures by about 40 K.

The temperature-time profiles for the combustion conditions of run 92380.62 are plotted in Figure 5.45. The effective wall temperature for this condition was 1225 K, and the mean preheat temperature was 464 K, both of which are significantly lower than the corresponding parameters for the conditions represented in Figures 5.40 and 5.41. Both the peak particle temperatures and the gas temperatures are noticeably lower (by about 125 and 170 K, respectively) for this condition than in the previous figures.

In Figure 5.46 are plotted the temperature-time profiles obtained assuming the same combustor conditions as in Figure 5.40. However, the particle combustion model used to obtain the profiles in this figure assumed infinitely-fast kinetics for the homogeneous oxidation of CO, resulting in a CO oxidation flame at or near the particle surface (See Chapter 4). The result of this assumption is higher gas and particle temperatures than for the case of no CO oxidation near the particle (Figure 5.40). The peak particle temperature is about 200 K higher than the peak gas temperature. Previously the peak particle temperature was slightly below that of the gas. Particle temperature differences vary from about 140 K to 350 K, and the difference in the peak gas temperature is of order 100 K. The exhaust gas temperature is the same

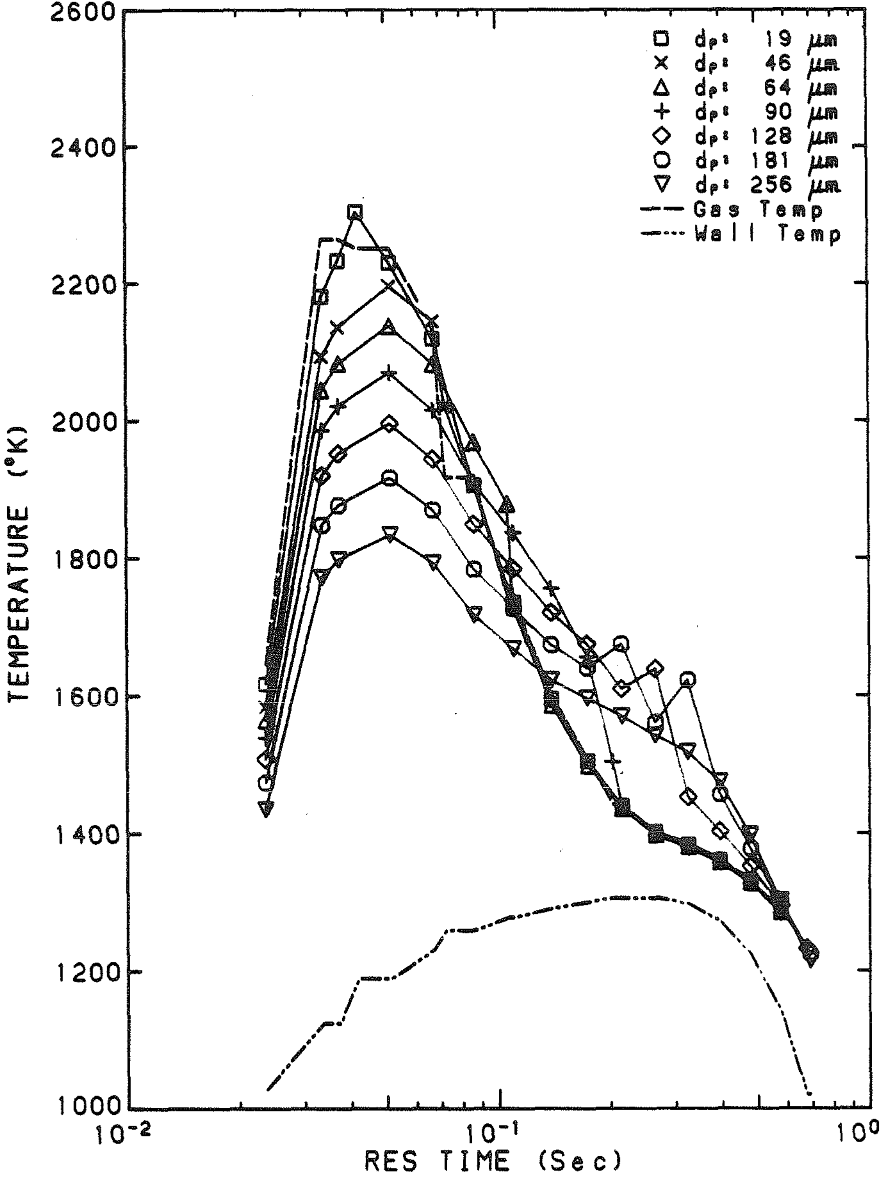

Figure 5.45: Particle temperatures vs combustor residence time from model calculation for run 92380.62. Gas and wall temperatures for corresponding residence times are also indicated. CO osidation assumed slow.

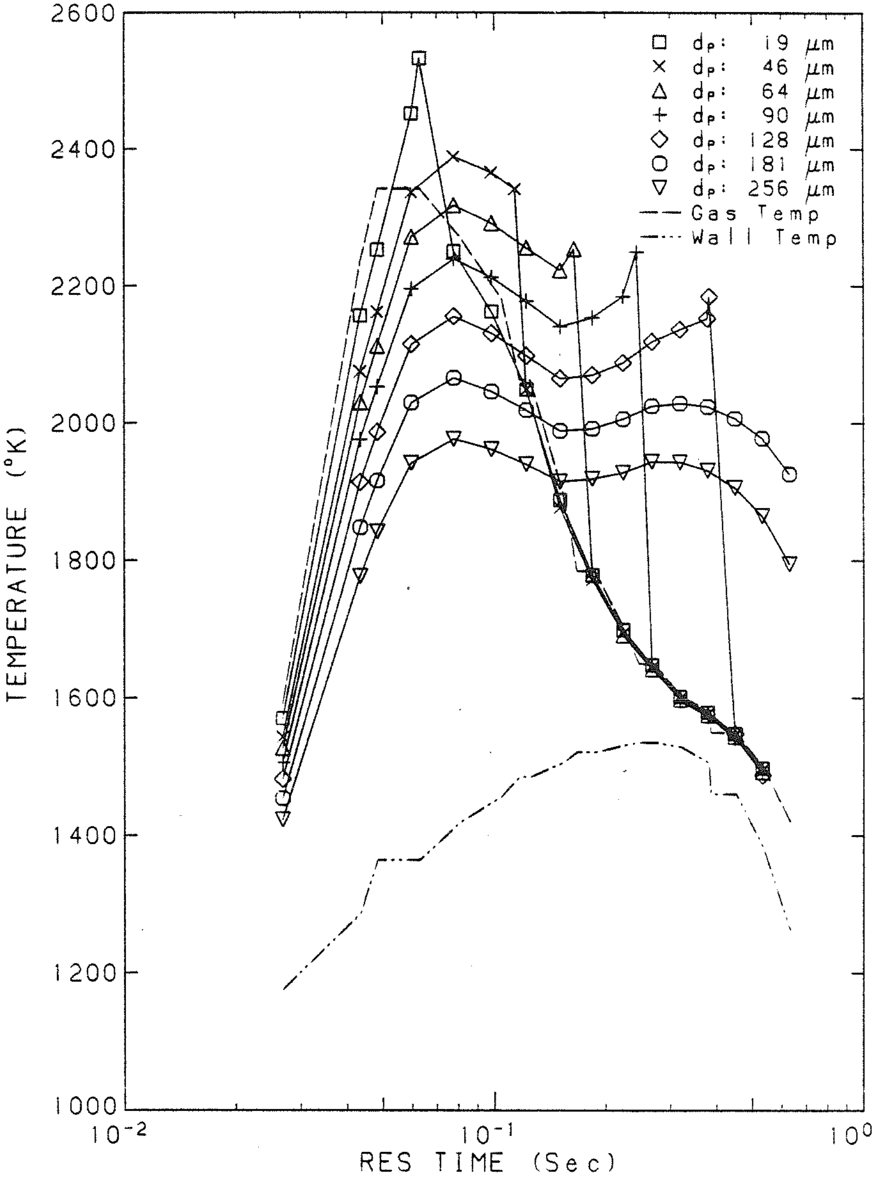

Figure 5.46: Particle temperatures vs combustor residence time from model calculation for run 92380.51. Gas and wall temperatures for corresponding residence times are also indicated. CO oxidation assumed infinitely fast.

in both cases, as expected from energy balance considerations. The particle combustion rates, however, are seen to be not much different from those indicated using the previously-assumed model, since the particle burnout times are apparently comparable in the two figures. The latter observation is consistent with Figure 5.42 which suggests that the combustion rate is primarily diffusion- rather than kinetic-limited.

4.2 RESULTS OF KINETIC PARAMETER ESTIMATION

In treating the ash vaporization during the combustion process, the mineral matter in the parent coal was treated as a single species and ´effective´ values of the Arrhenius kinetic parameters for the ash as a whole were estimated. In Table 5.3 are listed the results of this analysis, together with the data of other investigators.

The table lists the estimated values of the Arrhenius factor (B) and activation energy (E) for the vaporization process, as determined by a least-squares fit of the measured submicron particle mass concentrations to the prediction of the Arrhenius rate expression, using the particle temperature histories calculated using the combustor model (see Chapter 4). Calculations were done for the case of zero order and inverse square dependence of the pre-exponential factor on d_p in the vaporization rate expression (See Eq. 4.41). Results from both calculations are given. Values in the table indicate that the estimated activation energy for total ash vaporization in this work is significantly higher (by a factor of about 2 to 4) than those reported elsewhere. The high activation energy reflects the large range of measured aerosol concentrations and a relatively small range of calculated particle temperatures.

The measured range of aerosol concentrations could reflect a lower activation energy if either of the following were true. The peak

Table 5.3

Reported Values of Arrhenius Kinetic Parameters B, E for Vaporization

where: $\frac{dm}{dt} = -mB\exp(-E/T)$

Species	B (sec^{-1})	E (^{o}K)	Source	Comments
Total Ash	$1.0x10^{8}$	42,800	Present Work	dp^{0} dependence of B
"	$1.3x10^{10}$	50,300	" "	dp^{-2} dependence of B
"	510.	20,370	Neville, et al. (1980)	ASTM ash, externally-heated laminar furnace
"	10,790	20,401	Mims, et al. (1979)	Montana lignite, externally-heated laminar furnace
Ca	62,000	34,800	"	"
Mg	99,700	25,000	"	"
Al	10,400	27,900	"	"
Fe	28,900	24,000	"	"

particle temperatures were lower than those calculated (1700 K rather than 2400 K). Alternatively, the variation in the particle temperatures during the runs was higher than that calculated (200 K rather than 100 K). Combustion particle temperatures as low as 1700 K are not likely. However, a 200 K variation in particle temperature is an upper bound suggested by the 210 K variation in effective wall temperature. This might indicate that the role of heat transfer to the wall was underestimated in the current model. The fact that calculated peak particle temperatures closely follow gas temperature suggests that the model deficiency is due to underestimation of convective and/or radiative exchange between the flame cloud and the wall.

It should be noted that while the estimated activation energies from this work are higher than reported elsewhere, they are not unreasonable in light of high activation energies for vaporization of pure mineral species in the ash considered separately. Enthalpies of vaporization for liquid SiO_2, Al_2O_3 and Fe at 2500 K resulting in formation of gaseous SiO, AlO_2, and Fe are, respectively, 181, 283, and 87 kcal/mole, indicating activation energies for vaporization ($\Delta h_{vap}/R$) of 91,000; 143,000; and 44,000 K. The estimated values of 42,800 and 50,300 K from the present work do not appear unreasonably high considering these values.

The kinetic parameters represented in Table 5.3 are shown by the Arrhenius plot in Figure 5.47. The band indicated for the present work

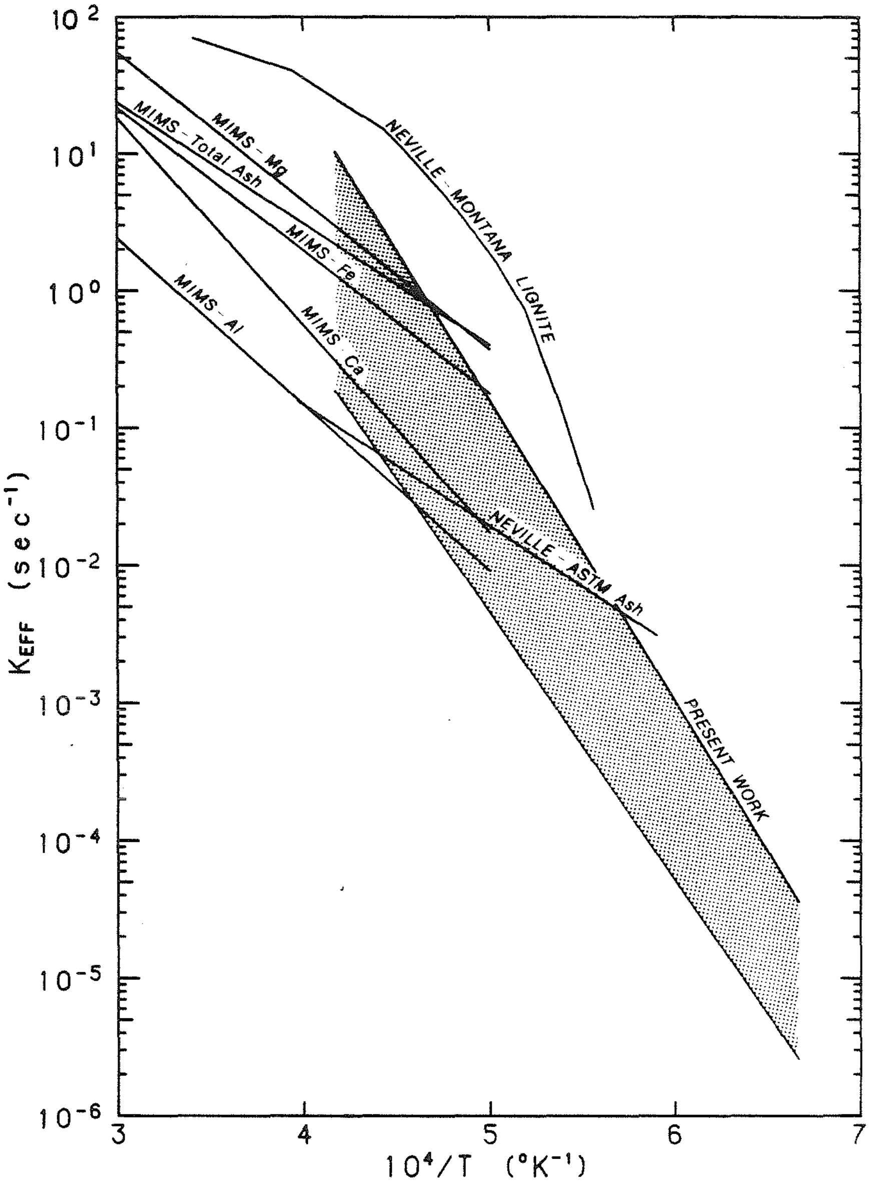

Figure 5.47: Arrhenius plot of effective vaporization rate constant, K_{EFF} vs reciprocal temperature, T. K_{EFF} is defined from the equation $\frac{dm}{dt} = -K_{EFF} m$

$(K_{EFF} \equiv B \exp [-E/T])$

Data of Mims are from Mims, et al. (1979) and of Neville, from Neville, et al. (1980)

was obtained by considering both zeroth and second order dependence on size of the pre-exponential term, and allowing for the possibility of sulfate contribution to submicron aerosol mass (A maximum of 39%, by weight, of sulfur was considered, based on results of elemental analysis of submicron particle mass samples).

To study the effect of the peak particle temperature on the total mass of ash vaporized, the fraction of the total mass vaporized due to particles in each size class was calculated as a function of residence time, using the Arrhenius rate expression (Eq. 4.41) and the calculated particle temperature-time histories. The results of this calculation for the combustor conditions obtained during run 92380.51 are indicated in Figures 5.48 and 5.49.

Comparison of these figures with Figure 5.40 indicates that, as expected, the majority of ash vaporization occurs during the period of high particle temperatures. Figure 5.48 indicates that a d_p^{-2} dependence of the pre-exponential term in the Arrhenius rate expression (Eq. 4.41) results in a substantially higher contribution of the smallest particles to the mass of vaporized ash than in the case of d_p^0 dependence (Figure 5.49). The figures indicate, however, that for either case the contribution of 46-micron particles is much higher than that of other particle sizes. This is due to the high mass fraction of particles in this size range in the parent coal.

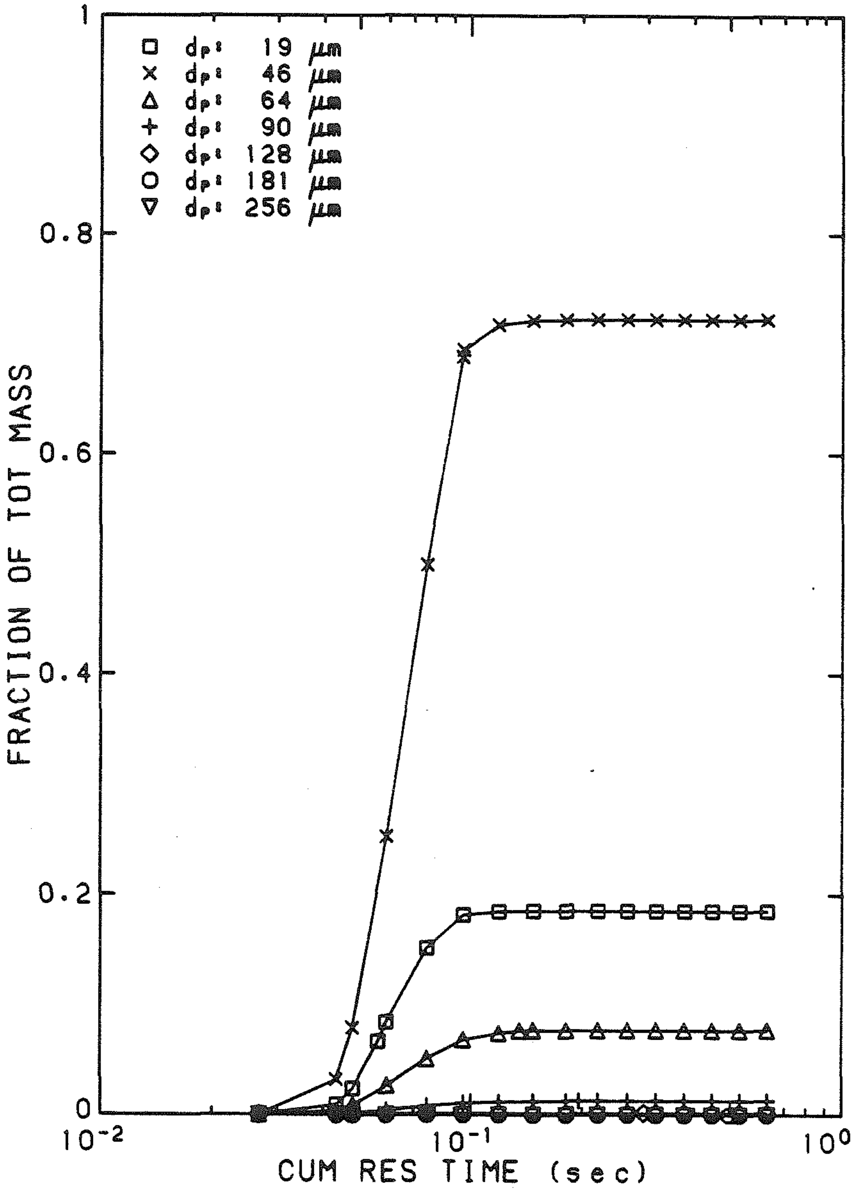

Figure 5.48: Fraction of total ash vaporized due to vaporization from particles in indicated size classes vs combustor residence time for run 92380.51. Vaporization rate assumed to vary as d_p^{-2}.

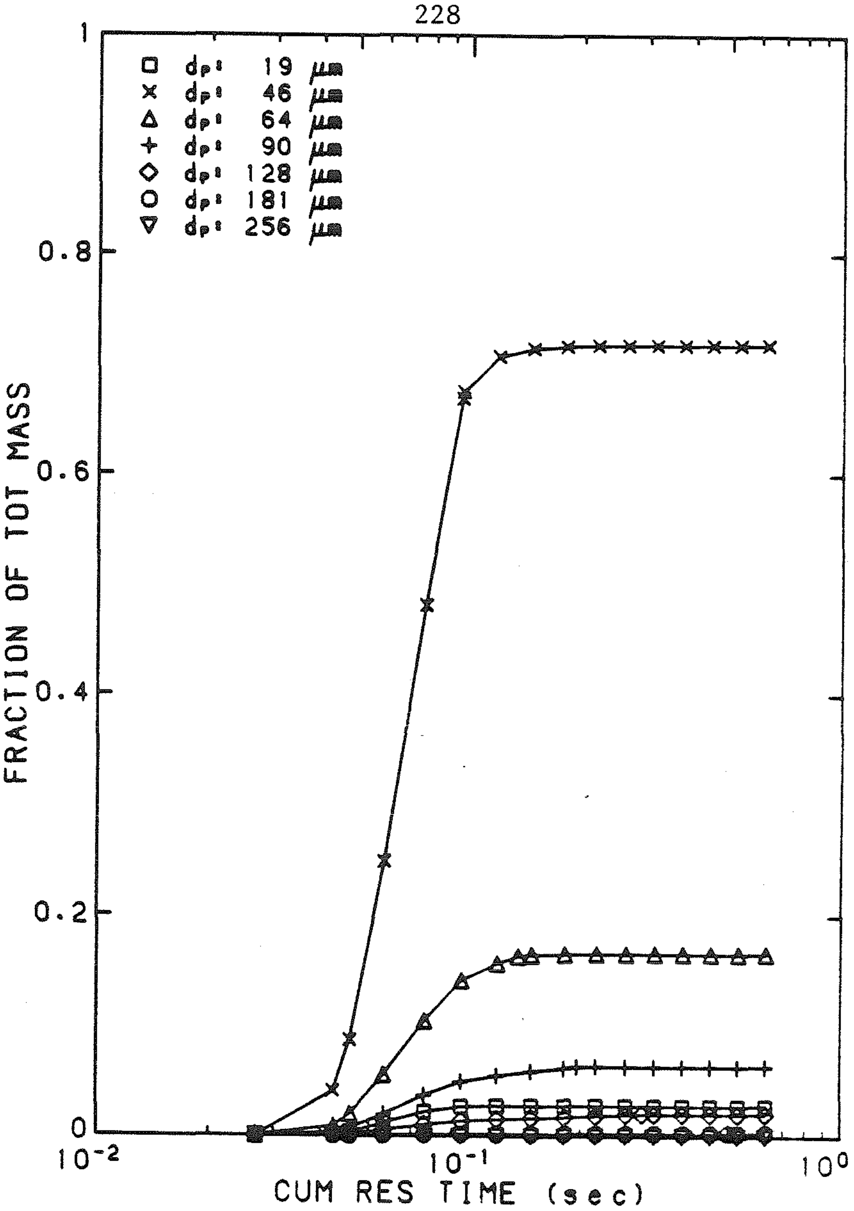

Figure 5.49: Fraction of total ash vaporized due to vaporization from particles in indicated size classes vs combustor residence time for run 92380.51. Vaporization rate assumed to vary as $d_p^{\,0}$.

To compare the mass-specific vaporization rates for different particle sizes the total mass vaporized from particles in each size range was normalized by the total mass of ash due to particles in that range. The results are shown in Table 5.4. Assuming either d_p^{-2} or d_p^{0} dependence of the pre-exponential term in the rate expression leads to the conclusion that the smaller particles contribute most (per unit mass) to the ash vaporization. However, the variation of the mass-specific vaporization with particle size is (predictably) more pronounced for d_p^{-2} dependence. In this case the indicated variation is a factor of about 2500 over the range of particle sizes. For d_p^{0} dependence the corresponding factor is about 34.

Table 5.4

Mass of Ash Vaporized per unit Mass Ash

For Different Particle Sizes

Particle Size (μm)	Mass Fraction in Coal	Fraction of Total Ash Vaporized		Mass Vaporized (d_p) Mass Ash (d_p)	
		$\bar{d}_p^2$ Rate Dep.	d_p^0 Rate Dep.	$\bar{d}_p^2$ Rate Dep.	d_p^0 Rate Dep.
19	.011	.18	.028	4.1×10^{-2}	6.2×10^{-3}
46	.55	.72	.72	3.2×10^{-3}	3.2×10^{-3}
64	.20	.078	.16	9.3×10^{-4}	2.0×10^{-3}
90	.13	.013	.064	2.4×10^{-4}	1.2×10^{-3}
128	.074	.0018	.020	5.9×10^{-5}	6.7×10^{-4}
181	.216	.0001	.0034	1.1×10^{-5}	3.8×10^{-4}
256	.008	.0000	.0006	$<1.5 \times 10^{-5}$	$<1.8 \times 10^{-4}$

4.3 EVALUATION OF THE KINETIC MODEL

To evaluate the quality of the Arrhenius model for vaporization kinetics, the model predictions were compared with the measured values of total submicron mass concentration for various combustion conditions. The results of this comparison are shown graphically in Figures 5.50 and 5.51, where the data from different burners are identified by different symbols. Figure 5.50 represents the comparison for d_p^{-2} dependence of the pre-exponential term in the rate expression (Eq. 4.41) and Figure 5.51 for d_p^{0} dependence. The figures indicate that for the ten data points used to estimate the values of the kinetic parameters, there is reasonably good agreement between model predictions and measurements.

One of the burner 1 data points, however, differs significantly from the predictions. The higher aerosol mass concentration measured for burner 1 may have been due to aerodynamic effects which were neglected in the computer model. The data suggest that the neglect of these effects was not serious in the case of burners 3 and 4, where the primary jet velocity was substantially lower than in the case of burner (See Appendix F).

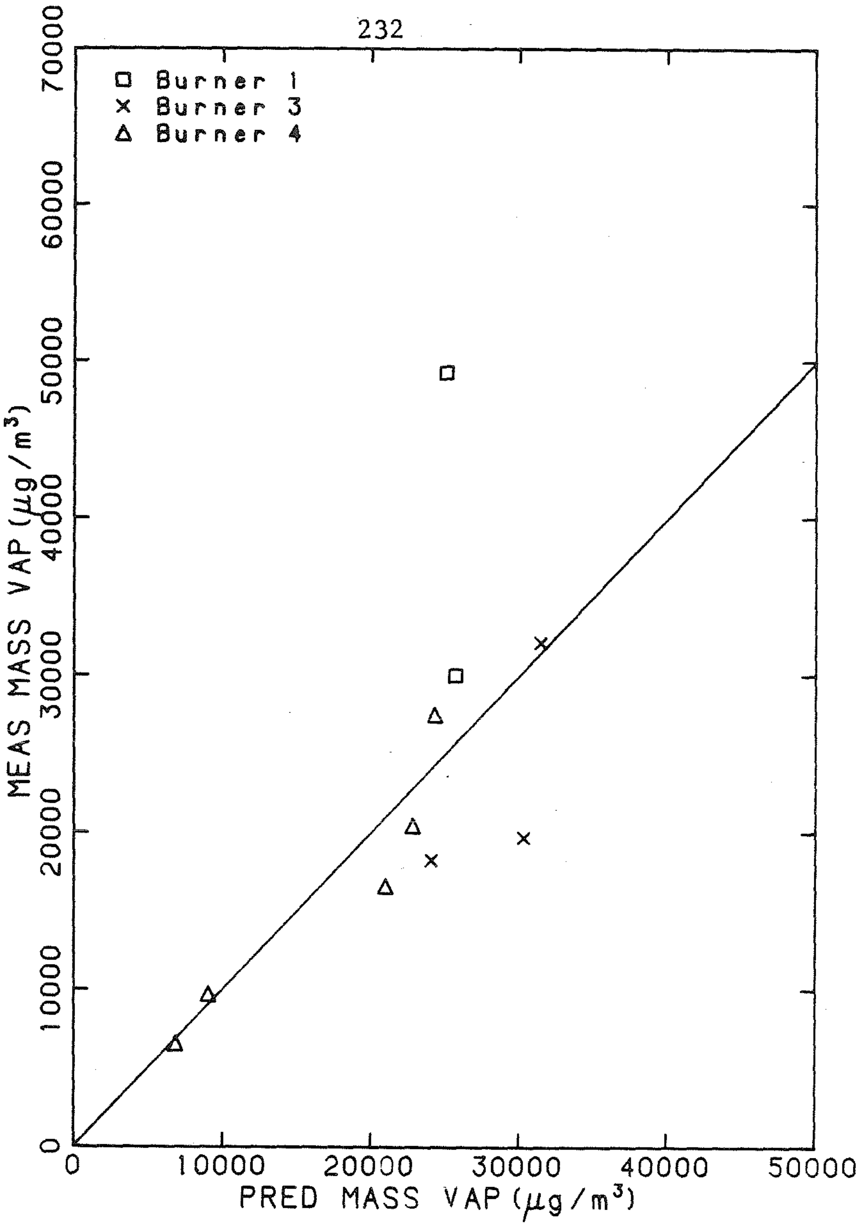

Figure 5.50: Measured submicron particle mass concentration vs mass concentration of vaporized ash calculated from Arrhenius rate expression fitted to the data. Vaporization rate assumed to vary as d_p^{-2}.

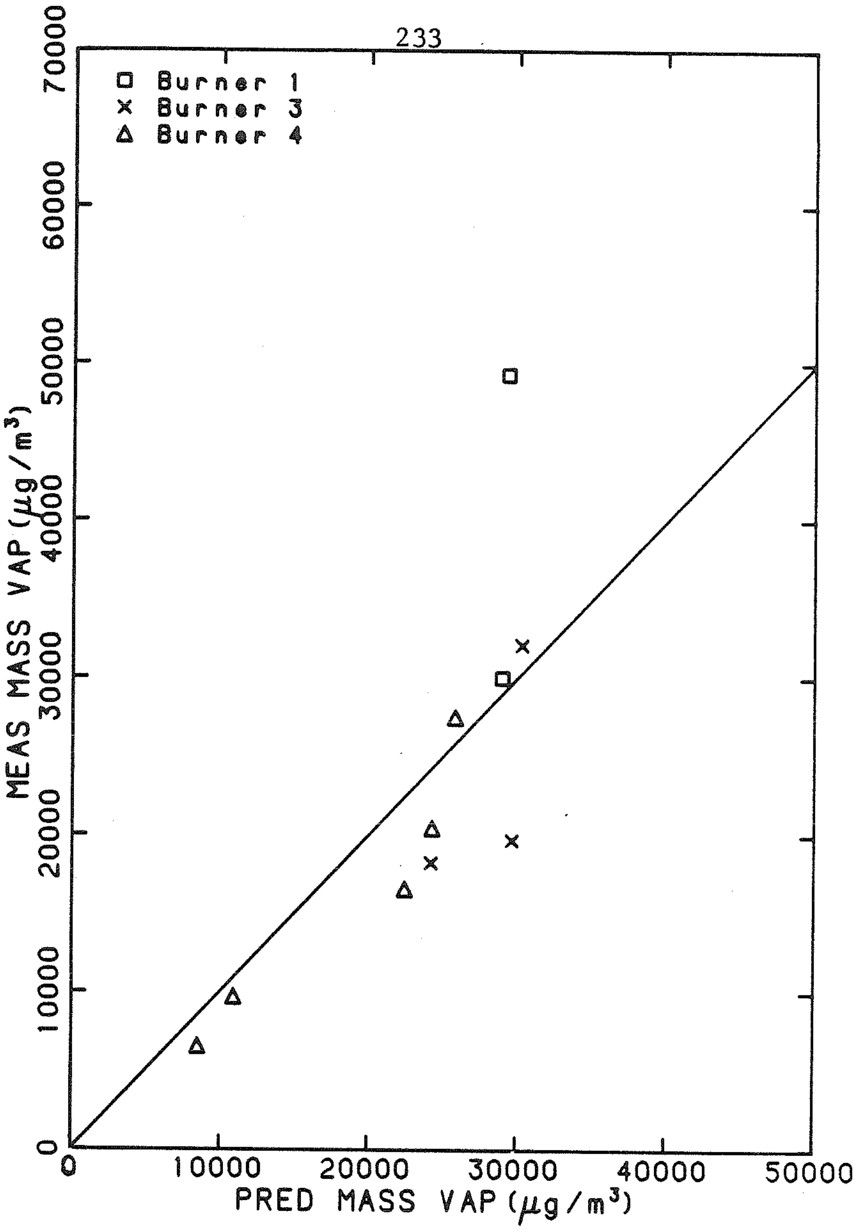

Figure 5.51: Measured submicron particle mass concentration vs mass concentration of vaporized ash calculated from Arrhenius rate expression fitted to the data. Vaporization rate assumed to vary as d_p^0.

CHAPTER 6

SUMMARY, CONCLUSIONS, RECOMMENDATIONS FOR FURTHER WORK

Fine particle emissions from pulverized coal combustion sources pose a potentially-serious environmental hazard. Current plans for increased use of coal underscore a need to understand the mechanism of formation of the particles in order to be able to control their emission. This work has had as its objective the enhancement of this understanding.

A laboratory furnace was designed and constructed to burn pulverized coal under conditions simulating those in a full-scale boiler. In scaling considerations for design purposes, the principal mode of mass transfer to burning coal particle surfaces was assumed to be molecular diffusion. Particle Reynolds numbers in both laboratory and full-size units are sufficiently small to assume that mass transfer is not significantly influenced by microscale turbulence. Characteristic combustion times were thus assumed to be determined principally by particle temperatures and bulk gas compositions in the flame. This assumption made it possible to simulate particle combustion processes in a large furnace by controlling wall temperature and overall combustion stoichiometry. Due to higher combustor surface area to volume ratio in the laboratory furnace significantly higher wall temperatures were required than in larger units.

The laboratory facility consisted of a cylindrical down-fired combustor coupled to a shell-and-tube cooling section to simulate the cooling history of combustion products in a full-scale boiler. The total residence time of particles in the hot section of the combustor was of the order of a second. The combustor wall temperature ranged from about 1000 to 1500 K. A low-sulfur Utah sub-bituminous coal was used in all experiments. Firing rates were from 1.2 to 3.2 kg/hr, corresponding to heating rates of about 9,700 to 26,000 watts. Flame geometry was controlled by varying the burner swirl and velocity of the primary fuel-air jet. Results were obtained for four different burner types.

Measurements were made of wall temperature profiles, secondary combustion air preheat temperatures, air mass flow rates and exhaust gas concentrations of CO, CO_2, NO, and O_2. These measurements were then used to calculate the following six parameters assumed to characterize the combustion condition: (1)Effective weighted mean wall temperature for radiation (weighting factor T^4), (2)Mass-mean preheat temperature, (3)Mean (plug flow) combustor residence time, (4)Fuel-air equivalence ratio, (5)Dimensionless swirl of burner air flows, (6)Velocity difference between primary and secondary burner air flows.

Fine particle emissions from the furnace were characterized by measuring mass and composition distributions with respect to size. Sampling of combustion exhaust was performed just downstream of the cooling section and coagulation was stopped in the probe by rapid dilution cooling. Dilution ratio was measured by comparison of NO concentration in diluted and undiluted exhaust gas. Size distributions were measured with an electrical aerosol analyzer (EAA) and aerosol composition distributions were obtained from mass samples which were size classified using the Caltech low-pressure impactor (LPI). Elemental composition was determined by alpha particle induced X-ray emission (PIXE) techniques.

The total submicron fly-ash particle mass concentration was found to increase by about 420% for effective wall temperature increases of about 15% for a given burner type. This suggests that submicron particle formation is influenced by a high activation energy for vaporization of mineral species in coal.

The volume of submicron particles was, for all experiments, well-correlated with NO concentrations and independent of burner type, suggesting that NO concentration is a better indication of peak particle temperature than wall temperature alone. The laboratory data correlation of fine particle mass concentration with NO is consistent with a similar correlation reported by Ensor (1980) for field data. However, for comparable NO levels laboratory-measured particle concentrations were substantially lower (about half) those observed by Ensor in one coal-fired utility boiler. This difference may be due to wall temperatures in the laboratory system which were lower than those required to achieve comparable particle temperatures. It may also reflect differences in the coal types used in the laboratory and field units.

Data from elemental analysis of size-classified mass samples indicate a peak in the mass distribution around 0.04 microns, consistent with EAA measurements and observations from field data. The composition data further indicate that particle composition varies significantly from particle sizes of 0.03 to 2.0 microns. Highly refractory species such as alumina are major components in larger particles (and the bulk ash) but are minor components of the smallest particles in most experiments. The fine particle composition is also influenced by combustion conditions. Silica is present in significant quantities in experiments where high particle temperatures are obtained but not at lower temperatures.

The fine particles were found to contain significant quantities of sulfates. These species are thought to have condensed late in the cooling process due to their relatively high volatility. Iron was also found to be a major species in fine particles of some experiments.

The calcium, iron, and silica data show fairly consistent trends which are supportive of a vaporization-condensation mechanism for fine particle formation. Iron and calcium mass fractions increase with decreasing particle size in the size range where enrichment of vaporized species may occur due to surface condensation. Silica mass fraction decreases for these particle sizes, possibly because of increasing particle burning temperatures and vaporization rates resulting in depletion of silica. Iron is found to be a major species in fine particles when silica does not vaporize in significant quantities. When silica does vaporize its large contribution to very fine particle mass dilutes the concentrations of other vaporizing species such as iron.

Multiple linear regression analysis was used to explore the sources of variation in submicron particle volume concentration. Linear regressions of data from all burners resulted in a multiple correlation coefficient of $R^2=0.82$. Variation in burner shear rate and effective wall temperature were found to contribute most to the explained variance of the particle volume concentration. Higher correlation coefficients were obtained for regression analyses of data for different burner types considered separately. These observations suggest that burner aerodynamic processes exercise the strongest influence on submicron particle formation of any of the processes considered. Wall temperature is the second strongest influence.

A model of the combustion process in the laboratory furnace was developed to study the effects of macroscopic parameters on the combustion of char particles. Coal was assumed to devolatilize instantly on entry into the hot zone and chemical equilibrium was established between volatile combustible matter and the oxygen in the air entrained by the flame. After the volatile hydrocarbons were completely burned the residual char was oxidized. Oxidation of CO was assumed to occur in the far field of the char particles. Char oxidation rates and particle temperatures were computed as functions of combustor residence time and particle burning rates were found to be diffusion limited, though the importance of the diffusion limitation varied strongly with particle temperature. Particle burning temperature increased with decreasing particle size and was strongly influenced by gas temperature and free-stream oxygen concentration in the flame. Particle temperature was also increased if the rate of CO oxidation was assumed infinitely fast. Given the assumptions of the model, radiation was found to be the principal mode of heat transfer away from particles.

Submicron particles were assumed to be composed entirely of vaporized mineral species from the coal. Using this assumption together with calculated particle temperature histories an Arrhenius vaporization rate expression was fitted to measured mass concentrations of submicron ash particles. Calculations were done for the two limiting cases of vaporization rate dependence on particle size predicted by kinetic and external mass transfer limitations. The apparent activation energy for ash vaporization was between 42,000 and 53,000 K. The predicted vaporization rates were comparable with those determined by other investigators although activation energy was considerably higher for the present work.

Due to higher peak temperatures, mass-specific rates of ash vaporization were found to rise sharply with decreasing particle size for both limiting cases of particle size dependence of vaporization rate. The magnitude of the increase depends strongly on the assumed size dependence of the vaporization rate.

The work presented herein raises several questions and suggests specific recommendations for further work. The suggested influence of burner aerodynamics merits further investigation in order to confirm the indicated effect of burner shear rate and to explore in more depth other aspects ot flame aerodynamics such as swirl and induced recirculation.

Past studies of cold turbulent jets (See chapter 4) indicate that dimensionless far-field mass entrainment is independent of jet Reynolds number. These results were the basis for neglecting Reynolds number scaling in the current experiments. It would, however, be enlightening to investigate possible Reynolds number effects on entrainment and mixing in the reacting jet of a pulverized coal burner.

This work would clearly require more control and more complete combustion characterization than was obtained in these experiments. Among the recommended changes would be the following: (1)Direct control and measurement of mass flow rate of pulverized fuel, by gravimetric or other means, (2)Control of wall temperature by external controlled heating, (3)Better control and measurement of fluid temperatures at the burner outlet, (4)Easy access to the interior of the combustor to allow frequent removal of accumulated deposits and inspection for changes in wall surfaces, (5)Better estimates of particle mass losses by deposition on cooling section surfaces prior to sampling, (6)Resolution of discrepancies in particle mass concentrations indicated by EAA and PIXE measurements in these experiments, requiring a broader spectrum elemental analysis of mass samples than in the present work, (7)Measurement of the contribution of soot to fine particle mass concentrations.

Beyond the scope of the present experiments it would also be instructive to measure particle temperatures directly, by optical pyrometry or other means, to aid in resolving the question of where the majority of the CO oxidation occurs. The influence of coal type on the vaporization of specific individual species should also be investigated and those chemical species identified which most strongly influence the vaporization chemistry during combustion. The author sees merit in an empirical investigation of this kind both from the standpoint of the practical value of the data so generated, and also from the standpoint of shedding further light on the fundamental chemical processes responsible for the observed coal type dependence of ash vaporization.

REFERENCES

Bell, K. A. (1974). Aerosol Deposition in Models of a Human Lung Bifurcation. Ph.D. thesis, Department of Chemical Engineering, California Institute of Technology, Pasadena, California.

Biermann, A. H.; Ondov, J. M. (1980). Application of Surface-Deposition Models to Size-Fractionated Coal Fly Ash. Atmospheric Environment, 14: 289-295.

Bird, R. B.; Stewart, W. E.; Lightfoot, E. N. (1960) Transport Phenomena. John Wiley and Sons, New York.

Booth, F. (1949). On the Radiation from Transient Light Sources. Proceedings of the Physics Society of London, 62A: 95-113

Breen, B. P. (1976). Combustion in Large Boilers: Design and Operating Effects on Efficiency and Emissions. Sixteenth Symposium (International) on Combustion. The Combustion Institute, Pennsylvania.

Cahill, T. A. (1975). "Environmental Analysis of Environmental Samples," in New Uses of Ion Accelerators, J. Ziegler, Ed., 1-75, Plenum Press, New York.

Caram, H. S.; Amundson, N. R. (1977). Diffusion and Reaction in a Stagnant Boundary Layer about a Carbon Particle. Industrial and Engineering Chemistry Fundamentals, 16(2): 171.

Carberry, J. J. (1976). Chemical and Catalytic Reaction Engineering. McGraw-Hill, New York.

Coles, D. G.; Ragaini, R. E.; Ondov, J. M. Fisher, G. L.; Silberman, D.; Prentice, B. A. (1979). Chemical Studies of Stack Fly Ash from a Coal-Fired Power Plant. Environmental Science and Technology, 13: 455-459.

Davison, R. L.; Natusch, D. F. S.; Wallace, J. R. (1974). Trace Elements in Fly Ash. Environmental Science and Technology, 8: 1107-1113.

Desrosiers, R. E. (1977). DOE Interim Report FE 2205-5, March, 1977. Also, DOE Quarterly Report FE 2205-11, June, 1978.

Desrosiers, R. E.; Riehl, J. W.; Ulrich, G. D.; Chiu, A. D. (1978) Submicron Fly Ash Formation in Coal-Fired Boilers. Seventeenth Symposium (International) on Combustion, The Combustion Institute, Pennsylvania.

Dobner, S. (1976). Modelling of Entrained Bed Gasification: The Issues. Electric Power Research Institute Memo.

Draper, N. R.; Smith, H. (1966). Applied Regression Analysis. John Wiley and Sons, New York.

Dutta, S.; Wen, C. Y.; Belt, R. J. (1975). Reactivity of Coal and Char in CO_2 Atmosphere. American Chemical Society, Division of Fuel Chemistry, Preprints, 20(3): 103-114.

Eckert, E. R. G.; Drake, R. M., Jr. (1972). Analysis of Heat and Mass Transfer. McGraw-Hill, New York.

Ensor, D. S. (1980). Aerosol Emissions Due to the Combustion of Coal. Presented at the Symposium on Plumes and Visibility: Measurements and Model Components, Grand Canyon, Arizona, Novermber 10-14, 1980.

Field, M. A.; Gill, D. W.: Morgan, B. B.; Hawksley, P. G. W. (1967). Combustion of Pulverized Coal. The British Coal Utilization Research Association (B.C.U.R.A.), Leatherhead.

Fisher, G. L.; Chang, D. P. Y.; Brummer, M. (1976). Fly Ash Collected from Electrostatic Precipitators: Microcystalline Structures and the Mystery of the Spheres. Science, 192: 553-555.

Flagan, R. C., and Friedlander, S. K. (1976). Particle Formation in Pulverized Coal Combustion - A Review. Presented at the Symposium on Aerosol Science and Technology at the Eighty-Second National Meeting of the American Institute of Chemical Engineers, Atlantic City, New Jersey, August 29 - September 1, 1976.

Flagan, R. C. (1978). Submicron Particles From Coal Combustion. Seventeenth Symposium (International) on Combustion. The Combustion Institute, Pennsylvania.

Flagan, R. C.; Taylor, D. D. (1980). Laboratory Studies of Submicron Particles From Coal Combustion. Presented at the Eighteenth Symposium (International) on Combustion, University of Waterloo, Ontario, Canada, August, 1980.

Friedlander, S. K. (1977). Smoke, Dust and Haze: Fundamentals of Aerosol Behavior. Wiley-Interscience, New York.

Hering, S.V.; Flagan, R.C.; Friedlander, S.K. (1978). Design and Evaluation of New Low-Pressure Impactor. I. Environmental Science and Technology, 12: 667-673.

Hidy, G. M.; Brock, J. R. (1965). Some Remarks about the Coagulation of Aerosol Particles by Brownian Motion. Journal of Colloid Science, 20: 477-491.

Howard, J. B.; Williams, G. C.; Fine, D. H. (1973). Kinetics of Carbon Monoxide Oxidation in Postflame Gases. Fourteenth Symposium (International) on Combustion. The Combustion Institute, Pennsylvania.

Im, K. H., and Chung, D. M. (1980). Nucleation and Evolution of Slag Droplets in Coal Combustion. AIChE Journal, 26(4): 655.

John, W., and Reischl, G. (1980). A Cyclone for Size Selective Sampling of Ambient Air. Journal of the Air Pollution Control Association, 30: 872-876.

Kreith, F. (1965). Principles of Heat Transfer, (second edition). International Textbook, Pennsylvania.

Lai, F. S.; Friedlander, S. K.; Pich, J.; Hidy, G. M. (1972). The Self-Preserving Particle Size Distribution for Brownian Coagulation in the Free-Molecule Regime. Journal of Colloid and Interface Science, 39: 395.

Leary, W. A.; Tsai, D. H. (1951). Metering of Gases by Means of the A.S.M.E. Square-Edged and Orifice with Flange Taps. Publication No. 74.1 WAL DHT 7-51, Sloan Laboratory For Automotive and Aircraft Engines, Massachusetts Institute of Technology.

Libby, P. A., and Blake, T. R. (1979). Theoretical Study of Burning Carbon Particles. Combustion and Flame, 36: 139.

Lilley, D.G.; Wendt, J. O. L. (1977). Modeling Pollutant Formation in Coal Combustion. Proceedings of the Heat Transfer and Fluid Mechanics Institute, 25th, University of California at Davis, June, 1976, Stanford University Press.

Littlejohn, R. F. (1966). Mineral Matter and Ash Distribution in "As Fired" Samples of Pulverized Fuels. Journal of the Institute of Fuel, 39: 59-67.

Liu, B. Y. H.; Lee, K. W. (1976). Efficiency of Membrane and Nuclepore Filters for Submicrometer Aerosols. Environmental Science and Technology, 10: 345-350.

Liu, B. Y. H.; Pui, D. Y. H.; Kapadia, A. (1976). Electrical Aerosol Analyzer: History, Principle, and Data Reduction. Presented at Aerosol Measurement Workshop, University of Florida, Gainesville, Florida, March 1976. (Part. Tech. Lab. Pub. No. 303.)

May, K. R. (1967). "Physical Aspects of Sampling Airborne Microbes," in Airborne Microbes, Gregory, P. H.; Monteith, J. L., eds, Cambridge Univ. Press, Cambridge.

McAdams, W. H. (1954). Heat Transmission, 3d edition, McGraw-Hill, New York.

McCain, J. D.; Gooch, J. P.; Smith, W. B. (1975). Results of Field Measurements of Industrial Particulate Sources and Electrostatic Precipitator Performance. Journal of the Air Pollution Control Association, 25: 117-21.

Mims, C. A.; Neville, M; Quann, R. J., and Sarofim, A. F. (1979). Laboratory Studies of Trace Element Transformations During Coal Combustion. Presented at the National 87th AIChE Meeting, Boston, Mass., August 19-22, 1979.

Mitchell, R. J.; Gluskoter, H. J. (1976). Mineralogy of Ash of some American Coals: Variations With Temperature and Source. Fuel (London), 55: 90-96.

Mon, E., and Amundson, N. R. (1978). Diffusion and Reaction in a Stagnant Boundary Layer about a Carbon Particle. 2. An Extension. Industrial and Engineering Chemistry Fundamentals, 17(4): 313.

Mulcahy, M. F. R.; Smith, I. W. (1969). Kinetics of Combustion of Pulverized Fuel: A Review of Theory and Experiment. Review of Pure and Applied Chemistry, 19: 81.

Natusch, D. F. S.; Taylor, D. R. (1980). Environmental Effects of Western Coal Utilization: Part IV: Chemical and Physical Characteristics of Coal Fly Ash. EPA Report No. EPA-600/3-80-094.

Neville, M.; Quann, R. J.; Haynes, B. S.; Sarofim, A. F. (1980). Vaporization and Condensation of Mineral Matter during Pulverized Coal Combustion. Presented at the Eighteenth Symposium (International) on Combustion, Waterloo, Canada, August, 1980.

O'Gorman, J. V.; Walker, P. L., Jr. (1971). Mineral Matter Characteristics of Some American Coals. Fuel (London), 50: 135-151.

Ouimette, J. R. (1981). Chemical Species Contributions to the Extinction Coefficient. Ph.D. Thesis, Department of Environmental Engineering Science, California Institute of Technology, Pasadena, California.

Padia, A. S. (1976). The Behavior of Ash in Pulverized Coal Under Simulated Combustion Conditions. D.Sc. Thesis, Department of Chemical Engineering, Massachusetts Institute of Technology, Cambridge, Massachusetts.

Pershing, D. W., and Wendt, J. O. L. (1976). Pollutant Control through Staged Combustion of Pulverized Coal. DOE Interim Report FE-1817-2, July, 1976.

Pershing, D. W., and Wendt, J. O. L. (1977). Pollutant Control Through Staged Combustion of Pulverized Coal. Doe Interim Report FE-1817-3, January, 1977.

Raask, E., and Wilkins, D. M. (1965). Volatilization of Silica in Gasification and Combustion Processes. Journal of the Institute of Fuel, 38 (293): 255.

Raask, E. (1968). Cenospheres in Pulverized-Fuel Ash. Journal of the Institute of Fuel, 41:339-344.

Raask, E. (1969). Fusion of Silicate Particles in Coal Flames. Fuel, 48: 366-374.

Ragaini, R. C., and Ondov., J. M. (1975). Trace Contaminants from Coal-Fired Power Plants. Presented at the International Conference on Environmental Sensing and Assessment, Las Vegas, September 1975.

Ramsden, A. R., and Smith, I. W. (1968). "Further Evidence for Internal Burning in Particles of Pulverized Coal," letter to the editor. Fuel (London), 47: 253-256.

Ramsden, A. R. (1969). A Microscopic Investigation into the Formation of Fly Ash during the Combustion of a Pulverized Bituminous Coal. Fuel (London), 48: 121-137.

Reid, W. T. (1971). External Corrosion and Deposits-Boilers and Gas Turbines. American Elsevier,New York.

Ricou, F. P., and Spalding, D. B. (1961). Measurements of Entrainment by Axisymmetrical Turbulent Jets. Journal of Fluid Mechanics, 11: 21-32.

Roberts, P. T., and Friedlander, S. K. (1976). Analysis of Sulfur in Deposited Aerosol Particles by Vaporization and Flame Photometric Detection. Atmospheric Environment, 10: 403.

Ruck, R. R.; Gluskoter, H. J.; Shimp, N. F. (1974). Occurrence and Distribution of Potentially Volatile Trace Elements in Coal. EPA Report No. EPA-650/2-74-054.

Schlicting, H. (1968). Boundary Layer Theory, 6th edition, McGraw-Hill, New York.

Smith, R. D.; Nielson, K. K.; Campbell, J. A. (1979). Concentration Dependence upon Particle Size of Volatilized Elements in Fly Ash. Environmental Science and Technology, 13: 553-558.

Stull, D. R., and Prophet, H. (1971). JANAF Thermochemical Tables, 2nd edition, U. S. Government Printing Office, Washington, D.C.

Taylor, D. D., and Flagan, R. C. (1980). Laboratory Studies of Submicron Particles from Pulverized Coal Combustion. Presented at the Western States Section Meeting of the Combustion Institute, Irvine, California, April 1980.

Twomey, S. (1975). Comparison of Constrained Linear Inversion and Interactive Non-Linear Algorithm Applied to the Indirect Estimation of Particle Size Distributions. Journal of Computational Physics, 18: 188.

Ulrich, G. D. (1971). Theory of Particle Formation and Growth in Oxide Synthesis Flames. Combustion Science and Technology, 4: 47.

Ulrich, G. D.; Milnes, B. A.; Subramanian, N. S. (1976). Particle Growth in Flames. II: Experimental Results for Silica Particles. Combustion Science and Technology, 14: 243.

Ulrich, G. D.; Riehl, J. W.; French, B. R.; Desrosiers, R. (1977). Mechanism of Sub-Micron Fly Ash Formation in a Cyclone, Coal Fired Boiler. Presented at the ASME International Symposium on Corrosion and Deposits from Combustion Gases, Henniker, New Hampshire, June 28, 1977.

Ulrich, G. D., and Subramanian, N. S. (1977). Particle Growth in Flames. III. Coalescence as a Rate-Controlling Process. Combustion Science and Technology, 17: 119.

Wendt, J. O. L., and Pershing, D. W. (1977). Physical Mechanisms Governing the Oxidation of Volatile Fuel Nitrogen in Pulverized Coal Flames. Combustion Science and Technology, 16:111-121.

Whitby, K. T., and Cantrell, B. K. (1979). Electrical Aerosol Analyzer Constants, in Aerosol Measurement, D. A. Lundgren, S. S. Harris, Jr., W. H. Marlow, M. Lippman, W. E. Clark, M. D. Durham, Eds., University Presses of Florida, Gainesville, Florida.

Winterfield, G. (1965). On Turbulent Exchange Processes behind Flame Holders. Tenth Symposium (International) on Combustion. The Combustion Institute, Pennsylvania.

Zebel, G. (1978). "Some Problems in Aerosol Sampling," in Recent Developments in Aerosol Science, D. T. Shaw, editor, John Wiley and Sons, New York.

APPENDIX A

ERROR ANALYSIS OF SIZE DISTRIBUTION DATA

1.0 EXPERIMENTAL PROCEDURE IN DETERMINING SIZE DISTRIBUTIONS

Figure A.1 is a schematic representation of the system used to obtain size distributions of the submicrons particles. The procedure used to obtain the data was as follows:

1. After establishing the desired combustion conditions the concentration of NO in the exhaust gas was measured using the chemiluminescent NO analyzer (Teco) coupled to a chart recorder. The stream was monitored for a period of five to fifteen minutes in order to obtain a chart record representative of the fluctuations in the NO level for the given combustion condition.

2. The aerosol sampling probe was activated by turning on the aerosol dilution air to the probe, and at the same time applying vacuum to the cyclones to draw off the excess diluted aerosol sample stream.

3. Part of the flow from the cyclones was drawn into the EAA to obtain size distribution data. Each channel of the instrument was allowed to stabilize and then four or five sequential

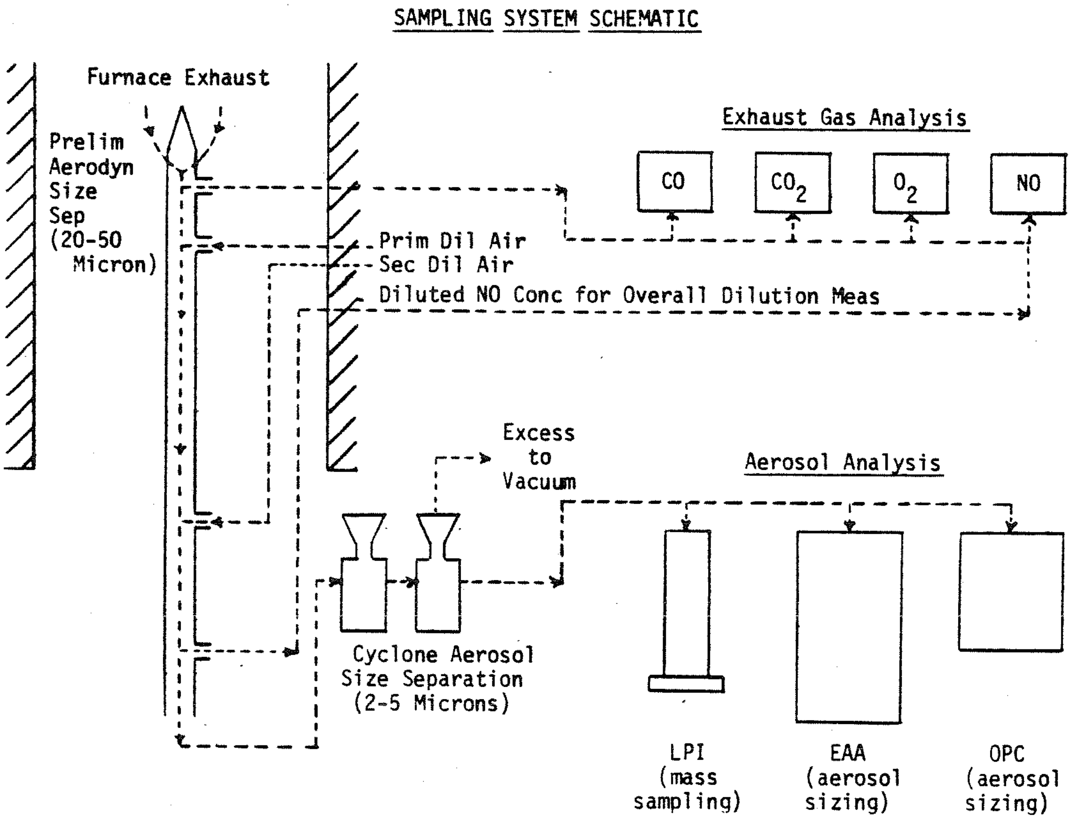

Figure A.1: Schematic of sampling system and sample flow pattern used in present experiments.

readings over approximately 10-15 seconds were manually recorded. This procedure was followed for each of ten channels of the instrument (channels 2-11).

4. Concurrently with the EAA measurements, a portion of the aerosol stream was drawn through the Teco. The chart recorder was operative during the entire EAA sampling period of 3-5 minutes and the resulting record indicated the temporal variation of the NO concentration in the aerosol stream after dilution.

As discussed in Chapter 5 the size distribution of the sampled aerosol was approximated by a histogram obtained from the EAA channel currents. The histogram was calculated from the formula:

$$N'(d_1,d_2) = C_i \times \Delta I_i \qquad (A.1)$$

where:

$N'(d_1,d_2)$ = Number concentration of particles in size range (d_1,d_2) for diluted aerosol

$\Delta I_i = I_i - I_{i+1}$

I_i = EAA current (measured) in channel i

C_i = Constant to convert EAA current difference between channels i and (i+1) to number concentration for particle size corresponding to those channels.

The size distribution of the undiluted exhaust aerosol, normalized to standard conditions described in Chapter 5, was obtained as follows:

$$N(d_1,d_2) = N'(d_1,d_2) \times F \times D \qquad (A.2)$$

where:

F = Normalizing factor to correct to standard conditiions

D = Dilution ratio

= NO conc(exhaust gas)/NO conc(sample stream).

2.0 OVERVIEW OF SIZE DISTRIBUTION MEASUREMENT ERROR

There were a number of uncertainties in the measured parameters used to determine the factors in the above equation for $N(d_1,d_2)$. These uncertainties resulted from variations and measurement errors which were grouped as follows:

1. Variations in the combustion conditions (due to variations in coal feed rate, flame instabilities, etc.);

2. Variations in the dilution ratio, due to flow instabilities in the sampling probe;

3. EAA and NO instrument errors.

All uncertainty in $N(d_1,d_2)$ was attributed to uncertainties in ΔI_i and D due to the factors above. $N(d_1,d_2)$, ΔI_i, and D were treated as random variables, and ΔI_i and D were assumed independent. Ninety percent confidence intervals for $N(d_1,d_2)$ were estimated by multiplying the 95% confidence limits of ΔI_i by the corresponding limits of D, and then scaling these limits by the factor C x F.

3.0 NINETY-FIVE PERCENT CONFIDENCE LIMITS ON ΔI_i

Ninety-five percent confidence limits on ΔI_i were computed as follows:

1. Each channel current I_i was assumed to be normally distributed.

2. Variations in different channel currents were assumed independent.

3. Variances of the channel currents were approximated with the measured sample variances.

The above assumptions imply that the difference of any two channel currents is also a normally distributed random variable, whose variance is the sum of the variances of the two currents. Thus, approximating the mean of the difference of two currents by the difference of the sample means, the 95% confidence limits on ΔI_i were estimated by:

$$(\bar{I}_i - \bar{I}_{i+1}) \pm 1.96\,\zeta_i \tag{A.3}$$

where:

$$\zeta = (\mathrm{var}(I_i) + \mathrm{var}(I_{i+1}))^{1/2}$$

4.0 NINETY-FIVE PERCENT CONFIDENCE LIMITS ON D

Assuming NO oxidation was frozen for temperatures below 500 K the dilution ratio is given by:

$$D = NO_S/NO_D \tag{A.4}$$

where:

NO_S = Stack exhaust concentration of NO

NO_D = Diluted exhaust concentration of NO.

The true values of NO_S and NO_D were not known. Thus, they were represented as normally distributed random variables. It is shown hereafter that the two concentrations could be represented as follows:

$$NO_S = \overline{NO}_S(1+\varepsilon_C+\varepsilon_H) \tag{A.5}$$

$$NO_D = ((\overline{NO}_D-B)/A) \times (1+\varepsilon_C+\varepsilon_L) \tag{A.6}$$

where:

$\overline{NO}_S$ = Mean value of NO_S (from chart record)

$\overline{NO}_D$ = Mean value of NO_D (" " ")

$\varepsilon_C, \varepsilon_H, \varepsilon_L$ = Independent normal random variables of zero mean (each is discussed below).

Thus:

$$D = \left[\overline{NO}_S(1+\varepsilon_C+\varepsilon_H)\right] / \left[((\overline{NO}_D-B)/A)(1+\varepsilon_C+\varepsilon_L)\right]. \qquad (A.7)$$

The 95% confidence limits on D were estimated by assuming that ε_C , ε_H, and ε_L are independent, and computing 98.3% (= 100% x $(.95)^{1/3}$) confidence intervals for these variables. The maximum and minimum values of the above ratio corresponding to all possible combinations of the extrema of these limits were then used to estimate the 95% confidence limits of D.

The above representations of the diluted and undiluted concentrations of NO as random variables are considered below.

5.0 REPRESENTATION OF HIGH-LEVEL (UNDILUTED) NO CONCENTRATION

The chemiluminescent nitric oxide analyzer (Teco) is a linear-response instrument on all of its scales. Calibration at high NO levels (100-1000 ppm) indicated that it is reasonable to assume:

$$NO_{Act} = NO_{Tec} \times (1+\varepsilon_H') \qquad (A.8)$$

where:

NO_{Act} = True NO concentration

NO_{Tec} = NO concentration indicated by Teco

ε_H' = Dimensionless normally distributed term due to inherent instrument error.

The parameter var(ε_H') was estimated by calculating the sample variance of (NO_{Act}-NO_{Tec}) for several random measurements of NO concentration in the span gas (Nominal span gas NO concentration was assumed to be exact).

From the chart record of exhaust gas NO concentration, the temporal variation of exhaust (stack) NO could be represented by:

$$NO_{S,Tec} = \overline{NO}_S(1+\varepsilon_S) \qquad (A.9)$$

where:

$NO_{S,Tec}$ = Teco measurement of exhaust (stack) NO concentration

$\overline{NO}_S$ = Mean measurement of NO by Teco from chart record

ε_S = Dimensionless normal error term, with zero mean, and variance determined from sample variance of chart record.

Presumably, the error term ε_S was due to combustion condition variation and instrument variation, which were assumed independent. Thus:

$$\varepsilon_S = \varepsilon_H{}' + \varepsilon_C \qquad \text{(A.10)}$$

where:

$\varepsilon_{\check{C}}$ = Dimensionless normal variation in NOS due to combustion condition variation.

Var(ε_C) was thus evaluated from the following equation:

$$\text{var}(\varepsilon_S) = \text{var}(\varepsilon_H{}') + \text{var}(\varepsilon_C) \qquad \text{(A.11)}$$

implying:

$$\text{var}(\varepsilon_C) = \text{var}(\varepsilon_S) - \text{var}(\varepsilon_H{}').$$

Var(ε_S) was estimated directly from the sample variance determined by manually digitizing the chart record, and $\varepsilon_H{}'$ was previously estimated from calibration results (See above).

Thus, from the assumed form of the relation above between NO_{Act} and NO_{Tec}:

$$NO_{Act} = NO_{Tec} \times (1 + \varepsilon_H{}') \qquad \text{(A.12)}$$

$$= \overline{NO}_S \times (1+\varepsilon_S) \times (1+\varepsilon_H') \qquad (A.13)$$

$$= \overline{NO}_S \times (1+\varepsilon) \qquad (A.14)$$

where:

$$\varepsilon = \varepsilon_S + \varepsilon_H' + \varepsilon_S\varepsilon_H' .$$

By neglecting the second-order term, and defining $\varepsilon_H = 2 \times \varepsilon_H'$, the representation of $NO_{S,Act}$ as a random variable claimed above (Eq. A.5) was obtained, and 98.3% confidence intervals were estimated by a straightforward computation, using the assumed normal form of the error terms and the variances calculated aove.

6.0 REPRESENTATION OF LOW-LEVEL (DILUTED) NO CONCENTRATION

The error in the diluted NO measurement was due to instrument error, combustion variation, and dilution ratio variations in the probe. To evaluate the instrument error, the Teco was calibrated for low NO concentrations using a span gas (206 ppm) which was diluted with high-purity bottled nitrogen to obtain arbitrary NO concentrations. Gas flows were measured with Matheson rotameters which had been calibrated using bubble flowmeters and a stopwatch. From the calibration data for the rotameters the following relation was assumed:

$$q = Q + \varepsilon' \qquad (A.15)$$

where:

q = Actual volume flow rate through rotameter

Q = Nominal flow rate from curve fit to calibration data

ε' = Assumed normally distributed random error term of zero mean and variance var(ε').

Var(ε') was estimated by using the sample variance of the data points.

From the low-level (0-10 ppm) Teco calibration the following approximate relation was assumed:

$$\overline{NO}_{Tec} = (\overline{NO}_{Nom} + B) \times A \qquad (A.16)$$

where:

Bars indicate mean values

$\overline{NO}_{Tec}$ = NO concentration indicated by mean Teco reading

$\overline{NO}_{Nom}$ = nominal NO concentration calculated from mean rotameter measurement of span and dilution gas flows

A,B = linear least squares regression coefficients for the relationship between $\overline{NO}_{Nom}$ and $\overline{NO}_{Tec}$.

Rearranging the above relation:

$$\overline{NO}_{Nom} = (\overline{NO}_{Tec} - B)/A \qquad (A.17)$$

From this equation the relation between the measured values of NO_{Nom} and NO_{Tec} for any given run was approximated by:

$$NO_{Nom} = ((NO_{Tec} - B)/A) \times (1 + \varepsilon'') \qquad (A.18)$$

where:

ε'' = normally distributed error term of zero mean.

Since the mean value of NO_{Nom} is NO_{Act}, it was assumed that the relationship between NO_{Act} and NO_{Tec} is identical to that above, except for a different error term:

$$NO_{Act} = ((NO_{Tec}-B)/A) \times (1+\varepsilon_L) \qquad (A.19)$$

The parameter $var(\varepsilon_L)$ was estimated from calibration data by reasoning as follows. The true concentration of NO in the calibration gas is:

$$NO_{Act} = (q_1 \times \gamma)/(q_1+q_2) \qquad (A.20)$$

where:

q_1 = flow rate of span gas

q_2 = flow rate of diluent gas

γ = NO concentration in span gas.

Substituting the relations between measured and actual flow rates

(Eq. A.15):

$$NO_{Act} = (q_1 \times \gamma)/(q_1+q_2) \qquad (A.21)$$

$$= ((Q_1+\varepsilon_1) \times \gamma)/((Q_1+Q_2)+(\varepsilon_1+\varepsilon_2)) \qquad (A.22)$$

where:

ε_1, ε_2 = Normal error terms from rotameter calibration results.

To simplify calculations, it was assumed that:

$$NO_{Act} = NO_{Nom} + \varepsilon_R \qquad (A.23)$$

where:

ε_R = Normal random variable of zero mean

NO_{Nom} = Nominal NO concentration from rotameter-determined flow rates

$= (Q_1 \times \gamma)/(Q_1+Q_2)$

and var(ε_R) was estimated by calculating:

$$\gamma^2 \times E\left[(q_1/(q_1+q_2)) - (Q_1/(Q_1+Q_2))\right] \qquad (A.24)$$

where:

$E[x]$ = expected value of random variable, x

for various values of q_1 and q_2 representative of the calibration runs, and then averaging these values.

The desired parameter var(ε_L) (variance of low-level NO instrument) was then obtained by using the previous equation(Eq. A.19):

$$NO_{Act} = ((NO_{Tec}-B)/A) \times (1+\varepsilon_L), \qquad (A.25)$$

substituting NO_{Act} from Eq. A.23:

$$NO_{Nom} = ((NO_{Tec}-B)/A) \times (1+\varepsilon_L) - \varepsilon_R. \qquad (A.26)$$

This implies:

$$\mathrm{var}(NO_{Nom}-((NO_{Tec}-B)/A)) = \mathrm{var}(((NO_{Tec}-B)/A \times \varepsilon_L)-\varepsilon_R) \qquad (A.27)$$

Assuming independence of ε_L and ε_R , and assuming some fixed value of NO_{Tec}, (NO_{Nom} then is considered the random variable) the variance of the right side of the above equation is given by:

$$\mathrm{var}(RHS)=((NO_{Tec}-B)/A)^2 \times \mathrm{var}(\varepsilon_L)) + \mathrm{var}(\varepsilon_R). \qquad (A.28)$$

The variance of the left side of Eq. A.27 was estimated from the sample variance of the expression in parentheses using calibration data and the least squares fit parameters A and B. Thus:

$$\text{sample var(LHS)} = \mathrm{var}(RHS) = ((NO_{Tec}-B)/A)^2 \times \mathrm{var}(\varepsilon_L) + \mathrm{var}(\varepsilon_R) \qquad (A.29)$$

which implies:

$$\mathrm{var}(\varepsilon_L)=(\text{sample var(LHS)}-\mathrm{var}(\varepsilon_R))/((NO_{Tec}-B)/A)^2. \qquad (A.30)$$

Using the above expression for the instrument error ε_L, the total measurement error in the diluted NO concentration of the diluted aerosol sample stream may now be considered. The form of the relation between NO_{Act} and NO_{Tec} (Eq. 4.19) suggests a similar form for the relation between NO_{Act} and the mean value of NO measured from the chart record for the diluted NO concentration in the sample aerosol stream. Thus:

$$NO_{Act} = ((\overline{NO}_C-B)/A) \times (1+\varepsilon''') \qquad (A.31)$$

where:

$\overline{NO}_D$ = Mean value of $NO_{D,Tec}$ from the chart record

ε''' = Assumed normal error term of zero mean

= $\varepsilon_P+\varepsilon_C+\varepsilon_L$

ε_P = Dimensionless error due to variation in actual dilution ratio in the probe

ε_C = Dimensionless error due to variation in the combustion condition

ε_L = Dimensionless low-level NO instrument error.

The error due to the variation of dilution ratio inside the probe was manifest in two measurements: (1) The particle current indicated by the EAA, and (2)The NO concentration in the diluted stream. To avoid counting the probe dilution error twice in the calculation of the stack aerosol size distribution, it was now discarded from the expression for NO_{Act}, since it had already been incorporated in the variance of the EAA current difference ΔI_i. Thus:

$$NO_{D,Act} = ((\overline{NO}_D - B)/a) \times (1 + \varepsilon_C + \varepsilon_L) \qquad (A.32)$$

as originally claimed (Eq. A.6).

The required confidence intervals for NO in the denominator of the expression for D were computed using the above variance estimates in a straightforward manner from the normal form of the distributions of the error terms and their assumed independence. From these confidence intervals the uncertainty limits for the particle size distribution histogram approximation were calculated, as previously discussed.

APPENDIX B

SAMPLING SYSTEM PERFORMANCE

In this appendix are discussed three aspects of the performance of the sampling system used in the experiments: (1)The predicted performance of the probe sampling tip in separating large particles from the sample flow, as indicated by a crude simulation; (2)The biasing effect of non-isokinetic sampling in the secondary probe (See discussion of probe in Chapter 3); (3)The biasing of the measured size distribution due to particle losses to the walls of the sampling system.

1.0 DESIGN CALCULATIONS FOR SAMPLING PROBE TIP

The purpose of the aerosol sampling probe was to collect a representative sample of the submicron particles from the furnace exhaust to be analyzed for mass and composition distribution with respect to particle size. Particles larger than 5-10 microns in diameter were not analyzed and thus to minimize probe fouling it was desirable to eliminate such particles from the sample stream at the probe inlet. To accomplish this objective the probe inlet configuration discussed in Chapter 3 was utilized (See Figure 3.10). The performance of this configuration was evaluated analytically by using the results of Zebel (1978) who studied the effect of such sampling configurations in biasing the measured size distributions of sampled aerosols.

Zebel estimated the biasing effect of the axisymmetric sampling configuration shown in Figure B.1(a) (which is similar to the probe configuration used in these experiments) by analyzing the analogous two-dimensional flow shown in Figure B.1(b). He computed the velocity field of the gas entering the slit in the two-dimensional flow field by assuming inviscid potential flow into the slit, and superposed a uniform velocity field U, which represents the velocity field of the sampled exhaust stream. Using this velocity field he computed particle trajectories by numerical solution of the equations describing the particle motion:

$$\ddot{x} = (v_x - \dot{x})/St$$

$$\ddot{y} = (v_y - \dot{y})/St$$

where:

(x,y) = Position of particle at time t

v_x, v_y = Fluid velocity components at (x,y)

St = Stokes number

$= m \times B \times V / R$

m = Particle mass

B = Particle mobility

$= 1/(\pi \mu r_p)$

μ = Fluid viscosity

r_p = Particle radius

V = Fluid velocity into sampling slit

R = Slit half-width.

Zebel then defined a particle collection efficiency parameter S, as follows:

$$S = c_s(d_p)/c_o(d_p)$$

where:

$c_s(d_p)$ = Concentration of particles of size d_p in sample stream entering slit

$c_o(d_p)$ = Concentration of particles of size d_p in sampled stream.

Using the results of his particle trajectory calculations he calculated S for various values of St and the uniform flow velocity U. His results showed that S may be expressed as a function of the Stokes number with respect to the uniform flow velocity U (St′), and independent of V, as follows:

$$S = 1/(1 + 1.09St')$$

where:

$St' = m \times B \times U/R$

Using Zebel′s two-dimensional model and the above relation to describe the performance of the sampling probe in the present experiments the following table of values of S was calculated using exhaust gas flow conditions which were typical:

d_p (microns):	1.0	10.0	25.0	50.0	100.0
S :	.99	.88	.55	.24	.071

The above table indicates that the submicron particle concentration in the gas entering the probe was within 1.0% of the exhaust gas being sampled, while the concentration of 25-micron particles was reduced by nearly 50%. It was concluded that the probe was effective in achieving the desired aerodynamic separation of large particles from the sample stream.

2.0 EFFECT OF NON-ISOKINETIC SAMPLING INSIDE THE PROBE

As previously discussed, in order to maintain total dilution air flows under 20 lpm, it was necessary to sample only a fraction of the inlet flow to the probe. The ′probe-within-a-probe′ flow fractionating scheme utilized (see Figure 3.10) ideally required isokinetic sampling by the secondary probe. May (1967) has studied the problem of biasing particle size distribution measurements due to non-isokinetic sampling in such a sampling configuration. He performed experiments with particles of unit density. His results indicate that for particle sizes below 5.0 microns diameter, and for values between 0.0 and 2.0 of the velocity ratio:

U_m/U_s

where:

U_m = Velocity of stream to be sample parallel to sampling probe

U_s = Velocity of sample stream entering probe

the difference between the particle concentration in the sampled aerosol stream and the aerosol entering the probe is less than 10%. For particles of specific gravity 2.0 one would expect the same conclusion to be valid but for all particles smaller than about 2.5 microns. Since the above velocity condition was nominally satisfied in all of the current experiments, the biasing of the submicron particle size distribution due to non-isokineticity in the secondary probe was assumed to be negligible.

3.0 WALL PARTICLE LOSSES IN THE PROBE AND SAMPLE LINES

Diffusion of particles to the walls of the probe and/or sample lines could bias the particle size distribution measurements. Turbulent and laminar diffusion of suspended particles inside a tube or duct have been discussed by Friedlander (1977). Utilizing the expressions he uses for fractional losses by wall diffusional deposition in laminar and turbulent duct flow, expected particle losses were calculated as a function of particle size in the sampling probe and lines in the present experiments.

For typical sampling flow rates and sampling line dimensions the following particle penetrations were calculated:

Penetration:	Particle diameter (microns)			
	0.01	0.025	0.05	0.1
Probe:	0.77	0.94	0.98	1.0
Sampling lines:	0.97	0.99	1.0	1.0

For the particle size range of interest, predicted sampling line and probe losses were deemed sufficiently small to be neglected, and no back-corrections of aerosol size distribution were done to account for diffusional losses in the probe and sampling lines.

APPENDIX C

CONFIDENCE LIMITS ON SPECIES MASS FRACTIONS

To estimate 95% confidence limits on the mass fractions of the refractory species in size-segregated mass samples from the low-pressure impactor the following procedure was used.

First, it was assumed that the true mass of a given species in any specific mass sample could be represented as a random variable as follows:

$$w_j = \bar{w}_j + \varepsilon_j$$

where:

$\bar{w}_j$ = Nominal measured mass of species j from PIXE analysis of sample

ε_j = Normal random variable (GRV) of zero mean and standard deviation (σ_j) equal to the value reported with the PIXE analysis of the sample.

Such a representation implies a non-zero probability that the true mass of species is negative. The normal representation also admits a non-zero probability of any finite value of the mass. Thus, in order to eliminate the possibility of a negative value for the true mass of species, and to truncate the probability distribution function at some finite value (in order to perform the numerical integrations required to evaluate the expected mean and standard deviation of the mass fraction), a second representation (w_j') of the probability distribution function for the true mass of species was introduced. It was obtained by truncating the originally-assumed normal distribution at zero and $3\sigma_j$, and then normalizing by the area under the distribution in order that the zeroeth moment be unity, as required.

The mass fraction of species j is given by the following equation:

$$f_j = w_j/(w_j+W_j)$$

where:

$W_j = \sum_{k\neq j} w_k$ = Total mass of species other than species j.

The total mass (W_j) of all species other than species j in a given mass sample was calculated from the sum of its normally distributed components. The sum is also normally distributed with mean and standard deviation calculated from the means and standard deviations of its components as follows:

$$W_j = N_j + S_j$$

where:

$N_j = \text{mean}(W_j) = \sum_{k\neq j} \overline{w}_k$

S_j = GRV of zero mean and standard deviation, η_j, equal to $(\sum_{k\neq j} \text{var}(\varepsilon_k))^{1/2}$.

The distribution of W_j was truncated as in the case of the individual species′ distributions to obtain a second variable W_j'.

The mean and variance of the mass fraction f_j of species j was obtained by numerical evaluation of the appropriate integrals using w_j' and W_j', as follows:

$$\mathrm{mean}(f_j) = \int_0^{3\eta_j}\int_0^{3\sigma_j} \left(\frac{w_j'}{w_j'+W_j'}\right) p(w_j')\,p(W_j')\,dw_j'\,dW_j'$$

$$\mathrm{var}(f_j) = \int_0^{3\eta_j}\int_0^{3\sigma_j} \left(\frac{w_j'}{w_j'+W_j'} - \mathrm{mean}(f_j)\right)^2 p(w_j')\,p(W')\,dw'\,dW'$$

where;

p(x) = Probability density function for variable x.

Finally, the 95% confidence limits on the value of the mass fraction f_j were calculated by treating f_j as if it were a normal random variable, and computing the interval within which f_j would be expected to lie with 95% probability; i.e., the 95% confidence limits were estimated to be:

$$\mathrm{mean}(f_j) \pm (1.96 \times (\mathrm{var}(f_j))^{1/2}).$$

APPENDIX D

DISCREPANCY BETWEEN MASS CONCENTRATIONS BY EAA AND BY PIXE

The discrepancy between the EAA and PIXE measurements of total submicron mass concentration may arise for a number of reasons. First, the EAA measurements may be artificially high. In converting the current outputs from the instrument into particle number concentrations it is assumed that entering particles are electrically neutral. If entering particles were already charged then larger particle currents would be indicated in the instrument than if particles were initially uncharged, resulting in higher measured particle concentrations than actually existed.

To investigate this possibility it was necessary to perform two independent measurements of particle concentrations in the combustion aerosol from the combustor--one utilizing the EAA and the other utilizing another measurement technique. This was done by collecting weighable size-segregated mass samples of flyash aerosol, and comparing the mass concentrations determined gravimetrically with those indicated by the EAA. The Caltech low-pressure impactor is not suitable for this type of measurement, since typical sample weights of fine particles collected using the LPI are of the order of ten micrograms. This is approximately the measurement error of the microgram balance used to weigh the samples. For this reason, a Sierra Instruments Marple cascade impactor was used, since the eccentric positioning of the jets in this instrument permits spreading the collected sample over a much larger area than in the case of the LPI. This allows one to collect much larger mass samples without overloading the impactor collection surfaces. Thus, measurement errors due to particle bounceoff are minimized.

Size distributions of the fine particles indicated by the EAA indicated that most of the mass is in particles below about 0.05 microns in diameter. Consequently, the first six stages of the Sierra impactor were used with a volume flow rate of approximately 3.0 lpm (In contrast with the LPI, the flow rate is adjustable in the Sierra impactor). Using the calibration procedure supplied with the impactor, this flow rate together with the assumption of a particle specific gravity of 2.0, resulted in a calculated 50% cutoff diameter of about 0.044 microns for the sixth stage of the impactor. Assuming that the impactor efficiently collects all particles larger that 0.044 microns, the particles collected on a total filter downstream of the impactor stages would therefore be expected to be the same size as those seen by the EAA. Thus, the mass concentration calculated from the mass of particles collected on the filter should give some indication whether the error in the EAA mass measurements is of the order indicated by the discrepancy with the PIXE measurements (typically a factor of 1 to 4).

In performing the experiment a Fluoropore filter (No. FA-1.0 μm) was chosen because of its superior performance as a total filter for submicron particles (Liu and Lee, 1976). The results of the measurements are shown in Figures D.1 and D.2. The X- and Y-axes are the same as in previous representations of size distribution data. The results of the impactor measurements are indicated by the solid lines, and the error bounds for total mass measurements are reported in the subheading. These bounds are based on the assumption that the entire error in the mass distribution determination is due to errors in the dilution measurement. Since the masses of impactor samples were substantially larger than the absolute error of the balance it was assumed that the weighing error was essentially zero.

In each figure the EAA curves plotted represent the mean of two EAA measurements. Error bounds for the total measured mass concentrations are reported for both measurements. The figures indicate fairly good agreement in the total sub-0.44-micron mass concentrations indicated by the two measurements, implying that the error in the EAA mass concentration measurements was probably not as high as a factor of 4, as the discrepancy with PIXE measurements might suggest. Thus, EAA mass distributions indicated in the foregoing data were assumed to be reasonable (on this basis). Fair agreement in the submicron mass concentration between the laboratory data and field data (Figure 5.14) also suggests that the mass concentrations from EAA measurements are accurate.

A second possible explanation for the discrepancy between EAA and

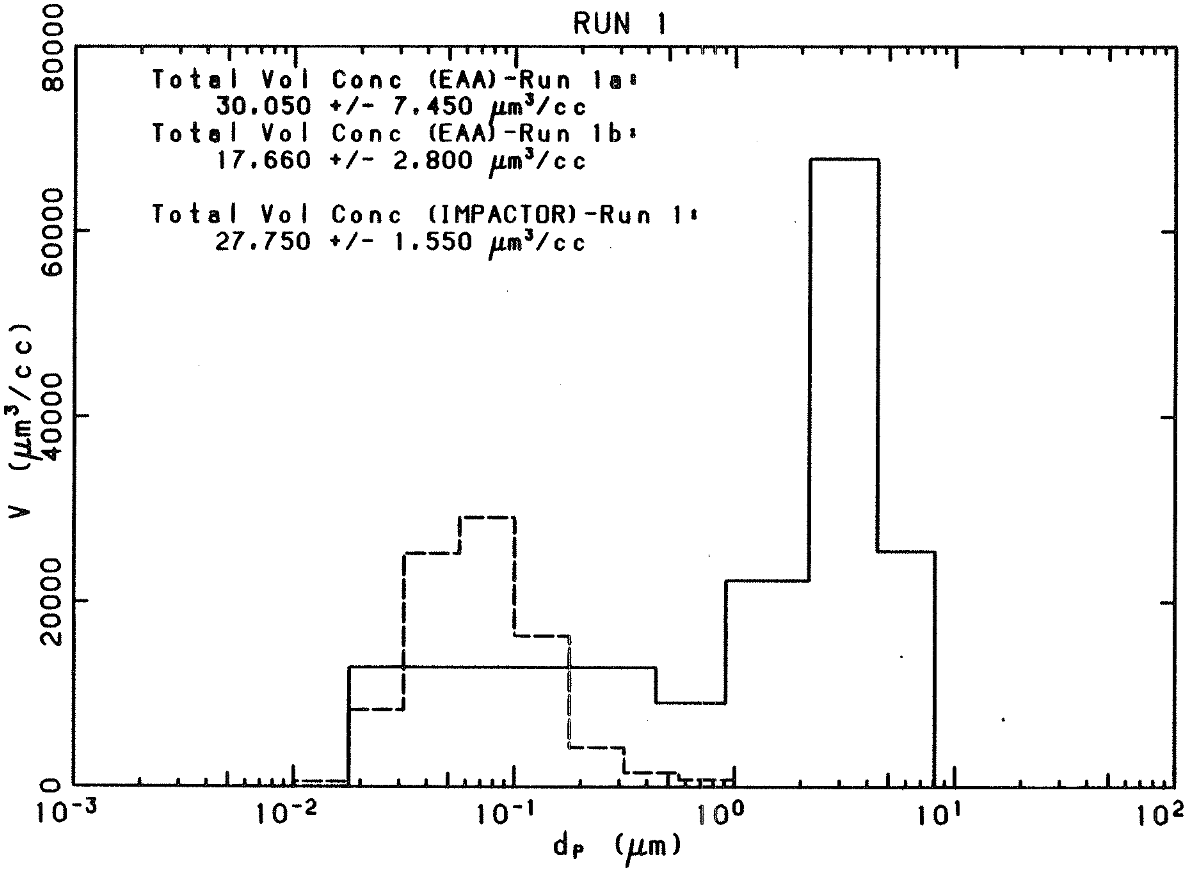

Figure D.1: Mass distribution of fly ash particles measured by EAA compared to that indicated by cascade impactor (Sierra Instruments Marple) measurements. EAA measurements were taken before and after impactor sampling.

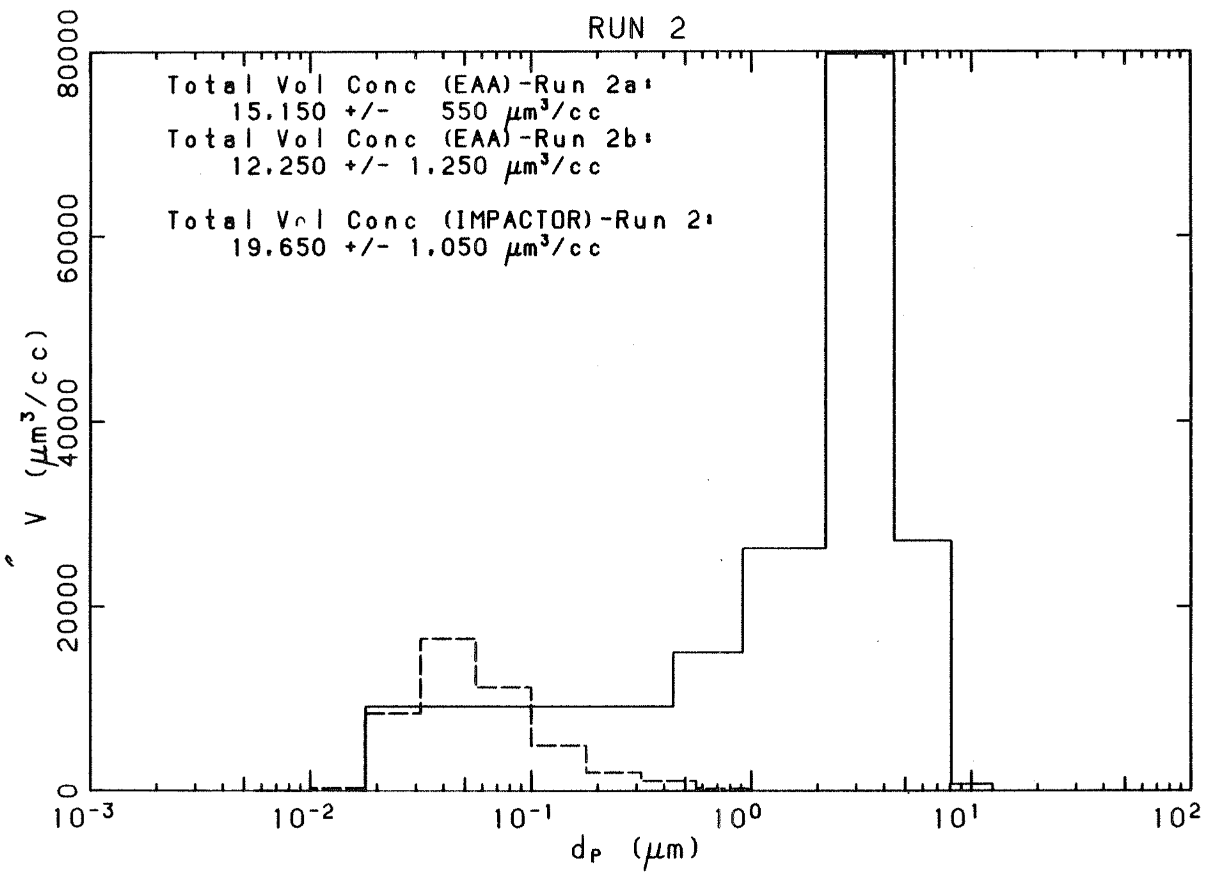

Figure D.2: Mass distribution of fly ash particles measured by EAA compared to that indicated by cascade impactor (Sierra Instruments Marple) measurements. EAA measurements were taken before and after impactor sampling.

PIXE mass concentrations is that species not detectable by the PIXE analysis contributed significantly to the particle mass measured by the EAA. Among these species are carbon and water, either or both of which could be present in the particles in substantial quantities (water, from the oxidation of hydrogen in the coal, and carbon from unburned char and/or soot leaving the combustor).

A third possibility is that the PIXE analysis was inaccurate. To investigate this possibility, independent analyses of the compositions of similar mass samples were performed and compared with the results of PIXE measurements. In addition, composition measurements by PIXE for mass samples of known composition were obtained.

In the first comparison, aerosol samples were collected concurrently in two cascade impactors. The samples from one impactor were analyzed by PIXE, while those of the second impactor were analyzed for sulfur only by the method of flash vaporization/flame photometric detection of sulfur (Roberts and Friedlander, 1976). The comparison of the results is shown in Figures D.3, D.4, and D.5.

In these figures the size distribution of the sulfur in the ash, as indicated by PIXE is shown by the solid line, while that indicated by flashing is shown by the broken line. The figures indicate qualitative agreement between the two techniques, although on some impactor stages discrepancies appear to be larger than measurement error (Accuracy esti-

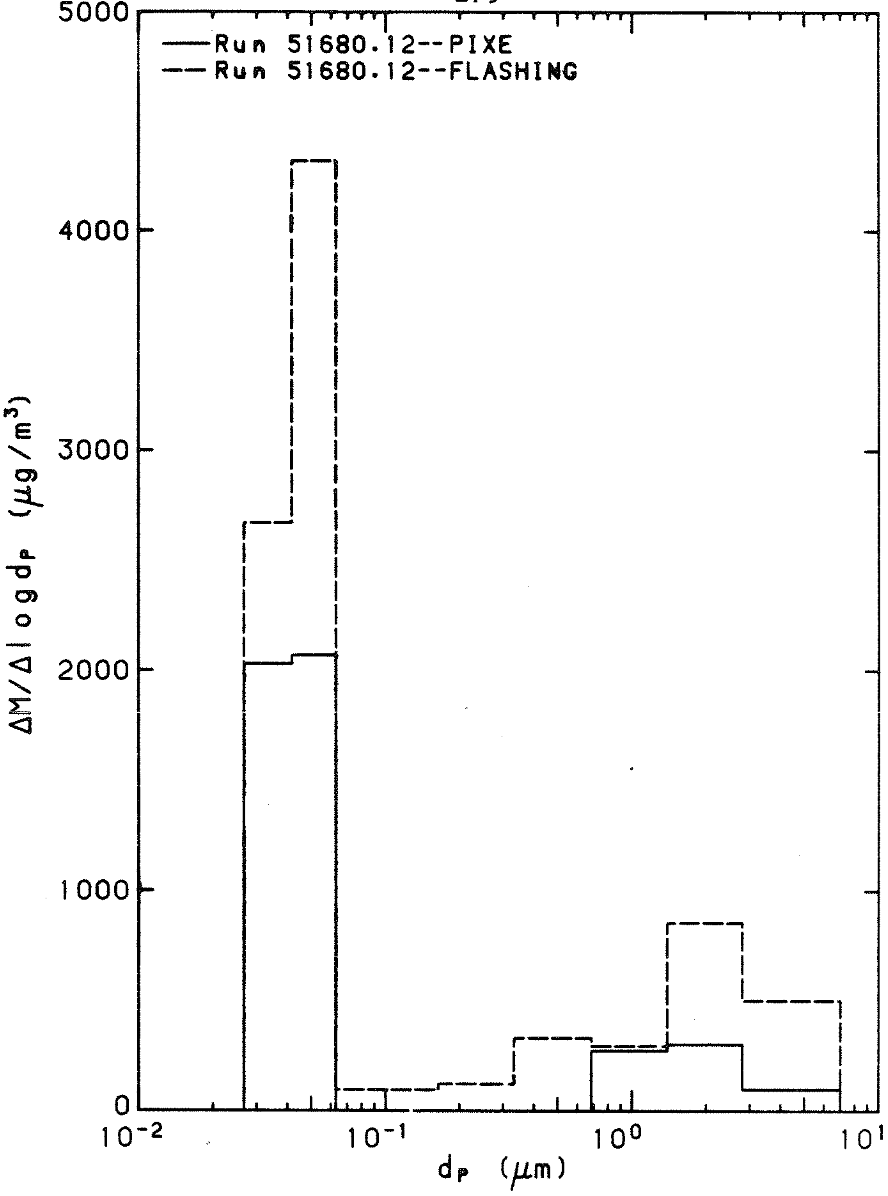

Figure D.3: Mass distribution of sulfur indicated by PIXE compared with that determined from flashing for run 51680.12.

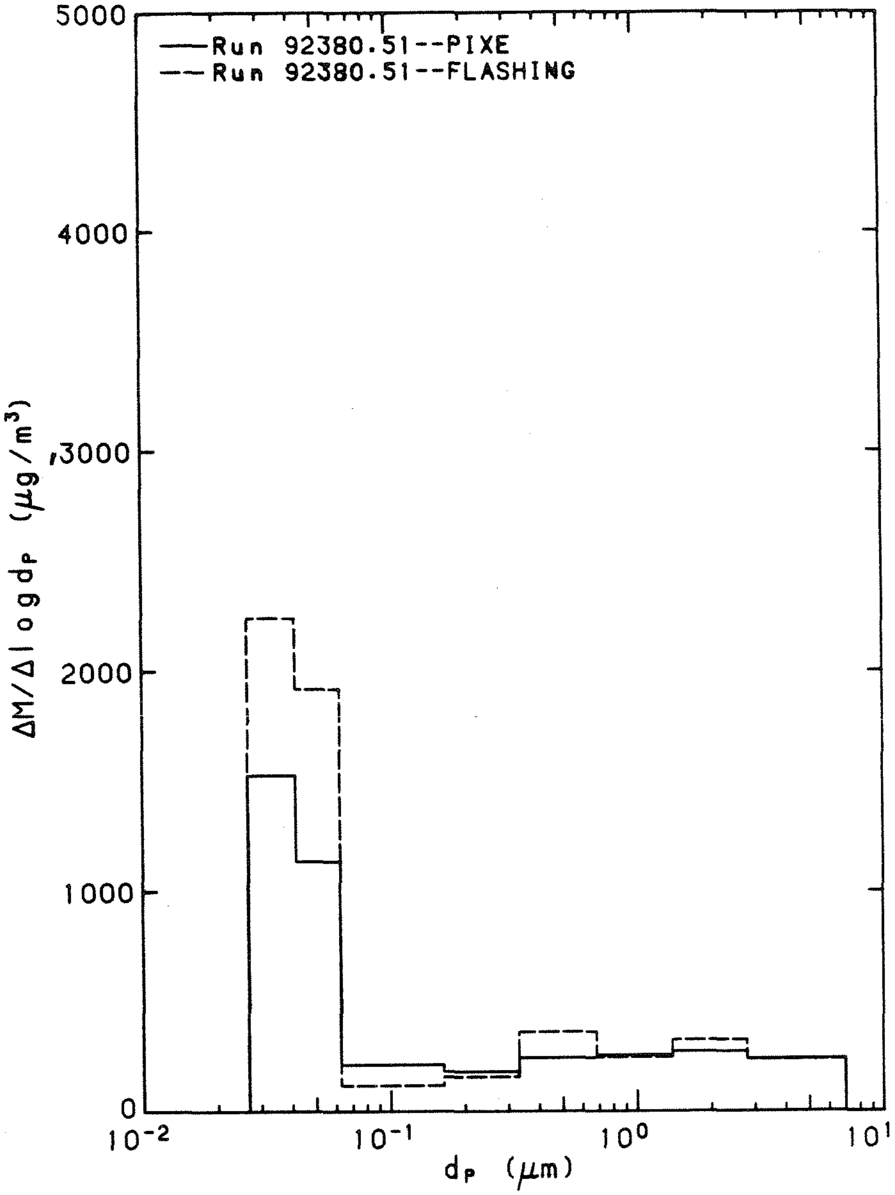

Figure D.4: Mass distribution of sulfur indicated by PIXE compared with that determined from flashing for run 92380.51.

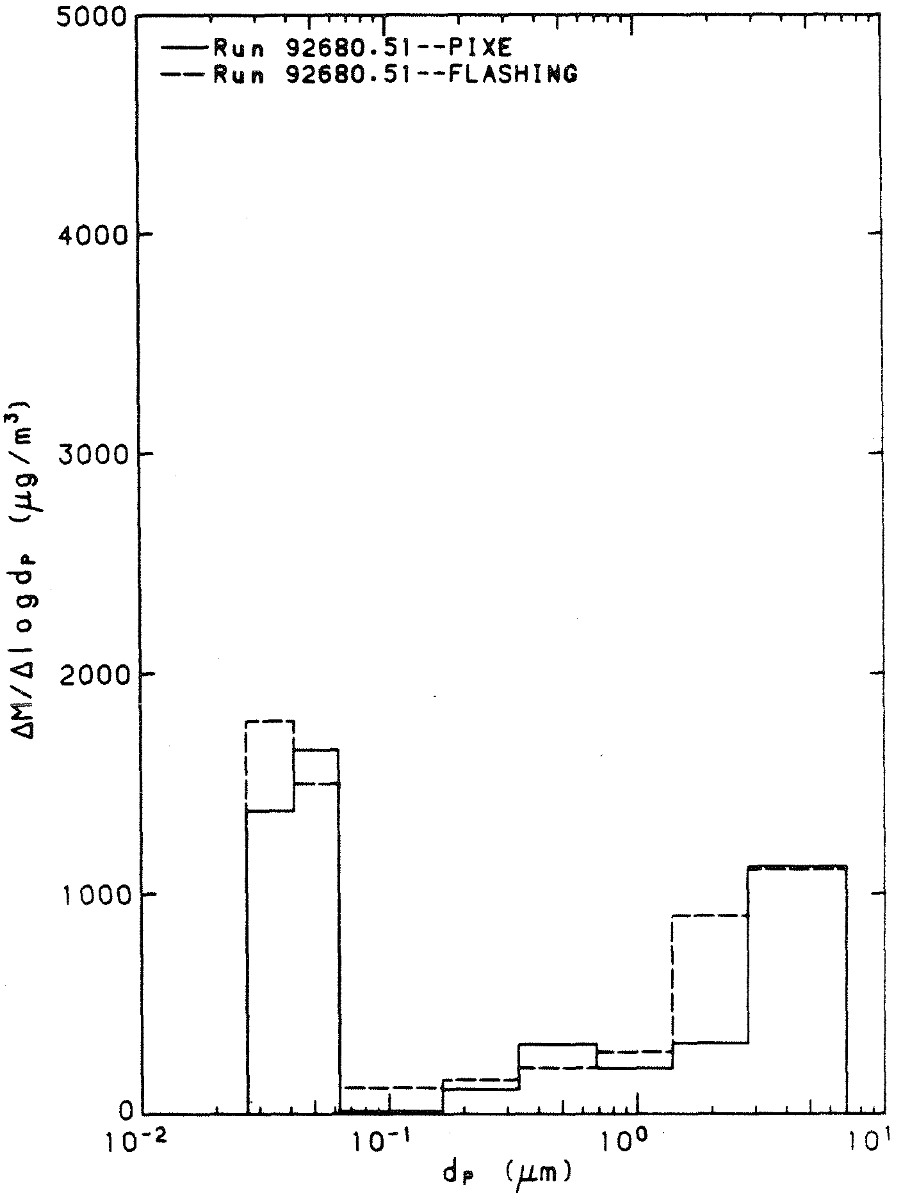

Figure D.5: Mass distribution of sulfur indicated by PIXE compared with that determined from flashing for run 92680.51.

mates for PIXE and for the flashing technique are generally about ±10% of the nominal value). One might first suspect that the two sets of samples collected were not identical due to unavoidable differences between the two impactors and the sampling lines. Due to unavailability of identical stripping stages (See Chapter 3 for a discussion of the use of stripping stages to eliminate large particles from the sampled aerosol) for both impactors, the first three stages of the two cascades were not identical. This would affect the indicated mass distribution of the larger particles (corresponding to the first three stages) but it would not be expected to affect that of the smallest particles, unless there were some bounce-off of large particles. Since visual inspection of larger-particle stages of the impactor following the stripping stages indicated much lower mass loading than on the three stripping stages themselves, and since there was no indication of bounce in the lower-stage PIXE data (A small number of large particles on the lower stages from bounce-off would have resulted in much higher total mass loadings on the lower stages), it was concluded that significant bounce-off did not occur. Thus, the data suggest a possible random error as high as a factor of two or three between the PIXE and the flashing techniques.

The second technique used to evaluate the accuracy of the PIXE analysis involved the preparation of standard solutions of known composition. Mass samples of suitable size were prepared from these solutions for analysis by PIXE. The solutions were prepared by dissolving standard reagents in strongly-acidic solutions, and then transferring measured microliter volumes of these solutions to substrates suitable for PIXE. A description of the solutions and the reagents used is given in Table D.1.

The masses of three species in the solutions indicated by PIXE, and by the gravimetric preparation of the solutions, is indicated in Table D.2(a) and (b) . The data in Table D.2(a) indicate discrepancies in the masses of the three species of 7 to 86% for the two measurements. Since the solutions were generally acidic, it is possible that part of the iron discrepancy is due to partial dissolution of iron in the stainless-steel tip of the microliter syringe used to prepare the analyzed samples. This might account for the higher masses of iron indicated by PIXE in samples 1 and 3.

It is also possible that less volume of solution was transferred by the syringe than the nominal value indicated by the graduation on the syringe. However, one would not expect an error of more than 10% of the maximum capacity of the syringe. This error is lower than the highest observed discrepancy. In addition one would expect that if the gravimetric analysis of the solution composition and the PIXE indication of the species masses on the prepared substrates were correct then the relative concentrations of the sulfur and silicon should be identical for both analyses, independent of the actual volume transferred to the substrates. As indicated in Table D.2(b), however

Table D.1

Description of Solutions Used for Comparison of PIXE and Gravimetric Analyses of Composition

---

Stock Reagents Used:

A Solid Na_2SiF_6

Sodium Fluorosilicate CB1020 SX560
Reagent, powder F.W. 188.05

B Sodium Sulfate Solution, 0.31240M

From 'Baker Analyzed' Reagent grade Anhydrous Sodium Sulfate Na_2SO_4 F.W. 142.04

C Iron Solution, 0.044652M Fe, 1/5 conc. HCl

From 'Baker Analyzed' Reagent grade Iron Wire-.009" 2234, Lot 90647 At. Wt. 55.85

And from Mallickrodt A.C.S. Hydrochloric Acid, HCl, F.W. 36.5. 37.7%

D Iron Solution, 0.044464M Fe, 2/5 conc. HNO_3

From G. Frederick Smith Hydrated yellow Ferric Perchlorate, reagent $Fe(ClO_4)_3 \cdot 6H_2O$ #39 F.W. 462.32

And from Mallickrodt A.C.S. Nitric Acid, HNO_3, F.W. 63.0. 70.2%

Composition by Gravimetric Determination:

Concentration (gm/lit)	Sample 1	Sample 2	Sample 3
Fe	1.00	.745	1.24
S	.401	.280	.200
Si	.888	.587	.481
Iron Solution Used	C	D	D

there is some discrepancy in this parameter as well.

Contamination of the mass samples and solutions may have occured, thus biasing the results in an unknown manner. Barring this possibility, there may be some justification for suspecting the accuracy of the PIXE measurements.

Table D.2

Comparison of Composition by PIXE and by Gravimetric Analyses

(a) Absolute Mass (μgm):	Sample 1		Sample 2		Sample 3	
	PIXE	GRAV	PIXE	GRAV	PIXE	GRAV
Fe	2.8	1.5	.57	1.1	3.4	1.9
S	.45	.60	.18	.42	.38	.30
Si	.77	1.3	.29	.88	.77	.72
(b) Mass Relative to Sulfur:						
Fe	6.2	2.5	3.2	2.7	8.8	6.2
S	1.0	1.0	1.0	1.0	1.0	1.0
Si	1.7	2.2	1.6	2.1	2.0	2.4

APPENDIX E

EFFECT OF DISSOCIATION ON FLAME TEMPERATURE

To estimate the effect of dissociation of CO, CO_2, and H_2O on the gas temperature calculated from energy balance considerations a simple equilibrium calculation was performed as follows.

For a given gas temperature and overall stoichiometry typical of the model calculations described earlier, the mass-specific mixture enthalpy was calculated assuming complete oxidation of carbon and hydrogen to CO_2 and H_2O. The temperature of the mixture was then recalculated assuming the same mass-specific enthalpy but assuming equilibrium concentrations of CO, H_2O, CO_2, H_2, and O_2, established via the following reactions:

$$CO + H_2O = CO_2 + H_2$$

$$CO_2 = CO + 1/2O_2$$

Data for calculation of equilibrium constants were taken from JANAF tables (Stull and Prophet, 1971).

The results of the calculation are shown in Figure E.1. Mixture temperature with complete oxidation of carbon and hydrogen is plotted against mixture temperature with dissociation. Overall equivalence ratio is indicated as a parameter.

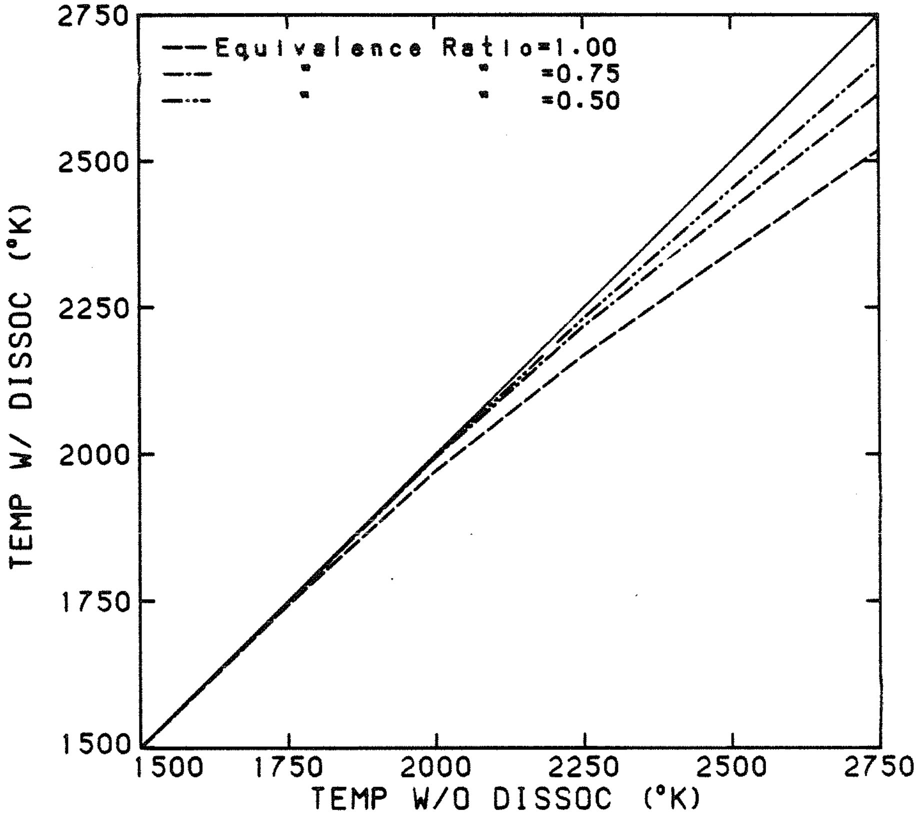

Figure E.1: Gas temperature assuming no gas dissociation vs temperature with equilibrium dissociation of CO_2 and H_2O, for various values of local equivalence ratio.

The calculation indicates that the maximum error in neglecting dissociation in calculations of gas temperature is about 250 K. In the present study the calculated peak gas temperature was about 2400 K and the local equivalence ratio was between 1.0 and 0.5. Thus, the figure indicates that the maximum error in the temperature due to neglect of dissociation is about 50-75 K.

APPENDIX F

COMBUSTION PARAMETERS AND AEROSOL CONCENTRATIONS FROM EXPERIMENTS

(Units of Parameters on Page 293)

Run	V	T_w	T_{pre}	ϕ	t	NO	S	U
110179.01	******	1427.	707.	0.90	2.02	503.	4.40	-265.
121879.01	******	1494.	684.	0.77	1.44	575.	0.32	430.
121879.02	******	1492.	653.	0.79	1.44	600.	0.24	408.
121879.03	******	1493.	659.	0.76	1.48	560.	0.19	467.
121879.04	******	1494.	668.	0.83	1.48	630.	0.20	465.
121879.06	******	1498.	670.	0.83	1.48	630.	0.21	452.
121879.07	******	1499.	686.	0.81	1.47	610.	0.21	489.
121879.09	******	1509.	673.	0.81	1.48	520.	0.18	454.
121879.11	******	1516.	680.	0.80	1.47	540.	0.17	472.
121879.12	******	1514.	679.	0.81	1.50	525.	0.17	493.
121879.13	******	1514.	685.	0.82	1.50	535.	0.17	496.
121879.14	******	1525.	704.	0.84	1.49	515.	0.17	510.
121879.15	******	1523.	705.	0.81	1.50	480.	0.35	529.
121879.16	******	1522.	716.	0.77	1.42	1230	0.48	2968.
121879.17	******	1520.	736.	0.78	1.54	340.	0.71	508.
121879.18	******	1514.	659.	0.76	1.44	990.	0.16	2737.
122179.01	******	1475.	622.	0.78	1.45	720.	0.13	513.
122179.02	******	1473.	677.	0.79	1.52	720.	0.14	411.
122179.03	******	1474.	686.	0.79	1.53	715.	0.14	419.
122179.04	******	1477.	693.	0.79	1.52	715.	0.14	527.
122179.05	******	1478.	701.	0.77	1.53	715.	0.14	502.
122179.06	******	1477.	703.	0.76	1.53	660.	0.15	569.
122179.07	******	1473.	707.	0.75	1.53	700.	0.15	561.
122179.08	******	1464.	704.	0.73	1.51	765.	0.14	1620.
122179.09	******	1461.	705.	0.74	1.52	765.	0.14	1607.
122179.10	******	1458.	706.	0.74	1.53	820.	0.13	2135.
11080.01	******	1427.	682.	0.78	1.64	790.	0.13	1974.
11080.02	******	1423.	710.	0.76	1.65	775.	0.13	1998.
11080.05	******	1425.	726.	0.75	1.67	690.	0.15	1881.
11080.07	******	1428.	696.	0.74	1.66	700.	0.15	1763.
11080.08	******	1414.	691.	0.60	1.66	685.	0.19	1890.
11080.10	******	1400.	689.	0.66	1.67	770.	0.19	1833.
11080.12	******	1393.	687.	0.66	1.68	770.	0.19	1809.
11080.13	******	1406.	687.	0.84	1.68	810.	0.17	1896.
11080.14	******	1419.	685.	0.77	1.66	810.	0.17	1886.
11080.17	******	1431.	685.	0.80	1.65	830.	0.17	1853.
11080.18	******	1437.	685.	0.81	1.64	795.	0.15	1739.
11080.19	******	1431.	681.	0.80	1.64	790.	0.15	1739.
11080.20	******	1440.	680.	0.84	1.63	790.	0.15	1694.

Run	V	T_w	T_{pre}	ϕ	t	NO	S	U
11080.21	******	1452.	678.	0.84	1.62	690.	0.16	713.
11080.22	******	1461.	675.	0.84	1.61	560.	0.17	691.
12480.01	******	1488.	690.	0.79	1.70	550.	0.19	1738.
12480.04	******	1488.	692.	0.78	1.71	540.	0.19	1689.
12480.06	******	1490.	693.	0.74	1.71	525.	0.19	1646.
12480.07	******	1490.	694.	0.76	1.72	500.	0.19	1621.
12480.10	******	1497.	696.	0.72	1.72	470.	0.19	1564.
12480.11	******	1500.	696.	0.72	1.67	460.	0.19	1881.
12480.12	******	1480.	662.	0.76	1.70	455.	0.20	1522.
12480.13	******	1490.	681.	0.75	1.70	495.	0.19	1528.
20580.01	******	1490.	675.	0.86	1.69	530.	0.16	1610.
20580.02	******	1452.	695.	0.84	1.75	500.	0.18	1643.
20580.03	******	1452.	693.	0.86	1.75	535.	0.18	1640.
20580.04	******	1457.	695.	0.85	1.75	520.	0.18	1647.
20680.06	******	1388.	688.	0.79	1.83	560.	0.18	1616.
20680.07	******	1439.	725.	0.67	1.82	585.	0.21	659.
20680.11	******	1408.	723.	0.65	1.86	595.	0.21	658.
20780.12	******	1419.	686.	0.65	1.85	595.	0.19	624.
20780.15	******	1400.	695.	0.64	1.87	575.	0.20	632.
20780.19	******	1384.	701.	0.66	1.89	615.	0.20	638.
20780.20	******	1375.	739.	0.50	1.91	640.	0.22	686.
20780.23	******	1349.	711.	0.50	1.95	640.	0.22	648.
20780.27	******	1332.	716.	0.50	1.97	640.	0.22	653.
20780.28	******	1344.	718.	0.80	1.95	610.	0.23	655.
20780.31	******	1386.	791.	0.72	1.90	665.	0.21	721.
20780.37	******	1386.	791.	0.73	1.91	675.	0.21	725.
20780.39	******	1349.	807.	0.37	1.96	585.	0.21	739.
21880.06	21426.	1346.	594.	0.51	2.66	694.	0.30	405.
21880.08	21455.	1330.	804.	0.51	2.00	688.	0.21	713.
21880.09	20796.	1326.	806.	0.51	2.00	686.	0.21	714.
21880.10	21176.	1323.	807.	0.51	2.01	684.	0.21	715.
21880.13	16407.	1307.	811.	0.53	2.04	697.	0.21	720.
21880.17	14123.	1287.	809.	0.51	2.07	702.	0.21	719.
21880.24	13072.	1246.	805.	0.51	2.14	631.	0.21	715.
21880.25	13040.	1242.	804.	0.51	2.15	623.	0.21	715.
21880.26	12644.	1237.	804.	0.51	2.15	614.	0.21	714.
31080.18	14409.	1352.	676.	0.62	1.61	632.	0.15	487.
31080.26	13710.	1350.	675.	0.61	1.61	624.	0.15	487.
31180.07	15473.	1355.	673.	0.60	1.61	635.	0.15	485.
31180.13	16951.	1351.	673.	0.60	1.61	634.	0.15	485.
31180.15	16145.	1350.	673.	0.61	1.61	634.	0.15	485.
31180.19	17482.	1348.	672.	0.61	1.62	638.	0.15	484.
32380.18	16419.	1354.	674.	0.61	1.61	641.	0.16	486.
32380.24	17239.	1351.	674.	0.60	1.62	647.	0.16	485.
32580.06	15275.	1309.	712.	0.59	1.67	625.	0.15	513.
32580.14	14759.	1290.	715.	0.57	1.69	622.	0.15	515.
32580.20	15008.	1285.	715.	0.58	1.70	621.	0.15	515.
50880.04	8560.	1234.	694.	0.58	1.77	580.	0.16	-160.
50880.06	8380.	1231.	694.	0.57	1.78	574.	0.16	-160.
50880.12	7118.	1189.	697.	0.55	1.84	530.	0.16	-161.

Run	V	T_w	T_{pre}	ϕ	t	NO	S	U
51280.02	11508.	1263.	701.	0.56	1.74	581.	0.16	-160.
51280.04	11868.	1260.	701.	0.57	1.74	580.	0.16	-160.
51280.12	13949.	1221.	703.	0.55	1.82	570.	0.16	-152.
51680.04	8323.	1225.	702.	0.59	1.79	534.	0.16	-163.
51680.12	7931.	1171.	696.	0.55	1.88	500.	0.17	-155.
82280.10	9156.	1225.	667.	0.58	1.79	478.	0.61	-153.
82280.16	10268.	1218.	671.	0.57	1.80	523.	0.62	-154.
82280.21	8831.	1227.	669.	0.58	1.79	535.	0.16	-153.
82280.22	8404.	1227.	668.	0.58	1.79	533.	0.16	-153.
82980.10	7830.	1361.	675.	0.57	1.61	466.	0.16	-397.
82980.12	6727.	1344.	673.	0.58	1.63	448.	0.16	-395.
82980.35	4170.	1271.	681.	0.57	1.72	355.	0.16	-402.
82980.36	4549.	1272.	683.	0.57	1.72	355.	0.16	-405.
82980.37	4439.	1274.	685.	0.57	1.72	345.	0.16	-406.
82980.38	4514.	1275.	686.	0.58	1.72	343.	0.16	-407.
91680.05	13335.	1462.	723.	0.76	1.51	444.	0.16	-435.
91680.20	19015.	1428.	747.	0.84	1.55	424.	0.16	-449.
91680.22	17493.	1428.	747.	0.81	1.55	422.	0.16	-449.
91980.15	30277.	1365.	782.	0.79	2.01	332.	0.20	-220.
91980.17	27325.	1366.	784.	0.82	2.00	330.	0.20	-222.
91980.41	4762.	1238.	691.	0.57	1.78	359.	0.15	-407.
91980.43	4769.	1240.	696.	0.57	1.77	360.	0.15	-412.
91980.45	4545.	1244.	704.	0.57	1.77	362.	0.15	-419.
91980.47	5022.	1248.	716.	0.58	1.76	365.	0.15	-428.
92380.51	11952.	1434.	742.	0.57	1.52	449.	0.16	-463.
92380.52	11249.	1418.	741.	0.57	1.54	446.	0.16	-463.
92380.53	9826.	1401.	741.	0.57	1.55	440.	0.16	-462.
92380.54	8890.	1389.	742.	0.57	1.57	434.	0.16	-463.
92380.55	9560.	1381.	743.	0.56	1.59	428.	0.16	-458.
92380.56	8911.	1371.	744.	0.56	1.60	420.	0.16	-459.
92380.57	7209.	1349.	742.	0.58	1.63	405.	0.16	-457.
92380.58	7005.	1347.	743.	0.58	1.63	403.	0.16	-457.
92380.59	4217.	1300.	467.	0.56	1.68	418.	0.20	-213.
92380.60	4303.	1298.	465.	0.56	1.68	415.	0.19	-212.
92380.61	3007.	1220.	464.	0.53	1.79	355.	0.17	-211.
92380.62	2847.	1225.	464.	0.54	1.78	350.	0.16	-211.
92680.51	13500.	1433.	744.	0.71	1.55	251.	0.17	-456.
92680.52	11847.	1431.	744.	0.71	1.55	272.	0.17	-456.
92680.53	15073.	1374.	601.	0.71	1.60	225.	0.19	-328.
121180.53	15753.	1333.	684.	0.57	1.65	354.	0.18	-406.
121180.54	16065.	1331.	686.	0.57	1.65	354.	0.18	-408.
121180.61	12393.	1305.	741.	0.59	2.09	412.	0.29	-327.
121180.62	11846.	1308.	745.	0.59	2.09	408.	0.28	-330.
121180.71	12416.	1311.	753.	0.54	2.09	386.	0.28	-336.
121180.72	11926.	1311.	753.	0.54	2.09	386.	0.28	-336.
121680.12	15862.	1273.	714.	0.58	2.08	362.	0.22	-323.
121680.14	41699.	1271.	708.	0.59	2.08	366.	0.23	-319.
121680.16	14817.	1269.	696.	0.59	2.08	370.	0.23	-311.
121680.18	7719.	1267.	687.	0.57	2.09	374.	0.23	-304.
121680.20	11712.	1262.	684.	0.58	2.09	380.	0.23	-301.

Run	V	T_w	T_{pre}	ϕ	t	NO	S	U
121680.22	27075.	1259.	681.	0.61	2.10	387.	0.24	-299.
121680.24	23087.	1257.	720.	0.60	2.09	391.	0.21	-333.
121680.26	22144.	1259.	679.	0.58	2.08	404.	0.22	-303.

Units of parameters in Appendix F:

V:	$\mu m^3/cc$
T_w:	Degrees Kelvin
T_{pre}:	" "
ϕ:	(Dimensionless)
t:	Seconds
NO:	PPM (parts per million)
S:	(Dimensionless)
U:	cm/sec